SMALL-SCALE GRADIENTS IN AEROSOL SIZE DISTRIBUTION AND AEROSOL CHEMICAL COMPOSITION ACROSS THE EXTRATROPICAL TROPOPAUSE

Dissertation
zur Erlangung des Grades
„Doktor der Naturwissenschaften“
am Fachbereich Physik, Mathematik und Informatik
der Johannes Gutenberg-Universität
in Mainz

PHILIPP JOPPE

geb. in Koblenz

Mainz, den 15. September 2025

1. Berichterstatter: PD Dr. Johannes Schneider
2. Berichterstatter: Prof. Dr. Christiane Voigt

Tag der mündlichen Prüfung: 26. November 2025

ZUSAMMENFASSUNG

Die chemische Zusammensetzung der Tropopausenregion, genauer gesagt der oberen Troposphäre und unteren Stratosphäre (UTLS), spielt eine wichtige Rolle bei Veränderungen der Oberflächentemperatur. Veränderungen in der chemischen Zusammensetzung können große Auswirkungen auf den Strahlungshaushalt der Erdatmosphäre haben. Die UTLS und ihre chemische Zusammensetzung werden durch den horizontalen Transport von Luftmassen, den vertikalen Transport in Verbindung mit (hochreichenden) Konvektionssystemen und warm conveyor belts (WCBs), schnellen turbulenten Mischungsprozessen sowie photochemischen Reaktionen beeinflusst.

Die vorgestellten Studien basieren auf zwei verschiedenen flugzeuggetragenen Messkampagnen über Europa aus den Jahren 2020 und 2024, die mit Schwerpunkt auf Mischungsprozessen von Aerosolpartikeln über die Tropopause hinweg analysiert wurden. Dafür wurde die chemische Zusammensetzung von nicht-refraktären Aerosolpartikeln im Submikronbereich, sowie die Gesamtkonzentration und Größenverteilung der Aerosole in Kombination mit In-situ-Spurengasdaten untersucht, um Mischungsprozesse zu identifizieren. Es zeigt sich, dass Sulfataerosol in der unteren Stratosphäre (LMS) durch Vulkanausbrüche beeinflusst wird, die in die obere Troposphäre reichen und bei denen durch anschließendes Mischen über die Tropopause hinweg eine Umwandlung von Gas zu Partikeln stattfindet.
Zusätzlich wurde ein Filament mit einer hohen Aerosolanzahlkonzentration (> 800 cm^{-1}) in Kombination mit hohen CO-Mischungsverhältnissen (> 100 ppbv) in chemisch stratosphärischer Luft ($N_2O < 338$ ppbv) innerhalb einer WCB-Ausflussregion beobachtet. Größenverteilungsmessungen sowie Offline-Analysen von Impaktorproben liefern Hinweise auf Biomasseverbrennung (BB). Trajektoriendaten stützen dies, indem sie den Ursprung der Luftmasse über Kanada in der Nähe aktiver Waldbrände mit anschließendem Transport in niedriger Höhe in Richtung Europa und einem mit einem WCB verbundenen Aufstieg zur UTLS zeigen.

Zusammenfassend liefert diese Arbeit wertvolle Informationen über den Einfluss kleinräumiger Mischungsprozesse auf Aerosolpartikel in der extratropischen UTLS. Darüber hinaus zeigt sie die Bedeutung verschiedener Transportprozesse auf, die für den Aerosoltransport berücksichtigt werden müssen. Sie bildet eine Grundlage für zukünftige Studien und mögliche Modellentwicklungen, um die beobachteten Prozesse in aktuellen Modellen korrekt darzustellen.

ABSTRACT

The chemical composition of the tropopause region, and more precisely the upper troposphere and lower stratosphere (UTLS), plays an important role on surface temperature changes. Changes in the chemical composition may have large impacts on the radiation budget of the Earth's atmosphere. The UTLS and its chemical composition are influenced by horizontal transport of air masses, vertical transport associated with (deep) convective systems and warm conveyor belts (WCBs), rapid turbulent mixing as well as photochemical reactions.

The presented studies are based on two different airborne measurement campaigns over Europe in 2020 and 2024 which were analyzed with the focus on cross-tropopause mixing of aerosol particles. Therefore, the chemical composition of non-refractory submicron aerosol particles as well as the total aerosol number concentration and size distribution measurements were investigated in combination with in-situ trace gas data to identify mixing processes. It is shown that the sulfate aerosol in the lowermost stratosphere (LMS) is influenced by upper tropospheric volcanic eruptions and subsequent cross-tropopause mixing and gas-to-particle conversion.
Additionally, a filament with high aerosol number concentration (> 800 cm^{-1}) in combination with high carbon monoxide (CO) mixing ratios (> 100 ppbv) was observed in chemically stratospheric air (nitrous oxide (N_2O) < 338 ppbv) within a WCB outflow region. Size distribution measurements as well as off-line analysis of impactor samples show indications for biomass burning (BB). Trajectory data support this by showing the air mass origin over Canada close to active wildfires with subsequent low-level transport towards Europe and uplift associated with a WCB to the UTLS.

Summarizing, this thesis yields valuable information on the influence of small-scale mixing processes on aerosol particles in the extratropical UTLS. Furthermore, it shows the importance of different transport processes that need to be considered for aerosol transport. It builds a strong basis for future studies and possible model development in order to represent the observed processes in current models correctly.

CONTENTS

Part I

THESIS

1 INTRODUCTION

1.1 MOTIVATION

The extratropical tropopause region plays an important role with respect to the Earth's surface temperature and the radiative budget of the atmosphere (Riese et al., 2012; Kremser et al., 2016; Murphy et al., 2021). Even small changes in the chemical composition of the tropopause region relating to trace gases, such as methane (CH_4), ozone (O_3) and water (H_2O), have a large radiative effect on the surface temperature (Riese et al., 2012). A similar overview study focusing on the radiative effect of aerosol particles with regard to changes in number concentration, size distribution and chemical composition is not available at the current date. However, there are studies that examine the effect of individual aerosol properties: The effective radiative forcing (ERF) is mainly dependent on the chemical composition of the aerosol particles. For instance, sulfate aerosol, which is emitted by anthropogenic and natural processes (see Section 1.2.4), has a cooling effect due to back scattering of sunlight (Li et al., 2022). This cooling is particularly observed after strong volcanic eruptions, like the Pinatubo eruption in 1991 (e.g., Hansen et al., 1992; Molineaux and Ineichen, 1996; Soden et al., 2002). Other compounds such as black carbon (BC) or soot have a warming effect as a consequence of absorption of sunlight (e.g., Jacobson, 2001; Ramanathan and Carmichael, 2008).
Furthermore, the ERF depends on the aerosol size distribution. Previous studies showed that aerosol particles with a diameter of 0.5 µm scatter most of the sunlight back to space, and therefore have a cooling effect on the surface temperature (Murphy et al., 2021). However, aerosol particles with an effective diameter larger than 2 µm or smaller than 0.1 µm do not have such an efficient scattering and therefore have no significant cooling effect as other sizes (Lacis et al., 1992; Murphy et al., 2021).
Further, Lacis et al. (1992) show that the infrared heating of aerosol particles is strongly dependent on the aerosol particle size and insensitive to the chemical composition of the aerosol. However, this composition impacts the role of aerosol particles in other processes, like cloud or heterogeneous ice formation. As shown by Riese et al. (2012), the most sensitive region in the atmosphere is the tropopause region as a transition from a turbulent, mixed regime (in the troposphere) towards a stable regime (in the stratosphere). The tropopause region in the extratropics and thus also its atmospheric constituents are influenced by many different processes on different spatial and temporal scales,

such as turbulent cross-tropopause mixing (e.g., Holton et al., 1995; Tuck et al., 1997; Gettelman et al., 2011). These processes may lead to changes in the chemical composition of the tropopause region and therefore have an impact on the radiation budget of the atmosphere and consequently the Earth's surface temperature. The ERF of trace gases is understood quite well in current climate studies (Arias et al., 2021), whereas the ERF of aerosol particles is subject to large uncertainties. In numbers, the overall aerosol ERF in the last Intergovernmental Panel on Climate Change (IPCC) report (AR6) from 2021 (Arias et al., 2021) is around $-1\,\mathrm{W\,m^{-2}}$ with an uncertainty of roughly 75 % ($-1.8\,\mathrm{W\,m^{-2}}$ to $-0.4\,\mathrm{W\,m^{-2}}$). Furthermore, the ERF is strongly influenced by the chemical composition with positive forcing by components like BC and cooling for example by organic carbon (OC).
Compared to the previous assessment report (AR5), there are some improvements in the understanding the climate effect of aerosol particles, but the level of knowledge is still low. One reason for this is that modeling of atmospheric aerosol remains challenging even for state-of-the-art climate models (Szopa et al., 2021). These challenges arise due to the complex optical properties of aerosol particles, which depend on various parameters such as the shape, the relative humidity, and chemical composition, the latter of which is affected by complex chemical reactions. In atmospheric research, these challenges are tackled by intensive research infrastructures (e.g., "The Tropopause Region in a Changing Atmosphere (TPChange)", "Arctic amplification: Climate relevant atmospheric and surface processes and feedback mechanisms (AC^3)") to foster the development of climate models and support the modeling by in-situ observations.
This thesis is part of the research infrastructure project "TPChange" and uses airborne measurements of aerosol chemical composition and size distributions in order to identify cross-tropopause mixing processes of aerosol particles.

1.2 SCIENTIFIC BACKGROUND

As this thesis deals with aerosol particles and processes in the extratropical tropopause region, the following schematic Fig. 1 describes the framework: The tropopause region can also be referred to as upper troposphere and lower stratosphere (UTLS). In this region, certain dynamical processes occur which influence changes the chemical composition of the stratosphere by mixing with tropospheric air and vice versa. This cross-tropopause mixing leads to the formation of a transition layer, the extratropical transition layer (ExTL) (Hoor et al., 2002).
The stratosphere, with the Brewer-Dobson circulation (BDC) as overarching meridional circulation, can be divided into the "pure stratosphere" or "overworld" (Holton et al., 1995) and the lowermost stratosphere (LMS). The

barrier between those two regimes is the 380 K isentrope starting at the tropical tropopause (Holton et al., 1995).

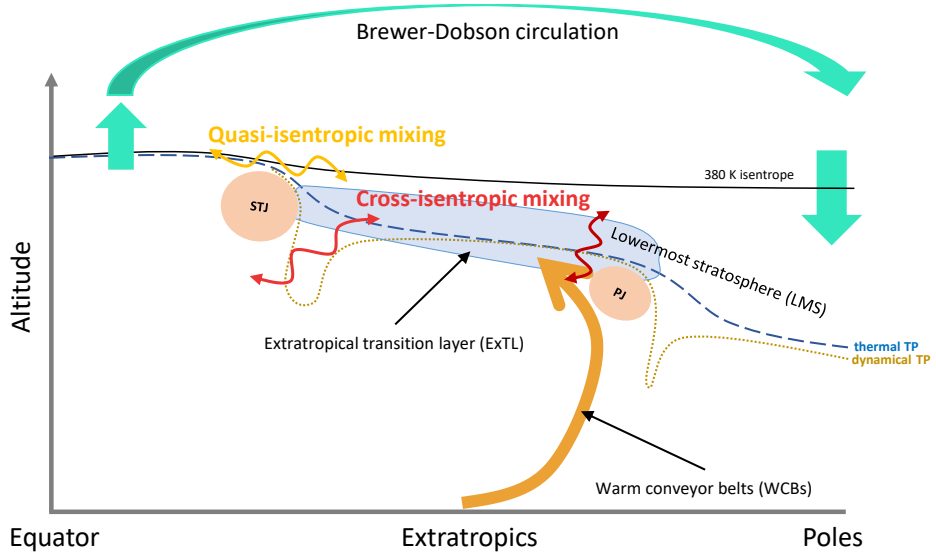

Figure 1: Schematic cross-section of the atmosphere with the key processes which are relevant for this thesis. The bright green arrows denote the BDC reaching from the tropical tropopause (380 K isentrope; black solid line) towards the poles. The extratropics are bounded by the sub-tropical jet stream (STJ) and the polar (front) jet stream (PJ), which leads to a steep gradient in the thermal tropopause (thermal TP, dashed blue line) and tropopause folds in the dynamical tropopause (dynamical TP, dotted dark yellow line). In the vicinity of the jet streams and other dynamical processes, such as WCB uplift (thick orange arrow), cross-tropopause mixing in the form of quasi-isentropic mixing (yellow, wavy double arrow) or cross-isentropic mixing (red, wavy double arrows) can occur. Adapted from Gettelman et al. (2011) and www.tpchange.de (last access: 12.09.2025).

1.2.1 *Tropopause definitions*

There exist several definitions of the tropopause depending on the scientific focus. The most common definitions are introduced below.

Thermal tropopause

The definition of the thermal tropopause is the oldest definition (Dines, 1919; World Meteorological Organization, WMO, 1957). It is based on the temperature profile of the atmosphere which was explored by balloon measurements in the early 20th century. The World Meteorological Organization (WMO) revisited this observation and defined the thermal tropopause as follows: The thermal tropopause is the lowest altitude where the vertical temperature

gradient (also called lapse rate) is lower than $2\,\mathrm{K\,km^{-1}}$ and does not exceed this value for the next at least 2 km (Dines, 1919; World Meteorological Organization, WMO, 1957; Hoinka, 1997). One application of this tropopause is the evaluation and analysis of radiosonde profiles, but also model output can be evaluated with this definition. There is the possibility that multiple tropopauses occur applying this definition of a lapse-rate tropopause (LRT). Further disadvantages arise from the challenging definition in dynamically very active regions, such as the subtropical jetstream or in polar regions with no variations in the temperature profile during polar night (Tinney et al., 2022).

Stability-based tropopause

There are additional definitions of the tropopause, in order to account for some of the problems raised by the definition of the LRT. Several ballon studies of temperature profiles found a layer above the tropopause with very stable conditions, such as a high static stability (Squared Brunt-Väisälä frequency, N^2) (e.g., Birner et al., 2002; Birner et al., 2006). This static stability is mainly the measure of the vertical gradient of potential temperature Θ:

$$N^2 = \frac{g}{\Theta} \cdot \frac{d\Theta}{dz} \tag{1}$$

In this equation g represents the gravitational acceleration.
Tinney et al. (2022) use this approach of the static stability and composition analysis by balloon observations in combination with the global reanalysis data set Modern-Era Retrospective Analysis for Research and Applications, Version 2 (MERRA2) to derive a tropopause definition based on the potential temperature gradient. Based on their findings, the stability-based tropopause is defined as the lowest altitude where the vertical gradient of potential temperature exceeds $10\,\mathrm{K\,km^{-1}}$ and remains above that threshold in an adjacent layer of 2 km. Advantages of this metric are the global applicability and the good agreement in composition analyses. One challenge with this method, in particular for airborne in-situ measurements, is the need of vertical profiles along the flight path. This requirement forces the use of model data in place of direct temperature and pressure measurements.

Dynamical tropopause - potential vorticity (PV) isosurface

The commonly used dynamical tropopause is based on the potential vorticity (PV), a conserved quantity in adiabatic regimes. The PV is defined as follows (Rossby, 1940; Ertel, 1942; Hoskins, 1991):

$$PV = \frac{\zeta_a}{\rho} \cdot \nabla_z \Theta \tag{2}$$

Here, ζ_a is the absolute vorticity, ρ the density of air and $\nabla_z\Theta$ the vertical gradient of Θ. The unit of the PV can be expressed as potential vorticity units (PVUs); expressed in SI-units $1\,\mathrm{PVU} = 10^{-6}\mathrm{m}^2\mathrm{s}^{-1}\mathrm{Kkg}^{-1}$.
As seen in Eq. 2, and similar to the stability-based tropopause, the vertical gradient of potential temperature is taken into account. For this reason, the PV can be used as a tropopause marker as well. In the tropopause region, PV increases from low tropospheric values to higher values in the stratosphere. There is no strictly defined value of PV for the dynamical tropopause. In the literature values between 1.5 and 4 PVU are found, corresponding to the strongest increase in the PV-gradient.
The big advantage of this tropopause definition is the conservation of PV during adiabatic processes. Therefore, the tropopause can be seen as transport barrier for diabatic processes, such as turbulent mixing (Kunkel et al., 2019). However, as absolute vorticity is undefined at the equator, a disadvantage of this tropopause definition is that it is also undefined at the equator, and the tropopause is already very high in tropical regions close to it. Furthermore, the PV underlies dynamical processes and thus it is variable in certain situations which arise from the applicability issue of using only one single PV-isosurface (Kunz et al., 2011a).

Dynamical tropopause - PV-Gradient

One solution to account for the problem of the variability of the PV, is to use gradients of PV along one isentrope instead of fixed PV thresholds (Kunz et al., 2011a; Turhal et al., 2024). In this approach, model data is used to calculate the PV which is later transformed to equivalent latitude on each isentrope (Kunz et al., 2011a). The before-mentioned method has the advantage that it is independent of seasonality and the choice of isentropes. The exact definition and calculation is rather complex and is going beyond the framework of this thesis. It is described in detail by Kunz et al. (2011a). Compared to the chemical transition from the troposphere to the stratosphere, the PV-gradient tropopause represents the transport barrier between both spheres (Kunz et al., 2011b). Here, Kunz et al. (2011b) show that this tropopause definition is in agreement with profiles of trace gases such as carbon monoxide (CO) and O_3. However, this definition reaches its limits in very complex dynamical situations, such as double tropopauses induced by Rossby wave breaking (Kunz et al., 2011b).

Chemical tropopause

Further, the tropopause can be determined on the basis of measured composition in form of trace gases. This is not possible with all possible constituents since one has to account for the sources and sinks of the species as well as their atmospheric lifetimes. Regarding the sources and sinks, it is necessary

that the trace species has only a source in the troposphere and a sink in the stratosphere or vice versa, with no additional source in the stratosphere or troposphere, respectively. Otherwise, the effects of sources and sinks in the same atmospheric layer might cancel each other out. Additionally, the mentioned atmospheric lifetime needs to be long enough to get a well-mixed state in the troposphere in order to achieve a homogeneous distribution without disturbances by local source regions. Two trace gases that are very well suited are O_3 and nitrous oxide (N_2O) which are used in this thesis (e.g., Bethan et al., 1996; Pan et al., 2004; Müller et al., 2015; Joppe et al., 2024).

Summarizing, there are multiple ways to define the tropopause and the list of definitions given above is not complete. Depending on the application, it is important to compare different definitions. In this thesis, the analysis mostly refers to the chemical tropopause and partly to the dynamical tropopause with a fixed PV-isosurface.

1.2.2 *Atmospheric transport mechanisms*

The tropopause region and more precisely, the stratosphere are influenced by several processes which also affect the chemical composition in these regions. These processes are roughly sketched in Fig. 1. In the following, some of the transport processes are described in more detail with respect to their corresponding scales.

Brewer-Dobson circulation

On the large scale, the most common transport mechanism is the BDC. It was first described by the observation of trace constituents, such as H_2O and O_3, and is still topic of on-going research (e.g., Brewer, 1949; Dobson, 1956; Solomon et al., 2010; Thompson et al., 2011). The BDC is the overarching meridional stratospheric circulation where tropospheric air is entering the stratosphere in the tropics and is subsequently transported polewards (e.g., Brewer, 1949; Dobson, 1956; Butchart, 2014; Cohen et al., 2014). Compared to the tropospheric circulation patterns, the BDC is a wave-driven circulation (Cohen et al., 2014). This means that the BDC is mainly driven by tropospheric dynamics, such as Rossby-waves on the large scale, but also to a minor extent by small-scale gravity waves (e.g., Butchart, 2014; Cohen et al., 2014). Observations and model studies also reveal that the LMS in extratropical regions is affected by a lower branch of the BDC (Bönisch et al., 2011; Ploeger et al., 2021).

Warm conveyor belts (WCBs)

Warm conveyor belts (WCBs) are transport processes not on the planetary but on the synoptical scale and are one key process for transporting air masses from the planetary boundary layer (PBL) into the UTLS region. This transport process is called WCB and is associated with cyclones. A WCB can be described in a quasi-Lagrangian perspective as air stream with strong vertical uplift (e.g., Harrold, 1973; Eckhardt et al., 2004; Madonna et al., 2014; Heitmann et al., 2024). This uplift can reach an altitude difference of around 600 hPa in less than 2 days or in coordinates of potential temperature experience an increase of 20 K (Madonna et al., 2014; Heitmann et al., 2024). Furthermore, WCBs are associated with water vapor transport into the UTLS and moist processes, such as condensation and precipitation (Madonna et al., 2014; Schwenk and Miltenberger, 2024). On the synoptical scale, WCBs are capable to transport pollutants, such as trace gases or aerosol particles into the UTLS far away from their sources. In current literature, there are only a few studies which investigate the transport of pollutants via WCBs, such as trace gases and aerosols, in the extratropics (e.g., Birmili et al., 2010).

Cross-tropopause mixing

On the small-scale, the process of cross-tropopause mixing occurs. As mentioned earlier, the tropopause can act as a transport barrier for trace gases and aerosol particles (e.g., Fischer et al., 2000; Hoor et al., 2002; Hoor et al., 2004; Hegglin et al., 2009; Gettelman et al., 2011; Kunkel et al., 2019; Lachnitt et al., 2023). Nevertheless, there are small-scale processes which allow mixing of air masses across the tropopause in both directions. These mixing processes can be identified by so-called tracer-tracer correlation plots (see Appendix Sect. A). These correlations are introduced for instance by Fischer et al. (2000). The method is based on the use of two tracers: One tropospheric tracer with sources only in the troposphere, a rather constant background mixing ratio in the stratosphere and a sufficient long atmospheric lifetime to get transported into the LMS, such as CO or H_2O. The second tracer is a so-called stratospheric tracer with a homogeneous distribution in the troposphere and a sink or source in the stratosphere, such as N_2O or O_3. Without mixing across the tropopause, the tracer-tracer correlation would show an L-shape, but with active mixing across the tropopause, diagonal mixing-lines are observed which connect both reservoirs (e.g., Konopka and Pan, 2012) (see Fig. 19 in Sect. A).
Cross-tropopause mixing can be divided into quasi-isentropic mixing and cross-isentropic mixing. In the quasi-isentropic case, isentropes cross the tropopause associated with synoptic and planetary waves and therefore allow air masses to cross the tropopause. One case-study on this phenomenon is given by Kunkel et al. (2019). The other possibility of cross-isentropic mixing

can occur for diabatic processes and is, therefore, irreversible. These diabatic processes are mostly found in turbulent regimes, such as areas of strong wind shear along the jet streams or gravity waves, as described by Kaluza et al. (2019) and Lachnitt et al. (2023).
In summary, multiple transport mechanisms exist which have an impact on the composition of the extratropical tropopause region. As mentioned, all these processes have different scales and therefore some challenges for in-situ observations arise. It needs to be clarified that not always only one specific process is responsible for the observed chemical composition in the UTLS, but with suitable methods and measurements it is possible to differentiate between the processes and assign them to the observations.

1.2.3 *Atmospheric aerosol formation and lifetimes*

Atmospheric aerosol particles can be differentiated between primary and secondary aerosol particles. Primary aerosol is directly emitted by its source into the atmosphere, whereas secondary aerosol is generated by chemical reactions from the gas phase, such as gas-to-particle conversion from sulfur dioxide (SO_2) to sulfate aerosol. Another possibility of secondary aerosol formation is condensation of gases on already existing aerosol particles (Pandis et al., 1995). In Section 1.2.4, more information on the different sources of atmospheric aerosol will be provided.

Aerosol size modes

In terms of the size, atmospheric aerosol particles can be divided into different size modes and linked to possible processes, which is sketched in Fig. 2 (e.g., Heintzenberg et al., 2003; Brasseur and Jacob, 2017). Freshly formed aerosol particles from the gas phase are found in the nucleation mode with a particle diameter between 0.001 µm and 0.01 µm and have the largest number concentrations of all presented modes (Brasseur and Jacob, 2017). Here, sulfuric acid is the most common species for aerosol nucleation due its low saturation pressure (Curtius, 2006; Brasseur and Jacob, 2017). Aitken-mode particles show the second largest number fraction of the size distribution and the diameter in this mode ranges from around 0.01 µm and 0.1 µm. Particles in the Aitken-mode are developing through condensation processes on nucleation mode aerosol and subsequent particle growth. Both, Aitken- and accumulation-mode, have a sink in coagulation processes (Brasseur and Jacob, 2017). The next size mode is the accumulation mode with particle sizes from around 0.05 µm up to 1 µm. This size mode is in focus of this thesis in the following chapters. Particles in this size range also form through the mentioned processes of condensation and coagulation, but additionally can be primary aerosol with sources from combustion processes (see also 1.2.4) (e.g.,

Pandis et al., 1995; Brasseur and Jacob, 2017). The largest aerosol particles with the lowest number fraction fall into the coarse mode. Here, particle sizes can reach up to 10 µm and more. These particles are mostly primary particles from natural sources (Brasseur and Jacob, 2017).

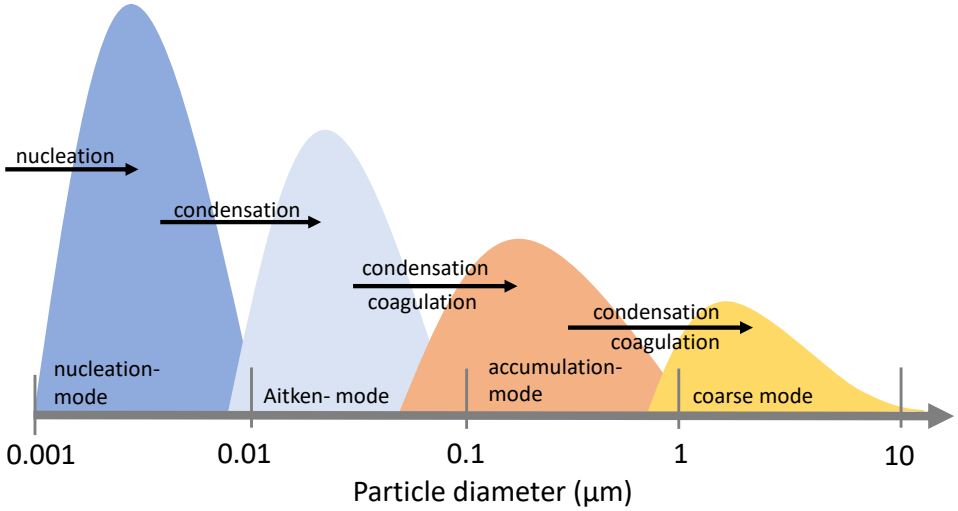

Figure 2: Schematic overview of different size modes of atmospheric aerosol particles and processes leading to a transition between the different modes. Reproduced from Heintzenberg et al. (2003) with permission from Springer Nature.

Atmospheric lifetime

The atmospheric lifetime, or residence time, of aerosol particles is dependent on their size, the altitude as well as their chemical composition and reactivity. On average, the atmospheric lifetime is in the order of a few days up to around one week in lower altitudes and the free troposphere (Andreae, 2007; Jaenicke, 1980a,b). At higher altitudes, the lifetime of aerosol increases to one month in the tropopause region and even up to 2 years in the stratosphere (Jaenicke, 1980a). Thereby, the particle size and removal processes change over the different altitudes. The smaller, newly formed particles are removed by coagulation processes with other particles, whereas the large particles are heavier and fall out of the atmosphere, which is called sedimentation (Jaenicke, 1980b). The aerosol particles commonly observed in the tropopause region are in the accumulation mode. The only way to remove these particles is the process of wet-deposition, which is done by aerosol-cloud interaction (Petzold and Kärcher, 2012). This process does not count for the stratosphere. Here, the particles get lost by the transition to the troposphere due to dynamics (see Fig. 1) and local loss processes like chemical reactions.

1.2.4 *Sources of atmospheric aerosol*

There are multiple sources of atmospheric aerosol particles. Here, only a few examples of natural and anthropogenic aerosol particles will be given.

Natural sources

An important natural aerosol is sea salt aerosol, as most parts of the Earth are covered by oceans. This particle type is formed by physical processes on the surface of the oceans, e.g., wave breaking (Andreae et al., 2009). Sea salt aerosol exists in the size range from Aitken-mode up to the coarse mode and shows a characteristic mode at 500 nm (e.g., Campuzano-Jost et al., 2003; Andreae et al., 2009).
Another and the most abundant natural aerosol is dust aerosol (also mineral dust or soil dust). Source regions of mineral dust are typically deserts, such as the Sahara desert in Africa. Here, the aerosol is generated by wind erosion of loose soil (Miller and Tegen, 1998). Dust aerosol is very good visible on satellite images and can travel over long distances. Current studies estimate that mineral dust has a cooling effect in the atmosphere by interactions with clouds, chemistry and radiation (Kok et al., 2023).
Besides these two surface originating aerosol types, there are some more natural aerosol sources, which will be investigated in more detail later in this thesis. First, volcanic sulfate aerosol is mentioned. Volcanic eruptions can emit large amounts of volcanic gases and ash particles. The emitted gases, such as SO_2, act as precursor gases for volcanic (sulfate) aerosol particles (Kremser et al., 2016). This aerosol has a strong cooling effect in the atmosphere and caused a reduction in Earth‘s surface temperature by up to 1.5 degree (e.g., Lacis et al., 1992; Santer et al., 2014; McGraw et al., 2024). Volcanic eruptions are capable to emit these gases and aerosol particles directly into the stratosphere, where its prevalence is quite stable and residence times of more than 1 yr are observed (see 1.2.3).
The last mentioned natural source of aerosol particles can also be attributed to anthropogenic sources, depending on the exact definition. This type is biomass burning (BB) aerosol from forest fires, e.g., occurring frequently in Canada or Africa. These fires can naturally be caused by lightning strikes and are therefore also counted as natural source. This BB aerosol consists mainly of organic compounds (biomass burning organic aerosol (BBOA)) and soot particles or BC.
Additional natural sources of aerosol particles, not further discussed in this thesis, are pollen, meteoric aerosol (Schneider et al., 2021) and secondarily formed organic aerosol (OA) from tree emissions in the rain forest (Curtius et al., 2024).

Anthropogenic sources

Besides the natural sources for aerosol particles, there are also anthropogenic source processes. Here, the industrial sector as well as the traffic sector have large impacts on the aerosol particles and their formation in urban areas. Large fractions of SO_2 are emitted by industry and therefore secondarily formed sulfate aerosol is commonly present in industrial areas (Seinfeld and Pandis, 2016).
The mentioned traffic sector provides multiple emission sources for anthropogenic aerosol. First, the burned fossil fuels by vehicles emit nitrogen oxides (NO_x), which later contribute to the formation of nitrate aerosol, but also sulfur compounds are emitted. This holds especially for the air traffic sector that is the major source of primary aerosol particles in the upper troposphere (UT) (Petzold et al., 1999). Furthermore, in current research, the focus shifts to non-exhaust emissions of road-traffic. This term includes for instance emissions by brake-wear or tire abrasion, which emits ultrafine particles and creates an additional source for health issues (Löber et al., 2024).
In urban areas, domestic cooking may also contribute to large fractions (up to 30 %) of OA and thus needs to be taken into account in the context of anthropogenic aerosol, at least in the PBL (Pikmann et al., 2024).
Especially in regions with intense agricultural use, e.g., the Netherlands or parts of Northern Germany, this kind of land use has an effect on aerosol particle formation. In these regions, ammonia (NH_3) is emitted to the atmosphere in large amounts through e.g., land fertilization (Behera et al., 2013; Beaudor et al., 2025). This is the main precursor for ammonium aerosol which is present in the form of ammonium nitrate or ammonium sulfate (Behera et al., 2013).
As discussed for the natural sources, BB can also be attributed to anthropogenic sources as it can be forced by fire raising, for example to gain areas for agriculture. The aerosol chemical composition of this aerosol type is explained in the section above.

1.2.5 *Atmospheric radiation and the effect of aerosol particles*

The sun is the energy source entering the atmosphere. This energy is in form of electromagnetic radiation with wavelengths spanning many magnitudes from which only a small part is visible for humans.
The total amount of incoming solar radiation at the top of the atmosphere (TOA) is the solar constant around $1360\,\mathrm{W\,m^{-2}}$ (Wallace and Hobbs, 2006; Guermoui et al., 2020). From this, only one fourth is reaching the surface due to the spherical shape of the earth ($\approx 340\,\mathrm{W\,m^{-2}}$). The global mean albedo of 0.3 is responsible for the reflection of almost 1/3 of this incoming radiation at the surface reaching radiation back to space. Thus, a net incoming radiation

of approximately 238 W m^{-2} is left at the surface (Wild et al., 2018). This is schematically shown in Fig. 3. In the theory of blackbody radiation, an equilibrium temperature of 255 K would establish assuming a total absorption of this remaining energy. However, this is not the case as there is on average an equilibrium temperature of 288 K (Seinfeld and Pandis, 2016; Wallace and Hobbs, 2006). This concludes that there must be interaction between the atmosphere and the incoming and outgoing radiation, known as greenhouse effect. The exact numbers of radiation fluxes are controlled by the chemical composition of the atmosphere and physical processes depending on the composition. In the following, only aerosol relevant processes are described even though gases interact with radiation.

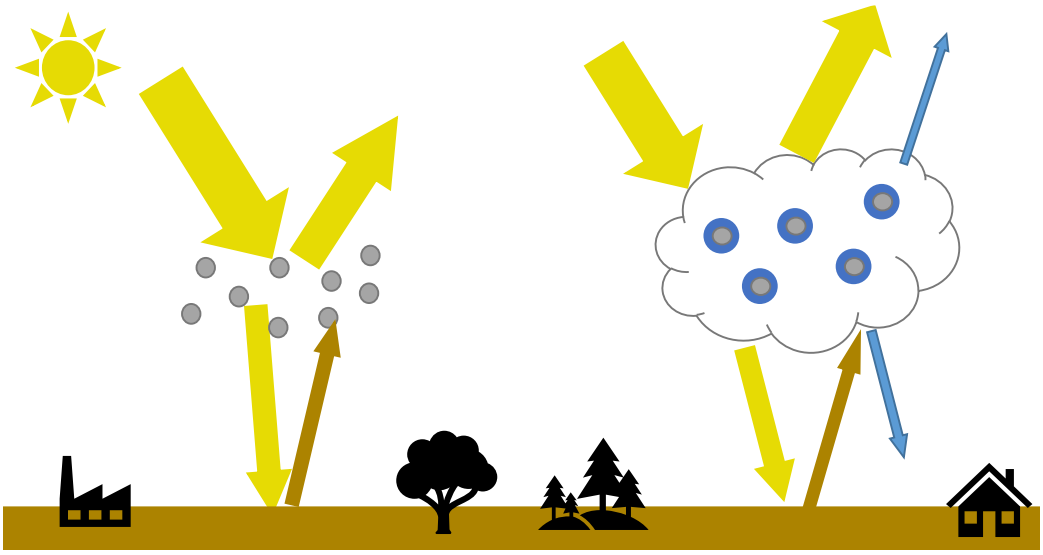

Figure 3: Schematic of the radiation budget and aerosol effects in the atmosphere. Yellow arrows indicate solar radiation, brown arrows show radiation by the surface and blue arrows atmospheric fluxed. The figure is adapted from Li et al. (2022) with permission from Springer Nature.

Direct aerosol effect

There are two major interaction processes of aerosol particles with radiation. One is the process of absorption. Here, the energy of the radiation is removed at one or more wavelengths and converted to internal (thermal) energy in terms of a blackbody.
Another interaction process is scattering which plays an important role in the context of this thesis. In case of scattering, the aerosol particle transfers the incoming energy of the light into internal electric charges, which leads to oscillation of the particle. The charges reradiate from the particle at the same wavelength into all directions. In the atmosphere, the free path length

between individual particles (and molecules) is large enough to account for independent scattering of all constituents.
The interaction of scattering can be divided into two different theories and regimes, the Rayleigh-scattering and the Mie-Lorenz-scattering, better known as Mie-scattering (Mie, 1908).
The Rayleigh scattering is valid for wavelengths much larger than the particle (molecule) size ($\lambda >> d_p$), so mostly for air molecules. Here, the scattered radiation is equally divided between forward and backward scattering. In the atmosphere, Rayleigh scattering is visible in form of the blue sky.
The Mie-theory expands the scattering theory for larger particles with a size in the range of the wavelength ($\lambda \approx d_p$), such as dust particles for the infrared light, which is the reason for intense red sunsets in dusty periods. Mie-scattering results in a strong forward component in the scattering according to the phase function (Mie, 1908; Bohren and Huffman, 1998).
The combination of scattering and absorption is called extinction and is referred to the direct aerosol effect in the sense of climate feedback (Liou, 2002; Seinfeld and Pandis, 2016; Wallace and Hobbs, 2006).

Indirect aerosol effect

Besides the direct effect, aerosol particles also influence the atmospheric radiation budget indirectly: Aerosol particles can act as cloud condensation nuclei (CCN) and ice nucleating particles (INPs) and therefore influence cloud formation and with this also the radiative feedback of clouds (Forster et al., 2021).
In mixed-phase clouds, anthropogenic aerosol mostly influences the liquid part of the cloud as it adds CCN to the cloud. More CCN at a constant cloud liquid water content result in smaller droplets, which enhances cloud scattering and as consequence leads to a higher cloud albedo with a negative radiative feedback. Furthermore, the lifetime of clouds with smaller droplets is higher as the precipitation is suppressed (Forster et al., 2021).
For the ice formation in clouds, natural aerosol, such as sea spray or mineral dust is the most abundant component acting as INP (DeMott et al., 2015; Schrod et al., 2020). However, anthropogenic aerosol such as BC may additionally act as INP in cirrus clouds, because lower temperatures are needed for freezing (Forster et al., 2021).
In general, the cloud radiative feedback and with it the indirect aerosol effect can have both a positive and negative feedback. This is also dependent on the cloud properties, such as phase state and altitude (e.g., Ceppi et al., 2017).

1.2.6 *Aerosol chemical composition*

As mentioned above, the chemical composition of atmospheric aerosol particles depends on the sources of the corresponding aerosol. It determines the aerosol properties, such as radiative forcing, optical properties, hygroscopicity, reactivity and ability of acting as CCN or INP. Furthermore, the composition differs with different size ranges of the observed aerosol particles. The chemical composition can be divided into the classes of inorganic aerosol (e.g., sulfate, ammonium or nitrate), organic compounds (including a large subset of constituents) and elemental carbon (EC) that is often termed soot (Gilardoni and Fuzzi, 2017).
Additionally, atmospheric aerosol particles can conceptually differentiate between internally and externally mixed aerosol particles. Here, the external mixture means that the individual particles are chemically pure and therefore can be distinguished according to their individual chemical composition. The other type is the internal mixture, where different species are found in one particle (Boucher, 2015).
The final general classification of atmospheric aerosol, depending on the chemical composition, is the separation between refractory and non-refractory aerosol, where refractory particles are temperature-stable and can only be vaporized at temperatures greater than 500 °C (Canagaratna et al., 2007; Kremser et al., 2016). Here, one example is soot that is, therefore, also called refractory black carbon (rBC). The measurement technology used in this thesis is capable to analyze the chemical composition of non-refractory aerosol due to the exploited temperature. In the following, the most important aerosol species for this thesis will be described in detail.

Sulfate aerosol

Sulfate aerosol is the most abundant constituent of stratospheric aerosol particles. It is mainly produced by the oxidation of SO_2 and, in the unperturbed atmosphere, by the oxidation path from carbonyl sulfide (OCS) to SO_2 and further to sulfate aerosol (Seinfeld and Pandis, 2016). This chemical reaction is occurs in the gas phase via the reaction of chemical radicals and on the timescale of only a few days (Gilardoni and Fuzzi, 2017). Consequently, sulfate aerosol is commonly found as secondary aerosol resulting from the oxidation of sulfur-containing constituents. Sulfate aerosol and its precursor are emitted from different sources.
Large natural sources are the emissions of precursor gases, such as OCS and dimethyl sulfide (DMS) from oceans, but also volcanic activities can cause an increasing abundance of sulfate aerosol through primary emission or the emission of SO_2. Here, the relaxation time of the stratospheric sulfate aerosol after a volcanic injection can last up to multiple years, depending on the

strength of the volcanic eruption (Seinfeld and Pandis, 2016). Besides the natural sources, the majority of sulfate is emitted by anthropogenic sources in the industrial sector, shipping or biomass burning (Gilardoni and Fuzzi, 2017). In the troposphere, the typical lifetime of sulfate aerosol is about one week as a consequence of the loss processes through wet and dry deposition (Seinfeld and Pandis, 2016).

Organic aerosol (OA)

OA is the generic term for a set of many different subspecies, e.g., aromates or biogenic emissions. It can be distinguished between primary organic aerosol (POA) and secondary organic aerosol (SOA), where SOA is formed from precursor gases for example terpenes and isoprene over the Amazonian rain forest (Hoffmann et al., 1997; Kroll and Seinfeld, 2008; Carlton et al., 2009; Curtius et al., 2024). Furthermore, SOA may also depend on the abundance of POA through heterogeneous chemistry with evaporation of primary particles and the condensation from the gas phase to form new particles (Gilardoni and Fuzzi, 2017; Boucher, 2015). Tropospheric OA can account for a significant fraction of the aerosol mass in the UTLS (Froyd et al., 2009; Kremser et al., 2016; Curtius et al., 2024). Anthropogenic sources of OA are found in the industrial sector, through burning of fossil fuels and other combustion processes of e.g., wood, waste or coal. Natural sources are biomass burning (from forest fires), biogenic aerosol (like pollen and spores), biogenic precursors (e.g., isoprene or α-pinene) or marine aerosol (Gilardoni and Fuzzi, 2017).
The tropospheric lifetime of is in the order of one week and it is removed from the atmosphere as consequence of wet or dry deposition and evaporation (Seinfeld and Pandis, 2016). In the stratosphere, OA may have longer residence times due to missing sinks, however there is no in-situ production (Kremser et al., 2016).

Black carbon aerosol

BC, or also referred to as rBC, is only emitted during combustion processes through incomplete combustion. Here, anthropogenic sources are fossil fuel burning (as in the traffic sector) and heating through burning of coal, oil or gas. The main natural source of BC are forest fires, which can emit huge amounts of BC (Gilardoni and Fuzzi, 2017).
BC aerosol quickly becomes hygroscopic due to internal coating with organic carbon in the atmosphere (Boucher, 2015). Therefore, the tropospheric lifetime is around one week and can reach up to 10 days as a consequence of dry and wet deposition. Finally, similar to OA; long residence times in the stratosphere can be expected with partial in-situ production through air traffic (Seinfeld and Pandis, 2016; Kremser et al., 2016).

1.3 OBJECTIVES OF THIS WORK

As described in the motivation (Chapter 1.1), the understanding of aerosol particles is of great interest in current research projects since many aspects, such as cross-tropopause mixing or the radiative feedback are not fully understood by today. Furthermore, the tropopause region, more precisely changes in the chemical composition of the tropopause region, play an important role for the Earth‘s surface temperature, as described by Riese et al. (2012). Murphy et al. (2021) show that the radiative feedback of aerosol particles is influenced by the particle size due to different scattering efficiencies.
Therefore, the Collaborative Research Centre (CRC) - "The Tropopause Region in a Changing Atmosphere" (TPChange) - was initiated to investigate the tropopause region comprehensively. This CRC is an alliance led mainly by the Johannes Gutenberg University Mainz (JGU) and the Goethe University Frankfurt am Main (GUF). Other participating institutions are the Technical University Darmstadt (TuDa), the Forschungszentrum Jülich (FZJ), the Max Planck Institute for Chemistry (MPIC) and the German Aerospace Center (DLR). The consortium investigates the tropopause region and the effects of climate change on this region. For this, several experimental observations and one dedicated aircraft mission are combined and complemented by current state-of-the-art climate models to further improve the models.

This thesis is part of TPChange and focuses on aerosol properties in the extratropical tropopause region. More precisely, it addresses the following questions:

- How is the ExTL defined by aerosol particles, compared to trace gas observations?
- What is the influence of small-scale dynamical processes, such as turbulent mixing, on the aerosol particles in the ExTL?
- Which role does small-scale cross-tropopause mixing play on the radiation budget in the extratropical UTLS?

In order to answer these questions within this thesis, in-situ airborne observations of aerosol chemical composition, aerosol number concentration and aerosol size distributions during different field experiments are used. One focus of this work is the preparation and characterization of two Ultra-High Sensitivity Aerosol Spectrometers (UHSASs) for the deployment during the central TPChange field experiment "Tropopause composition gradients and mixing experiment (TPEx)". Another part comprises the data analysis of the conducted measurements.
The dissertation is structured as follows: In Chapter 1, the research topic is

motivated and the importance of aerosol research in recent years is demonstrated. Furthermore, the current knowledge and the scientific background underlying the discussion of the results is described. Thereafter, in Chapter 2, the applied methods are introduced. First, the used measurement principles and technologies are presented, followed by the complete laboratory characterization of the two UHSAS instruments for the deployment during TPEx. After the technical part of Chapter 2, the complementary data sets are listed and described. Chapter 2 ends with a description of the field experiments from which the measurement data is later evaluated and analyzed in this thesis. The results in Chapter 3 are composed of two peer-reviewed, first author publications in the journal Atmospheric Chemistry and Physics (ACP), using case-studies on different observed small-scale processes and their influence on aerosol particles in the UTLS. Additonally, a second author publication in the journal Atmospheric Measurement Techniques (AMT) is presented, which describes the technical setup of the measurement platform Tropopause Composition Towed Sensor Shuttle (TPC-TOSS). The final Chapter 4 summarizes the research conducted in this thesis and provides an outlook on how this findings can be used in future research projects.

2

METHODS

In this chapter, the primarily used measurement instruments and additionally used data sets are introduced, including characterization measurements in the laboratory. Afterwards, the two conducted field campaigns and their goals are presented briefly.

2.1 ULTRA-HIGH SENSITIVITY AEROSOL SPECTROMETER (UHSAS)

The UHSAS is a commercial aerosol spectrometer, manufactured by the company Droplet Measurement Technologies (DMT), located in Longmont, Colorado, USA. Originally, the UHSAS was developed in two different versions for specific applications: the laboratory version, in this thesis referred to as cabin UHSAS (UHSAS-C) (Fig. 5), and the airborne UHSAS (UHSAS-A) (Fig. 4) applied as underwing probe for aircraft measurements (Cai et al., 2008; Kupc et al., 2018; Mahnke et al., 2021). Meanwhile, the airborne unit is no longer manufactured and officially without technical support, with only a few devices remaining in operation around the world.
For the application of the TPEx measurement campaign in 2024, the UHSAS-C was rebuilt into a new housing for the mounting inside aircraft racks. This modification was done by enviscope GmbH in Frankfurt/Main.

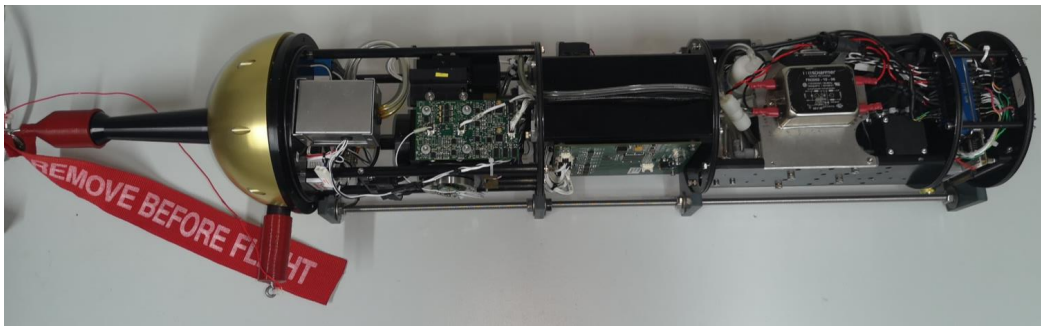

Figure 4: Photograph of the UHSAS-A outside the TPC-TOSS.

Figure 5: Photograph of the UHSAS-C in the new housing. The black tube was replaced with 1/8 inch stainless steel tubing.

2.1.1 *Measurement principle of the UHSAS*

The measurement principle of the UHSAS is based on laser-scattering in the Mie-regime (see 1.2.5). For this, a pumped semiconductor-diode solid-state laser with a wavelength of 1054 nm is used. This wavelength is achieved by using a pump laser at 797 nm in combination with a Nd^{3+}:$YLiF_4$ crystal to gain the higher wavelength. After passing the crystal, the laser beam is coupled into an intracavity pattern, which leads to a laser power around 1 kW cm^{-2}. This power is needed to detect small particles around and smaller than 100 nm.
The aerosol particles enter the detection unit perpendicular to the laser beam via a jet nozzle with a sample flow of 50 $cm^3\,min^{-1}$ (see Fig. 6). This sample flow is controlled by a mass flow controller (MFC) to be constant. Furthermore, the particle beam is embedded in a sheath flow in order to focus the particle beam to the detection plane. This sheath flow is passively controlled in the UHSAS-C by the remaining power of the pump by keeping the sample flow constant and is typically around 700 $cm^3\,min^{-1}$ at sea level. For the UHSAS-A, this sheath flow is controlled by an additional MFC and set to 600 $cm^3\,min^{-1}$.
The laser light which is scattered by the aerosol particles is collected in a range between 22° and 158° by Mangin mirrors and focused to the corresponding photodiodes which convert the photocurrent into a voltage signal. This

voltage can be assigned to a particle size by calibration (DMT, 2013; Bozem et al., 2025).

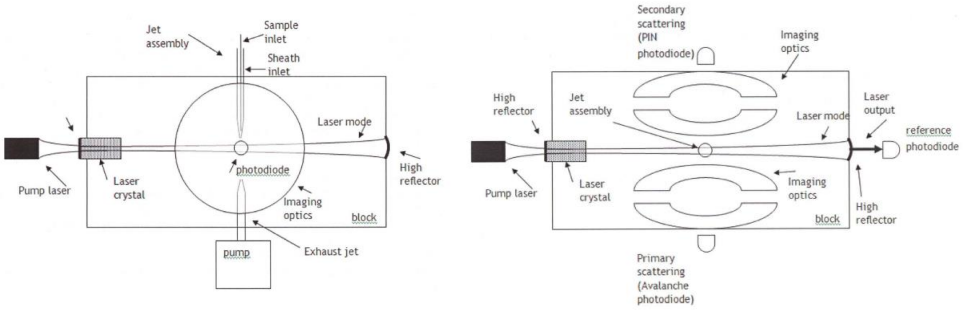

Figure 6: Side (left) and top (right) view on the optical block of the UHSASs. The schematic is from the manual with permission by DMT (DMT, 2013).

2.1.2 *Characterization of the UHSAS*

As already mentioned, two different types of the UHSAS were used for the airborne studies. Before the deployment during the TPEx campaign in June 2024, both systems were calibrated for different refractive indices to account for a broad range of atmospheric aerosol particles. These calibrations were necessary to reorder the measurements into a new bin-scheme of the size distribution to account for different atmospheric aerosol particles. Furthermore, the counting efficiency for different aerosol particle types, sizes and number concentrations was tested in the laboratory before the campaign.
In this chapter, the results of the performed characterization are presented briefly, as a short summary of the manuscript by Bozem et al. (2025) which describes the technical setup of the TPEx mission in more detail and contains a major contribution from these experiments. In the manuscript of Bozem et al. (2025), the description of the TPEx project and all UHSAS parts were written by myself as part of this thesis (see Chapter 3.3).
The calibration setup for these measurements is shown in Fig. 7. The calibration aerosol is generated with an atomizer, before the air flow gets dried in a combination of two diffusion dryers filled with silica gel. The size selection, especially of the non-polystyrene latex (PSL) particles, is done by a differential mobility analyzer (DMA) (TSI Model 3080) with an included X-ray neutralizer to make sure that the charge of the particles in in a Boltzmann equilibrium. After the DMA, the air flow is split up into both UHSAS systems with the same flow rate to allow for homogeneous flow splitting.

Size calibration

As mentioned above, the scattered light is detected by photodiodes and converted into a voltage signal which can be translated into a particle size. This

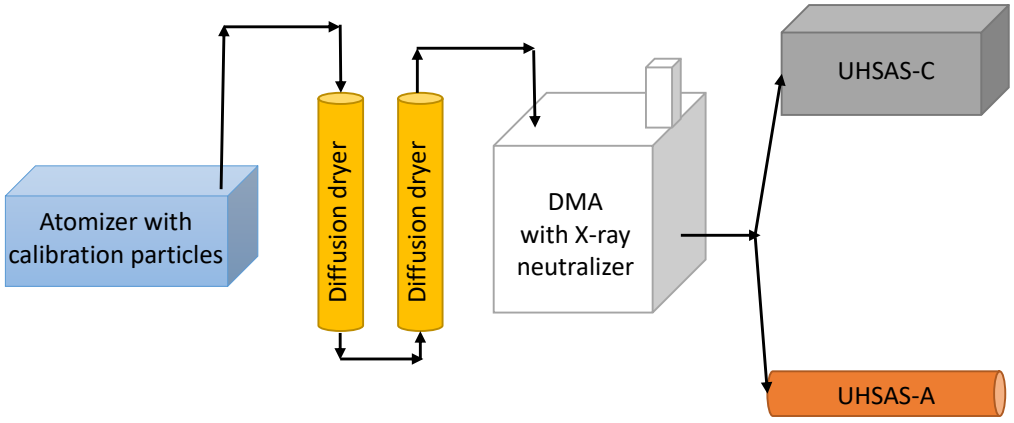

Figure 7: Schematic overview of the calibration setup for the described calibration measurements.

is achieved by using a calibration curve of the different gain stages in order to assign the particle size correctly. This calibration curve is constructed out of a relative and an absolute gain calibration. Here, the relative gain calibration is done by sampling ambient aerosol only, while the software determines the coefficients of the gain stages. In contrast to this, the absolute gain calibration makes use of fixed particle sizes of PSL particles which then are attributed to measured gain voltages for the correct assignment.
For the preparation of the TPEx campaign, we used the method of the absolute gain calibration to validate the previously performed calibration and to compare both instrument versions. Furthermore, the instruments were calibrated with additional substances with different refractive indices than the one of PSL (n=1.59). This was done to check the instrument behavior and the dependency of the particle size assignment on different aerosol particle types. The refractive indices ranged from n=1.34 for glucose, simulating organic containing aerosol, over n=1.53 for salts, like sodium chloride, to n=1.57 for ammonium nitrate.
The performed size calibration measurements were evaluated for each calibration aerosol and selected size individually (see Fig. 8). Therefore, a log-normal fit was calculated for the respective size distribution. The diameter of the fit-maximum was used for the later analysis in comparison to the selected diameter at the DMA and to determine the new bin scheme (see Fig. 9a and Fig. 12).

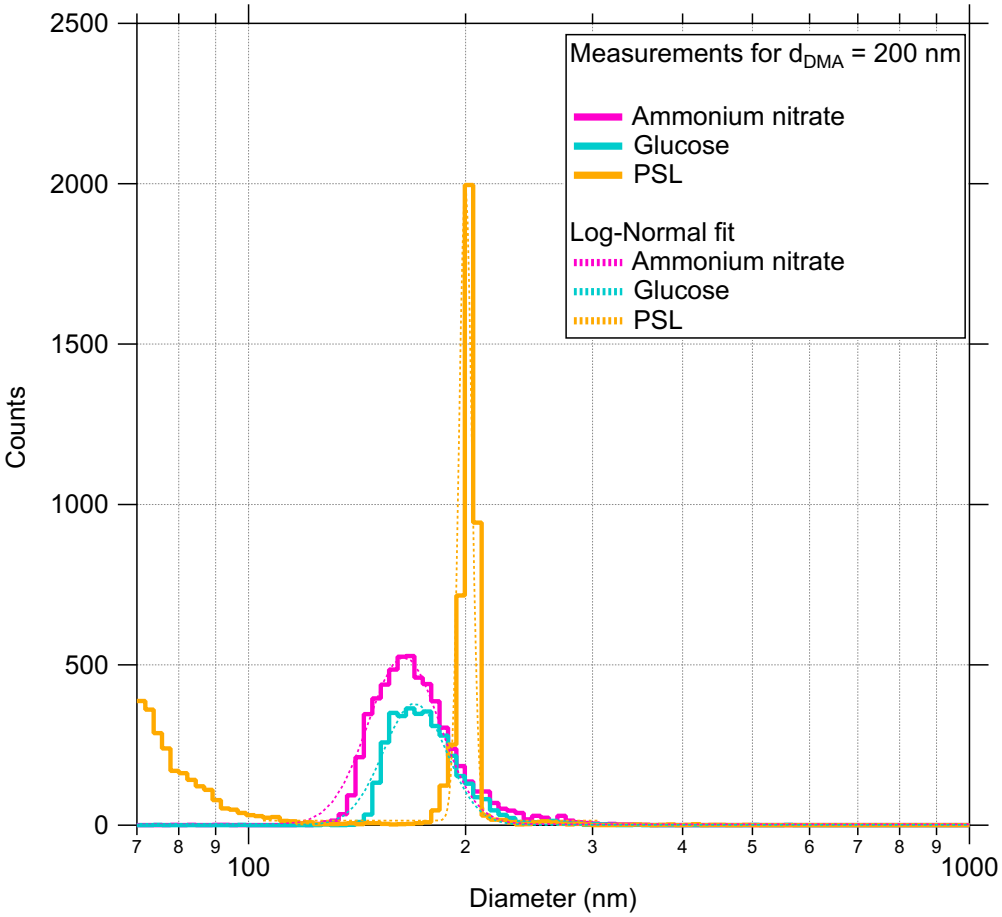

Figure 8: Example for a size calibration measurement. Here, ammonium nitrate (pink), glucose (bright blue), and PSL (orange) are shown as calibration aerosol for a selected size of 200 nm. The dashed-lines represent the log-normal fits which are used for the later evaluation.

Both instrument versions show an offset to smaller particle diameters between the DMA selected diameter compared to the maximum diameter of the size distributions (see Fig. 9a). By comparing the size alignment of both instrument versions with each other, they show a very good agreement and are distributed around the 1:1-line (see Fig. 9b). These calibrations prove that both instruments are suitable for in-flight comparison. From this calibration (Fig. 9a), a new bin scheme of size bins for post-processing of the data was retrieved. The detailed bins are shown in Sect. B.1.

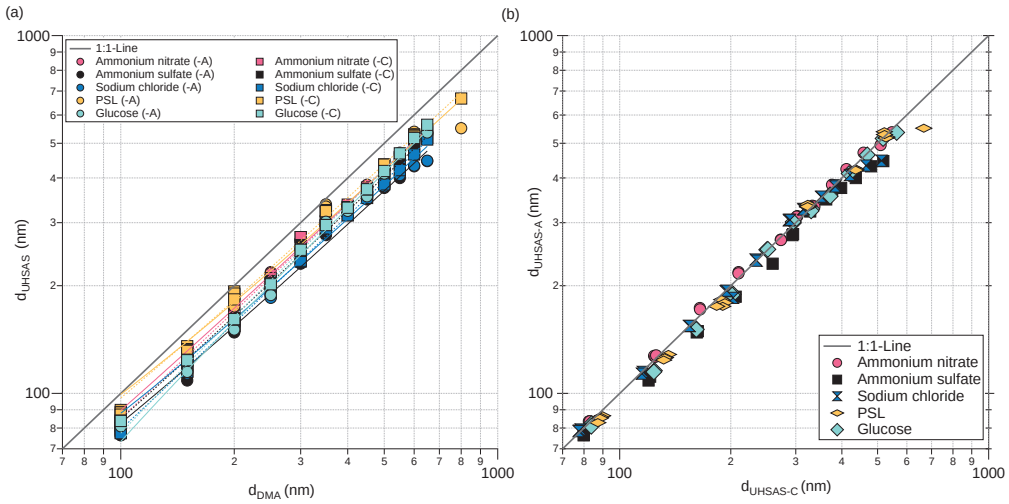

Figure 9: Results of the size calibration measurements for both UHSAS instruments (UHSAS-A in circles and UHSAS-C in squares) as published in Bozem et al. (2025). The comparison of the size distribution for different substances against the selected diameter at the DMA (a). The comparison of both instrument versions against each other (b).

Since the measurement principle is based on Mie-theory, see Chapter 1.2.5, it is possible to determine the relative signal intensity as a function of size and refractive index, see Fig. 10. The calculation was done using the Mie-calculator, developed and described by Vetter (2004).

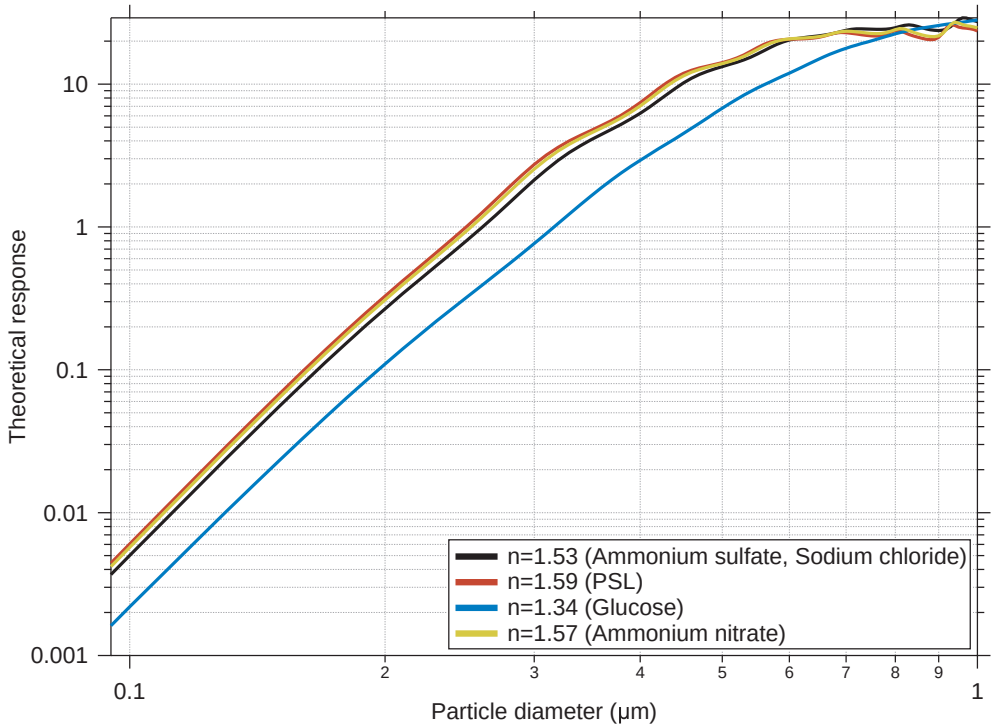

Figure 10: Calculated theoretical particle signal according to Mie-theory for different refractive indices and substances, applying the Mie-calculator by Vetter (2004). Published in Bozem et al. (2025).

Bin scheme

As pointed out in the previous Section 2.1.2, the results from the size calibration measurements yield a deviation from the 1:1-line with some differences depending on the measured species and therefore on the refractive index. This is due to the non-linear properties by the Mie-theory (Sect. 1.2.5). As a consequence, the highly resolved measurement with 99 logarithmic size channels are not able to represent all size distributions correctly as there is no online correction of the refractive index. This means, for example, that a measured aerosol particle that scatters a certain amount of light can have a diameter of 300 nm when it is dominated by organic material such as glucose or around 220 nm when it consists of sodium chloride (see Fig. 10). For the correct analysis of the size distribution data, the size calibration measurements (see, for example, Fig. 8) are taken into account to create a new bin scheme to account for the different sizing issues. Here, all measurements are evaluated with a log-normal fit to determine the maximum of the size distribution which is then mapped against the original diameter set on the DMA (see Fig. 11a).

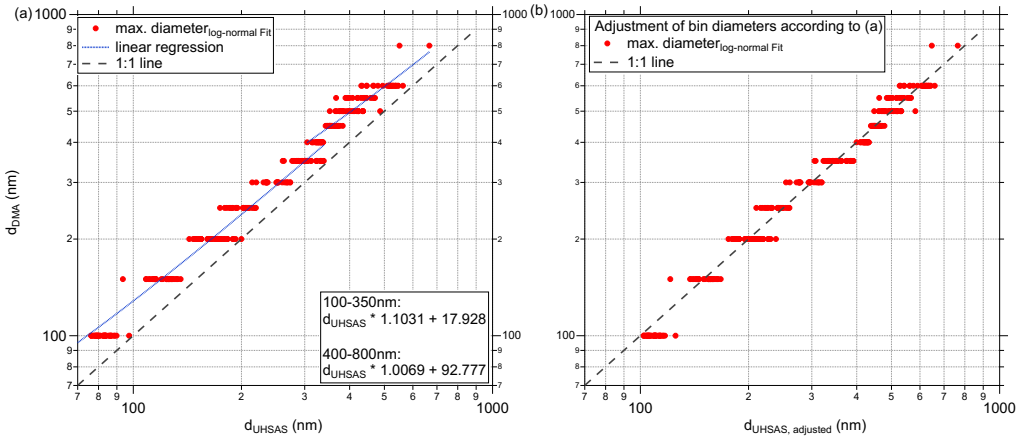

Figure 11: Distribution of the log-normal fit maxima against the DMA-diameter for the adjustment of the bin scheme. The bins are adjusted by performing a linear regression through the distribution (a) in order to shift the original diameter accordingly towards the 1:1-line (b). The jump within the linear regression in (a) around 375 nm is due to possible gain detection problems.

The goal of the first step of the bin scheme correction is to bring all measurements as close to the 1:1 line as possible. Therefore, a linear regression of the maxima is performed and then added to the bin boundaries of the old scheme. This linear regression is performed in two different size ranges, due to a step in the distribution of the log-normal maxima at 375 nm. This step might be caused by possible gain detection problems. The final adjustment of the bin boundaries is shown in Fig. 11b. In Fig. 12, the adjusted size calibration measurements are summarized in a box-whisker-plot against the adjusted bins. The new bin scheme was defined to comprise all data between the 25 % and 75 % percentiles for each size in a new channel and also includes even most data between the 10 % and 90 % percentiles. As a consequence, the number of channels in the new bin scheme reduces from 99 channels originally to only 9 new channels, but it considers the dependency on the refractive index in the measurements.

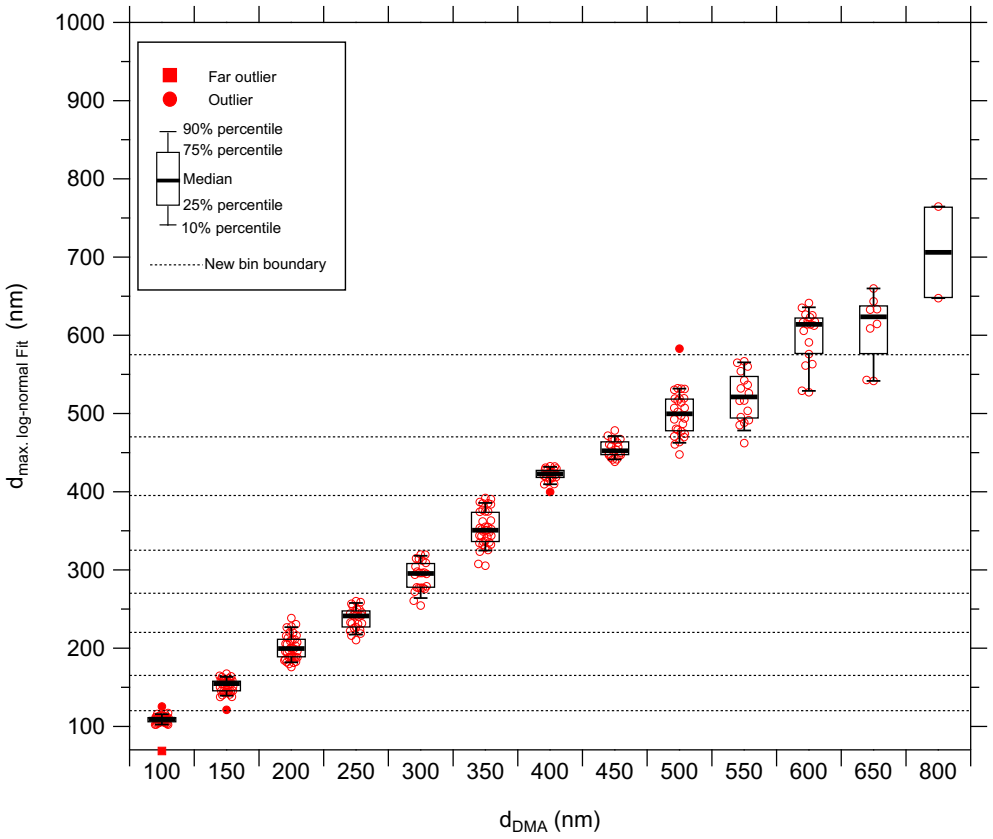

Figure 12: Determination of the new bin scheme of the UHSAS measurements from the size calibrations performed for TPEx. The diameter of the log-normal fit maximum for all size calibration measurements over the complete size range and for all calibrated refractive indices is visualized as a box-whisker distribution (given the quartiles, medians, 10 and 90 % percentiles). The horizontal lines highlight the 9 new bin boundaries. Empty circles represent the data within the statistical range, filled circles mark outlier and filled squares are far outliers.

2.1.3 *Quality assurance*

The results in Chapter 3 are based on airborne measurements. Compared to ground-based measurement stations, the measurements presented here undergo large pressure variations as consequence of climbs and descents of the aircraft as well as temperature changes. Furthermore, we operated the two UHSAS on different platforms to obtain vertically resolved measurements with a vertical distance of around 200 m (Bozem et al., 2025). For the analysis and the calculation of vertical gradients, both instruments have to be comparable with each other and also reliable in relation to other size distribution measurements.
Since the inlet system of the UHSAS-C is not suitable for cloud measurements, the data inside clouds might be influenced by inlet artifacts, such

as steel abrasion from the inlet caused by ice particles. Additionally, both UHSAS are not designed for measurements in condensing environments, so the measurement data inside clouds can not be used for the analysis.
Finally, the inlet system inside the Learjet cabin enlarges the sample length and therefore adds particle losses to the measurements due to diffusion losses on the tubing or gravitational losses of larger particles in horizontal tubings. In the following, important steps in terms of quality assurance are described in more detail.

Counting efficiency

In addition to the size calibration, both UHSAS were tested for their counting efficiency. The manufacturer states an efficiency of 99 % (DMT, 2013). For this characterization, the same measurements were used as for the size calibration. The calibration aerosol was probed using different concentrations to investigate a possible dependency on the number concentration. Here, the maximum concentration applied by the manufacturer (3000 cm^{-3}) was exceeded to check the behavior for potentially very strong pollution events. The main focus of this calibration was the comparison between the two UHSAS.
The results of the characterization measurements done for both UHSAS are shown in Fig. 13. Here, the good agreement between both UHSAS systems is again observed with a spread around the 1:1-line mostly in the range of the uncertainties. The largest discrepancies are observed at concentrations around 1000 cm^{-3}. Here, the UHSAS-C detects up to 25 % more particles than the UHSAS-A. According to the manufacturer's statement, this is unexpected and the instruments should work properly in this concentration range. One possible explanation for this deviation could be that the aerosol flow is not split homogeneously and there is no equal distribution of the calibration aerosol. Unfortunately, this can not be tested and excluded completely for parallel operation. However, to investigate this phenomenon in more detail, the counting efficiency is analyzed as a function of diameters and the ratio between both UHSAS. The results are shown in Fig. 14. Here, the largest discrepancies occur between 350 and 550 nm, where all measurements including different concentrations show an agreement of less than 80 %, while more particles are detected by the cabin instrument (ratio airborne/cabin below 1). One possible explanation is that the laser alignment of the UHSAS-A, which was done by the manufacturer on a best-effort basis since the official support has been discontinued, shows some weakness in sense of intra-cavity. Furthermore, wrong gain detection of particles might play a role. If a gain stage calibration is not perfectly correct, a detected aerosol particle may be assigned to the wrong size channel. As the laser alignment

was done on best guess, followed by a gain stage calibration in the laboratory, this effect should be reduced but can not fully be excluded.

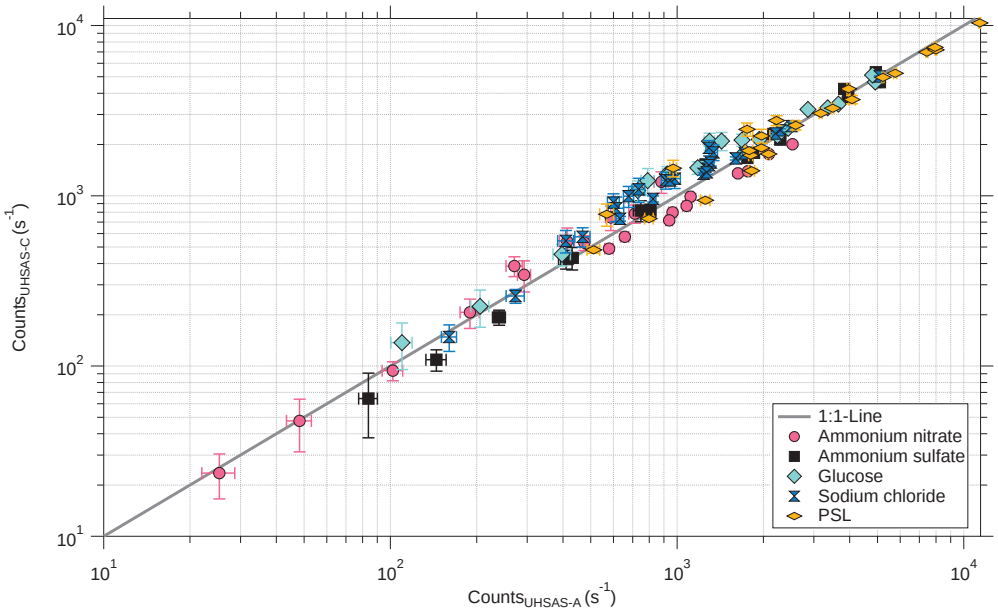

Figure 13: Characterization with respect to counting efficiency, as published in Bozem et al. (2025). The number concentration of the UHSAS-A is correlated with the UHSAS-C for different substances. The black line gives the 1:1-line.

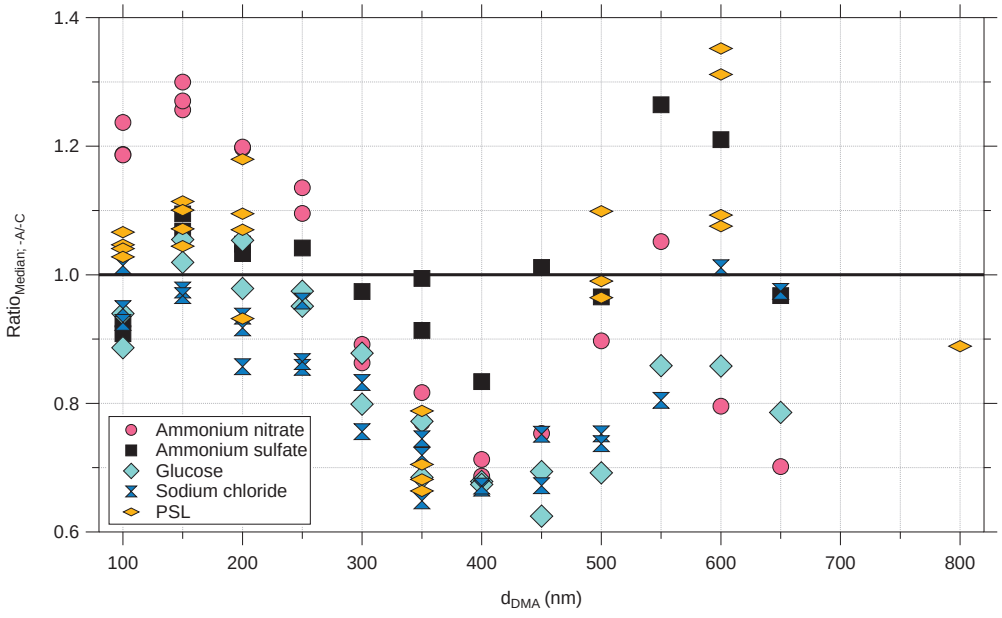

Figure 14: Characterization with respect to counting efficiency as a ratio between the two UHSASs, depending on particle size, as published in Bozem et al. (2025). Multiple points at one DMA size for the same substance indicate different concentrations.

STP correction

As mentioned above, the atmospheric conditions show large variations in pressure and temperature during the flights. In order to compare the measurements between the Learjet and the TPC-TOSS as well as with other data sets, a standard temperature and pressure (STP) correction is needed. For this correction, Eq. 3 is used with T_{STP} = 288.15 K and p_{STP} = 1013.25 hPa as standard conditions based on the International Civil Aviation Organization-International Standard Atmosphere (ICAO-ISA). Here, dp is the measured size distribution matrix, T the sample temperature in K and p the pressure at the inlet in hPa. As there is no temperature measurement available directly in the air flow, it is approximated with the box temperature of the UHSAS. The correction is applied to all size channels of each individual data point and therefore also referred to in post-processing quantities as the total aerosol number concentration or volume distributions.

$$dp_{STP} = dp \cdot \frac{T}{288.15} \cdot \frac{1013.25}{p} \tag{3}$$

In-flight comparison

One goal during TPEx was to derive vertical gradients in the tropopause region, also in aerosol quantities such as number concentration and size distribution. Therefore, one has to be sure that the measurement instruments, here the UHSAS, are comparable. For the laboratory experiments, this was already demonstrated in the previous Section 2.1.2. For the atmospheric measurements, the TPC-TOSS was held at the minimum safe vertical distance of around 43 m during one flight segment of research flight F10 (20.06.2024), in order to obtain comparison measurements for all redundant measurements (Bozem et al., 2025). During the analysis, the aerosol size, volume and surface distribution measurements were averaged over one minute and compared to an additional distribution measured by a GRIMM SkyOPC in the Learjet cabin. The results are published in Bozem et al. (2025) and also shown here in Fig. 15. The corresponding timeseries of the total aerosol number concentration measured by both UHSAS is depicted in Fig. 15a, including the altitudes of both instruments.
The instruments show a really good agreement with each other and also compared to the optical particle counter (OPC) measurements. The differences in the larger size ranges are possibly due to low statistics and single particle detection has large impacts on the average.

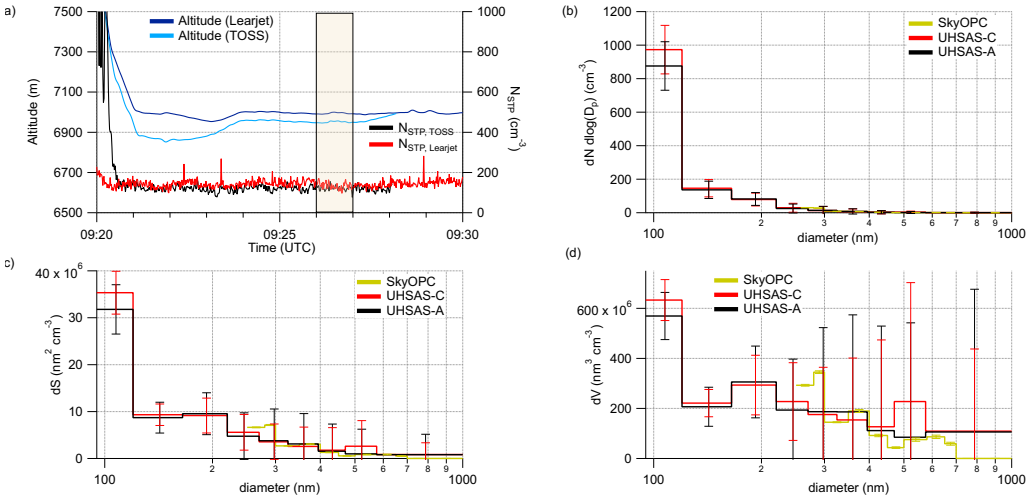

Figure 15: In-flight comparison of both UHSAS compared to a GRIMM SkyOPC onboard the Learjet at a vertical distance of 40 m between the UHSAS-C (Learjet) and UHSAS-A (TPC-TOSS), as published in the revised version of Bozem et al. (2025). (a) Timeseries of the total aerosol number concentration and the altitude for both UHSAS instruments. The shaded area highlights the selected time range for the averaged size (b), surface (c) and volume (d) distributions.

Particle loss calculation

Measuring aerosol particles is challenging due to particle losses in the sample inlet as consequence of diffusion, affecting smaller particles and gravitational and inertial losses affecting larger particles. So, the sample line has to be designed in a way to minimize these losses. For an estimation of particle losses in an experimental setup, von der Weiden et al. (2009) developed a software allowing for calculation of particle transmission and losses dependent on the tubing, sample flow and ambient conditions, such as temperature and pressure. Figure 16 shows the transmission efficiency curves for the tubing between the aircraft inlet and the UHSAS in the Learjet cabin in the measured size range between 100 nm and 1 µm for several ambient pressures. The particle loss calculation was done using different pressures for different measurement altitudes and a constant temperature of 303 K, which matches the temperature in the cabin. The cabin temperature can be used because the aerosol flow heats up as soon as it enters the cabin of the Learjet. The particle losses at the UHSAS-A are not calculated, because the inlet is short (see Fig. 4). There was no transmission correction applied to the measurements from the UHSAS-C. This results from the unknown or only estimated conditions at the UHSAS-A and both instruments need to be considered equally in order of the comparison.

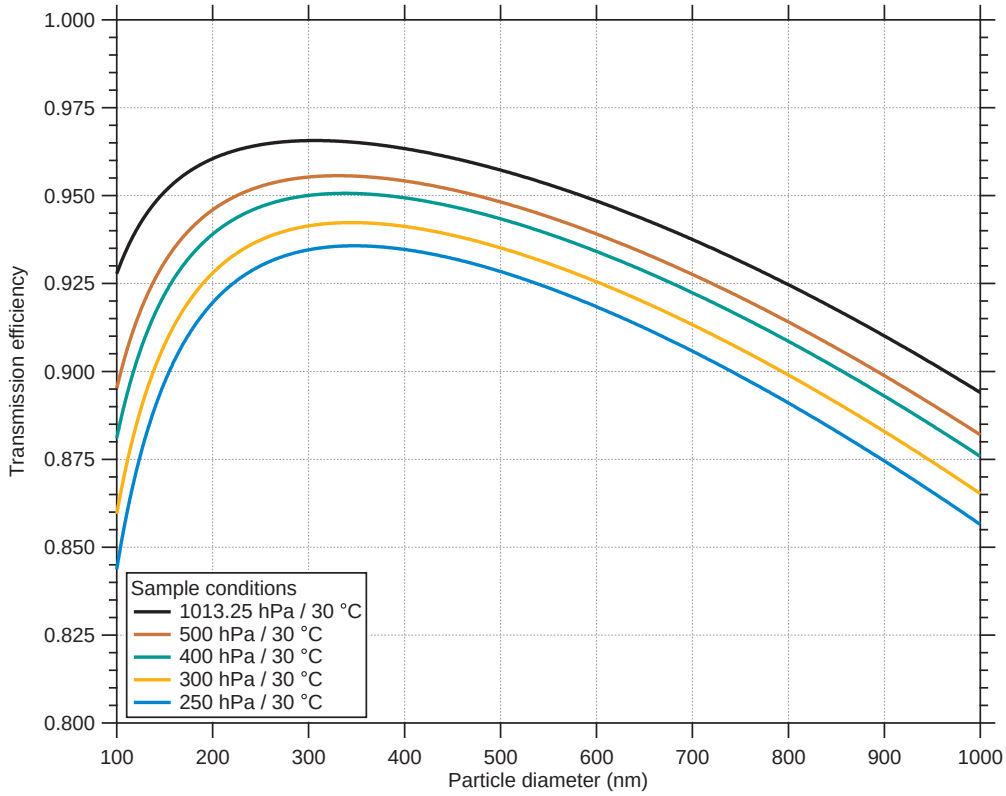

Figure 16: Particle loss calculation using the particle loss calculator (PLC) by von der Weiden et al. (2009) for the inlet system of the UHSAS-C at different inlet pressures while the cabin temperature was always around 30 °C.

2.2 COMPLEMENTARY DATA

In addition to the measured aerosol size distributions from the UHSAS, the presented studies use much more data to provide a comprehensive overview. A complete list of the used data is given in Appendix B.5. In the following, the most important complementary data is shortly described.

2.2.1 *Aerosol mass spectrometer (AMS) data*

The chemical composition of aerosol particles is measured by an aerosol mass spectrometer (AMS). Here, two different versions of an AMS are used, both operated by the aerosol field experiments group of my supervisor at the MPIC. In general, the AMS measurements provide a quantitative information about the chemical composition of non-refractory aerosol particles between 50 and 800 nm. More precisely, a mass concentration of particulate organics, nitrate (NO_3), ammonium (NH_4), chloride (Chl) and sulfate (SO_4) is obtained.
The analysis, presented in Chapter 3.1, is using the data measured by the

compact time-of-flight aerosol mass spectrometer (C-ToF-AMS) which was deployed onboard the High Altitude and LOng range research aircraft (HALO). In the study of Joppe et al. (2025), in Chapter 3.2, the data of the Civil Aircraft for the Regular Investigation of the Atmosphere Based on an Instrument Container (CARIBIC)-AMS is used. This is a fully automated version of an AMS that was developed at the MPIC for the deployment in the In-service Aircraft for a Global Observing System (IAGOS)-CARIBIC project (Schneider et al., 2025). For the purpose of the TPEx mission, it was deployed on the Learjet and operated manually by the scientific operator onboard.

The measurement principle of both AMS is based on flash vaporization with subsequent ionization, extraction and separation by their mass to charge ratio (m/z). The signals are detected by a micro-channel plate (MCP) in the time-of-flight mass spectrometer. For the measured mass concentrations a total uncertainty of 30 % has to be taken into account (Drewnick et al., 2005; Canagaratna et al., 2007; Middlebrook et al., 2012; Schulz et al., 2018; Kaiser, 2024; Schneider et al., 2025).

The measured sulfate mass concentration can be used as stratospheric marker and under strictly defined conditions as identification for the chemical tropopause in combination with trace gas measurements, as done in Joppe et al. (2024) (Chapter 3.1).

Additionally, by comparing the total mass concentration derived from the sampled aerosol particles, it is possible to identify differences between the AMS and the UHSAS. These differences may be due to refractory compounds that cannot be detected by the AMS as their vaporisation temperature is too high. However, it is possible to estimate the mass of refractory aerosol by calculating the mass difference between the UHSAS and the AMS, as it is done in Joppe et al. (2025) (Chap. 3.2).

2.2.2 *Trace gas data*

As described before, the combination of aerosol data with trace gas measurements is very important for the interpretation of the measurements. Especially, trace gases like O_3, N_2O and CO can be particularly helpful when interpreting data in relation to polluted or clean air masses, or whether the air masses are tropospheric or stratospheric. Furthermore, measurements of precursor gases, such as SO_2 help by interpreting the aerosol measurements with respect to gas-to-particle conversion.

A complete list of these measurements is given in Appendix B.5.

A detailed description of the measurements and their references are provided with the according acknowledgments and contributions by co-authors in the respective studies by Joppe et al. (2024, 2025) and Bozem et al. (2025).

2.2.3 *Trajectory data*

In order to investigate the air mass history and the development of observed plumes of enhanced aerosol concentrations, the presented studies in this thesis use different sets of trajectory data which will be introduced briefly in the following.
In the study of Joppe et al. (2024) in Chapter 3.1, dispersion simulations by Hybrid Single-Particle Lagrangian Integrated Trajectory model (HYSPLIT) (Stein et al., 2015) are used to track the volcanic plume in the first days after the Shiveluch eruption. This model allows the tracking of particle dispersion on user-defined heights using a volcanic database for the initial coordinates, where the plume starts. The meteorological data chosen in this study is the GFS global data with a horizontal grid spacing of 0.25 °, which is the highest resolution on the global scale. Volcanic ash was chosen as material while the mass eruption rate was calculated by HYSPLIT based on the eruption height. The dispersion was analyzed on different height levels which are typical tropopause heights in the extratropics (9 to 11 km). All of these calculations are done on the open-access web based application (https://www.ready.noaa.gov/hypub-bin/dispasrc.pl, last access: 12.09.2025).
The air mass history in both studies (Joppe et al. (2024, 2025)) is investigated by using Lagrangian analysis tool (LAGRANTO) back trajectories (Sprenger and Wernli, 2015). These trajectories are calculated 10 days back in time. In Joppe et al. (2024), the trajectories are calculated on the basis of ECMWF reanalysis fifth generation (ERA5) meteorological data on a grid around the aircraft position. Here, the calculations were done by Daniel Kunkel from the Institute for Physics of the Atmosphere, Mainz (IPA) at the JGU within the central data management project of TPChange.
The study of Joppe et al. (2025) uses LAGRANTO back trajectories based on Icosahedral Nonhydrostatic (ICON)-global model analysis data, started every second along the flight path. These calculations were done by Annette Miltenberger from the IPA at the JGU within the project B08 of TPChange. A detailed description of the trajectory data set is provided in the respective publications in Chapter 3.1 and 3.2.

2.2.4 *ERA5 Reanalysis data*

For the analysis of the observations and the placement in the meteorological context, the ERA5 data set is used. This data set is produced by the European Centre for Medium-Range Weather Forecast (ECMWF) and is the fifth generation of reanalysis. It covers the atmosphere over the whole globe since 1940 on a hourly timestamp for atmospheric, oceanic and land surface variables. The horizontal resolution is 31 km distributed over 137 model levels from the surface up to 1 hPa or roughly 80 km. The data is available

on different levels, more precisely on pressure levels, potential temperature levels, model levels, PV levels and single levels (Hersbach et al., 2020). The access to ERA5 data is possible with registration on the Copernicus Climate Data Store (https://cds.climate.copernicus.eu/, last access: 12.09.2025) on open-access. In this thesis, the ERA5 data is partly interpolated on the flight path of the aircraft in order to obtain more detailed information of the 4D-field. This interpolation was done by Hans-Christoph Lachnitt from the IPA at the JGU within the central data management project of TPChange.

2.2.5 CAMS global composition forecast

As this thesis deals with the chemical composition of the atmosphere with special focus on aerosol chemical composition, the CAMS global atmospheric composition forecast data is from high interest.
This data set is also provided by the ECMWF and gives a forecast of aerosol, pollutant and trace gases properties on a global scale. As input for the model forecast, satellite data is assimilated and merged with model simulation which are then calculated into the future to get the forecast. Therefore, the ECMWF in-house Integrated Forecasting System (IFS) model is used with an additional setup for chemistry. These additional modules allow not only the transport of the included species, but also emissions, removal processes and microphysical properties (e.g., Inness et al., 2015; Rémy et al., 2019). The data can be accessed in the atmosphere data store by the Copernicus initiative (https://ads.atmosphere.copernicus.eu/, last access: 12.09.2025) free of charge.
For the global composition data set same holds as for the ERA5 data set. It is partly interpolated on the flight path to obtain curtain plots and local forecast data to compare with the measurements. This interpolation and the curtain plots were done by Daniel Kunkel from the IPA at the JGU within the central data management project of TPChange.

2.2.6 *Global fire assimilation system (GFAS)*

In the second presented study by Joppe et al. (2025) (Chapter 3.2), the CAMS global fire assimilation system (GFAS) data set is used to identify regions with active biomass burning. The data is mainly assimilated by satellite observations of fire radiative power (FRP) on the basis of thermal surface anomalies. Thus, false indications are possible, caused by volcanic activities, gas flaring or reflecting surfaces. GFAS uses a Kalman filter in order to fill observational gaps (Kaiser et al., 2012).
In the used version of GFAS (v 1.2), the satellite retrievals are combined with model calculations of the Plume Rise Model and the IS4FIRES Model. Through the additional model calculations, information of the injection height

and surface parameters are available (Rémy et al., 2017).
The used data is accessible open-source on the atmospheric data store, operated by Copernicus and the ECMWF (Copernicus Atmosphere Monitoring Service, 2022).

2.3 FIELD EXPERIMENTS

In this thesis, the results are based on measurements during two research aircraft missions over Europe. In this section, some more details on the missions are given.

2.3.1 *Chemistry of the Atmosphere: Field Experiment over Europe (CAFE-EU)/BLUESKY*

Joppe et al. (2024) (Chapter 3.1) uses the data collected during the Chemistry of the Atmosphere: Field Experiment over Europe (CAFE-EU)/BLUESKY mission. This mission includes two German research aircraft, namely HALO and the DLR-Falcon. It took place from 16 May until 9 June 2020, during the early COVID-19 lockdown in Europe (Voigt et al., 2022). The mission was led by the MPIC and the DLR. In total, 20 research flights were conducted, from which eight flights were performed with HALO. The payload of both aircraft was specialized for trace gas and aerosol measurements, including volatile organic compound (VOC) measurements.
Since the campaign was carried out from Oberpfaffenhofen, Germany, during the COVID-19 lockdown, the focus of this campaign was to investigate changes in atmospheric composition as consequence of reduced anthropogenic emissions (Voigt et al., 2022). Resulting on this specific question, the focus was more on low altitude flights and profiling the atmosphere than on probing the UTLS. Nevertheless, the measurements reach up to 14 km and provide at least some data around the tropopause region allowing to study small-scale processes. As this campaign is not focus of this thesis, more details can be found in the campaign overview manuscript by Voigt et al. (2022).
The measurements during CAFE-EU/BLUESKY were conducted not by me, but a large team from the MPIC and DLR. The key data for the study by Joppe et al. (2024) was recorded, processed and provided by Katharina Kaiser, Johannes Schneider, Lenard Röder, Horst Fischer (all MPIC), Andreas Zahn (Karlsruhe Institute of Technology (KIT)), Laura Tomsche and Christiane Voigt (DLR, JGU). A detailed contribution is given in the acknowledgments of Joppe et al. (2024).

2.3.2 *Tropopause composition gradients and mixing Experiment (TPEx)*

The TPEx mission is the central airborne measurement campaign within the TPChange CRC. It was carried out in June (10 to 21) 2024 with its base at Hohn air base in Northern Germany. The measurement platform was a Learjet 35A by the company Gesellschaft für Flugzieldarstellung GmbH (GFD) that was equipped with several trace gas and aerosol measurements in the cabin and a wingpod under the left wing of the aircraft. In addition to the online measurements, filter samplers and impactor samples were collected with focus on INPs and aerosol particles. Furthermore, the aircraft was able to deploy a second measurement platform towed on a steel rope below the aircraft, the TPC-TOSS. This TPC-TOSS was equipped with redundant measurements to the aircraft itself to be able to calculate vertical gradients in temperature, O_3 and aerosol size distributions. A detailed description of these measurements is provided in the manuscript by Bozem et al. (2025) in Chapter 3.3.
The TPEx mission aimed for the following research topics (https://tpchange.de/field-campaigns/tpex/, last access: 12.09.2025):

- Identification of mixing processes across the extratropical tropopause
- Probing and analysing the vertical transport from the PBL to the UTLS by processes like convection and warm conveyor belt (frontal) uplift, with its effects on new particle formation (NPF) in the UTLS
- Probing the water vapor distribution in the UTLS over Europe
- Source allocation of aerosol particles and INPs to understand the main pathway towards the UTLS

In total, one scientific test flight and eight scientific flights were conducted during TPEx, from which four flights were performed using the TPC-TOSS. The deployment of the TPC-TOSS is coupled to strong safety restrictions, so the deployment was only possible in a restricted air space. Therefore, two possible areas were available for TPC-TOSS operation during the mission, one over the Baltic Sea close to Rügen and one over the North Sea close to Helgoland. Figure 17 shows the spatial coverage of the measurement flights. In the vertical, measurements were taken up to 38000 ft (11500 m) without and 32000 ft (9700 m) with the TPC-TOSS. As the deployment of the TPC-TOSS influenced the performance of the Learjet, the flight time varied between 2.5 h with and up to 4 h without the TPC-TOSS (Bozem et al., 2025).
The TPC-TOSS was not connected electrically to the Learjet, so that all instruments had to run autonomously, only a radio communication between the instruments and the Learjet was possible in order to observe the measurements

during flight. During operation, the vertical distance between both platforms was around 200 m with a horizontal offset of roughly 1 km. Additionally, the speed of the Learjet was reduced during TPC-TOSS operations, to around 160 $\mathrm{m} \cdot \mathrm{s}^{-1}$ as safety measure.

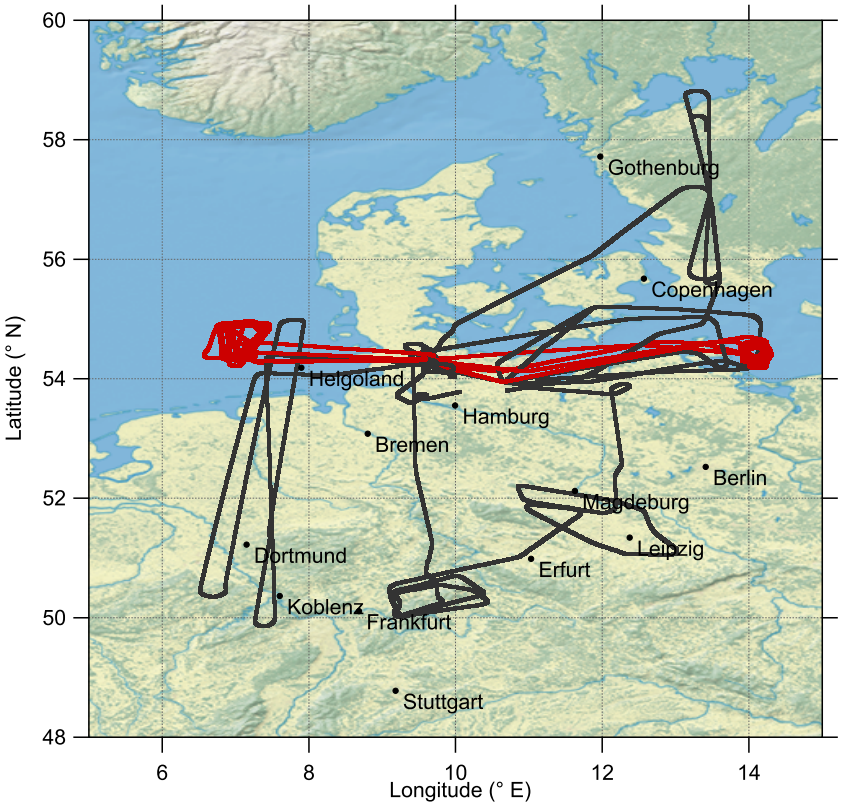

Figure 17: Overview map of all scientific flights during the TPEx mission in June 2024. The red colored flight paths indicate flights with deployed TPC-TOSS in the restricted areas whereas the black flight paths indicate the standard operation without the TPC-TOSS. The map is also published in Bozem et al. (2025) and was created from public-domain GIS data from the Natural Earth website (http://www.naturalearthdata.com, last access: 12.09.2025).

Flight planning and meteorology

The flights during TPEx were planned according to the research topics and the suitable meteorological conditions. For this, the high-resolution model ICON-D2 by the Deutscher Wetterdienst (DWD) was used in combination with the ECMWF forecast model. Additionally, predictions by the CAMS model and the Chemical Lagrangian Model of the Stratosphere (CLaMS)-Ice model (McKenna et al., 2002; Spichtinger and Gierens, 2009a,b) were used in order to have forecasts on the chemical composition and the probability of ice clouds in the measurement region. The meteorological forecast data as well as the chemical forecast were compiled in the mission support system (MSS)

tool, which is a user interface for detailed scientific flight planning (Rautenhaus et al., 2012; Bauer et al., 2022). Besides the direct meteorological data, trajectory data based on the forecasts in the restricted air spaces was generated as forecast of potential WCB outflow regions.

The meteorological conditions during the TPEx mission were favorable for the scientific objectives of the campaign. As consequence of a stable westerly drift over Northern Germany without a stable blocking ridge, the tropopause region was reached with the Learjet (Fig. 18a). Following this westerly drift, several low pressure systems passed the measurement region, causing dynamical processes such as frontal uplift. Thereby, June 2024 marked a month with comparatively low pressure, resulting also in anomalous low tropopause heights over the North Sea compared to the reference period (1991-2020) (Fig. 18b-c). The exceptional lifting processes are also visible by looking at the vertical movement in the free-troposphere at 500 hPa with the tendency of higher lifting velocities than usual (Fig. 18d).

These meteorological conditions caused the possibility of probing cross-tropopause mixing with variable tropopause heights also with the TPC-TOSS, which was one goal of the campaign. Further, it was possible to measure some WCB outflows over Northern Germany and deep convective systems over Sweden and Central Germany.

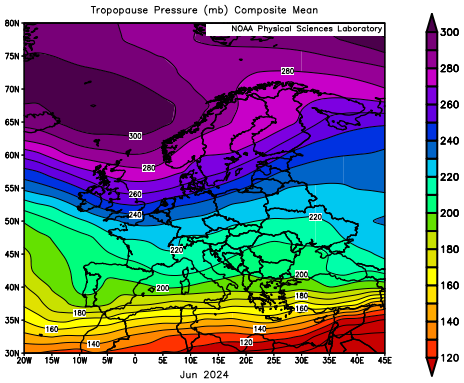

(a) Mean tropopause pressure in mb (hPa).

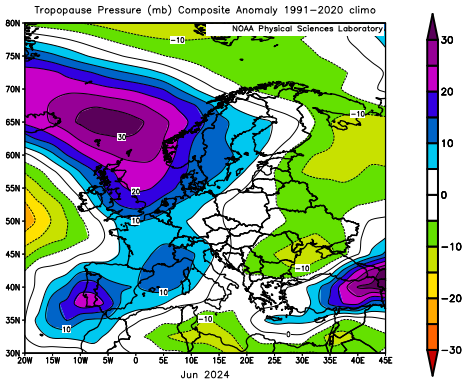

(b) Anomaly of tropopause pressure in mb (hPa).

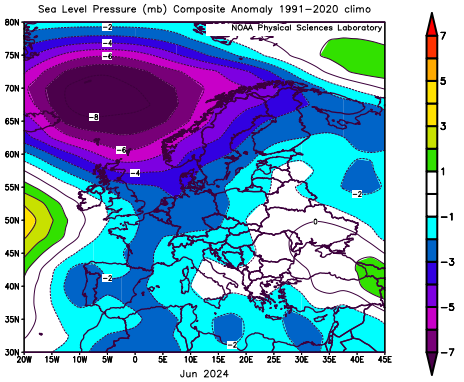

(c) Sea level pressure anomaly in mb (hPa).

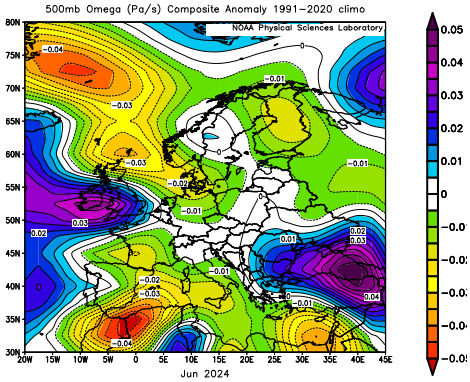

(d) Anomaly of vertical movement at 500 hPa pressure level in Pa/s.

Figure 18: Images of the meteorological situation in June 2024 based on the National Centers for Environmental Prediction (NCEP)-National Center for Atmospheric Research (NCAR) Reanalysis data (Kalnay et al., 1996) produced by the National Oceanic and Atmospheric Administration (NOAA) Physical Sciences Laboratory, Boulder Colorado from their open-access website (https://psl.noaa.gov/; last access: 12.09.2025).

3

RESULTS

In this chapter, the main results are presented in the form of scientific publications, that are accepted or currently under review in the peer-review journals of Copernicus, ACP and AMT.
The two studies by Joppe et al. (2024, 2025) investigate small-scale gradients in aerosol size distribution and chemical composition through cross-tropopause mixing in the extratropical regions, more precisely over Europe. The third study by Bozem et al. (2025) is the technical description of a new measurement platform that was set up for the TPEx mission with significant contributions by myself, including also the data analysis that was required for this task.
Each section will begin with a short summary of the study and a list of my contributions.

3.1 THE INFLUENCE OF EXTRATROPICAL CROSS-TROPOPAUSE MIXING ON THE CORRELATION BETWEEN OZONE AND SULFATE AEROSOL IN THE LOWERMOST STRATOSPHERE (JOPPE ET AL., 2024)

This study focuses on sulfate aerosol in the LMS measured during the CAFE-EU/BLUESKY mission 2020. The sulfate aerosol shows a linear correlation with O_3 in the stratosphere, with some variability on the timescale of days. This variability is investigated in more detail and is caused by a non-stratospheric volcanic eruption on the Kamchatka Peninsula in the beginning of April 2020. This eruption reached the tropopause region in the vicinity of the jet stream, there the sulfate aerosol and the precursor gas SO_2 was continuously mixed into the LMS with subsequent gas-to-particle conversion.
The data was provided by all co-authors, since I was not part of the campaign. I analyzed the data, created the figures and wrote the manuscript. I received valuable feedback on the manuscript by all co-authors. During the review process, I wrote the author replies and created the revised version, which was finally published in ACP on 3 July 2024.

Atmos. Chem. Phys., 24, 7499–7522, 2024
https://doi.org/10.5194/acp-24-7499-2024

Atmospheric Chemistry and Physics
Open Access
EGU

The influence of extratropical cross-tropopause mixing on the correlation between ozone and sulfate aerosol in the lowermost stratosphere

Philipp Joppe[1,2], Johannes Schneider[2], Katharina Kaiser[1,2], Horst Fischer[3], Peter Hoor[1], Daniel Kunkel[1], Hans-Christoph Lachnitt[1], Andreas Marsing[4], Lenard Röder[3], Hans Schlager[4], Laura Tomsche[1,4], Christiane Voigt[1,4], Andreas Zahn[5], and Stephan Borrmann[1,2]

[1]Institute for Atmospheric Physics, Johannes Gutenberg University Mainz, Mainz, Germany
[2]Particle Chemistry Department, Max Planck Institute for Chemistry, Mainz, Germany
[3]Atmospheric Chemistry Department, Max Planck Institute for Chemistry, Mainz, Germany
[4]Institute of Atmospheric Physics, Deutsches Zentrum für Luft- und Raumfahrt (DLR), Oberpfaffenhofen, Germany
[5]Karlsruhe Institute of Technology, Institute of Meteorology and Climate Research, Karlsruhe, Germany

Correspondence: Philipp Joppe (phjoppe@uni-mainz.de)

Received: 2 January 2024 – Discussion started: 10 January 2024
Revised: 30 April 2024 – Accepted: 30 April 2024 – Published: 3 July 2024

Abstract. The chemical composition of the upper troposphere/lower stratosphere region (UTLS) is influenced by horizontal transport of air masses, vertical transport within convective systems and warm conveyor belts, rapid turbulent mixing, as well as photochemical production or loss of species. This results in the formation of the extratropical transition layer (ExTL), which is defined by the vertical structure of CO and has been studied until now mostly by means of trace gas correlations. Here, we extend the analysis to include aerosol particles and derive the sulfate–ozone correlation in central Europe from aircraft in situ measurements during the CAFE-EU (Chemistry of the Atmosphere Field Experiment over Europe)/BLUESKY mission. The mission probed the UTLS during the COVID-19 period with significantly reduced anthropogenic emissions. We operated a compact time-of-flight aerosol mass spectrometer (C-ToF-AMS) to measure the chemical composition of non-refractory aerosol particles in the size range from about 40 to 800 nm. In our study, we find a correlation between the sulfate mass concentration and O_3 in the lower stratosphere. The correlation exhibits some variability exceeding the mean sulfate–ozone correlation over the measurement period. Especially during one flight, we observed enhanced mixing ratios of sulfate aerosol in the lowermost stratosphere, where the analysis of trace gases shows tropospheric influence. However, back trajectories indicate that no recent mixing with tropospheric air occurred within the last 10 d. Therefore, we analyzed volcanic eruption databases and satellite SO_2 retrievals from the TROPOspheric Monitoring Instrument (TROPOMI) for possible volcanic plumes and eruptions to explain the high amounts of sulfur compounds in the UTLS. From these analyses and the combination of precursor and particle measurements, we conclude that gas-to-particle conversion of volcanic SO_2 leads to the observed enhanced sulfate aerosol mixing ratios.

Published by Copernicus Publications on behalf of the European Geosciences Union.

1 Introduction

The chemical composition of upper-tropospheric aerosol particles is highly variable because primary aerosols from natural and anthropogenic ground sources reach this altitude (Martinsson et al., 2019), and secondary aerosols are formed here from gas-to-particle conversion. However, the stratospheric aerosol composition is less complex as the main component is particulate sulfate (SO_4^{2-}) with concentrations between 0.1 and 40 $\mu g\,m^{-3}$ accompanied by minor tropospheric compounds (Deshler, 2008; Murphy et al., 2013; Brimblecombe, 2014; Kremser et al., 2016).

The stratospheric aerosol layer, also known as the Junge layer (Junge and Manson, 1961), is part of the lowermost stratosphere (LMS) and is located roughly between 15 and 25 km (Hofmann and Rosen, 1981). The chemical composition of the aerosol layer underlies seasonal variations induced by the Brewer–Dobson circulation (Martinsson, 2005; Friberg et al., 2014) and volcanic activity, which may increase the aerosol optical depth (AOD) by up to 40 % (Friberg et al., 2018). Sulfate aerosol is formed due to oxidation of carbonyl sulfide (OCS) and sulfur dioxide (SO_2) (Crutzen, 1976; Brühl et al., 2012; Solomon et al., 2011; Kremser et al., 2016) and has an average radius under undisturbed conditions of 170 nm (e.g., Tilmes and Mills, 2014). Both precursor gases have their main sources in the troposphere. OCS is the main sulfur-containing trace gas in the atmosphere, with direct emissions by the oceans or biomass burning as well as photochemical production by oceanic emissions like dimethyl sulfide (DMS) or carbon disulfide (CS_2) (Andreae, 1990; Brühl et al., 2012; Kremser et al., 2016). SO_2 is primarily emitted by industrial processes like the fossil fuel burning. While degassing volcanoes contribute to the tropospheric SO_2 budget (Voigt et al., 2014), explosive eruptions can directly inject SO_2 into the lower stratosphere (Kremser et al., 2016). Other direct sulfate aerosol sources are aircraft which emit soot and volatile sulfate-containing particles at cruise altitudes into the upper troposphere/lower stratosphere (UTLS) (Voigt et al., 2010; Williamson et al., 2021; Tomsche et al., 2022).

Transport processes of aerosol particles into the UTLS have been the subject of several studies, for example with a focus on tropical processes or the Asian tropopause aerosol layer (ATAL) (e.g., Appel et al., 2022; Fadnavis et al., 2013; Froyd et al., 2009; Höpfner et al., 2019). Tracer correlations of aerosol particles with ozone (O_3) and nitrous oxide (N_2O) based on high-altitude in situ measurements have also been used in the context of polar vortex dynamics after a major volcanic eruption (Borrmann et al., 1993, 1995). In those studies, the temporal evolution of the correlation between the mixing ratios of sulfate aerosol, surface area for aerosol particles with a size between roughly 10 nm and more than 1 µm as well as O_3 inside and outside of the polar vortex was analyzed over the course of 22 months after the Mt. Pinatubo eruption in 1991. The observations revealed a slow development of a linear correlation between the O_3 versus aerosol number and surface mixing ratios in the midlatitude UTLS, which degraded again later on. This demonstrated the suitability of aerosol properties as dynamical tracers once the microphysical processes like new particle formation, coagulation and condensational growth following a volcanic eruption into the stratosphere ceased. Furthermore, a temporally stable equilibrium of particle size or surface area has been established.

In the extratropics, the chemical composition of the tropopause region is influenced not only by the Brewer–Dobson circulation, but also by convection, mixing along the subtropical and polar frontal jet streams, breaking of gravity and Rossby waves as well as vertical wind shear (e.g., Gettelman et al., 2011; Kaluza et al., 2021). This forms a transition layer above the tropopause called the extratropical transition layer (ExTL), where tropospheric as well as stratospheric influence is observed (Hoor et al., 2004; Hegglin et al., 2009; Gettelman et al., 2011; Konopka and Pan, 2012; Barré et al., 2013). The effect of these small-scale mixing processes on the chemical composition of aerosol particles in the ExTL has not been well known until now (Kunkel et al., 2019). The lifetime of atmospheric aerosol particles with diameters lower than 1 µm can reach 1 month or more (Jaenicke, 1980). This is sufficient for the particles to be transported up into the tropopause region over long distances and, subsequently, by mixing processes into the stratosphere. Furthermore, the lifetime of more than 1 month corresponds to the timescale that gas-to-particle conversion needs to form sulfate aerosol particles from SO_2 as a precursor gas in the UTLS (Jurkat et al., 2010; Gorkavyi et al., 2021; Rollins et al., 2017).

In our study, we use tracer–tracer correlations as a tool for mixing diagnostics to identify stratospheric air masses and the underlying mixing processes. The basic principle of this method is to use a tropospheric tracer with sources in the troposphere and a rather constant stratospheric background, e.g., carbon monoxide (CO) and water vapor (H_2O), and a tracer with only a stratospheric increase or decrease and a fairly constant mixing ratio in the troposphere, e.g., O_3 or N_2O. In a scatterplot with the tropospheric tracer on the abscissa and the stratospheric tracer on the ordinate, one would expect two separated reservoirs that are not connected if no mixing processes occur. If mixing takes place, both reservoirs are connected by mixing lines, where the mixing ratios are between the two regimes, depending on the state of mixing (Fischer et al., 2000; Hoor et al., 2002).

With this study we want to introduce particulate sulfate as a stratospheric tracer in the correlation with O_3 and find processes that are responsible for the variability of the correlation between sulfate aerosol and O_3 mixing ratios. Therefore, we use in situ aircraft measurements from the CAFE-EU (Chemistry of the Atmosphere Field Experiment over Europe)/BLUESKY mission, conducted in spring 2020 from Oberpfaffenhofen, Germany.

2 Methods

2.1 Data overview

The CAFE-EU/BLUESKY measurement campaign was conducted with the research aircraft HALO (High Altitude and Long Range Research Aircraft) and DLR-Falcon, both operated by the German Aerospace Center (DLR). The measurement flights were performed over central Europe and the North Atlantic between 16 May and 9 June 2020, partly co-located with both aircraft (see Fig. 1). The measurements were conducted during the first COVID-19 lockdown in Germany and Europe, such that the main goal of the campaign was to investigate the atmospheric changes during reduced industrial activity and lower emissions compared to other times (Voigt et al., 2022). This point leads to flight planning during the campaign with a focus on urban areas and low-altitude profiles and less on studying processes in the UTLS region. Therefore, it was not possible to conduct measurements over the complete vertical extent of the ExTL during May 2020. Nevertheless, we were able to obtain measurement data up to 14 km altitude representing the chemical composition of the UTLS. During the campaign period, air traffic was significantly reduced over Europe by up to 80 % (Schumann et al., 2021a, b). Krüger et al. (2022) found substantial reduction in aerosol particles in the lower troposphere in this period, and Reifenberg et al. (2022) could explain the observed reduction in some tracer concentrations with the reduced emissions of pollutants. Tomsche et al. (2022) investigated the SO_2 concentrations in the UTLS region above Europe, which was influenced by changes in sulfur sources such as aviation as well as sinks. Here we focus on the transport processes in the extratropical transition layer, which has been probed with a set of instrumentation on board HALO and DLR-Falcon.

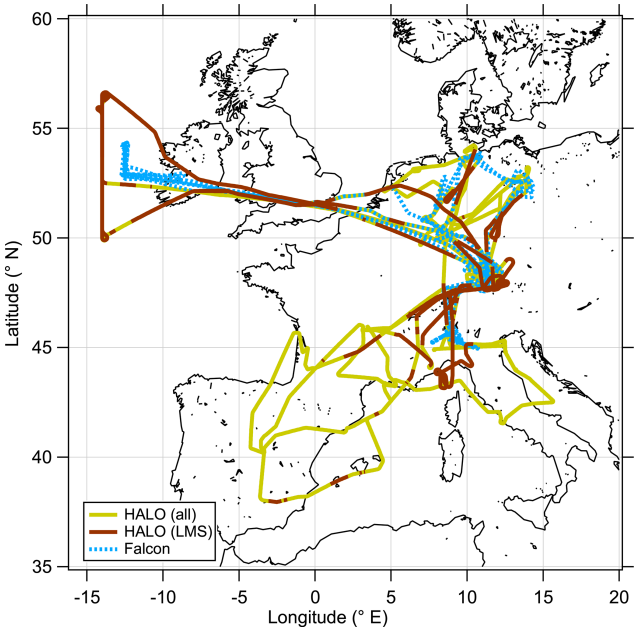

Figure 1. Overview map of all measurement flights performed during the CAFE-EU/BLUESKY measurement campaign between 16 May and 9 June 2020. The HALO flight path as solid line is divided into the complete dataset (yellow) and stratospheric (brown) segments, while the DLR-Falcon flight path is shown as a dashed blue line.

2.2 Instrumentation

For our study, we use the chemical composition of aerosol particles measured on board HALO and trace gas measurements on board HALO and DLR-Falcon. The chemical composition of non-refractory aerosol particles was measured on HALO with a compact time-of-flight aerosol mass spectrometer (C-ToF-AMS) for particles in the size range between 40 and 800 nm (Drewnick et al., 2005; Schulz et al., 2018) and with this within the same size range as previous studies (e.g., Borrmann et al., 1995). We obtain quantitative information on the mass concentration of sulfate, nitrate, ammonium, organic matter and chloride normalized to STP (standard temperature and pressure) conditions. The measurement interval of the C-ToF-AMS during the campaign was 30 s, resulting in a spatial resolution of about 6 km in the UTLS region. The accuracy of the AMS is about 30 % (Bahreini et al., 2009; Canagaratna et al., 2007; Middlebrook et al., 2012). In the following, we use the mixing ratio instead of the mass concentration for comparison with the trace gas measurements. Integrated into the C-ToF-AMS, we use an optical particle counter (OPC) manufactured by GRIMM (OPC 1.129) to measure the aerosol size distribution in 31 size channels from 250 nm to larger than 32 µm.

In addition to the aerosol chemical composition and size data, we use trace gas measurements, like SO_2, CO, H_2O, O_3 and nitric acid (HNO_3), on board HALO and DLR-Falcon.

CO measurements on HALO were performed with the quantum cascade laser absorption spectrometer TRISTAR (Tadic et al., 2017; Röder et al., 2023) with a total measurement uncertainty of 3 % at 10 s time resolution. O_3 on HALO was measured by FAIRO, which measured on the basis of a UV photometer and chemiluminescence (Zahn et al., 2012). On board DLR-Falcon, CO and O_3 were measured with a cavity ring-down spectrometer (PICARRO G2401) and a dual-cell UV photometer (TE 49C), respectively. Both instruments were calibrated before and after the flights with standards that can be traced back to the GAW Hohenpeissenberg station. The precision and accuracy of the CO and O_3 measurements are 3 ppbv/5 ppbv and 3 %/5 %, respectively. An additional in situ dataset is provided by the atmospheric chemical ionization mass spectrometer (AIMS) deployed on DLR-Falcon and includes information on gaseous SO_2, HNO_3 and SF5 (pentafluorosulfanyl). For the detection of upper-tropospheric and lower-stratospheric SO_2 and HNO_3 mixing ratios, the AIMS uses SF_5^- reagent ions (Voigt

et al., 2014; Jurkat et al., 2016; Marsing et al., 2019; Tomsche et al., 2022). The 1-sigma detection limit is 0.0006 to 0.0017 ppbv and 0.005 to 0.009 ppbv for SO_2 and HNO_3, respectively. The total uncertainty for SO_2 is 22.7 % (Tomsche et al., 2022) and 16 % for HNO_3 (Ziereis et al., 2022).

2.3 Meteorology and trajectories

In addition to the in situ measurement data, we use model data interpolated onto the flight path of both aircraft. For meteorological information, we use the ERA5 reanalysis dataset with a temporal resolution of 6 h and a grid spacing of 1° in the horizontal and a vertical spacing of approximately 500 m in the UTLS (Hersbach et al., 2020). Based on the native variables, we additionally calculated potential vorticity (PV) and equivalent latitude. The equivalent latitude is a framework to account for reversible transport under adiabatic conditions and thus get information on potential diabatic transport or mixing. For the calculation, for different isentropes a PV contour line with the same potential vorticity and potential temperature is transformed into a pole-centered circle. The equivalent latitude is the enclosing latitude of this circle (e.g., Lary et al., 1995; Hegglin et al., 2006; Krause et al., 2018). These calculations are done over isentropic surfaces from 240 up to 2000 K from the ERA5 reanalysis data interpolated onto potential temperature.

For our analysis of the air mass origin and possible transport pathways, we use trajectories calculated with the Lagrangian analysis tool (LAGRANTO; Sprenger and Wernli, 2015). Therefore, we initialize a set of 231 trajectories every 30 s along the flight path. The starting points of each trajectory set are placed in a three-dimensional cross around the initial point of the flight path to gain a better statistic and to minimize interpolation errors between the measurements and the model grid. More specifically, we take the location of the aircraft and add five additional points every 0.01° in all four horizontal directions (north, east, south and west), resulting in 21 points arranged in a cross shape (including the aircraft position and location). This cross pattern of 21 points is repeated at 10 additional vertical levels in 1 hPa steps, 5 levels above the flight altitude and 5 levels below the flight altitude. Thus, we get a total of 231 trajectory starting locations at each release time, providing information for 10 d back in time with quantities such as potential temperature and potential vorticity.

3 Results

3.1 Part 1: correlation of particulate sulfate and ozone

O_3 is a suitable tracer for identifying stratospheric air masses due to the photochemical production of O_3 in the stratosphere and its low abundance in the troposphere and its local chemical lifetime of years in the lower stratosphere. There are several ways of identifying the tropopause and thus the lower boundary of the stratosphere from measured O_3 mixing ratios. For example, fixed threshold values of typically 70 or 100 ppbv have been used (e.g., Bethan et al., 1996; Staehelin, 2003). This method has the disadvantage of neglecting the seasonal cycle of O_3, and thus the threshold value can be too low or too high when periods exceeding 1 month are analyzed. Another way of determining the O_3-based tropopause is to take the seasonal cycle into account by using a daily threshold for the O_3 tropopause. This method is described in Zahn et al. (2004) and Thouret et al. (2006) on the basis of long-term observations. In our study we use the method of Zahn et al. (2004) to calculate daily O_3 thresholds for the tropopause. Figure 2 shows the seasonal cycle of the O_3 mixing ratio at the chemical tropopause and the 2 PVU (potential vorticity units, $10^{-6}\,m^2\,s^{-1}\,K\,kg^{-1}$) dynamical tropopause, both calculated following Zahn et al. (2004). For the period of our study (16 May to 9 June), we only see small differences in the results between the chemical and dynamical tropopause since both thresholds are close together around 120 ppbv O_3 during the time of our measurements. We extracted all stratospheric data (i.e., all data points with O_3 mixing ratios larger than the daily threshold) and calculated the frequency distribution of the potential vorticity from the ERA5 dataset (Fig. 2) to verify that the chemical tropopause inferred from the measured O_3 mixing ratios and the calculated thresholds correspond to the dynamical tropopause. This shows that the vast majority of the stratospheric data points have PV values larger than 2 PVU. In Fig. 2, we observe two modes in the PV distribution of the stratospheric data which can be explained by the different stratospheric ages of the sampled air masses (Bönisch et al., 2009). The first mode results from air freshly mixed into the stratosphere with PV values close to the dynamical tropopause. The second mode with values larger than 8 PVU describes air originating from the high stratosphere with no tropospheric influence. In total, less than 4 % of the stratospheric data points have PV values below the 2 PVU threshold. Thus, we use the definition of the chemical tropopause based on O_3 mixing ratios following Zahn et al. (2004) in this study.

Besides O_3, there are other trace gases used as indicators of stratospheric air masses, e.g., H_2O or N_2O. Moreover, within limits, aerosol particle properties can be applied as well (Borrmann et al., 1993, 1995). A good example is the mass concentration of particulate sulfate, which increases in the stratosphere due to the formation from precursors, which takes 30 to 60 d and reaches its maximum in the Junge layer, where particulate sulfate is present in the form of binary solution droplets with inclusions of sulfuric acid (Junge and Manson, 1961; Brühl et al., 2012; Kremser et al., 2016). Thus, we expect a positive correlation between particulate sulfate and O_3 in the stratosphere. The observations made on HALO during the CAFE-EU/BLUESKY campaign confirm this (Fig. 3). Here, two distinct regimes appear in the correlation plot of particulate sulfate and O_3. In the tropospheric regime, the sulfate mass concentration shows high variabil-

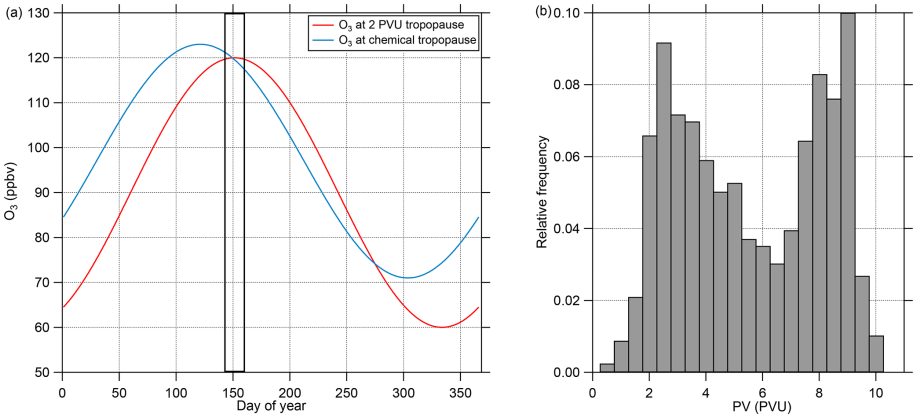

Figure 2. **(a)** Calculated seasonal cycle of O_3 mixing ratios at the 2 PVU dynamical tropopause and the chemical tropopause, both calculated following Zahn et al. (2004). The measurement period is marked with the solid frame. **(b)** Relative frequency of PV values interpolated to the AMS data points from CAFE-EU/BLUESKY identified as stratospheric using the calculated O_3 mixing ratios at the chemical tropopause. Less than 4 % of the data points show PV values lower than 2 PVU, indicating a negligible amount of tropospheric air. The complete stratospheric dataset holds 2049 data points, which represent 100 % of this subset.

ity at O_3 levels below 100 ppbv, depending on the source regions within the boundary layer, e.g., industrial areas. In the stratosphere, we observe a linear correlation between the two species with a slope of 900 to 2300 ppbv ppbv^{-1}, but with variations between the individual measurement flights, i.e., on short timescales of a few days. Note that the accuracy of the C-ToF-AMS of about 30 % (Bahreini et al., 2009) does not affect the observed different slope regimes in the correlation of sulfate aerosol and ozone, because the quantities determining the accuracy (ionization efficiency, collection efficiency and inlet transmission efficiency) do not change over the short period of a 2-week measurement campaign.

This analysis shows that the correlation between particulate sulfate and O_3 can be used as a tool for analyzing air masses in terms of their stratospheric character. The variations in the slope and compactness of the correlation appear on short timescales of a few days. The aim of this study is to understand these variations and link them to possible atmospheric processes. There are a number of different pathways by which sulfur species can be transported from the troposphere into the stratosphere and thus be a possible reason for the observed variability (e.g., Kremser et al., 2016). Feinberg et al. (2019) show the modeled atmospheric sulfur budget under volcanically quiescent conditions and the pathways that lead to the formation of particulate sulfate in the stratosphere. Among these pathways, the most efficient one is the mixing of precursor gases such as OCS and SO_2 into the stratosphere, where OCS is oxidized to SO_2 and SO_2 is further converted to sulfuric acid, forming sulfate aerosol. It is important to emphasize that this budget is valid for volcanically quiescent conditions, because in the presence of volcanic eruptions an additional large source of SO_2 adds up to the other pathways. In this case, SO_2 is transported in the eruption column up into the free troposphere or even

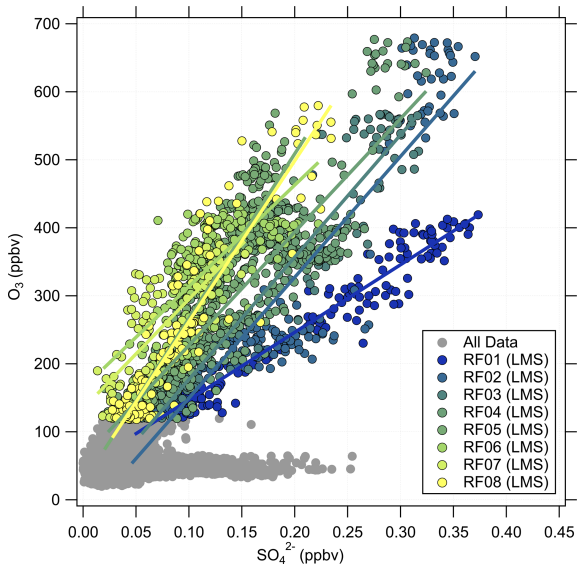

Figure 3. Correlation between the particulate sulfate mixing ratio and the O_3 mixing ratio for the full CAFE-EU/BLUESKY dataset. The color-coded data points indicate the stratospheric data derived from the chemical tropopause O_3 mixing ratios. The grey data show the complete dataset, including the tropospheric data. The solid color-coded lines represent the linear regressions for the individual flights.

the UTLS region, depending on the strength of the eruption. Then SO_2 is converted to sulfuric acid and particulate sulfate, also in the upper troposphere or even in the stratosphere (Kremser et al., 2016).

The low sulfate mixing ratios at the chemical tropopause (Fig. 3) show that direct mixing of high sulfate aerosol concentrations from the troposphere to the stratosphere was not

observed during the campaign, so some other processes need to be taken into account. This observation of low particulate sulfate aerosol amounts at the chemical tropopause is very robust over the whole campaign period, and there it might be controlled by atmospheric processes that need more investigation.

Previous studies with a focus on the Raikoke eruption in 2019 determined no significant contribution from this volcanic eruption (Tomsche et al., 2022; Reifenberg et al., 2022). The following section will show the possible influence of cross-tropopause mixing, especially of the precursor gas SO_2 and the potential influence of a more recent volcanic eruption.

3.2 Part 2: case study on aerosol chemical composition related to mixing processes

Volcanic influence is one of the possibilities that can explain the observed variability in the correlation. One major eruption occurred in 2019 with the Raikoke volcano. However, Tomsche et al. (2022) and Reifenberg et al. (2022) showed that this eruption did not have a significant impact on the measurements during CAFE-EU/BLUESKY. In the following, we focus on a case study to explain the variability of the particulate sulfate correlation with O_3, especially for research flight RF01, as the slope in the O_3–SO_4^{2-} correlation for this flight clearly differs from the other flights (see Fig. 3).

The anticorrelation between CO and O_3 can be used to identify mixing processes between the troposphere and stratosphere (Fischer et al., 2000; Hoor et al., 2002). The presence of mixing lines connecting the sampled tropospheric and stratospheric air masses indicates recent mixing processes. In Fig. 4, most of the stratospheric data of the whole campaign dataset lie in a region of anticorrelated CO and O_3. Thus, it can be concluded that the measured air masses in the stratosphere are influenced by tropospheric air that was mixed across the tropopause. As expected, the correlation in Fig. 4b shows much higher particulate sulfate mixing ratios at higher O_3 levels in the stratosphere and lower mixing ratios close to the tropopause. However, we can identify an anomaly of high particulate sulfate mixing ratios (yellow points) at about 400 ppbv O_3 and 40 ppbv CO (see also Figs. C1 and C4). Here, the measured mixing ratios of sulfate aerosol are in the range we would expect higher up in the stratosphere.

In the following, we will analyze whether this anomaly is caused by a cross-tropopause mixing event and whether such events can explain the observed variability in the SO_4–O_3 correlation. For this analysis, we binned our dataset along equivalent latitude, which can be used as a dynamical tracer (Butchart and Remsberg, 1986; Hegglin, 2005), and potential temperature to see where the anomaly is located (see Fig. 5). The observed sulfate anomaly occurs in Fig. 5b between 40 and 45° N at potential temperatures between 345 and 350 K. It is not connected to the observed stratospheric aerosol layer that starts at higher altitudes, above the 370 K isentrope (see Fig. 5). The potential vorticity indicates that this region is in the vicinity of the jet stream, and with this mixing processes might have occurred or even be present. The O_3 distribution does not show such an anomalous observation as found in the particulate sulfate (Fig. 5a), but we can observe the expected increase from the troposphere to the stratosphere. This location of the anomaly is in good agreement with the previous observation that the anomaly is located on a mixing line in the CO–O_3 correlation in a transition regime between the troposphere and the stratosphere.

We further investigate the meteorology over the campaign period to determine whether the anomaly might be influenced by mixing processes. In particular, we use the vertical wind shear S^2 and the static stability N^2 (see also Appendix B) to identify regions with higher potential for mixing processes. Kaluza et al. (2021) and Kunkel et al. (2019) showed in their study that, in regions with high vertical wind shear ($S^2 > 4 \times 10^{-4}\,s^{-2}$), conditions are favorable for rapid mixing. Figure 6 shows the analysis of the stability parameters mentioned above along with the resulting gradient Richardson number. The vertical wind shear shows high values in the region of the sulfate anomaly (see Fig. 6b), exceeding the mentioned threshold for enhanced mixing. This also results in a reduction in the gradient Richardson number in the same bin to values close to the critical threshold of 0.25 (see Fig. 6c), which indicates favorable conditions for turbulence. The static stability shows the expected transition from tropospheric to stratospheric values (see Fig. 6a). However, regarding the stability analysis, we probed several regions which show favorable conditions for instability and cross-tropopause mixing. Nevertheless, here we focus on the region with the strongest signal, where the observed sulfate anomaly was measured.

These findings suggest that mixing occurred in this measurement region and is one influence on the variation of the SO_4–O_3 correlation. To prove this, we investigated the data in the region of the sulfate anomaly in more detail. Therefore, we extracted the data points that contribute to the anomaly. In total, there are 45 measurement points from the C-ToF-AMS in the bin between 40 and 50° N and $\Theta = 345$ to 350 K. The majority of these points (41 points) were sampled during research flight RF01 in a time span of 20 min (see Fig. 3). The flight was conducted on 23 May 2020 over Germany, while the anomaly was measured in an area over Lower Saxony (see also Figs. C1, C2 and C4). A time series of the measurements from this flight is shown in Figs. 7 and E3, while the period of the anomaly is marked with a colored box.

Figure 4 reveals the correlation between CO and particulate sulfate in the lower troposphere as well as the positive correlation between particulate sulfate and O_3 and the anticorrelation between sulfate and CO in the stratosphere. To identify mixing from the measurements, we use two types of scatterplots. The first is the previously introduced scatterplot using CO and O_3 with different color coding (Fig. 8a–c),

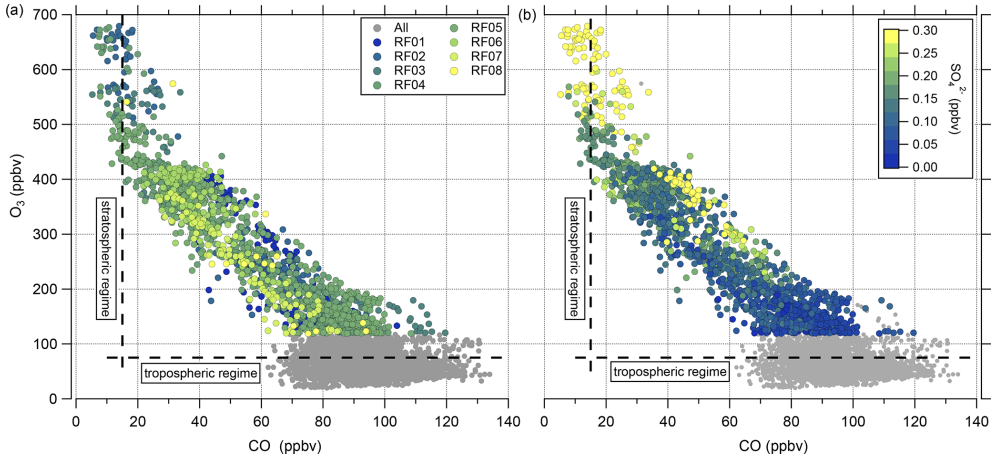

Figure 4. **(a)** CO–O_3 correlation for all data points in grey and the stratospheric data color-coded with the flight numbers. **(b)** The same correlation, but the stratospheric data are color-coded with the sulfate aerosol mixing ratio. In addition, the dashed lines indicate the mean tropospheric and stratospheric regimes without mixing processes.

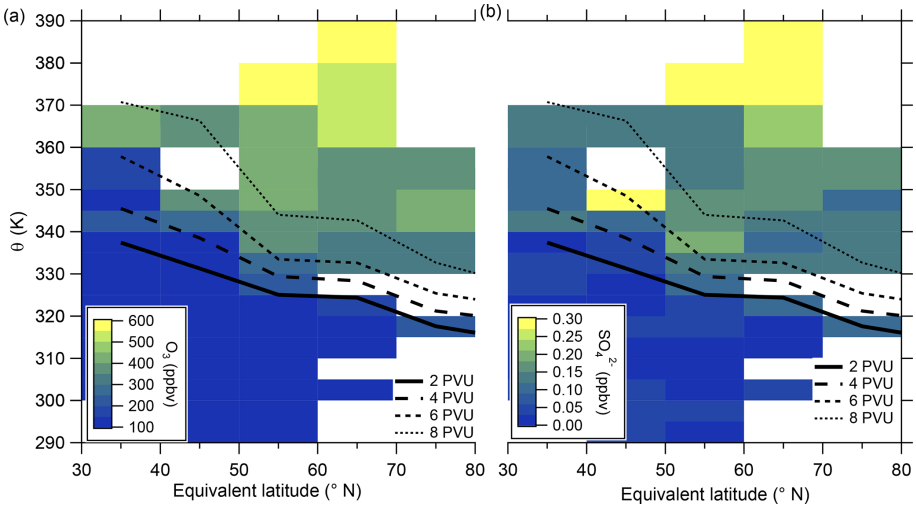

Figure 5. Median of the O_3 mixing ratio **(a)** and sulfate aerosol mixing ratio **(b)** in the θ-equivalent latitude space. Below 350 K, we use 5 K vertical resolution and 10°-equivalent latitude bins. Above 350 K, we enlarge the vertical bins to 10 K to obtain a higher statistical evaluation basis (see Fig. A1). In general, only bins with more than 10 data points are evaluated. We added the 2 to 8 PVU lines to show the location of the dynamical tropopause and the extent of the ExTL into the stratosphere. We only show the region of interest for our study between 30 and 80° N.

and the second is the scatterplot with H_2O and O_3 (Hegglin et al., 2009) (see Fig. 8d–f). This figure contains only data measured on 23 May 2020. The H_2O–O_3 method follows the same principle, with high water vapor mixing ratios in the troposphere and a constant stratospheric background value around 5 ppmv (Hegglin et al., 2009). In our dataset, the lowest observed H_2O values are around 10 ppmv, indicating that we did not fully reach stratospheric background conditions. All of these scatterplots show two separate branches of mixing lines. This feature is most obvious in the H_2O–O_3 correlation. Here, one mixing line connects the tropopause with around $H_2O = 40$ ppmv and $O_3 = 100$ ppbv and the LMS with decreasing H_2O (down to 10 ppmv) at $O_3 = 400$ ppbv. This mixing line also includes the measured sulfate anomaly and was observed over northern Germany (see Figs. 7 and C4). The second mixing line is not as pronounced, starting at drier air masses with $H_2O = 20$ ppmv and only reaching up to $O_3 = 200$ ppbv. These observations were made later on the flight over southern Germany (see also Figs. 7 and C4).

Regardless of the type of scatterplot, we observe an increase in the particulate sulfate mixing ratio and potential temperature along the mixing line, starting at the tropopause and extending into the stratosphere (Fig. 8). In contrast, we also observe a decrease in the CO mixing ratio. This result is consistent with the assumption that tropospheric air enters the stratosphere at lower potential temperatures with lower

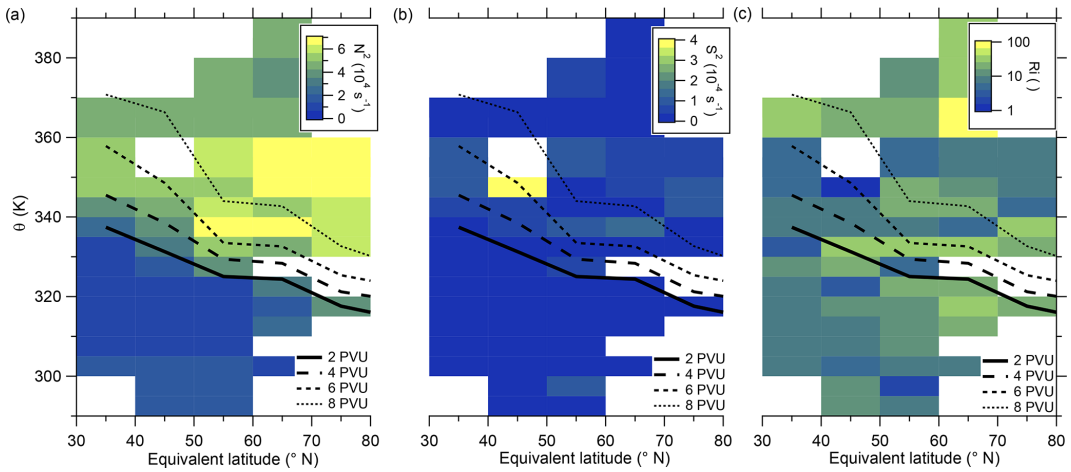

Figure 6. Median of static stability N^2 **(a)**, vertical wind shear S^2 **(b)** and gradient Richardson number **(c)** in the θ-equivalent latitude space. Below 350 K, we use 5 K vertical resolution and 10°-equivalent latitude bins. Above 350 K, we enlarge the vertical bins to 10 K to obtain a higher statistical evaluation basis (see Fig. A1). In general, only bins with more than 10 data points are evaluated. We added the 2 to 8 PVU lines to show the location of the dynamical tropopause and the extent of the ExTL into the stratosphere. We only show the region of interest for our study between 30 and 80° N.

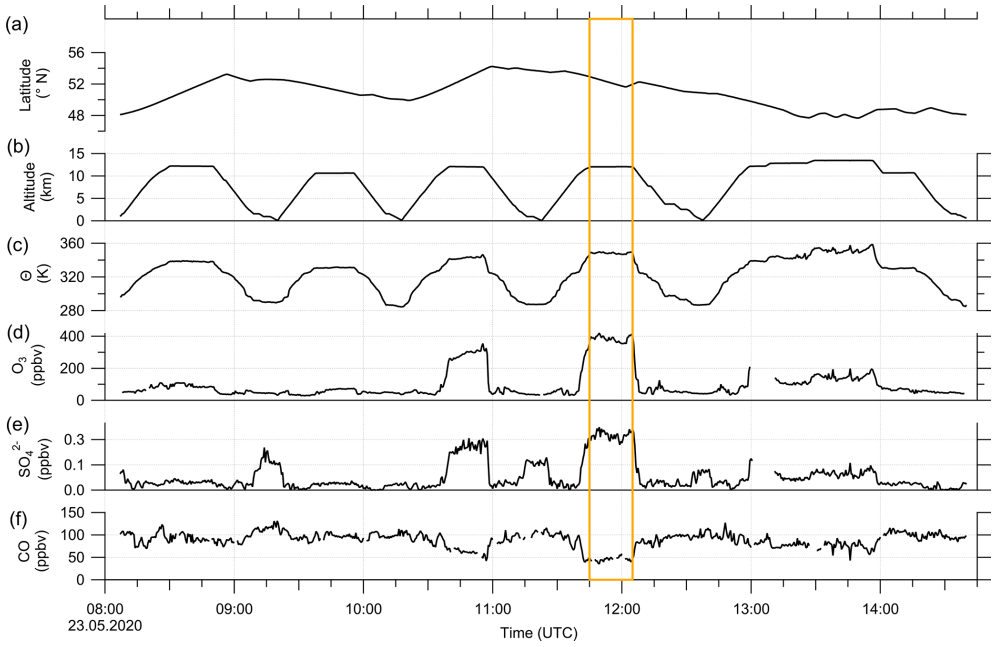

Figure 7. Time series of in situ measurements during research flight RF01 on 23 May 2020 in 30 s time steps. **(a)** Latitude, **(b)** altitude, **(c)** potential temperature θ, **(d)** O_3 mixing ratios, **(e)** sulfate aerosol mixing ratios and **(f)** CO mixing ratios. The orange box marks the period with the observed sulfate anomaly described in the text and shown in Fig. C1. In addition, we added a time series of all aerosol species to the Appendix (see Fig. E3).

amounts of sulfate aerosol, correspondingly higher mixing ratios of precursor gases, and higher CO. In the stratosphere, gas-to-particle conversion of OCS and SO_2 will lead to an increase in particulate sulfate. In contrast to sulfate, CO will decrease during the transport into the stratosphere, by both dilution and photochemical destruction, with an atmospheric lifetime of 1 to 3 months (Seinfeld and Pandis, 2016). This is almost the same time as the calculated e-folding time of gas-to-particle conversion of SO_2 to sulfate aerosol in the midlatitude LMS region (Jurkat et al., 2010).

Further evidence that the anomaly is caused by tropospheric influence is the lower O_3 values and the water vapor mixing ratios. If the air masses were of stratospheric origin, we would expect O_3 mixing ratios higher than 400 ppbv and

a water vapor mixing ratio around 5 ppmv. Instead, we observe lower O_3 mixing ratios and water vapor mixing ratios around 10–20 ppmv.

Similarly to the HALO measurements, we analyzed measurements conducted on DLR-Falcon for this analysis. DLR-Falcon performed a measurement flight on the same day and sampled in the area where the anomaly was encountered just 40 min later than HALO (Fig. C2), which allows a comparison of the measurements on both platforms with respect to dynamical processes. DLR-Falcon does not reach the same high altitudes as HALO, so the air masses were probed at lower levels and thus show higher CO mixing ratios. This time, we use the scatterplot of CO and HNO_3 to identify mixing in combination with gas-to-particle conversion (Fig. 9b). HNO_3 was already introduced as a stratospheric tracer by Proffitt et al. (1989) and Arnold et al. (1989) and utilized because the O_3 data for DLR-Falcon are not available for this flight. Additionally, we added the measurements from HALO to this figure (Fig. 9a) to directly link them to the process of gas-to-particle conversion. We identify a mixing line in the scatterplots, connecting the troposphere and stratosphere. The HALO measurements in Fig. 9a show an increase in the total particle number concentration along the mixing line, whereas the SO_2 mixing ratios on this mixing line (Fig. 9b) show a reduction with respect to the measured tropospheric maxima of 0.1 ppbv, which is an indication of gas-to-particle conversion along this mixing line. This conclusion is also supported by the correlation of the total particle number concentration with the individual species of chemical composition, measured by the C-ToF-AMS (see Fig. E5). Here we can see that the particles forming and growing are mainly sulfate aerosol particles, and the particles do not have a pure tropospheric composition. The process of gas-to-particle conversion requires a source of high mixing ratios of precursor gases, in this case SO_2. In addition, due to the high solubility of SO_2, it requires a very fast and mostly dry process for transport into the UTLS. One possible process that fulfills these conditions is volcanic eruptions, which leads to the assumption that the observed sulfate aerosol particles are most likely formed by volcanic influence.

As a complement to the measurement data, we analyzed the meteorological situation along the flight path for the period of the anomaly (Fig. B1). The flight path was located just above the maximum of the subtropical jet stream and a layer of strong vertical wind shear (Fig. B1a). Further, we see that the flight path crossed a layer of a low-gradient Richardson number (Fig. B1b) and later continued slightly above this layer. This indicated a region of instability which is an important factor in mixing processes.

The previous discussion has shown that mixing between tropospheric and stratospheric air masses most likely occurred before and during the in situ measurements.

Hereafter, we examine the origin of the air masses comprised of high mixing ratios of sulfate aerosol. Therefore, we exploit LAGRANTO back trajectories, starting at a grid around the flight path with 230 trajectories for each measurement point. The trajectories are calculated 10 d backward to see whether the air masses show any fresh influence from the troposphere or a rather stable flow within the lowermost stratosphere. For our analysis, we filtered the trajectories by selecting only those with a minimum potential temperature below 345 K and with an increase of at least 5 K potential temperature. Figure 10 shows that the selected trajectories are close together and move with the jet stream. The trajectories crossed the region of East Asia within 10 d before the measurement, and most of them crossed China and its megacities like Chengdu and Shanghai. The time series of potential temperature shows that no boundary layer air masses were transported to the measurement region in the last 10 d (Fig. 10a), considering the assumption that the trajectories can resolve convective uplift. As a consequence, the enhanced particulate sulfate needs to be older than 10 d and was most likely not directly mixed into the LMS as particulate sulfate, and this also supports the findings in the previous analysis (see, e.g., Figs. 9 and E5).

Alternatively, the sulfate aerosol, as mentioned earlier, could originate from gas-to-particle conversion of SO_2 that was mixed into the LMS. To examine this hypothesis, we start from Fig. 9, which shows that, close to the tropopause, the SO_2 values are quite high and decrease along the mixing line, whereas the aerosol total number concentration increases. This is an indicator of ongoing gas-to-particle conversion in combination with cross-tropopause mixing. To confirm this possible process, it needs a strong source of SO_2 which is strong enough to transport the SO_2 in a short time to high altitudes with as few as possible moist processes to not wash it out from the atmosphere. One possible source of such a process could be volcanic activities. Therefore, we searched for volcanic eruptions in the period of 2 months before the measurements, corresponding to the *e*-folding time of about 50 to 60 d (Jurkat et al., 2010). For the analysis, we used volcanic eruption databases in combination with daily TROPOspheric Monitoring Instrument (TROPOMI) retrievals in different volcanically active regions to identify possible source regions. Thereby, we identified the Kamchatka Peninsula in Russia as an origin of enhanced SO_2 emissions in the beginning of April 2020. This corresponds to the archived reports by the Kamchatka Volcanic Eruption Response Team (KVERT) (Institute of Volcanology and Seismology FEB RAS, 2023). In the report for 8 April 2020, an explosive eruption of the Sheveluch volcano is described, with a volcanic cloud height reaching up to 10 km and thus into the tropopause region. We performed HYSPLIT (Stein et al., 2015) forward-dispersion simulations of the Sheveluch volcano plume and analyzed the eruption plume in the model at different heights to get a broad overview of the distribution. Therefore, we calculated forward trajectories at heights between 9000 and 11 000 m with a vertical resolution of 500 m. In the following, we only consider the levels up to 9000 m (see Fig. D1) and between

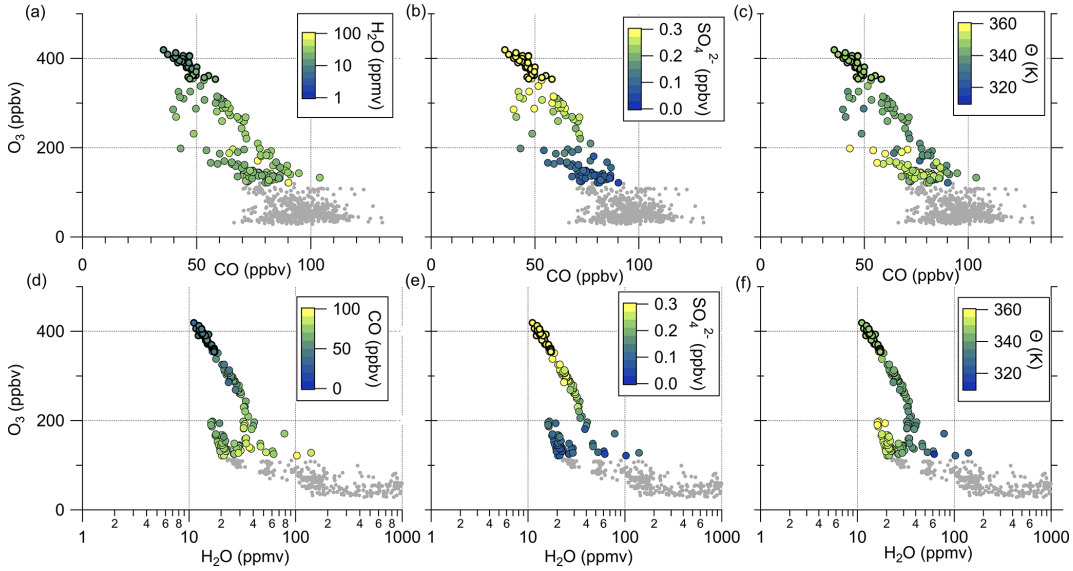

Figure 8. Tracer–tracer correlations for 23 May 2020 to identify mixing processes. The CO–O_3 correlations are color-coded with **(a)** H_2O, **(b)** SO_4^{2-} and **(c)** θ. The H_2O–O_3 correlations are color-coded with **(d)** CO, **(e)** SO_4^{2-} and **(f)** θ. The data correspond to the blue-colored data in Fig. 3 and the sulfur anomaly in Fig. 5.

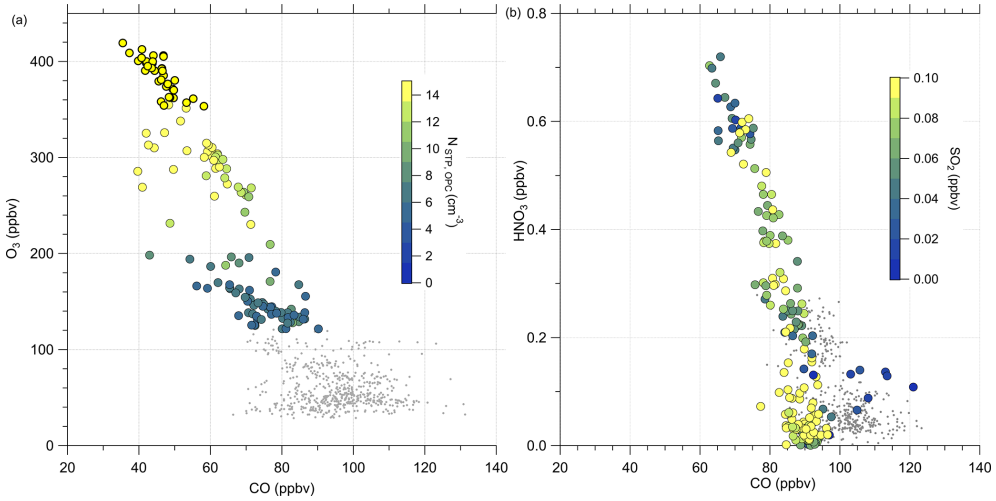

Figure 9. Scatterplot of CO and O_3 measured on HALO **(a)** and CO and HNO_3 measured on DLR-Falcon **(b)** for the investigated flight on 23 May 2020. In panel **(a)** the color code shows the total particle number concentration by the OPC. For the DLR-Falcon measurements in panel **(b)**, we color-coded with the SO_2 mixing ratio. Both measurement platforms observe a mixing line in the probed area. Whereas the total aerosol number concentration is increasing along this mixing line, the SO_2 measurements show a reduction. This is one possible indicator for the process of gas-to-particle conversion.

10 000 and 11 000 m (see Fig. 11), because here the model shows differences in the plume and indicates possible mixing into the stratosphere.

We observe a large volcanic plume up to 9000 m which is distributed, spread and stretched within the first 3 d over the North Pacific, reaching over Alaska and also eastwards, close to the Hudson Bay, Canada (see Fig. D1). For the layer between 10 000 and 11 000 m, the results look completely different (see Fig. 11). Here, we observe no signal of the volcanic plume on the first day. However, more areas with volcanic plume influence occur over Alaska, reaching towards Canada during the second day. These affected areas increase over time. Thus, the HYSPLIT dispersion model results also support the hypothesis of mixing volcanic emissions into the stratosphere within the first 3 d. This is an additional indicator of the mixing of SO_2 into the stratosphere, resulting in higher SO_2 mixing ratios compared to the background. After the mixing of SO_2 into the LMS, the process

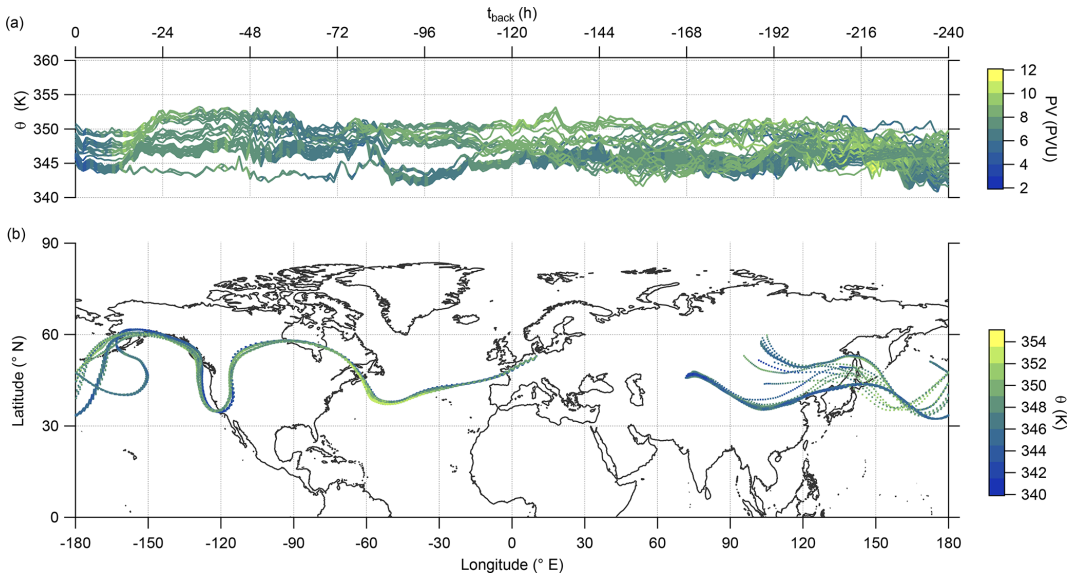

Figure 10. LAGRANTO 10 d back trajectories for cases with enhanced SO_4^{2-} in the lowermost stratosphere. The upper panel **(a)** shows a time series of θ color-coded with PV. The lower panel **(b)** shows the position of the trajectories on the map with θ as the color code.

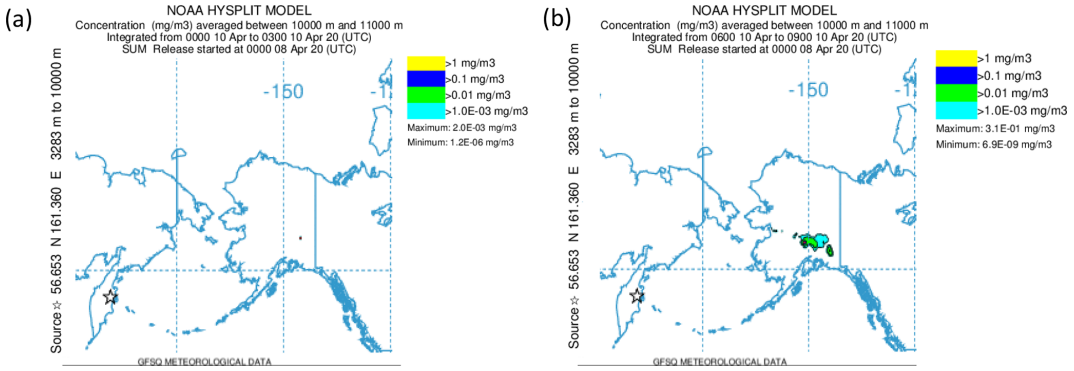

Figure 11. NOAA HYSPLIT dispersion model simulation (Stein et al., 2015) for the Sheveluch eruption on 8 April 2020 on the basis of GFS meteorological data. The particle concentration between 10 000 and 11 000 m is depicted. Panel **(a)** shows the averaging period on 10 April 2020 from 00:00 until 03:00 UTC, and panel **(b)** shows the next period on 10 April 2020 from 06:00 until 09:00 UTC.

of gas-to-particle conversion starts and forms particulate sulfate aerosol over several weeks. This results in the observation of higher mixing ratios of particulate sulfate in the LMS roughly 7 weeks after the eruption, especially for research flight RF01, where the flight path was close to the jet stream and crossed one filament of volcanically influenced air masses.

4 Conclusions

Usually, trace gas correlations, such as CO–O_3 or H_2O–O_3, have been used to study mixing processes between the troposphere and stratosphere. In our study, we showed that, in addition to trace gas measurements, aerosol measurements, especially particulate sulfate, can also be applied to identify troposphere–stratosphere exchange. Furthermore, we showed that the method to define the chemical tropopause proposed by Zahn et al. (2004) is in agreement with the dynamical tropopause definition for our campaign and is thus suitable for the separation of stratospheric and tropospheric air masses. Similar to the correlation between CO and O_3, the correlation of SO_4^{2-} and O_3 in the lowermost stratosphere also showed some variability induced by mixing events. In a case study during the CAFE-EU/BLUESKY mission, we observed air masses with high sulfate mixing ratios in the lowermost stratosphere, reaching values that are typically found at higher altitudes in the stratospheric aerosol layer. Meteorological and dynamical parameters such as vertical wind shear and gradient Richardson number indicated that mixing across the tropopause occurred in this region and along the transport and air mass history. Additionally, we found that this anomaly of higher particulate sulfate in the lowermost strato-

sphere occurred during one single flight. During this flight, we found one mixing line in the CO–O_3 correlation with increasing sulfate aerosol mixing ratios and total aerosol number concentration towards the stratosphere. In addition, we used measurements of the quasi co-located DLR-Falcon aircraft. In the same tracer–tracer correlation framework, using HNO_3 instead of O_3, we also found one mixing line. In contrast to the increasing sulfate aerosol for the HALO measurements, we observed decreasing mixing ratios of SO_2, which is a precursor gas for particulate sulfate. The combination of the sulfate aerosol mixing ratio, the total aerosol number concentration as well as the reduction in SO_2 in the same measurement region led to the hypothesis of upward mixing of precursor gases and ongoing gas-to-particle conversion in the lowermost stratosphere. Here, we could identify volcanic activities on the Kamchatka Peninsula, Russia, and the explosive eruption of the Sheveluch volcano as a possible source of the SO_2 in the tropopause region. The Sheveluch eruption injected SO_2 directly into the upper troposphere, from where it was mixed into the stratosphere, with subsequent gas-to-particle conversion to sulfate aerosol. We can thus conclude that the chemical composition of the aerosol in the lowermost stratosphere is affected by small-scale mixing processes and that the ExTL can thus also be characterized by aerosol properties. In addition to direct mixing of aerosol particles, the process of mixing of precursor gases with subsequent gas-to-particle conversion also needs to be considered, as we showed in our case study. We intend to use this method in the future with data obtained during previous airborne measurements in the UTLS to extend the analysis to a larger scale. Furthermore, we aim to compare the results with chemistry climate model studies to see whether chemical transport models can represent small-scale mixing across the tropopause and the associated gas-to-particle conversion processes. Another study should investigate how models represent the influence of volcanic eruptions on the lowermost stratosphere.

Appendix A: Supporting information about the two-dimensional binned cross sections

In the following, we explain the adjustment of our bin scheme for the two-dimensional binning analysis. Figure A1b shows the data distribution for the evenly distributed bin scheme in the vertical. Here, we see that many bins in the LMS contain less than 10 data points, so we could expect some bias in the median. Therefore, we enlarge the vertical bins at 350 K and above to 10 K to include more data points in one vertical bin and increase the statistic of the analysis without losing information.

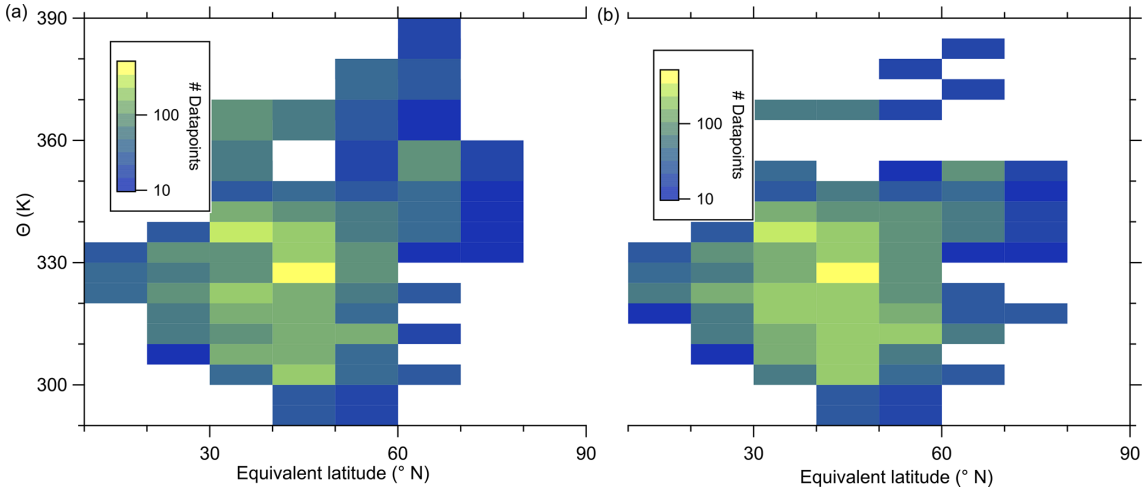

Figure A1. Number of data points in the two-dimensional cross sections (used in Figs. 5 and 6). **(a)** The used bin scheme with larger vertical bins starting at $\theta > 350$ K. **(b)** The even data distribution without any adjustment to the bin scheme.

Appendix B: Supporting information about the meteorological cross sections

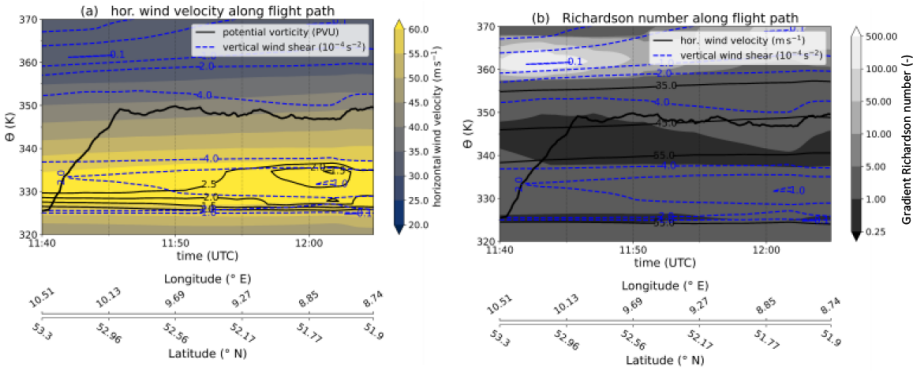

Figure B1. Meteorological cross sections along the flight path, calculated on the basis of ERA5 reanalysis data (Hersbach et al., 2020). Panel **(a)** contains the horizontal wind speed as a filled contour, the flight altitude as a black bold solid line, the PV contour as thin black lines and the vertical wind shear as dashed blue contour lines. In panel **(b)** the filled contour changed to the gradient Richardson number, and the thin black lines are contour lines of the horizontal wind speed. Latitude and longitude values are added to the time series for reference.

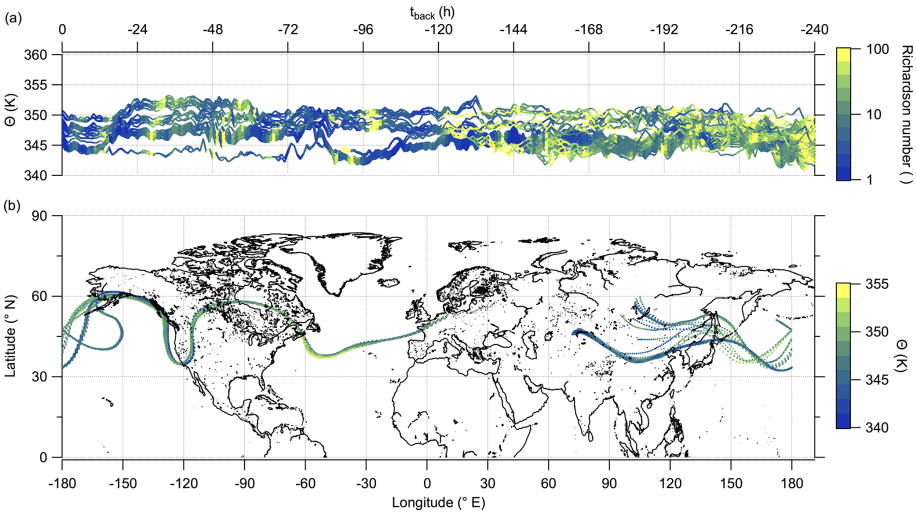

Figure B2. LAGRANTO 10 d back trajectories for cases with enhanced SO_4^{2-} in the lowermost stratosphere starting in northern Germany. **(a)** Time series of θ color-coded with the gradient Richardson number as a marker for potentially instable regions along the trajectories. **(b)** The position of the trajectories on the map and the potential temperature as a color code.

This section offers some meteorological analysis for the flight segment with the observed particulate sulfate anomaly (see Fig. B1). Afterwards, we show some additional data along the back trajectories. More precisely, we show the time series of the Richardson number to indicate potential instable regions the air masses have crossed before the measurement (see Fig. B2). First we want to introduce the used variables for our stability analysis, similar to, e.g., Kaluza et al. (2019) or Kunkel et al. (2019):

$$N^2 = -\frac{g}{\rho_0}\frac{\partial \rho(z)}{\partial z} \quad \text{(squared Brunt–Väisälä frequency)}, \tag{B1}$$

$$S^2 = \left(\frac{\partial u}{\partial z}\right)^2 + \left(\frac{\partial v}{\partial z}\right)^2 \quad \text{(vertical wind shear)}, \tag{B2}$$

$$Ri = \frac{N^2}{S^2} \quad \text{(gradient Richardson number)}. \tag{B3}$$

Turbulence may occur at a gradient Richardson number lower than 0.25.

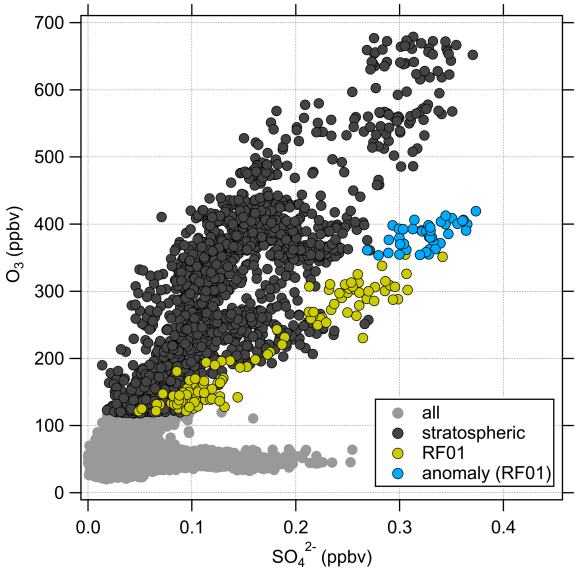

Figure C1. Scatterplot of the in situ measured SO_4^{2-} and O_3 containing or including all the campaign data in bright grey. Stratospheric data points are colored in dark grey. The mixing event of research flight RF01 is indicated in yellow and the sulfate anomaly identified during this flight in blue.

Appendix C: Supporting information about the sulfate anomaly

The following figures are supporting information on the observed anomaly of higher mixing ratios of particulate sulfate. This includes a detailed view of research flight RF01, where the anomaly was observed (Fig. C1). Figure C2 locates the flight segment of the anomaly on the map, including the quasi co-located DLR-Falcon flight path and the sulfur dioxide mixing ratio measured on DLR-Falcon. The last figure (Fig. C3) highlights two selected research flights and their corresponding accuracy within the correlation of the complete dataset.

The following maps (Fig. C4) of the measured stratospheric air during RF01 help to interpret both mixing lines found in Fig. 8. Herewith, we can differentiate between the measured elevated particulate sulfate over northern Germany and the more subtropical air over southern Germany with respect to their characteristics.

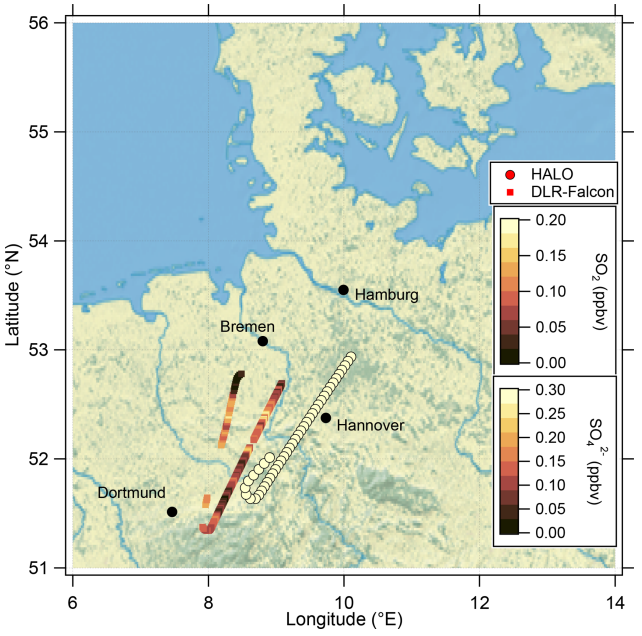

Figure C2. Location of the analyzed flight segment during the research flight on 23 May 2020 between 11:45 and 12:05 UTC, where the mixing event in the vicinity of the jet stream was observed. The flight path of HALO is shown with the filled circles color-coded with the sulfate mixing ratio, and the flight path of DLR-Falcon is shown with the filled squares color-coded with the SO_2 mixing ratio. The map was created from public-domain GIS data found on the Natural Earth website (http://www.naturalearthdata.com, last access: 2 January 2024).

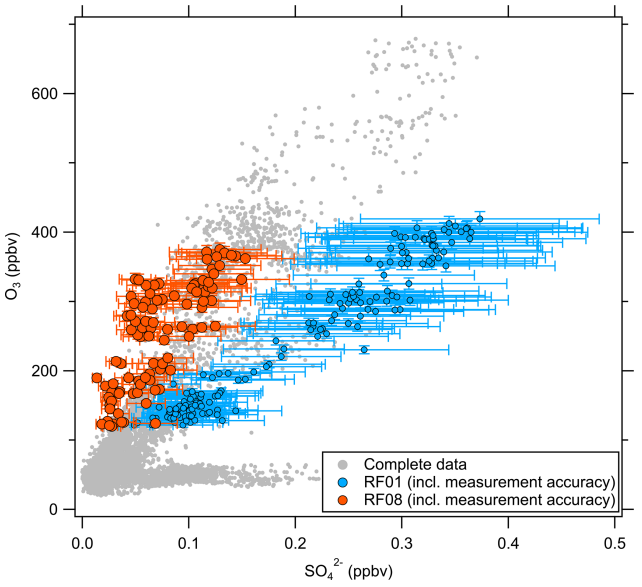

Figure C3. Scatterplot of particulate sulfate against O_3 for the complete campaign dataset. The data points for flights RF01 and RF08 are highlighted together with their measurement accuracy as examples.

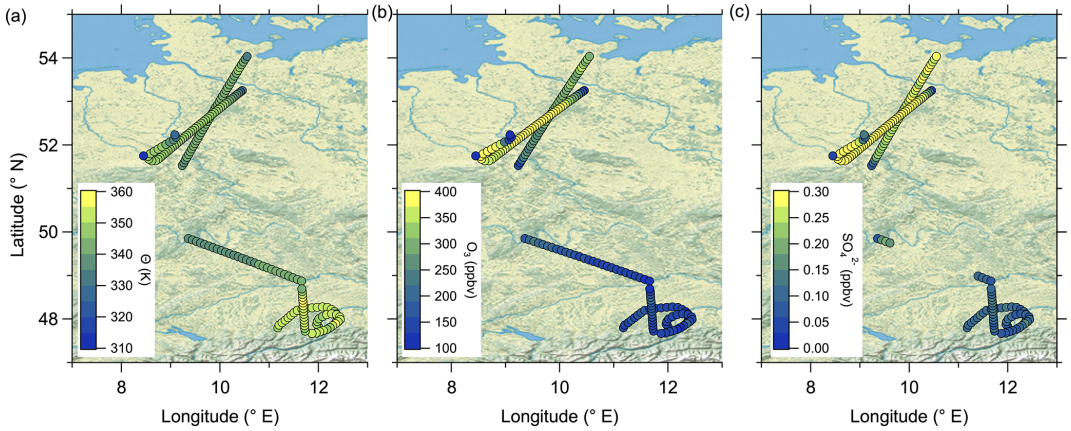

Figure C4. The stratospheric flight segments of RF01 on 23 May 2020 are shown and color-coded with **(a)** potential temperature θ, **(b)** O_3 mixing ratios and **(c)** particulate sulfate mixing ratios. The map was created from public-domain GIS data found on the Natural Earth website (http://www.naturalearthdata.com, last access: 2 January 2024).

Appendix D: Supporting information about the HYSPLIT dispersion simulation

The figure shown in this section is in addition to Fig. 11 and shows similar variables but for the altitude range from sea level up to 9000 m to show the entire volcanic main plume and its distribution.

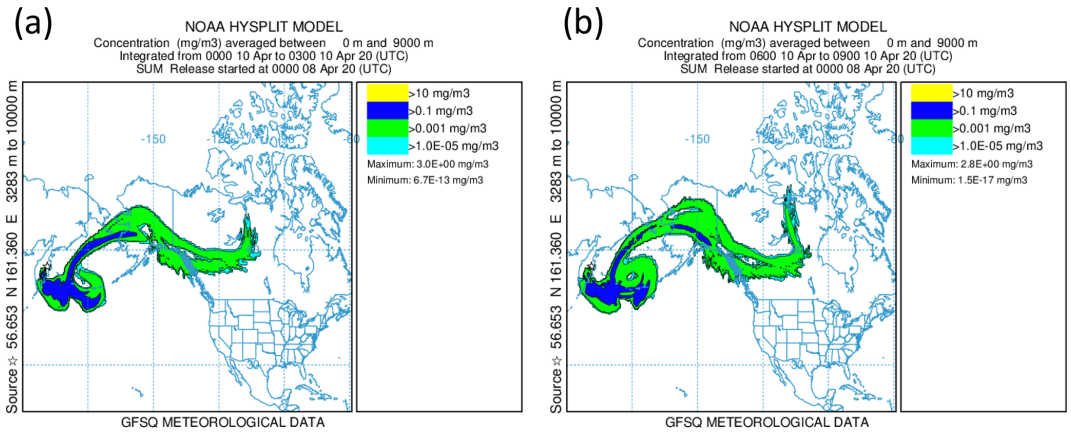

Figure D1. NOAA HYSPLIT dispersion model simulation for the Sheveluch eruption on 8 April 2020 on the basis of GFS meteorological data (Stein et al., 2015). The location of the Sheveluch volcano is given by a little star. Further, the particle concentration averaged between sea level and 9000 m is shown. Panel **(a)** includes the averaging period on 10 April 2020 from 00:00 to 03:00 UTC, and panel **(b)** shows the next period on the same day from 06:00 to 09:00 UTC.

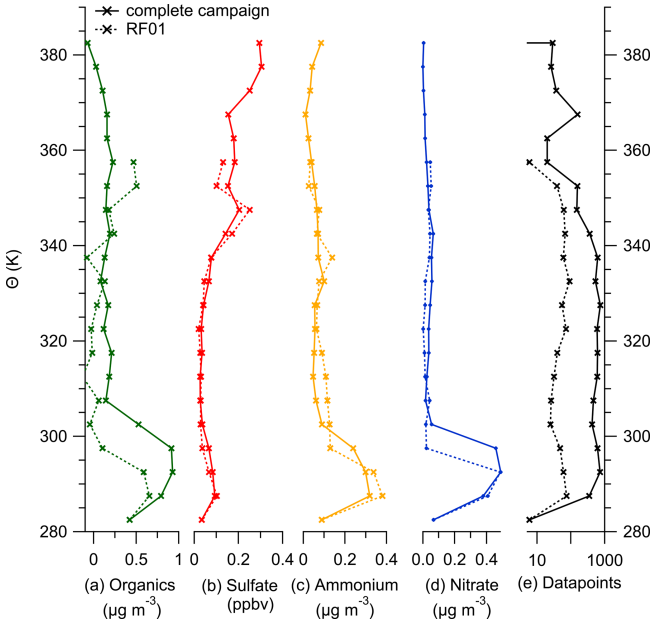

Figure E1. Binned vertical profiles for 5 K potential temperature bins for all species measured by the C-ToF-AMS: **(a)** organic aerosol, **(b)** sulfate aerosol, **(c)** ammonium aerosol and **(d)** nitrate aerosol. The number of data points for each bin is shown in panel **(e)**. The vertical profiles are divided into the complete dataset (solid lines) and data only from case study RF01 (dotted lines).

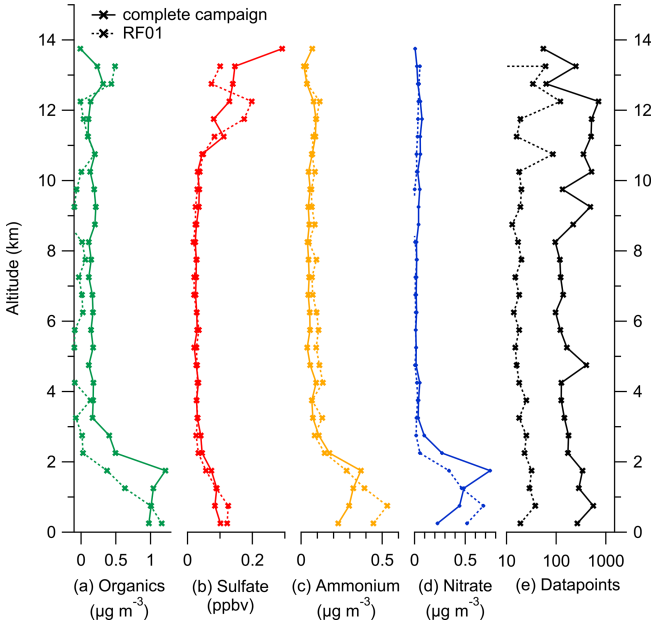

Figure E2. Binned vertical profiles for 500 m altitude bins for all species measured by the C-ToF-AMS: **(a)** organic aerosol, **(b)** sulfate aerosol, **(c)** ammonium aerosol and **(d)** nitrate aerosol. The number of data points for each bin is shown in panel **(e)**. The vertical profiles are divided into the complete dataset (solid lines) and data only from case study RF01 (dotted lines).

Appendix E: Additional measurement data conducted by the C-ToF-AMS

This section gives an overview of the complete dataset produced by the C-ToF-AMS in combination with the OPC that is integrated into the instrument system. In the following, we show vertical profiles of the aerosol species measured by the AMS relative to the potential temperature and the geometric altitude to support the anomalous observation of the sulfate concentration described in the case study.

The following plot shows the time series of the altitude and the aerosol measurements conducted by the C-ToF-AMS during RF01. The orange box indicates the time period when the sulfate anomaly was observed. Further, the different chemical composition of the probed air masses is visible, similar to the described characteristics in Figs. C4 and 7.

In addition to the chemical composition analysis, we looked at the aerosol size distribution and number concentration measured by the OPC. Therefore, we compare different stratospheric measurement periods. In Fig. E4, we show the size distribution corresponding to the 20 min of the sulfate anomaly and compare it with 20 min measurements for the stratospheric part over southern Germany under background conditions. During the anomaly, we observe up to 2 times more particles within the individual size bins below 1 µm.

To illustrate the chemical composition of the formed particles in Fig. 9a, we correlate the total number concentration N with the individual aerosol species in the next figure.

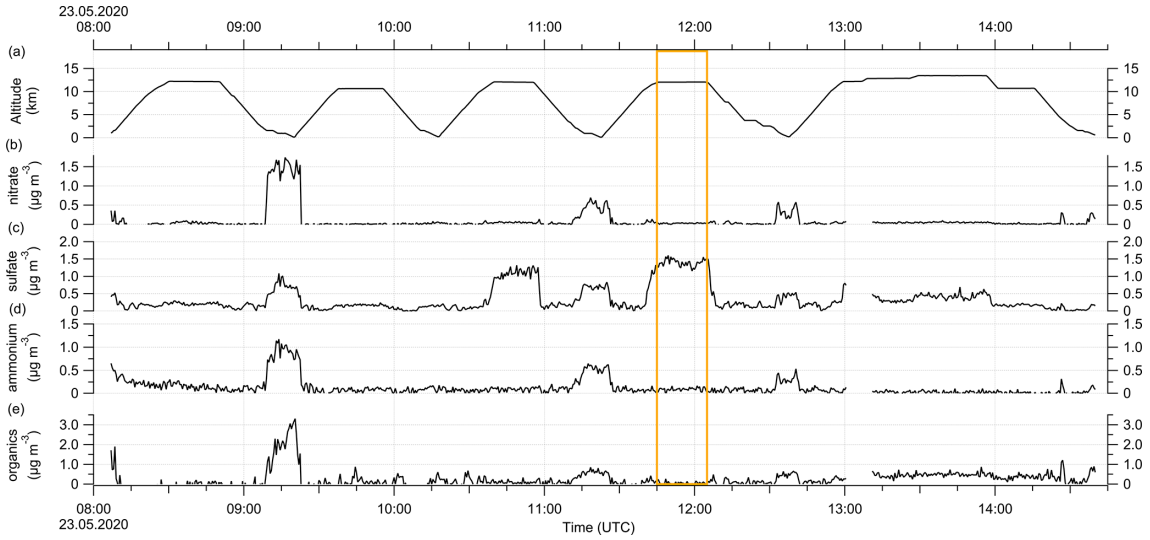

Figure E3. Time series of the aerosol measurements during RF01 on 23 May 2020 in 30 s time steps. **(a)** Altitude, **(b)** nitrate aerosol, **(c)** sulfate aerosol, **(d)** ammonium aerosol and **(e)** organic aerosol mass concentration. The orange box marks the period with the observed sulfate anomaly described in the text and shown in Fig. C1.

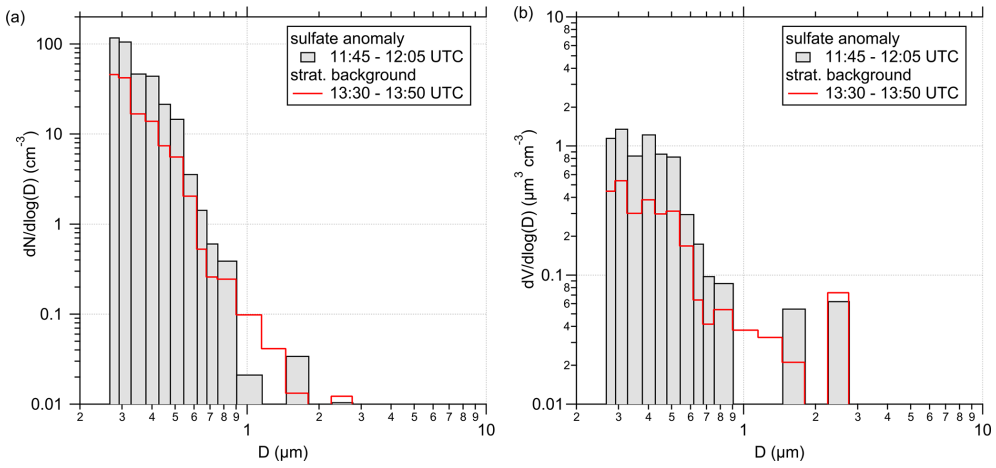

Figure E4. Size **(a)** and volume distribution **(b)**, STP-corrected and measured by the OPC. The distributions are averaged over a 20 min time period for two different measurement regimes. One is the described sulfate anomaly (grey-filled bars), and the other is a time period of the stratospheric background (red lines) later during this flight as a comparison.

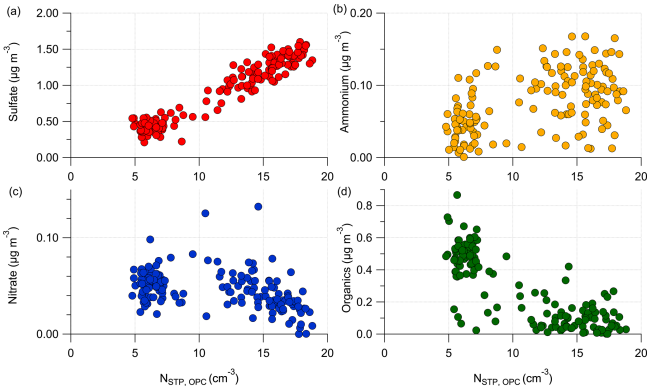

Figure E5. Correlation of the total aerosol number concentration N, STP-corrected and measured by the OPC with the aerosol species measured by the C-ToF-AMS: **(a)** with particulate sulfate, **(b)** with ammonium, **(c)** with nitrate and **(d)** with organic aerosol. The shown data represent the stratospheric measurements during RF01.

Data availability. Data measured on board HALO are available on request from the HALO database at https://halo-db.pa.op.dlr.de/mission/120 (HALO, 2024a). The DLR-Falcon basic aircraft data and the AIMS data are available on request from the HALO database at https://halo-db.pa.op.dlr.de/mission/119 (HALO, 2024b) or on request to the authors. The trajectories are published on Zenodo (Kunkel and Joppe, 2024) (https://doi.org/10.5281/ZENODO.11092106).

Author contributions. PJ set up the study together with JS, performed the data analysis and prepared the manuscript. KK and JS provided the AMS and OPC data and supported the analysis. LT, AM and CV provided the SO_2 and HNO_3 data. HS provided CO and O_3 data from DLR-Falcon. AZ provided the O_3 data from HALO. HF and LR provided CO data from HALO. HCL and DK provided model data and back trajectories as well as the code for the cross sections along the flight path. All the co-authors commented on the manuscript and discussed the presented results.

Competing interests. The contact author has declared that none of the authors has any competing interests.

Disclaimer. Publisher's note: Copernicus Publications remains neutral with regard to jurisdictional claims made in the text, published maps, institutional affiliations, or any other geographical representation in this paper. While Copernicus Publications makes every effort to include appropriate place names, the final responsibility lies with the authors.

Acknowledgements. Philipp Joppe is funded by the Deutsche Forschungsgemeinschaft (DFG, German Research Foundation) – TRR 301 – project ID 428312742, "The tropopause region in a changing atmosphere", subproject A04 coordinated by Johannes Schneider, Stephan Borrmann and Franziska Köllner. Laura Tomsche and Christiane Voigt are also funded by the TRR 301 – project ID 428312742 in subproject A01. The HALO measurement flights during CAFE-EU/BLUESKY were funded by the Max Planck Society. The authors thank the DLR team for making a campaign possible during the COVID-19 lockdown in Germany.

The authors thank the NOAA Air Resources Laboratory for providing the HYSPLIT dispersion calculations on their website.

Financial support. This research has been supported by the Deutsche Forschungsgemeinschaft (grant no. 428312742).

The article processing charges for this open-access publication were covered by the Max Planck Society.

Review statement. This paper was edited by Eduardo Landulfo and reviewed by two anonymous referees.

References

Andreae, M. O.: Ocean-atmosphere interactions in the global biogeochemical sulfur cycle, Mar. Chem., 30, 1–29, https://doi.org/10.1016/0304-4203(90)90059-l, 1990.

Appel, O., Köllner, F., Dragoneas, A., Hünig, A., Molleker, S., Schlager, H., Mahnke, C., Weigel, R., Port, M., Schulz, C., Drewnick, F., Vogel, B., Stroh, F., and Borrmann, S.: Chemical analysis of the Asian tropopause aerosol layer (ATAL) with emphasis on secondary aerosol particles using aircraft-based in situ aerosol mass spectrometry, Atmos. Chem. Phys., 22, 13607–13630, https://doi.org/10.5194/acp-22-13607-2022, 2022.

Arnold, F., Schlager, H., Hoffmann, J., Metzinger, P., and Spreng, S.: Evidence for stratospheric nitric acid condensation from balloon and rocket measurements in the Arctic, Nature, 342, 493–497, 1989.

Bahreini, R., Ervens, B., Middlebrook, A. M., Warneke, C., de Gouw, J. A., DeCarlo, P. F., Jimenez, J. L., Brock, C. A., Neuman, J. A., Ryerson, T. B., Stark, H., Atlas, E., Brioude, J., Fried, A., Holloway, J. S., Peischl, J., Richter, D., Walega, J., Weibring, P., Wollny, A. G., and Fehsenfeld, F. C.: Organic aerosol formation in urban and industrial plumes near Houston and Dallas, Texas, J. Geophys. Res.-Atmos., 114, D00F16 , https://doi.org/10.1029/2008jd011493, 2009.

Barré, J., El Amraoui, L., Ricaud, P., Lahoz, W. A., Attié, J.-L., Peuch, V.-H., Josse, B., and Marécal, V.: Diagnosing the transition layer at extratropical latitudes using MLS O_3 and MOPITT CO analyses, Atmos. Chem. Phys., 13, 7225–7240, https://doi.org/10.5194/acp-13-7225-2013, 2013.

Bethan, S., Vaughan, G., and Reid, S. J.: A comparison of ozone and thermal tropopause heights and the impact of tropopause definition on quantifying the ozone content of the troposphere, Q. J. Roy. Meteorol. Soc., 122, 929–944, https://doi.org/10.1002/qj.49712253207, 1996.

Bönisch, H., Engel, A., Curtius, J., Birner, Th., and Hoor, P.: Quantifying transport into the lowermost stratosphere using simultaneous in-situ measurements of SF_6 and CO_2, Atmos. Chem. Phys., 9, 5905–5919, https://doi.org/10.5194/acp-9-5905-2009, 2009.

Borrmann, S., Dye, J. E., Baumgardner, D., Wilson, J. C., Jonsson, H. H., Brock, C. A., Loewenstein, M., Podolske, J. R., Ferry, G. V., and Barr, K. S.: In-situ measurements of changes in stratospheric aerosol and the N_2O-aerosol relationship inside and outside of the polar vortex, Geophys. Res. Lett., 20, 2559–2562, https://doi.org/10.1029/93gl01694, 1993.

Borrmann, S., Dye, J. E., Baumgardner, D., Proffitt, M. H., Margitan, J. J., Wilson, J. C., Jonsson, H. H., Brock, C. A., Loewenstein, M., Podolske, J. R., and Ferry, G. V.: Aerosols as dynamical tracers in the lower stratosphere: Ozone versus aerosol correlation after the Mount Pinatubo eruption, J. Geophys. Res.-Atmos., 100, 11147–11156, https://doi.org/10.1029/95jd00016, 1995.

Brimblecombe, P.: The Global Sulfur Cycle, 559–591 p., Elsevier, https://doi.org/10.1016/b978-0-08-095975-7.00814-7, 2014.

Brühl, C., Lelieveld, J., Crutzen, P. J., and Tost, H.: The role of carbonyl sulphide as a source of stratospheric sulphate aerosol and its impact on climate, Atmos. Chem. Phys., 12, 1239–1253, https://doi.org/10.5194/acp-12-1239-2012, 2012.

Butchart, N. and Remsberg, E. E.: The Area of the Stratospheric Polar Vortex as a Diagnostic for

Tracer Transport on an Isentropic Surface, J. Atmos. Sci., 43, 1319–1339, https://doi.org/10.1175/1520-0469(1986)043<1319:taotsp>2.0.co;2, 1986.

Canagaratna, M. R., Canagaratna, M. R., Jayne, J. T., Jimenez, J. L., Allan, J., Alfarra, M. R., Alfarra, M. R., Zhang, Q., Zhang, Q., Zhang, Q., Onasch, T. B., Onasch, T. B., Drewnick, F., Coe, H., Middlebrook, A. M., Delia, A. E., Williams, L. R., Trimborn, A., Northway, M. J., Northway, M. J., DeCarlo, P. F., Kolb, C. E., Davidovits, P., and Worsnop, D. R.: Chemical and microphysical characterization of ambient aerosols with the aerodyne aerosol mass spectrometer, Mass Spectro. Rev., 26, 185–222, https://doi.org/10.1002/mas.20115, 2007.

Crutzen, P. J.: The possible importance of CSO for the sulfate layer of the stratosphere, Geophys. Res. Lett., 3, 73–76, https://doi.org/10.1029/GL003i002p00073, 1976.

Deshler, T.: A review of global stratospheric aerosol: Measurements, importance, life cycle, and local stratospheric aerosol, Atmos. Res., 90, 223–232, https://doi.org/10.1016/j.atmosres.2008.03.016, 2008.

Drewnick, F., Hings, S. S., DeCarlo, P. F., Jayne, J. T., Gonin, M., Fuhrer, K., Weimer, S., Jimenez, J. L., Demerjian, K. L., Borrmann, S., Borrmann, S., and Worsnop, D. R.: A New Time-of-Flight Aerosol Mass Spectrometer (TOF-AMS) – Instrument Description and First Field Deployment, Aerosol Sci. Technol., 39, 637–658, https://doi.org/10.1080/02786820500182040, 2005.

Fadnavis, S., Semeniuk, K., Pozzoli, L., Schultz, M. G., Ghude, S. D., Das, S., and Kakatkar, R.: Transport of aerosols into the UTLS and their impact on the Asian monsoon region as seen in a global model simulation, Atmos. Chem. Phys., 13, 8771–8786, https://doi.org/10.5194/acp-13-8771-2013, 2013.

Feinberg, A., Sukhodolov, T., Luo, B.-P., Rozanov, E., Winkel, L. H. E., Peter, T., and Stenke, A.: Improved tropospheric and stratospheric sulfur cycle in the aerosol–chemistry–climate model SOCOL-AERv2, Geosci. Model Dev., 12, 3863–3887, https://doi.org/10.5194/gmd-12-3863-2019, 2019.

Fischer, H., Wienhold, F. G., Hoor, P., Bujok, O., Schiller, C., Siegmund, P., Ambaum, M., Scheeren, H. A., and Lelieveld, J.: Tracer correlations in the northern high latitude lowermost stratosphere: Influence of cross-tropopause mass exchange, Geophys. Res. Lett., 27, 97–100, https://doi.org/10.1029/1999GL010879, 2000.

Friberg, J., Martinsson, B. G., Andersson, S. M., Brenninkmeijer, C. A. M., Hermann, M., Van Velthoven, P. F. J., and Zahn, A.: Sources of increase in lowermost stratospheric sulphurous and carbonaceous aerosol background concentrations during 1999–2008 derived from CARIBIC flights, Tellus B, 66, 23428, https://doi.org/10.3402/tellusb.v66.23428, 2014.

Friberg, J., Martinsson, B. G., Andersson, S. M., and Sandvik, O. S.: Volcanic impact on the climate – the stratospheric aerosol load in the period 2006–2015, Atmos. Chem. Phys., 18, 11149–11169, https://doi.org/10.5194/acp-18-11149-2018, 2018.

Froyd, K. D., Murphy, D. M., Sanford, T. J., Thomson, D. S., Wilson, J. C., Pfister, L., and Lait, L.: Aerosol composition of the tropical upper troposphere, Atmos. Chem. Phys., 9, 4363–4385, https://doi.org/10.5194/acp-9-4363-2009, 2009.

Gettelman, A., Hoor, P., Pan, L. L., Randel, W. J., Hegglin, M. I., and Birner, T.: THE EXTRATROPICAL UPPER TROPOSPHERE AND LOWER STRATOSPHERE, Rev. Geophys., 49, RG3003, https://doi.org/10.1029/2011RG000355, 2011.

Gorkavyi, N., Krotkov, N., Li, C., Lait, L., Colarco, P., Carn, S., DeLand, M., Newman, P., Schoeberl, M., Taha, G., Torres, O., Vasilkov, A., and Joiner, J.: Tracking aerosols and SO_2 clouds from the Raikoke eruption: 3D view from satellite observations, Atmos. Meas. Tech., 14, 7545–7563, https://doi.org/10.5194/amt-14-7545-2021, 2021.

HALO: HALO: Mission: CAFE-EU, HALO [data set], https://halo-db.pa.op.dlr.de/mission/120 (last access: 26 June 2024), 2024a.

HALO: Mission: BLUESKY, HALO [data set], https://halo-db.pa.op.dlr.de/mission/119 (last access: 26 June 2024), 2024b.

Hegglin, M. I.: Determination of eddy diffusivity in the lowermost stratosphere, Geophys. Res. Lett., 32, L13812, https://doi.org/10.1029/2005gl022495, 2005.

Hegglin, M. I., Brunner, D., Peter, T., Hoor, P., Fischer, H., Staehelin, J., Krebsbach, M., Schiller, C., Parchatka, U., and Weers, U.: Measurements of NO, NO_y, N_2O, and O_3 during SPURT: implications for transport and chemistry in the lowermost stratosphere, Atmos. Chem. Phys., 6, 1331–1350, https://doi.org/10.5194/acp-6-1331-2006, 2006.

Hegglin, M. I., Boone, C. D., Manney, G. L., and Walker, K. A.: A global view of the extratropical tropopause transition layer from Atmospheric Chemistry Experiment Fourier Transform Spectrometer O_3, H_2O, and CO, J. Geophys. Res., 114, D00B11, https://doi.org/10.1029/2008JD009984, 2009.

Hersbach, H., Bell, B., Berrisford, P., Hirahara, S., Horányi, A., Muñoz-Sabater, J., Nicolas, J., Peubey, C., Radu, R., Schepers, D., Simmons, A., Soci, C., Abdalla, S., Abellan, X., Balsamo, G., Bechtold, P., Biavati, G., Bidlot, J., Bonavita, M., Chiara, G., Dahlgren, P., Dee, D., Diamantakis, M., Dragani, R., Flemming, J., Forbes, R., Fuentes, M., Geer, A., Haimberger, L., Healy, S., Hogan, R. J., Hólm, E., Janisková, M., Keeley, S., Laloyaux, P., Lopez, P., Lupu, C., Radnoti, G., Rosnay, P., Rozum, I., Vamborg, F., Villaume, S., and Thépaut, J.-N.: The ERA5 global reanalysis, Q. J. Roy. Meteorol. Soc., 146, 1999–2049, https://doi.org/10.1002/qj.3803, 2020.

Hofmann, D. J. and Rosen, J. M.: On the Background Stratospheric Aerosol Layer, J. Atmos. Sci., 38, 168–181, https://doi.org/10.1175/1520-0469(1981)038<0168:otbsal>2.0.co;2, 1981.

Hoor, P., Fischer, H., Fischer, H., Fischer, H., Fischer, H., Lange, L., Lelieveld, J., and Brunner, D.: Seasonal variations of a mixing layer in the lowermost stratosphere as identified by the CO-O_3 correlation from in situ measurements, J. Geophys. Res., 107, ACL 1-1–ACL 1-11, https://doi.org/10.1029/2000jd000289, 2002.

Hoor, P., Gurk, C., Brunner, D., Hegglin, M. I., Wernli, H., and Fischer, H.: Seasonality and extent of extratropical TST derived from in-situ CO measurements during SPURT, Atmos. Chem. Phys., 4, 1427–1442, https://doi.org/10.5194/acp-4-1427-2004, 2004.

Höpfner, M., Ungermann, J., Borrmann, S., Wagner, R., Spang, R., Riese, M., Stiller, G., Appel, O., Batenburg, A. M., Bucci, S., Cairo, F., Dragoneas, A., Friedl-Vallon, F., Hünig, A., Johansson, S., Krasauskas, L., Legras, B., Leisner, T., Mahnke, C., Möhler, O., Molleker, S., Müller, R., Neubert, T., Orphal, J., Preusse, P., Rex, M., Saathoff, H., Stroh, F., Weigel, R., and Wohltmann, I.: Ammonium nitrate particles formed in upper troposphere from

ground ammonia sources during Asian monsoons, Nat. Geosci., 12, 608–612, https://doi.org/10.1038/s41561-019-0385-8, 2019.

Institute of Volcanology and Seismology FEB RAS: VONA/KVERT Information Release, Institute of Volcanology and Seismology FEB RAS, KVERT, http://www.kscnet.ru/ivs/kvert/van/?n=2023-161 (last access: 26 June 2024), 2023.

Jaenicke, R.: Atmospheric aerosols and global climate, J. Aerosol Sci., 11, 577–588, https://doi.org/10.1016/0021-8502(80)90131-7, 1980.

Junge, C. E. and Manson, J. E.: Stratospheric aerosol studies, J. Geophys. Res., 66, 2163–2182, https://doi.org/10.1029/JZ066i007p02163, 1961.

Jurkat, T., Voigt, C., Arnold, F., Schlager, H., Aufmhoff, H., Schmale, J., Schneider, J., Lichtenstern, M., and Dörnbrack, A.: Airborne stratospheric ITCIMS measurements of SO_2, HCl, and HNO_3 in the aged plume of volcano Kasatochi, J. Geophys. Res., 115, D00L17, https://doi.org/10.1029/2010JD013890, 2010.

Jurkat, T., Kaufmann, S., Voigt, C., Schäuble, D., Jeßberger, P., and Ziereis, H.: The airborne mass spectrometer AIMS – Part 2: Measurements of trace gases with stratospheric or tropospheric origin in the UTLS, Atmos. Meas. Tech., 9, 1907–1923, https://doi.org/10.5194/amt-9-1907-2016, 2016.

Kaluza, T., Kunkel, D., and Hoor, P.: Composite analysis of the tropopause inversion layer in extratropical baroclinic waves, Atmos. Chem. Phys., 19, 6621–6636, https://doi.org/10.5194/acp-19-6621-2019, 2019.

Kaluza, T., Kunkel, D., and Hoor, P.: On the occurrence of strong vertical wind shear in the tropopause region: a 10-year ERA5 northern hemispheric study, Weather Clim. Dynam., 2, 631–651, https://doi.org/10.5194/wcd-2-631-2021, 2021.

Konopka, P. and Pan, L. L.: On the mixing-driven formation of the Extratropical Transition Layer (ExTL), J. Geophys. Res.-Atmos., 117, D18301, https://doi.org/10.1029/2012jd017876, 2012.

Krause, J., Hoor, P., Engel, A., Plöger, F., Grooß, J.-U., Bönisch, H., Keber, T., Sinnhuber, B.-M., Woiwode, W., and Oelhaf, H.: Mixing and ageing in the polar lower stratosphere in winter 2015–2016, Atmos. Chem. Phys., 18, 6057–6073, https://doi.org/10.5194/acp-18-6057-2018, 2018.

Kremser, S., Thomason, L. W., von Hobe, M., Hermann, M., Deshler, T., Timmreck, C., Toohey, M., Stenke, A., Schwarz, J. P., Weigel, R., Fueglistaler, S., Prata, F. J., Vernier, J.-P., Schlager, H., Barnes, J. E., Antuña-Marrero, J.-C., Fairlie, D., Palm, M., Mahieu, E., Notholt, J., Rex, M., Bingen, C., Vanhellemont, F., Bourassa, A., Plane, J. M. C., Klocke, D., Carn, S. A., Clarisse, L., Trickl, T., Neely, R., James, A. D., Rieger, L., Wilson, J. C., and Meland, B.: Stratospheric aerosol-Observations, processes, and impact on climate, Rev. Geophys., 54, 278–335, https://doi.org/10.1002/2015rg000511, 2016.

Krüger, O. O., Holanda, B. A., Chowdhury, S., Pozzer, A., Walter, D., Pöhlker, C., Andrés Hernández, M. D., Burrows, J. P., Voigt, C., Lelieveld, J., Quaas, J., Pöschl, U., and Pöhlker, M. L.: Black carbon aerosol reductions during COVID-19 confinement quantified by aircraft measurements over Europe, Atmos. Chem. Phys., 22, 8683–8699, https://doi.org/10.5194/acp-22-8683-2022, 2022.

Kunkel, D. and Joppe, P.: Sulfate anomaly during CAFE-EU/BLUESKY 10 days LAGRANTO back trajectories, Zenodo [data set], https://doi.org/10.5281/ZENODO.11092106, 2024.

Kunkel, D., Hoor, P., Kaluza, T., Ungermann, J., Kluschat, B., Giez, A., Lachnitt, H.-C., Kaufmann, M., and Riese, M.: Evidence of small-scale quasi-isentropic mixing in ridges of extratropical baroclinic waves, Atmos. Chem. Phys., 19, 12607–12630, https://doi.org/10.5194/acp-19-12607-2019, 2019.

Lary, D. J., Chipperfield, M. P., Pyle, J. A., Norton, W. A., and Riishøjgaard, L. P.: Three-dimensional tracer initialization and general diagnostics using equivalent PV latitude–potential-temperature coordinates, Q. J. Roy. Meteorol. Soc., 121, 187–210, https://doi.org/10.1002/qj.49712152109, 1995.

Marsing, A., Jurkat-Witschas, T., Grooß, J.-U., Kaufmann, S., Heller, R., Engel, A., Hoor, P., Krause, J., and Voigt, C.: Chlorine partitioning in the lowermost Arctic vortex during the cold winter 2015/2016, Atmos. Chem. Phys., 19, 10757–10772, https://doi.org/10.5194/acp-19-10757-2019, 2019.

Martinsson, B. G.: Characteristics and origin of lowermost stratospheric aerosol at northern midlatitudes under volcanically quiescent conditions based on CARIBIC observations, J. Geophys. Res., 110, D12201, https://doi.org/10.1029/2004JD005644, 2005.

Martinsson, B. G., Friberg, J., Sandvik, O. S., Hermann, M., van Velthoven, P. F. J., and Zahn, A.: Formation and composition of the UTLS aerosol, npj Clim. Atmos. Sci., 2, 40, https://doi.org/10.1038/s41612-019-0097-1, 2019.

Middlebrook, A. M., Bahreini, R., Bahreini, R., Bahreini, R., Jimenez, J. L., and Canagaratna, M. R.: Evaluation of Composition-Dependent Collection Efficiencies for the Aerodyne Aerosol Mass Spectrometer using Field Data, Aerosol Sci. Technol., 46, 258–271, https://doi.org/10.1080/02786826.2011.620041, 2012.

Murphy, D. M., Froyd, K. D., Schwarz, J. P., and Wilson, J. C.: Observations of the chemical composition of stratospheric aerosol particles, Q. J. Roy. Meteorol. Soc., 140, 1269–1278, https://doi.org/10.1002/qj.2213, 2013.

Proffitt, M. H., Powell, J. A., Tuck, A. F., Fahey, D. W., Kelly, K. K., Krueger, A. J., Schoeberl, M. R., Gary, B. L., Margitan, J. J., Chan, K. R., Loewenstein, M., and Podolske, J. R.: A chemical definition of the boundary of the Antarctic ozone hole, J. Geophys. Res.-Atmos., 94, 11437–11448, https://doi.org/10.1029/jd094id09p11437, 1989.

Reifenberg, S. F., Martin, A., Kohl, M., Bacer, S., Hamryszczak, Z., Tadic, I., Röder, L., Crowley, D. J., Fischer, H., Kaiser, K., Schneider, J., Dörich, R., Crowley, J. N., Tomsche, L., Marsing, A., Voigt, C., Zahn, A., Pöhlker, C., Holanda, B. A., Krüger, O., Pöschl, U., Pöhlker, M., Jöckel, P., Dorf, M., Schumann, U., Williams, J., Bohn, B., Curtius, J., Harder, H., Schlager, H., Lelieveld, J., and Pozzer, A.: Numerical simulation of the impact of COVID-19 lockdown on tropospheric composition and aerosol radiative forcing in Europe, Atmos. Chem. Phys., 22, 10901–10917, https://doi.org/10.5194/acp-22-10901-2022, 2022.

Röder, L. L., Ort, L., Lelieveld, J., and Fischer, H.: Determination of Temporal Stability and Instrument Performance of an airborne QCLAS via Allan-Werle-plots, https://doi.org/10.21203/rs.3.rs-3619758/v1, pREPRINT (Version 1) available at: Research Square, 2023.

Rollins, A. W., Thornberry, T. D., Watts, L. A., Yu, P., Rosenlof, K. H., Mills, M., Baumann, E., Giorgetta, F. R., Bui, T. V., Höpfner, M., Walker, K. A., Boone, C., Bernath, P. F., Co-

larco, P. R., Newman, P. A., Fahey, D. W., and Gao, R. S.: The role of sulfur dioxide in stratospheric aerosol formation evaluated by using in situ measurements in the tropical lower stratosphere, Geophys. Res. Lett., 44, 4280–4286, https://doi.org/10.1002/2017gl072754, 2017.

Schulz, C., Schneider, J., Amorim Holanda, B., Appel, O., Costa, A., de Sá, S. S., Dreiling, V., Fütterer, D., Jurkat-Witschas, T., Klimach, T., Knote, C., Krämer, M., Martin, S. T., Mertes, S., Pöhlker, M. L., Sauer, D., Voigt, C., Walser, A., Weinzierl, B., Ziereis, H., Zöger, M., Andreae, M. O., Artaxo, P., Machado, L. A. T., Pöschl, U., Wendisch, M., and Borrmann, S.: Aircraft-based observations of isoprene-epoxydiol-derived secondary organic aerosol (IEPOX-SOA) in the tropical upper troposphere over the Amazon region, Atmos. Chem. Phys., 18, 14979–15001, https://doi.org/10.5194/acp-18-14979-2018, 2018.

Schumann, U., Bugliaro, L., Dörnbrack, A., Baumann, R., and Voigt, C.: Aviation Contrail Cirrus and Radiative Forcing Over Europe During 6 Months of COVID-19, Geophys. Res. Lett., 48, e2021GL092771, https://doi.org/10.1029/2021gl092771, 2021a.

Schumann, U., Poll, I., Teoh, R., Koelle, R., Spinielli, E., Molloy, J., Koudis, G. S., Baumann, R., Bugliaro, L., Stettler, M., and Voigt, C.: Air traffic and contrail changes over Europe during COVID-19: a model study, Atmos. Chem. Phys., 21, 7429–7450, https://doi.org/10.5194/acp-21-7429-2021, 2021b.

Seinfeld, J. H. and Pandis, S. N.: Atmospheric chemistry and physics: from air pollution to climate change, John Wiley & Sons, 39 pp., ISBN 978-1-118-94740-1, 2016.

Solomon, S., Daniel, J. S., Neely, R. R., Vernier, J.-P., Dutton, E. G., and Thomason, L. W.: The Persistently Variable "Background" Stratospheric Aerosol Layer and Global Climate Change, Science, 333, 866–870, https://doi.org/10.1126/science.1206027, 2011.

Sprenger, M. and Wernli, H.: The LAGRANTO Lagrangian analysis tool – version 2.0, Geosci. Model Dev., 8, 2569–2586, https://doi.org/10.5194/gmd-8-2569-2015, 2015.

Staehelin, J.: Ozone Measurements and Trends (Troposphere), in: Encyclopedia of Physical Science and Technology, 539–561 pp., Elsevier, https://doi.org/10.1016/b0-12-227410-5/00037-5, 2003.

Stein, A. F., Draxler, R. R., Rolph, G. D., Stunder, B. J. B., Cohen, M. D., and Ngan, F.: NOAA's HYSPLIT Atmospheric Transport and Dispersion Modeling System, B. Am. Meteorol. Soc., 96, 2059–2077, https://doi.org/10.1175/bams-d-14-00110.1, 2015.

Tadic, I., Parchatka, U., Königstedt, R., and Fischer, H.: In-flight stability of quantum cascade laser-based infrared absorption spectroscopy measurements of atmospheric carbon monoxide, Appl. Phys. B, 123, 1–9, 2017.

Thouret, V., Cammas, J.-P., Sauvage, B., Athier, G., Zbinden, R., Nédélec, P., Simon, P., and Karcher, F.: Tropopause referenced ozone climatology and inter-annual variability (1994–2003) from the MOZAIC programme, Atmos. Chem. Phys., 6, 1033–1051, https://doi.org/10.5194/acp-6-1033-2006, 2006.

Tilmes, S. and Mills, M.: Stratospheric Sulfate Aerosols and Planetary Albedo, 771–776 pp., Springer Netherlands, ISBN 9789400757844, https://doi.org/10.1007/978-94-007-5784-4_11, 2014.

Tomsche, L., Marsing, A., Jurkat-Witschas, T., Lucke, J., Kaufmann, S., Kaiser, K., Schneider, J., Scheibe, M., Schlager, H., Röder, L., Fischer, H., Obersteiner, F., Zahn, A., Zöger, M., Lelieveld, J., and Voigt, C.: Enhanced sulfur in the upper troposphere and lower stratosphere in spring 2020, Atmos. Chem. Phys., 22, 15135–15151, https://doi.org/10.5194/acp-22-15135-2022, 2022.

Voigt, C., Schumann, U., Jurkat, T., Schäuble, D., Schlager, H., Petzold, A., Gayet, J.-F., Krämer, M., Schneider, J., Borrmann, S., Schmale, J., Jessberger, P., Hamburger, T., Lichtenstern, M., Scheibe, M., Gourbeyre, C., Meyer, J., Kübbeler, M., Frey, W., Kalesse, H., Butler, T., Lawrence, M. G., Holzäpfel, F., Arnold, F., Wendisch, M., Döpelheuer, A., Gottschaldt, K., Baumann, R., Zöger, M., Sölch, I., Rautenhaus, M., and Dörnbrack, A.: In-situ observations of young contrails – overview and selected results from the CONCERT campaign, Atmos. Chem. Phys., 10, 9039–9056, https://doi.org/10.5194/acp-10-9039-2010, 2010.

Voigt, C., Jessberger, P., Jurkat, T., Kaufmann, S., Baumann, R., Schlager, H., Bobrowski, N., Giuffrida, G., and Salerno, G.: Evolution of CO_2, SO_2, HCl, and HNO_3 in the volcanic plumes from Etna, Geophys. Res. Lett., 41, 2196–2203, https://doi.org/10.1002/2013GL058974, 2014.

Voigt, C., Voigt, C., Lelieveld, J., Lelieveld, J., Schlager, H., Schlager, H., Schneider, J., Schneider, J., Curtius, J., Curtius, J., Meerkötter, R., Meerkötter, R., Sauer, D., Sauer, D., Bugliaro, L., Bugliaro, L., Bohn, B., Bohn, B., Crowley, J. N., Crowley, J. N., Erbertseder, T., Erbertseder, T., Groß, S., Groß, S., Hahn, V., Hahn, V., Li, Q., Li, Q., Mertens, M., Mertens, M., Pöhlker, M. L., Pöhlker, M. L., Pozzer, A., Pozzer, A., Schumann, U., Schumann, U., Tomsche, L., Tomsche, L., Williams, J., Williams, J., Zahn, A., Zahn, A., Andreae, M., Andreae, M., Borrmann, S., Borrmann, S., Bräuer, T., Bräuer, T., Dörich, R., Dörich, R., Dörnbrack, A., Dörnbrack, A., Edtbauer, A., Edtbauer, A., Ernle, L., Ernle, L., Fischer, H., Fischer, H., Giez, A., Giez, A., Granzin, M., Granzin, M., Grewe, V., Grewe, V., Harder, H., Harder, H., Heinritzi, M., Heinritzi, M., Holanda, B. A., Holanda, B. A., Jöckel, P., Jöckel, P., Kaiser, K., Kaiser, K., Krüger, O. O., Krüger, O. O., Lucke, J., Lucke, J., Marsing, A., Marsing, A., Martin, A., Martin, A., Matthes, S., Matthes, S., Pöhlker, C., Pöhlker, C., Pöschl, U., Pöschl, U., Reifenberg, S., Reifenberg, S., Ringsdorf, A., Ringsdorf, A., Scheibe, M., Scheibe, M., Tadic, I., Tadic, I., Zauner-Wieczorek, M., Zauner-Wieczorek, M., Henke, R., Henke, R., Rapp, M., and Rapp, M.: Cleaner skies during the COVID-19 lockdown, B. Am. Meteorol. Soc., 103, E1796–E1827, https://doi.org/10.1175/bams-d-21-0012.1, 2022.

Williamson, C. J., Kupc, A., Rollins, A., Kazil, J., Froyd, K. D., Ray, E. A., Murphy, D. M., Schill, G. P., Peischl, J., Thompson, C., Bourgeois, I., Ryerson, T. B., Diskin, G. S., DiGangi, J. P., Blake, D. R., Bui, T. P. V., Dollner, M., Weinzierl, B., and Brock, C. A.: Large hemispheric difference in nucleation mode aerosol concentrations in the lowermost stratosphere at mid- and high latitudes, Atmos. Chem. Phys., 21, 9065–9088, https://doi.org/10.5194/acp-21-9065-2021, 2021.

Zahn, A., Brenninkmeijer, C. A. M., and van Velthoven, P. F. J.: Passenger aircraft project CARIBIC 1997–2002, Part I: the extratropical chemical tropopause, Atmos. Chem. Phys. Discuss., 4, 1091–1117, https://doi.org/10.5194/acpd-4-1091-2004, 2004.

Zahn, A., Weppner, J., Widmann, H., Schlote-Holubek, K., Burger, B., Kühner, T., and Franke, H.: A fast and precise chemiluminescence ozone detector for eddy flux and airborne application, Atmos. Meas. Tech., 5, 363–375, https://doi.org/10.5194/amt-5-363-2012, 2012.

Ziereis, H., Hoor, P., Grooß, J.-U., Zahn, A., Stratmann, G., Stock, P., Lichtenstern, M., Krause, J., Bense, V., Afchine, A., Rolf, C., Woiwode, W., Braun, M., Ungermann, J., Marsing, A., Voigt, C., Engel, A., Sinnhuber, B.-M., and Oelhaf, H.: Redistribution of total reactive nitrogen in the lowermost Arctic stratosphere during the cold winter 2015/2016, Atmos. Chem. Phys., 22, 3631–3654, https://doi.org/10.5194/acp-22-3631-2022, 2022.

3.2 TRANSPORT OF BIOMASS BURNING AEROSOL INTO THE EXTRATROPICAL TROPOPAUSE REGION OVER EUROPE VIA WARM CONVEYOR BELT UPLIFT (JOPPE ET AL., 2025)

The study of Joppe et al. (2025) describes the observation of a filament with high aerosol number concentration and CO mixing ratios in a WCB outflow region with chemically stratospheric air masses. The analysis of size distribution measurements as well as the offline analysis of impactor samples using the scanning electron microscope (SEM) method show indications for BB influence on this air mass. LAGRANTO back trajectories, starting at the flight path, show that the origin of this polluted air masses was over Canada in low altitudes, crossing regions with active wild fires. These air masses were transported in low-levels across the Atlantic ocean and were lifted over Europe associated with a WCB uplift event with subsequent cross-tropopause mixing.

The data of this study was recorded during the CRC measurement campaign TPEx. I am responsible for the UHSAS and AMS data with support by Johannes Schneider and Jonas Wilsch. The other data in this study is provided by the co-authors according to the listed author contributions. The offline samplers of organic aerosol were analyzed by Anna Breuninger and colleagues from the GUF, whereas the impactor samples were analyzed by Martin Ebert and colleagues at TuDa. The study was set up by myself, including the general concept and the main part of the data analysis. Further, I was responsible for the writing of the manuscript. All co-authors contributed with helpful comments and instrument descriptions to the manuscript. The manuscript was submitted on 25 March 2025 and at the date of the submission of this thesis the open discussion has ended and the second peer-review phase is ongoing. For this reason small changes are still possible during the publication process and after acceptance the final publication will get a type-setting by Coperincus.

Transport of Biomass Burning Aerosol into the Extratropical Tropopause Region over Europe via Warm Conveyor Belt Uplift

Philipp Joppe[1,2], Johannes Schneider[2], Jonas Wilsch[2], Heiko Bozem[1], Anna Breuninger[5], Joachim Curtius[5], Martin Ebert[7], Nicolas Emig[1], Peter Hoor[1], Sadath Ismayil[7], Konrad Kandler[7], Daniel Kunkel[1], Isabel Kurth[1], Hans-Christoph Lachnitt[1], Yun Li[3], Annette Miltenberger[1], Sarah Richter[5], Christian Rolf[4], Lisa Schneider[7], Cornelis Schwenk[1], Nicole Spelten[4], Alexander L. Vogel[5], Yafang Cheng[6], and Stephan Borrmann[1,2]

[1]Institute for Atmospheric Physics, Johannes Gutenberg University Mainz, Mainz,Germany
[2]Particle Chemistry Department, Max Planck Institute for Chemistry, Mainz, Germany
[3]ICE-3: Troposphere, Forschungszentrum Jülich, Jülich, Germany
[4]ICE-4: Stratosphere, Forschungszentrum Jülich, Jülich, Germany
[5]Institute for Atmospheric and Environmental Sciences, Goethe University Frankfurt, Frankfurt am Main, Germany
[6]Aerosol Chemistry Department, Max Planck Institute for Chemistry, Mainz, Germany
[7]Institute for Applied Geoscience, Technical University Darmstadt, Darmstadt, Germany

Correspondence: Philipp Joppe (phjoppe@uni-mainz.de)

Abstract. Aerosol particles in the extratropical upper troposphere and lower stratosphere (exUTLS) play a crucial role for the Earth's radiative budget. High temporal and spatial resolution measurements in the exUTLS are important to study mixing processes and their climate impact. Here, we present measurements from the TPEx mission (Tropopause composition gradients and mixing Experiment) an aircraft mission in June 2024 over Europe. The measurement platform, a Learjet 35A, was equipped with in-situ trace gas and aerosol measurements and filter samplers for offline analysis. For vertical gradient measurements of trace species and aerosol, we conducted redundant measurements on a fully automated towed sensor shuttle (TOSS) 200 m below the aircraft.

On 17 June 2024, we observed a streamer with elevated aerosol number concentration of up to 800 particles per cm^3 between 100 nm and 1 $\mu\mathrm{m}$. This is higher by a factor of more than two, up to four, compared to the UTLS, respective tropospheric, background. Carbon monoxide (CO) mixing ratios were larger than 100 ppbv. Backward trajectories indicate that this pollution is transported from Canadian wildfires in the lower troposphere towards Europe, where it was uplifted on the edge of a warm conveyor belt into the tropopause region. There mixing with chemically stratospheric air occurred. The TOSS measurements also allow the calculation of the potential temperature gradient ($\Delta\theta \cdot \Delta z^{-1}$). We observed a change towards smaller gradients within the region of the polluted air masses, which is presumably due to an increase of θ at lower altitudes by radiative heating as a consequence of the transported refractory black carbon.

1 Introduction

The chemical composition of the upper troposphere and lower stratosphere (UTLS) is of high importance for the Earth's radiative budget (Kremser et al., 2016). Changes in the composition of this region have a large impact on the Earth's surface temperature, due to the radiative sensitivity of the surface temperature with respect to changes in trace gases such as ozone (O_3), water vapor (H_2O), and methane (CH_4) (Riese et al., 2012). The total aerosol effective radiative forcing (AERF) is highly variable and depends on the chemical composition of the aerosol particles. For example, at the top of the atmosphere (TOA), the global radiative effect of sulfate aerosol is a cooling effect up to about -1.3 Wm^{-2} whereas the global radiative effect of black carbon (BC) shows a strong heating effect of up to 0.9 Wm^{-2} (Masson-Delmotte et al., 2023; Kalisoras et al., 2024; Ramanathan and Carmichael, 2008; Räisänen et al., 2022). The aerosol chemical composition in the UTLS is influenced by different processes: In the tropical regions, aerosol particles and precursor gases are transported from the planetary boundary layer (PBL) into the tropical transition layer (TTL) by deep convection on a timescale of minutes to hours (Froyd et al., 2009; Fueglistaler et al., 2009; von Hobe et al., 2021). Such deep convective transport can be associated with new particle formation events, due to the presence of freshly oxidized volatile organic compounds (VOCs) and the nucleation of these oxidation products in the convective outflow at high altitudes (Curtius et al., 2024). The newly formed particles in the UTLS are redistributed towards the extratropical and polar regions under the influence of the Brewer-Dobson circulation (BDC) (Andersson et al., 2015; Kremser et al., 2016).

The chemical composition of the lowermost stratosphere (LMS) is influenced by the shallow branch of the BDC, where the meridional transport from tropical to polar latitudes takes from months up to more than one year (Ploeger et al., 2021). There are several additional processes which influence the chemical composition and other properties of the aerosol on shorter timescales and more locally, such as convective events, planetary and synoptic scale waves, associated with baroclinic instabilities and vertical transport from the PBL to the UT ahead the surface cold fronts by warm conveyor belts (WCBs). These processes often generate strong shear, thus favorable conditions for turbulence and mixing (Zahn et al., 2000; Brioude et al., 2007; Kaluza et al., 2021, 2022; Lachnitt et al., 2023).

A WCB is part of an extratropical cyclone, which is characterized by the transport of moist air masses over large horizontal distances in combination with a strong ascent into the UT (Harrold, 1973; Heitmann et al., 2024). WCBs can be described from a Lagrangian perspective as a compact trajectory bundle in the vicinity of a cyclone with special characteristics, such as strong ascent and drying of air masses (Heitmann et al., 2024; Schwenk and Miltenberger, 2024). WCBs are capable to transport trace gases, aerosol precursor gases, and aerosol particles from the PBL into the UTLS. Furthermore, WCB transport is able to enhance cross-tropopause mixing by triggering gravity waves, enhancing shear and radiative heating as a consequence of cloud formation. Therefore WCBs can affect the chemical composition of the UTLS (Cooper et al., 2004). Recent studies of WCBs focused on the transport of water vapor (H_2O), mineral dust, and the precursor gas sulfur dioxide (SO_2) into the tropopause region (Madonna et al., 2014; Marelle et al., 2015; Fromm et al., 2016; Schwenk and Miltenberger, 2024).

The chemical composition of stratospheric aerosol particles is influenced by tropospheric compounds that are transported to

the UTLS. Tropospheric sulfur compounds, including anthropogenic and volcanic SO_2 emissions, contribute to the abundance of sulfate in the stratospheric aerosol (Andersson et al., 2015; Joppe et al., 2024). In addition to sulfate, stratospheric aerosol particles also contain carbonaceous compounds, such as organic carbon (OC; or organic aerosol) and black carbon (BC). One major source for OC and BC in the UTLS is biomass burning (BB) (Murphy et al., 2007; Schwarz et al., 2008; Ditas et al., 2018; Ma et al., 2024).

Organic aerosol (OA) can be divided into two types of aerosol, primary organic aerosol (POA) which is directly emitted by the source (e.g., pollen, spores, sea salt and its coatings or biomass burning) and secondary organic aerosol (SOA) which is formed by gas-to-particle conversion out of precursor gases. During summer months, biomass burning organic aerosol (BBOA) contributes up to 16 % to the total OA over Europe while up to 70 % of this BBOA are formed secondarily (Theodoritsi and Pandis, 2019). Additionally, the BB aerosol contributes on average 10 %, sometimes up to 50%, to the aerosol number concentration for particle sizes between 0.25 and 2 μm in the northern LMS (Kremser et al., 2016). The transport of these aerosol particles into the LMS has been investigated for fast processes, like convective uplift and contributions by pyroconvection (Fromm et al., 2010; Yu et al., 2019; Peterson et al., 2021; Ma et al., 2024).

In this study we show that aerosol particles from small wildfires without large smoke plumes can be transported into the UTLS by WCB uplift and subsequent cross-tropopause mixing far away from the original source. Furthermore, we assess the effect of the observed small-scale pollution streamers on the static stability in the tropopause region. For this, we use in-situ measurement data in combination with transport diagnostics based on LAGRANTO back trajectories and model data from the TPEx (tropopause composition gradients and mixing experiment) mission, conducted over Germany and northern Europe in June 2024.

2 Methods

2.1 TPEx flight F07

The TPEx aircraft campaign was conducted over Germany and northern Europe for three weeks in June (03 - 21 June) 2024. The campaign base was at Hohn airfield ($54°18'49''$N, $9°32'17''$E), near Rendsburg, Germany. The research aircraft was a Learjet 35A, owned and operated by the Gesellschaft für Flugzieldarstellung (GFD), equipped with several online and offline measurement instruments inside the cabin and an underwing pod outside the cabin. In total, we conducted nine research flights reaching from the boundary layer up to 12 km. In this study we focus on research flight F07, which took place on 17 June 2024. For this flight we used the capability of the Learjet to tow a second measurement platform (The TropoPause Composition towed sensor shuttle; TPC-TOSS (Frey et al., 2009; Finger et al., 2016; Klingebiel et al., 2017; Bozem et al., 2025) on a steel cable below the aircraft. The TPC-TOSS and the aircraft were equipped with identical instrumentation for gradient measurements of temperature, ozone and aerosol number concentration between 100 nm and 1 μm. The goal of research flight F07 was to probe a region with a variable tropopause altitude (see Fig. 1a). As consequence we expected enhanced cross-tropopause mixing as a consequence of a low pressure system over the North Sea west of Norway and predicted low Richardson numbers in the restricted air space (not shown). The vertical cross-section along the flight path (Fig. 1b) indicates some predicted variability at

and above the 2 PVU tropopause as well as some stratospheric intrusions which are growing in spatial extent during the flight (green patches in Fig. 1b). Furthermore, the forecast for WCB outflow indicated the potential for aged WCB outflow in the area of interest (see Fig. 2).

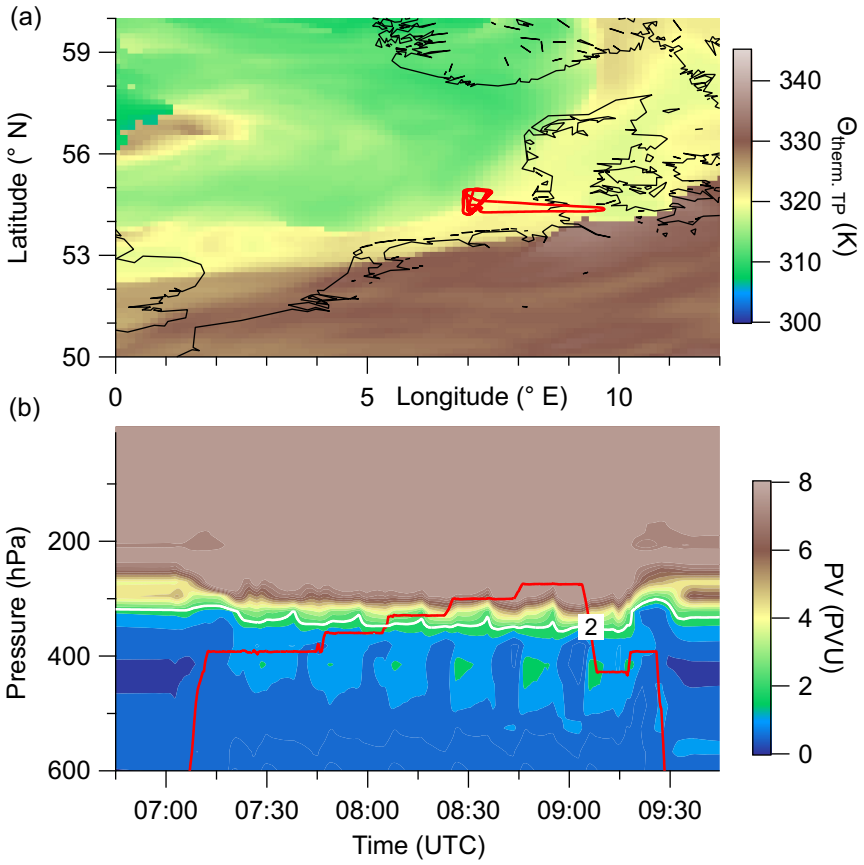

Figure 1. ECWMF forecast data for 17 June 2024, 06 UTC (F07). The potential temperature along the thermal WMO tropopause and the flight path of F07 (red solid line) are shown in panel (a). Panel (b) shows a vertical cross-section of potential vorticity (PV) along the flightpath (red solid) line with the 2 PVU surface as marker for the dynamical tropopause in the model (white solid line).

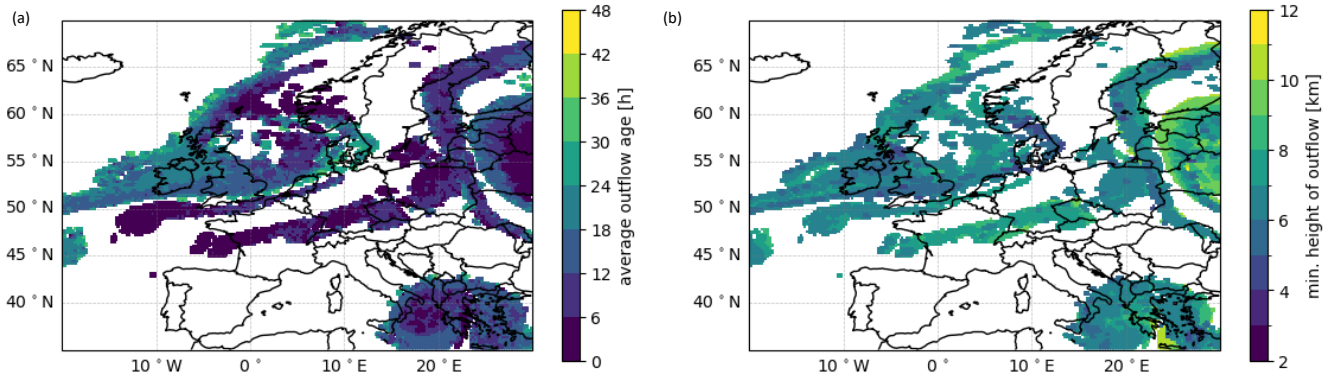

Figure 2. ICON-EU forecast data for the average WCB outflow age and the bottom altitude of the WCB outflow on basis of the forecast from 16.06.2024 00:00 UTC, valid for 17.06.2024 06:00 UTC.

2.2 Instrumentation

2.2.1 In-situ aerosol measurements

The size distribution and number concentration of aerosol particles in the accumulation mode between 100 and 1000 nm, were measured using two ultra-high sensitivity aerosol spectrometers (UHSAS, Droplet Measurement Technologies) (Cai et al., 2008; Kupc et al., 2018; Mahnke et al., 2021), one in the cabin of the Learjet and one in the TPC-TOSS (Bozem et al., 2025). Both instruments deliver measurement data with a resolution of 1 Hz. The measuring principle is based on light scattering in the infrared spectral range. The UHSAS uses a Nd^{3+}:$YLiF_4$ solid state laser with an operating wavelength of 1054 nm (Cai et al., 2008; Kupc et al., 2018). The laser mode has an intracavity power of approximately 1.1 kW $\cdot$ cm^{-2} and is perpendicular to the particle stream. Aerosol particles are actively pumped into the detection unit through a jet assembly with a sample flow of 50 $\mathrm{cm}^3 \cdot \mathrm{min}^{-1}$ and are focused to a narrow particle beam with a sheath flow.

The UHSAS in the cabin of the Learjet has been modified and rebuilt to a new housing for the use onboard a research aircraft. It is connected to the aerosol sampling inlet which consists of stainless steel and has a tip diameter of 1.55 mm. The inlet expands to 30 mm before it enters the cabin. From the cabin-side of the inlet, in total five 0.25 inch tubes are embedded into the large tube to connect the individual aerosol instruments with the inlet system. The flow was controlled by a software with input parameters for different aircraft speeds and altitudes aiming to sample close to isokinetic conditions. In the measured size range of the UHSAS we calculated transmission efficiencies of 86 % at the boundaries and 95 % at diameters around 300 nm. These calculations were performed for an ambient pressure of 300 hPa and 240 K using the Particle Loss Calculator by von der Weiden et al. (2009).

The UHSAS inside the TPC-TOSS is the special version of the instrument for airborne measurements (model UHSAS-A), manufactured for the use as an underwing probe. For previous operation at altitudes up to 21 km, the original pump had been replaced and an internal computer had been added for internal data recording and saving (Mahnke et al., 2021). The flow systems differ slightly between both instruments: The UHSAS-A in the TPC-TOSS is equipped with a second mass flow

controller (MFC) to also control the sheath flow whereas the cabin instrument uses only one MFC for the sample flow, and the sheath flow is supplied by the remaining air flow. Before the deployment during TPEx, we performed several characterization and calibration measurements to ensure the comparability of the measurements. These measurements and characterizations are described in Bozem et al. (2025).

For larger aerosol particles, we operated an optical particle counter (OPC, model 11-S, GRIMM) in the cabin of the Learjet to measure the aerosol size distribution of particles larger than 250 nm. Due to particle losses in the inlet system the OPC measurements yield particle size distributions up to around 10 $\mu\mathrm{m}$. The particle loss calculation was done using the Particle Loss Calculator described in von der Weiden et al. (2009). From these OPC we get information of the size distribution every 6 s.

The aerosol number concentration for nucleation and Aitken-mode particles was measured in the cabin of the Learjet by a multi-channel condensation particle counter (mc-CPC, consisting of 3 Grimm Aerosol Technik model 5410-Sky CPCs). The individual CPCs are operated with Fluorinert (FC-43 3M^{TM}) as working fluid and are set to different cut-off diameters in order to obtain information on new particle formation events and the particle growth. With the current configuration, we achieved cut-off diameters of 12 nm and 16 nm, inferred from laboratory calibrations. Here, we decided to operate two of the three mc-CPC channels at the same cutoffs, to cross-check the data quality of the aerosol number concentration during the flights.

The chemical composition of non-refractory aerosol particles between 50 and 800 nm was measured using an aerosol mass spectrometer in the cabin of the Learjet. This instrument, which is based on the miniAMS by Aerodyne Research Inc., had been designed for operation in the IAGOS-CARIBIC (In-service Aircraft for a Global Observing System - Civil Aircraft for the Regular Investigation of the Atmosphere Based on an Instrument Container) project (CARIBIC-AMS). It is operated with a time resolution of 30 s resulting in a horizontal resolution of around 5 km in the UTLS. The CARIBIC-AMS is thus comparable to other AMS instruments. Although it is designed to be operated fully automated during IAGOS-CARIBIC flights, we operated the CARIBIC-AMS manually during the TPEx mission (Schneider et al., 2025).

2.2.2 In-situ trace gas measurements

For the simultaneous measurement of the trace gases nitrous oxide (N_2O) and carbon monoxide (CO) the Quantum Cascade Laser based spectrometer University Mainz airborne QCL Spectrometer (UMAQS) is used (Müller et al., 2015; Kunkel et al., 2019). It is based on the Aerodyne Research Inc. Quantum Cascade Laser Mini Monitor which uses an astigmatic multi path Herriot cell with an optical pathlength of 76 m operated at a cell pressure of 53 hPa. The measurement principle is based on infrared absorption spectroscopy at characteristic absorption lines of N_2O and CO in the 2200 cm^{-1} range. For operating the instrument on airborne platforms, the pressure within the measurement cell is controlled at 53 hPa. The instrument is calibrated in-situ to account for instrument drifts. Data are obtained at a time resolution of 1 Hz, finally limited by the gas exchange time of the measurement cell. This allows to measure atmospheric concentrations of N_2O with a noise level of 0.08 ppbv (2σ) and a reproducibility of 0.2 ppbv (2σ). For CO measurements the noise level amounts to 0.38 ppbv (2σ) and for the reproducibility we reach 0.7 ppbv (2σ) (Müller et al., 2015; Kunkel et al., 2019).

Ozone was measured using two modified 2BTech Model 205 instruments (Johnson et al., 2014; Bozem et al., 2025). One O_3

instrument was mounted in the wing pod of the Learjet and the second one was operated in TPC-TOSS. The measuring principle is based on UV absorption at the wavelength of 254 nm at ambient pressure. The time resolution of these measurements is 2 seconds with an uncertainty of 0.5 $\%$ + 2.0 ppbv.

Temperature and humidity data on the Learjet and the TPC-TOSS are measured by MCH (MOZAIC capacacitive hygrometer sensors, which consist of a capacitive relative humidity sensor by the company Vaisala, Finland and a PT100 resistance sensor for the temperature measurements (Helten et al., 1998; Smit et al., 2014). These sensors have been in regular service during then the MOZAIC program and now the IAGOS research infrastructure (Petzold et al., 2015). The MCHs were calibrated against a dew point hygrometer (MBW373) before and after the campaign in the atmospheric simulation chamber at Jülich (Smit et al., 2014). Based on the calibration, the MCHs give an uncertainty of 5 % relative humidity with respect to liquid water in the upper troposphere, tropopause and lowermost stratosphere and 0.5 K for temperature (Smit et al., 2014)).

The Fast In-situ Stratospheric Hygrometer (FISH) provides reliable water vapor measurements with the Lyman-α photofragment fluorescence technique aboard research aircraft for almost 30 years (Zöger et al., 1999; Meyer et al., 2015). The uncertainty estimation based on our regular calibrations during the TPEx campaign is 4.9 % of the respective measured value plus a constant uncertainty of 0.77 ppmv.

2.2.3 Collection of filter and impactor samples for the offline analysis

In addition to the in-situ measurements, we operated an in-house developed and manufactured filter sampler to gain information on the chemical composition of organic aerosol particles (SOAP) (Breuninger et al., 2025). Here, the collection of up to five different filter samples (47 mm diameter, Whatman^{TM} QM-A, cytiva) was possible due to a system of switchable magnetic valves and a bypass. The filters were sampled with 60 L$\cdot$ min^{-1} at standard conditions. After sampling, the filters were sealed in aluminium foil and stored in a freezing box to minimize artefacts and losses of the collected aerosol particles (Resch et al., 2023).

The filter analysis was carried out by extracting the filters in either a mixture of 90 % ultrapure water and 10 % methanol or pure methanol. After cutting pieces of the filter and adding the solvent, the vials are placed on an orbital shaker (KS-15, Edmund Bühler GmbH) at 300 rpm. After extraction, the extract is filtered through a disposable polytetrafluoroethylene (PTFE) filter (pore size: 0.2 μm, macherey nagel). The extracts were measured by using ultra high-pressure liquid chromatography (Vanquish Flex) coupled with high-resolution orbitrap mass spectrometry (Q Exactive Focus Hybrid Quadrupole Orbitrap, both Thermo Fisher Scientific). The separation was carried out according to previous studies from (Ma et al., 2022; Ungeheuer et al., 2021; Thoma et al., 2022), on a C_{18}-Column (CORTECS^{TM} T3, 2.7 μm x 150 mm, Waters), using a gradient elution with ultrapure water and methanol. The peak identification and analysis was done using the software FreeStyle^{TM} 1.8 SP2 (Thermo Fisher Scientific).

Additionally, during all flights UTLS particle samples were collected by the miniaturized MultiMINI8 casacade impactor unit. This self-developed Integrated Aerosol Sampling System, which is based on the former MultiMINI design (Ebert et al., 2016) was designed for the use within the wing pod of the Learjet. In total 8 two stage impactors (particle diameter: fine stage 0.1 – 1 µm; coarse stage > 1 µm) are integrated in this sampling unit. Particles were deposited on TEM grids, which are best suited for

later offline individual particle analysis by electron microscopic methods. Size, morphology, and elemental composition of the particles were studied by scanning electron microscopy (SEM) and energy-dispersive X-ray microanalysis (EDX). SEM-EDX was carried out with a FEI ESEM Quanta 400F (Eindhoven, The Netherlands) equipped with a X max 80 energy-dispersive X-ray detector (Oxford Instruments, Abingdon, UK), which enables the analysis of elements with $Z \geq 5$. All investigations were carried out at 12.5 kV acceleration voltage and spot size 4 (beam diameter $\approx 30\,\mathrm{nm}$). The particles were studied without coating in the high vacuum mode of the instruments ($\approx 5 \cdot 10^{-6}\,\mathrm{mbar}$ sample chamber pressure). Particle types were classified based on chemical composition and in case of biomass burning particles and soot additionally based on their typical morphology.

2.3 Meteorological support data and transport diagnostics

For the analysis of meteorological parameters, we used the ERA5 reanalysis data with a temporal resolution of $1\mathrm{h}$ and a horizontal grid spacing of 0.3°. Additionally, on the basis of the native variables we calculated meteorological parameters such as vertical wind shear (S^2), static stability (squared Brunt-Vaisala frequency, N^2), potential vorticity (PV) and equivalent latitude (EQLAT) (e.g., Lary et al., 1995; Krause et al., 2018; Joppe et al., 2024). In order to gain additional information about the chemical composition of the UTLS, we used the forecast data of the Copernicus Atmosphere Monitoring Service (CAMS), which is based on the Integrated Forecasting System 48r1 (IFS) with additional chemical modules for the chemical analysis, such as aerosol, reactive gases and greenhouse gases. This forecast is available twice a day (00 and 12 UTC) with a horizontal resolution of 40 km and 137 vertical levels (e.g., Benedetti et al., 2009; Morcrette et al., 2009; Rémy et al., 2019). We interpolated the CAMS data onto the flight tracks as we did for the ERA5 data. For analyses of air mass origin, we calculated backward trajectories from the position of the Learjet with LAGRANTO (Sprenger and Wernli, 2015) based on combined ICON global operational analysis and forecasts. We used the ICON global model for the trajectories instead of ERA5 to make use of the higher horizontal resolution. ICON global analysis is available every 6 h and is combined with short-term forecast to achieve an hourly resolution of wind field data. ICON global analysis and forecast data are available on a native R03B07 grid (corresponding to about 13.5 km effective grid spacing) and has been re-gridded to a regular longitude-latitude grid with 0.15° spacing. In the vertical, ICON global data comprises 120 levels with a spacing of about 300 m between about 4 km and 13 km altitude. The trajectories are calculated 10 days back in time. In addition, we combined the backward trajectories with the CAMS Global Fire Assimilation System (GFAS) version 1.2 to check if the trajectories crossed potential biomass burning regions. GFAS assimilates fire radiative power (FRP) on basis of satellite measurements to give daily estimates for biomass burning locations (Kaiser et al., 2012; Rémy et al., 2017). The fire locations are taken from the GFAS data set with detected fire radiative power signals in cloud-free regions and reports by the Canadian Wildland Fire Information System (CWFIS, https://cwfis.cfs.nrcan.gc.ca/interactive-map; last access: 09.01.2025) in order to close the gap of the satellite retrievals in regions with clouds.

2.4 Determination of the tropopause

Several definitions for the extratropical tropopause exist, such as the dynamical tropopause based on a certain threshold value of potential vorticity (PV) or the gradient of PV (Kunz et al., 2011; Turhal et al., 2024). In addition to dynamical tropopause

definitions there are also definitions based on the temperature, such as the thermal tropopause defined by the temperature lapse rate (World Meteorological Organization (WMO, 1997)) or the tropopause defined on the static stability (gradient in potential temperature θ) (Tinney et al., 2022). Finally, one can also define a chemical tropopause, based on trace gases, such as O_3 or nitrous oxide (N_2O) (Bethan et al., 1996; Müller et al., 2015; Joppe et al., 2024). In our study, we use the chemical tropopause based on the mixing ratio of mainly N_2O similar to Müller et al. (2015). N_2O has no sinks in the troposphere and a lifetime exceeding 100 years, so its mixing ratio remains constant throughout the troposphere, with a gradient at the tropopause, caused by the sinks in the stratosphere. Therefore, we can chemically define tropospheric and stratospheric air masses, solely based on N_2O measurements (Müller et al., 2015). The tropopause height is highly variable in time and space and depends further on the used definition. During summer months the dynamical 2 PVU tropopause tends to be lower than thermal WMO tropopause or the PV-gradient tropopause (Kunz et al., 2011; Turhal et al., 2024).

3 Transported biomass burning aerosol and its effects in the LMS

3.1 Observation of an aerosol polluted filament

In this study, we focus on the first of the five triangular patterns flown within the restricted airspace between 07:20 and 07:50 UTC (Fig. 1). The time series shows a very small-scale pollution event with an increase in particle number concentration by more than a factor of two compared to the UTLS background (Fig. 3). Furthermore, we observe an enhancement in CO of more than 20 ppbv in a region with stratospheric N_2O (N_2O < 336 ppbv) and O_3 (O_3 > 150 ppbv). The features we investigate in the following are also visible at higher altitudes later in the flight, but less dominant. Figure 3 shows a period of the time series for selected in-situ measurements carried out on both platforms. The measurements on the TPC-TOSS were shifted in time according to the lateral offset of the measurement platform behind the towing Learjet.

In more detail, we focus on the four segments with increased aerosol number concentration of 0.1 to 1.0 $\mu\mathrm{m}$ particles measured by the UHSAS, i.e. 07:24 - 07:26; 07:27 - 07:29; 07:42 - 07:44 and 07:45 - 07:47 UTC, which coincide with enhanced CO and N_2O as well as with decreased H_2O. The O_3 mixing ratios also decrease, but only to a very small extent from above 160 ppbv to around 150 ppbv. The trace gas mixing ratios indicate tropospherically influenced air masses with values of more than 110 ppbv CO, while the N_2O clearly shows stratospherically influenced air with values around 335.5 ppbv, i.e. lower than the tropospheric background of 337 ppbv. The interpretation of the mixed air masses into chemically stratospheric air is also supported by the O_3 mixing ratios above 150 ppbv and H_2O values near 100 ppmv H_2O. From the aerosol perspective, we observe increased particle number concentrations compared to the tropospheric measurements between 07:30 and 07:40 UTC for particles between 100 nm and 1 $\mu\mathrm{m}$.

Several processes could have caused the observed high aerosol number concentration, which we discuss in the following. More precisely, enhanced aerosol number concentration can be caused by new particle formation with a high number of very small particles in the nucleation mode. Other possibilities for high aerosol number concentration are anthropogenic or biomass burning pollution events with high particle concentrations in the Aitken- and accumulation mode. Further sources are dust events or volcanic plumes which would result in a high aerosol number concentration in the coarse mode. Especially the

mc-CPC measurements can be used to differentiate between fresh new particle formation or more aged and enlarged aerosol particles. Between 07:43 and 07:46 UTC, we observe that the size channel with particles larger than 12 nm strongly differs from the channel with particles larger 16 nm. This might be an indication for a recent new particle formation event in this airmass. However, to prove this hypothesis, further analysis is required which is beyond the scope of this study.

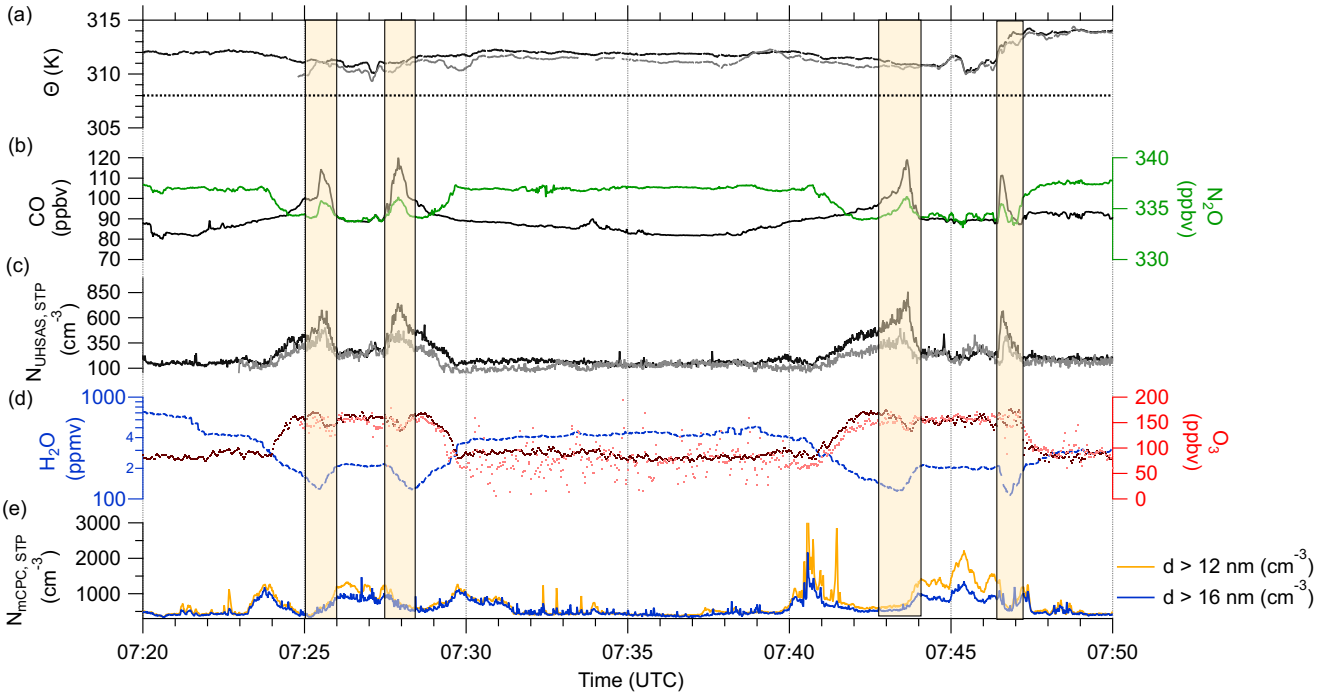

Figure 3. Time series of trace gas and aerosol in-situ measurements for F07 on 17 June 2024 for the period between 07:20 and 07:50 UTC. Measurements conducted on the Learjet are in darker colors whereas measurements from the TPC-TOSS are in lighter colors. Row (a) shows the potential temperature (θ) with the tropopause derived from vertical trace gas profiles (dashed line), (b) trace gases CO (black) and N_2O (green), (c) aerosol number concentration between 100 nm and 1 µm, (d) H_2O (blue) and O_3 (red) as well as (e) total aerosol number concentration from 12 nm (yellow) and 16 nm (blue) measurements. The orange shaded boxes mark the four analyzed periods with enhanced aerosol number concentration N_{UHSAS} and CO mixing ratio.

The presence of polluted air masses in chemically stratospheric air is also supported by the vertical profiles of the trace gases (Fig. A1), which can be used as stratospheric tracers, namely O_3 and N_2O. Both trace gases show rather constant mixing ratios in the troposphere and then a stratospheric increase for O_3, and a decrease for N_2O, respectively (Müller et al., 2015; Joppe et al., 2024). From these profiles (see Fig. A1), we identify the chemical tropopause at altitudes around 308 K potential temperature. We accounted for the tropopause variability of less than 5 K by taking the mean between initial ascent and descent. The observed pollution event is located 2 to 4 K above this chemical tropopause at potential temperatures of 311 K in a layer with decreasing N_2O which is clearly stratospheric air. Compared to the in-situ measurements, the interpolated ERA5 data along the flight path is showing a higher tropopause with a thermal tropopause at 315 K and a dynamical 2 PVU tropopause

50-70 hPa above the flight path of the first pattern (see Fig. 1). This model observation fits well to radiosonde sounding in Schleswig (12 UTC) which yield a tropopause height at 9.1 km or 320 K θ based on the definition of Tinney et al. (2022). Nevertheless, we use for our analysis the chemical tropopause based on in-situ measurements to minimize errors which might arise from the model resolution and other model deficiency.

Figure 4 shows the pattern of the first altitude stack at approximately 7400 m (FL240) after the TPC-TOSS deployment. The polluted air masses appear as a small band which is oriented north-eastwards, crossing the flight pattern. Furthermore, the different chemical characteristics of the probed air masses can be seen: While we observe clean and unpolluted tropospheric air masses in the eastern part of the pattern, the western part is characterized by stratospheric air with the polluted streamer embedded.

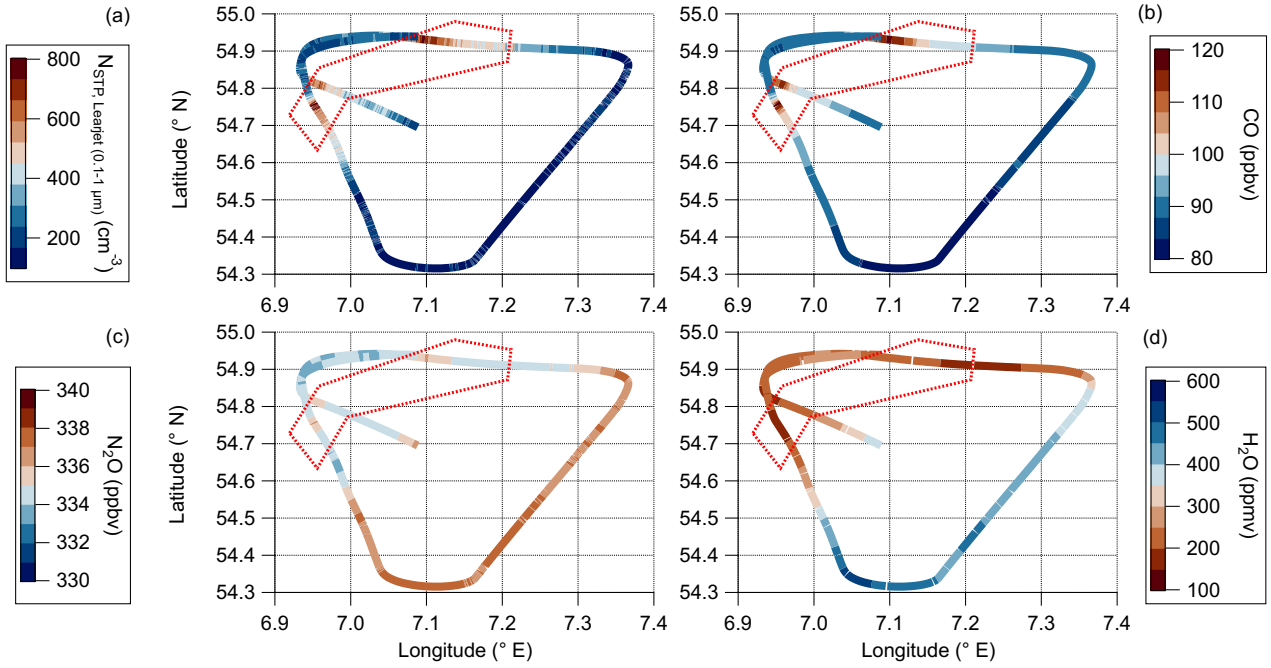

Figure 4. Flight track of the first complete triangular pattern with deployed TPC-TOSS within the restricted air space. The pattern is flown at FL240 (approx. 7400m) between 07:24 and 07:47 UTC. The colorcode represents different in-situ measurements onboard the Learjet: (a) total aerosol number concentration between 0.1 and 1 µm, (b) CO, (c) N_2O and (d) H_2O measurements. The red box surrounds the observed polluted air masses.

Figure 4 gives a rough overview of the pollution within the streamer. We are interested in its difference in particle size distribution compared to the local and the tropospheric background. For this purpose we focus in the following on the aerosol size distribution and the chemical composition with respect to non-refractory compounds, such as particulate sulfate, ammonium, nitrate and organics. We can clearly see that the particle number concentration measured by the UHSAS during the lowest

pattern correlates with the CO mixing ratio (see Fig. 5a). This suggests that the measured aerosol is of tropospheric origin with most likely the same source as the high CO mixing ratios within the LMS.

3.2 Identification of biomass burning in the UTLS

Possible sources for the observed high CO values in the stratosphere are advected biomass burning residues or local uplifted pollution from the surface. We analyzed the aerosol size distributions measured by the UHSAS at the Learjet in order to find some hints for possible biomass burning in these size distributions. Therefore, we calculated the aerosol volume distribution over 10 s, which is sufficient enough to average over the full peak of elevated aerosol number concentration. Furthermore, we also calculated volume distributions during the local UTLS background between the two consecutive pollution events and the tropospheric background in the middle of the pattern without observed pollution. The detailed times are also given in Table C1. As optical particle detection reveals some uncertainties due to absorbing aerosol particles, especially when calculating volume distributions, we additionally provide an uncertainty range. For this, we use the sizing uncertainties for a UHSAS according to Moore et al. (2021). Based on in-situ observations and laboratory studies, they provide sizing errors for different particle types, especially for wildfire biomass burning aerosol. Following Moore et al. (2021), we calculated the uncertainty range for potential 3 % oversizing up to 20 % undersizing as consequence of light absorption by wildfire biomass burning aerosol particles. The inferred volume distributions (Fig. 5b) show significant differences between the UTLS background and the polluted air masses. Even though the uncertainty range is high, we observe a modal distribution with a mode between 200 and 400 nm during the pollution events. This mode is robust against the measurement uncertainty and can be differentiated from the UTLS and tropospheric background. Such a mode in the volume distribution has previously been reported for observed aged biomass burning aerosol (Alonso-Blanco et al., 2014; Ditas et al., 2018; Brock et al., 2021; Schill et al., 2022; Holanda et al., 2023).

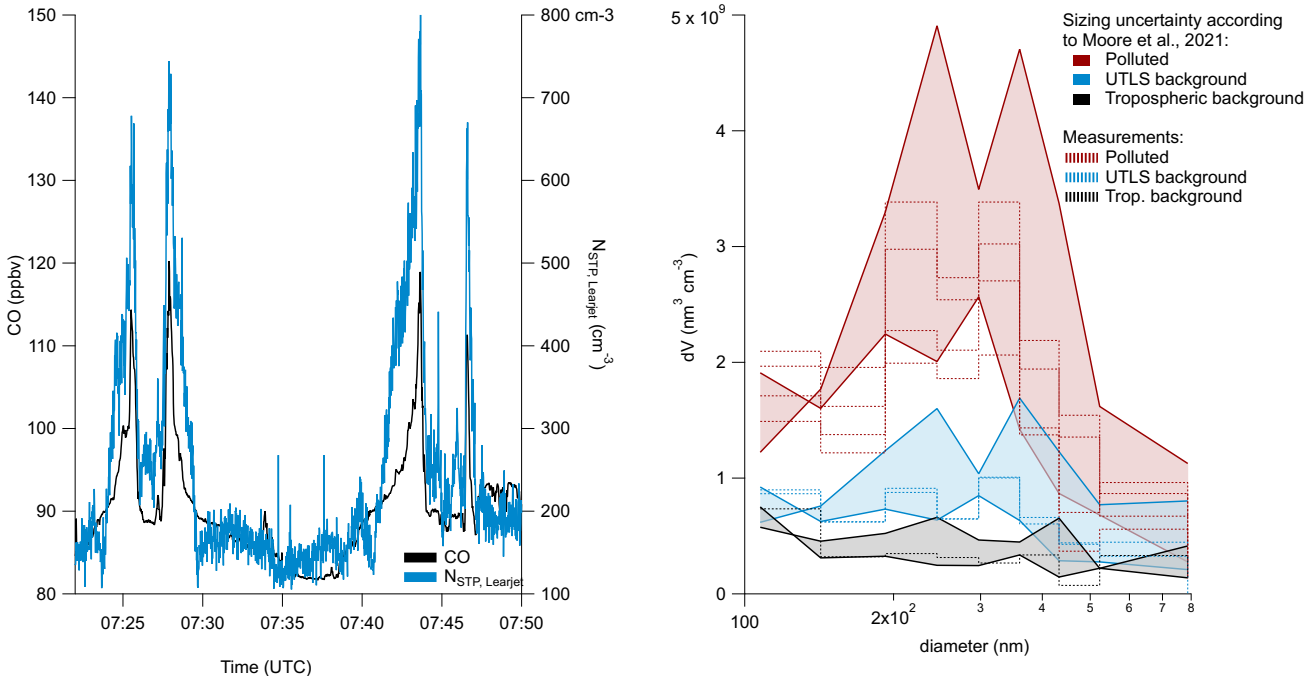

Figure 5. Detailed analysis of measured polluted air masses with a time-series of particle number concentrations measured by the UHSAS on the Learjet (blue), and CO (black) (a), as well as measured volume distribution averaged over 10 s (see Table C1) for the polluted air masses (dark red), the UTLS background (bright blue) and the tropospheric background for the pattern (black). The shaded area represents the uncertainty range due to sizing errors of absorbing particles (b). The dashed lines represent the original measurement data with the color corresponding to the atmospheric regime.

Particle composition information are gained by the individual particle analysis of the MultiMINI8 casacade impactor samples. Here, we performed offline analysis by SEM-EDX. In the analyzed impactor sample collected on the first leg in the restricted air space (7:16–7:44 UTC), BB particles were the most abundant refractory particle type. Two different types of BB particles can be identified in the SEM. Firstly, carbon dominated particles with increased potassium, sulfur and in some cases chlorine contents are observed. Secondly, soot particles, characterized by their typical morphology and the very low oxygen content of the C-rich particles are detected. These chemical signatures are highly characteristic for BB particles (Li et al., 2003). Two secondary electron images with the referring energy dispersive X-ray spectra for the two types of observed BB particles are shown in Fig. 6. Beside the BB particles, also some Ca-rich particles, Fe-rich particles and aluminosilicate (soil) particles were observed. The second used offline sampling method by the SOAP does only show very weak signals signals of BB influence for this flight. The results are given in appendix D.

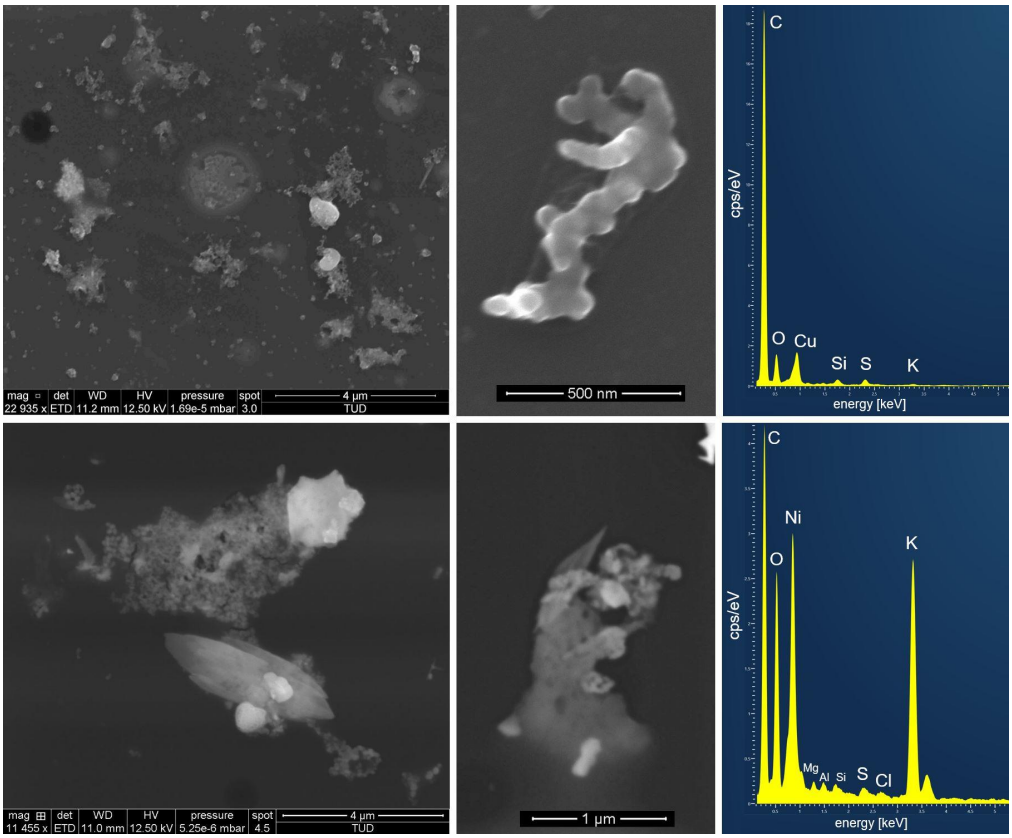

Figure 6. Secondary electron images and referring energy dispersive X-ray spectra of (upper row) two typical soot like BB particles and (lower row) two typical K-rich BB particles from the investigated sample (Ni and Cu-peaks in the spectrum are due to the Ni-grids respectively the Cu-grid holder used in SEM analysis).

After these indications for potential BB influence within the tropopause region, we use the CARIBIC-AMS measurements of non-refractory compounds to estimate the amount of refractory aerosol (rA) which may correspond to black carbon (BC). Here, we reduce the background noise, especially of the organic signal, of the CARIBIC-AMS measurements by calculating mean values of the mass concentrations symmetrically over 3.5 min with a running mean (Box-Car method), i.e. over 7 individual data points. We averaged the UHSAS data over the same time interval and calculated the mass concentration from this mean UHSAS volume distribution, assuming spherical particles with a density of 1.5 $\mathrm{g\ cm^{-3}}$. The time series of the mass concentrations measured by CARIBIC-AMS and calculated from UHSAS data is shown in Fig. 7.

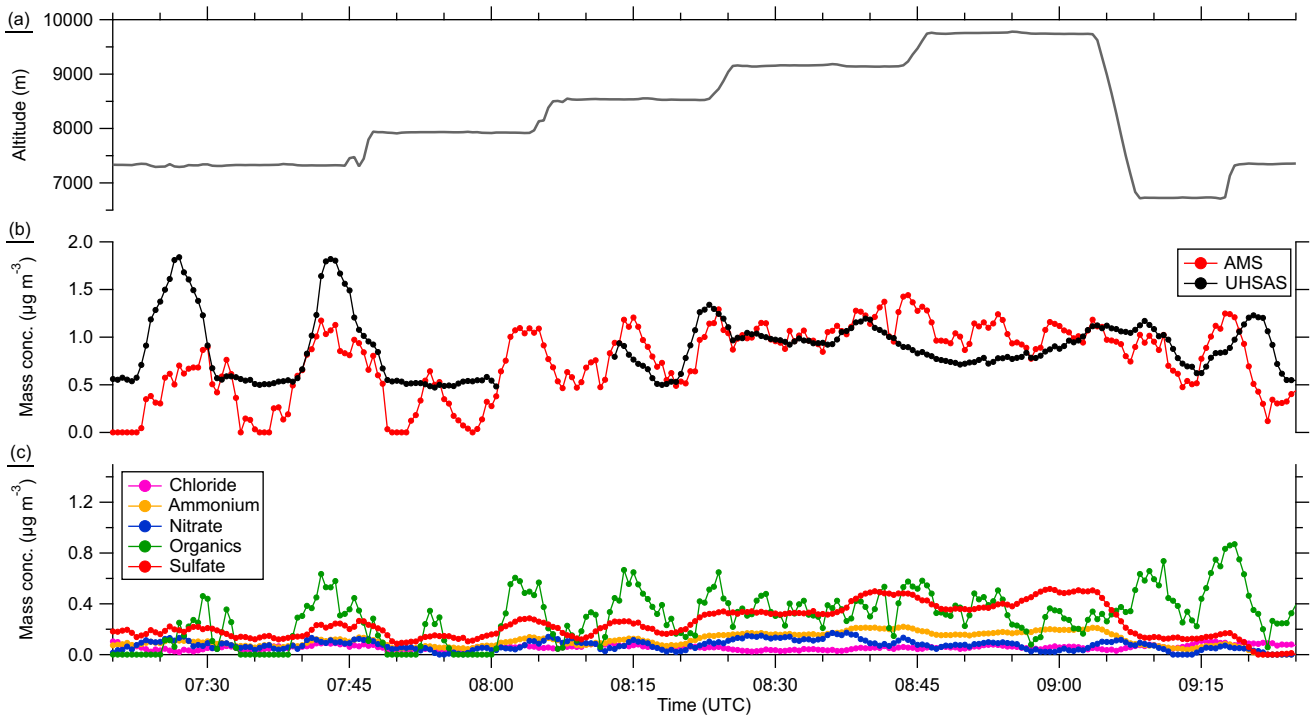

Figure 7. Time series of the GPS altitude (a), the total mass concentration of the AMS (b) and the UHSAS (b) and the individual mass concentrations for the AMS species (c). The AMS and UHSAS measurements are averaged over 3.5 min with the box-car method.

The estimation of the rA mass concentration is only possible, because both instruments measure in the same size range. We also have to emphasize that this estimation is only a best guess estimation with high uncertainties, based on several assumptions, and the estimated mass concentration has to be regarded as upper limit. The measurement uncertainties of the CARBIC-AMS are already in the range of 30 % (Canagaratna et al., 2007; Bahreini et al., 2009). The conversion of the number size distribution measured by the UHSAS to a volume distribution add a further considerable uncertainty. Since we used a difference between two measurements the calculated rA mass concentration can in principle include more than just one component, such as sea salt or mineral dust or BC. In the remote atmosphere, mineral dust and sea spray are typically found in the coarse mode above 1 μm diameter, although some contribution to the submicron aerosol mass has also been observed (Brock et al., 2021). Furthermore, BB aerosol may also contain non-refractory salts such as KCl (Dang et al., 2022). The gained amount of rA is too high for real atmospheric values of BC in the order of less than 5 % (Yu et al., 2019). Therefore, this approximation can be regarded only with caution, but it yields also the potential for BC as well as the CO and the SEM particle analysis. The information on rA and potential black carbon may serve as an indicator of particle origin, especially regarding biomass burning. Furthermore, the estimated rA fraction is influenced by an instrumental drift of the CARIBIC-AMS in the beginning of the flight due to short preparation times with respect to reducing the background in the vacuum system.

Comparing both mass concentrations of the UHSAS and the CARIBIC-AMS (Fig. 7), we observe two different periods. Dur-

ing the first period, under tropospheric influence as evident from N_2O and ozone and within the tropopause region (until 08:15 UTC), we found a difference between the two mass concentrations, indicating an instrumental drift but also a higher possible contribution of rA compared to the higher stratosphere. After 08:30 UTC, higher up in the stratosphere, we observe quite similar mass concentrations measured by the CARIBIC-AMS and the UHSAS and with this a much smaller possible contribution of the estimated rA. Compared to Fig. 5 we now analyze the complete flight with all altitude stacks. For this analysis, we divided the complete data set of F07 into five different regions, namely tropospheric background with N_2O larger than 336 ppbv, UTLS with N_2O between 330 and 336 ppbv, pollution events, stratospheric background with N_2O between 330 and 325 ppbv (LMS) and stratospheric background with N_2O lower than 325 ppbv (stratosphere) (see Fig. 8). This separation shows that within the UTLS including the polluted regions, we find higher estimated rA mass concentrations. The higher we get into the stratosphere, the less impact of polluted air masses is observed and we see an absolute increase of sulfate aerosol, which is typical for the stratosphere (Junge et al., 1961; Yue, 1981; Kremser et al., 2016).

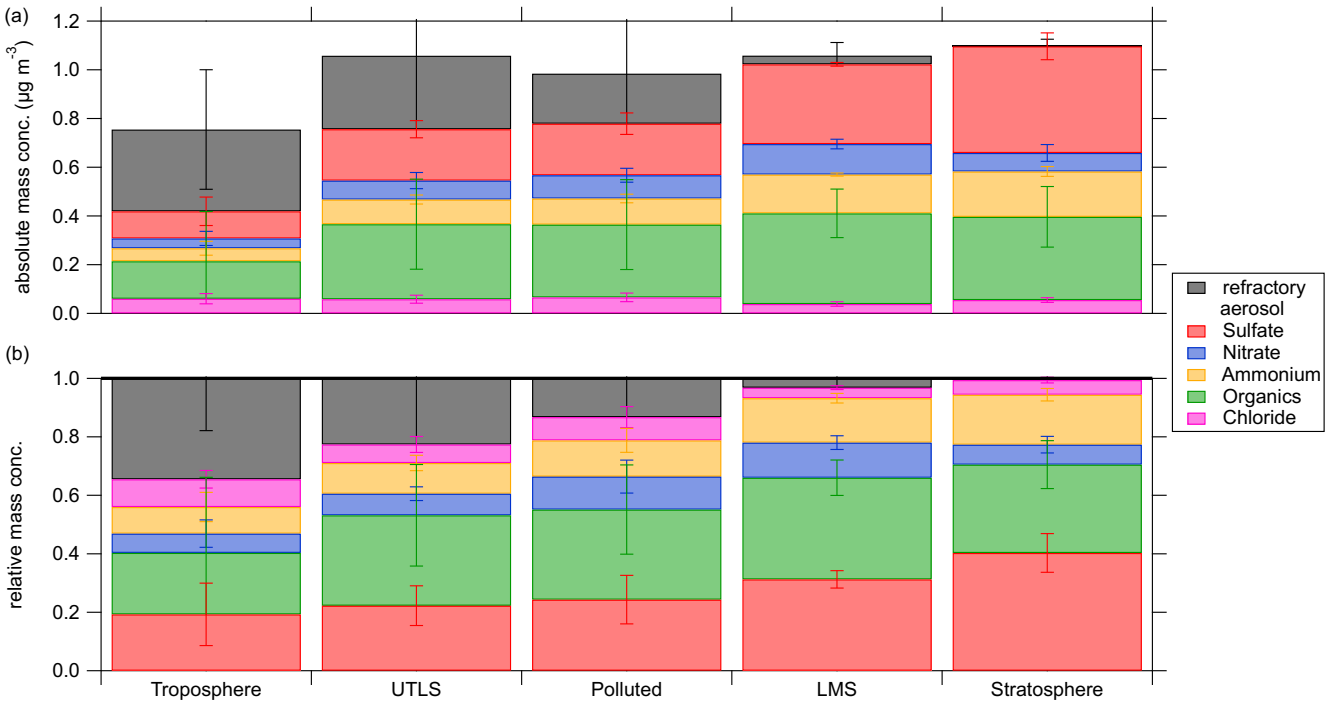

Figure 8. Average of the absolute (a) and the relative (b) mass concentrations (including standard deviations shown as error bars) for the non-refractory aerosol species and the estimated amount of refractory aerosol (rA) during different measurement periods during F07. The separation of the regions is done by N_2O measurements and the exact times are provided in Tab. C2.

3.3 Air mass history and transport diagnostics

In the following, we present 10 day backward trajectories, initialized along the flight track, in combination with GFAS data provided by satellites, to link the observed pollution events and possible BB influence to potential source regions with active BB during the days before the measurement. The trajectories show that the polluted air masses during Flight 07 were located over Canada, mostly in the Canadian Arctic in the mid troposphere, 10 days before being sampled by TPEx F07. Over Central Canada, the air masses partly descend to lower tropospheric altitudes of around 3 km and cross regions with active forest fires ten to seven days before the TPEx measurements. Subsequently, the air parcels cross the North Atlantic towards Europe at altitudes below 5 km embedded in a potential dry air mass with respect to specific humidity (see Fig. 9 and Fig. F1). The compact trajectory bundle is uplifted on the edge of a WCB over Germany up to about 400 hPa within 12 hours and transported as a compact bundle towards the measurement location (see Fig. 10). In contrast to the pollution trajectories, those trajectories, which indicate pristine UTLS background, are also crossing Canada and regions with active wildfires, but in higher altitudes (Fig. 9b and Fig. 10). The tropospheric background trajectories however start at the east coast of Canada in low altitudes but in a region with mostly no fire activity. While crossing the Atlantic, the air masses can be found in distinct altitude regions. The trajectories with the biomass burning pollution are in the mid-troposphere and descend to 700 hPa on the way towards Europe. In contrast, the air masses measured in the UTLS background are 100 to 200 hPa higher in the free troposphere and the trajectories that end in the tropospheric regime are just below 700 hPa. In addition to differences of the altitude of the trajectories, we observed differences between upwind velocity during the uplift process into the UTLS. Here, the UTLS background and the polluted air masses are quite similar with a strong ascent over the Baltic Sea and Scandinavia whereas the tropospheric background trajectories are lifted at an earlier stage over the North Sea (Fig. 9 and Fig. 10).

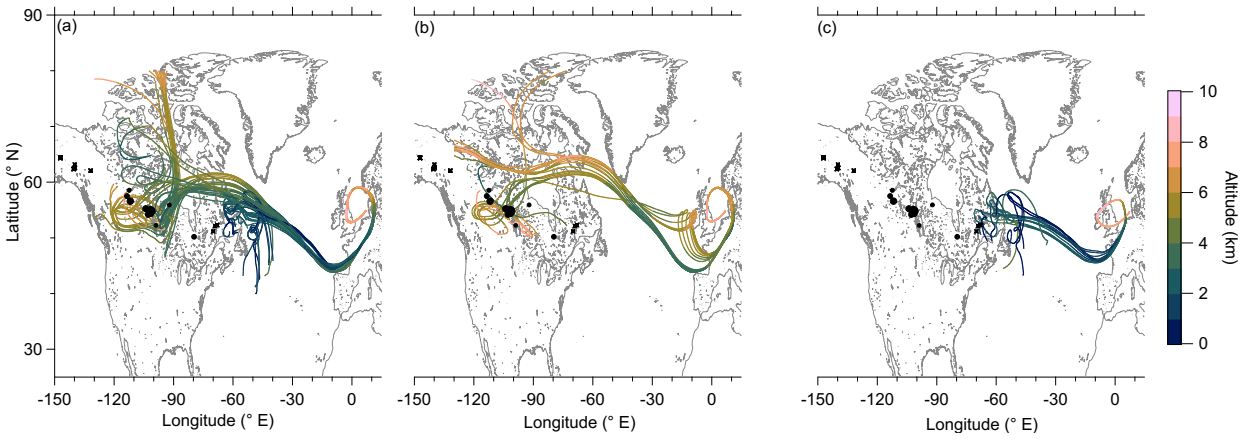

Figure 9. Back trajectories for the different observed regimes ((a) pollution events, (b) UTLS background and (c) tropospheric background) in F07. The altitude of the trajectories is represented by the colorcode of the solid lines. Additionally, we added fire observation data provided by CWFIS (circles) in the vicinity of the trajectories. The size of the circles represents the size of the forest fire. Furthermore, we added the fire locations detected by the satellite in the GFAS retrievals of 10 June 2024 with fire radiative power (crosses).

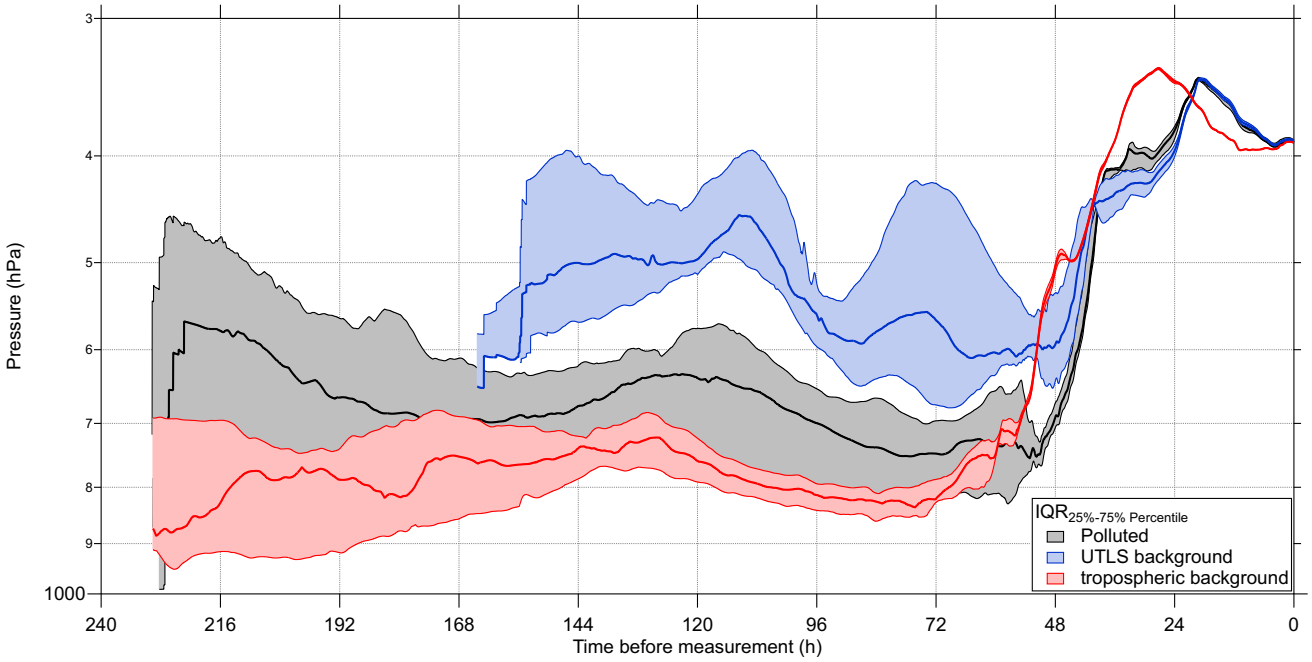

Figure 10. Time series of pressure for the calculated LAGRANTO trajectories divided into the different regimes (Table C1): Polluted air masses (black), UTLS background (blue) and tropospheric background (red). The shaded area is the interquartile range (IQR) between the 25 and 75 % percentile with the median as solid line in the middle. The UTLS timeseries is shorter, because the trajectories leave the model domain 7 d before the measurements.

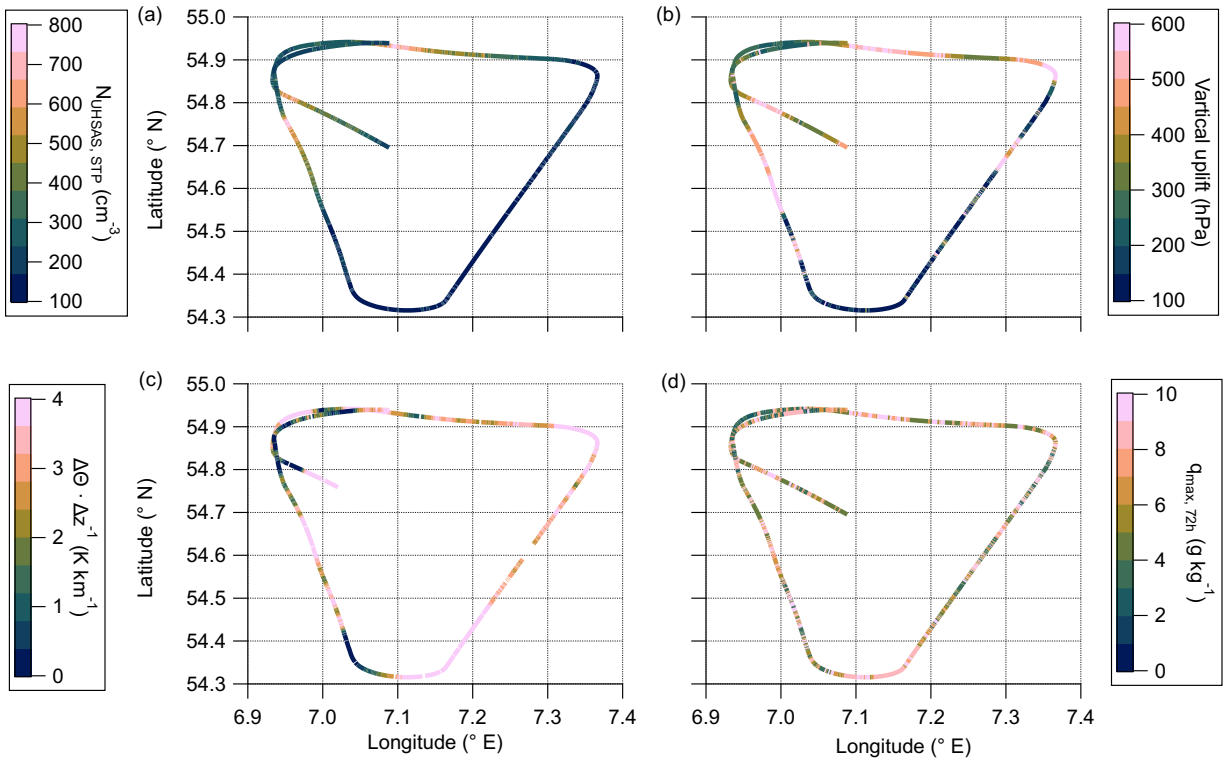

Figure 11. Top view of the first flight pattern within the restricted air space with deployed TPC-TOSS during F07. Colorcoded are measured quantities, such as the total aerosol particle number concentration by the UHSAS (a) and the vertical gradient of potential temperature (c). Furthermore, we analyzed meteorological parameters along the trajectories, namely the range between maximum and minium pressure (b) and the maximum specific humidity over the last 72 h before the measurements (d).

We use the meteorological data along the trajectories, to differentiate the air mass characteristics of the different air mass regimes. Therefore, we analyze the pressure difference between maximum and minimum pressure over the last 10 d as well as the maximum specific humidity over the WCB ascent period over the last 72 h before the measurements. Figure 11 shows that the observed pollution is found just in or directly next to a region where the air parcels experienced a strong vertical uplift of more than 400 hPa. This ascent ends one day before the measurements in the upper troposphere and allows time for subsequent small-scale cross-tropopause mixing. Regarding the moist processes within the WCB we are not able to identify significant differences between the polluted and unpolluted air masses (Fig. 11d), which leads to the conclusion that the wet deposition was in this case not efficient enough or other microphysics of BB aerosol is not resolved in the ICON model. As consequence we conclude that the BB aerosol can get transported to the UT and subsequently mixed into chemically stratospheric air masses.

To summarize, the measurement data show that the observed polluted air masses in the stratosphere show elevated aerosol particle number concentration and CO mixing ratios. Furthermore, the measured particle size distributions show a size range typical for biomass burning aerosol as previously reported in the literature. Additionally, the differences between the mass concentrations measured by the CARIBIC-AMS and calculated from the UHSAS data indicate that refractory compounds,

365 potentially also BC, were measured in the tropopause region and especially during the pollution events. In addition to the in-situ measurements, we analyzed filter samples for organic biomass burning tracers and impactor samples for individual particle composition to obtain more information on particles related to BB detected in the sampled air masses. Back trajectories started along the flight path show that the air masses originated from the lower troposphere over Canada, where active forest fires were reported and observed, and were lifted to the upper troposphere by a WCB over Europe about 1-2 days before the 370 measurements. Although the process of WCB is typically accompanied by moist processes, the aerosol was transported into the UTLS and mixed into the chemical LMS. From previous studies (e.g., Ramanathan and Carmichael, 2008) it is known that the atmospheric lifetime of BC is typically less than 7 days, due to wet deposition processes like rainfall which occurs also in the process of WCB uplift. Nevertheless, we observe BB aerosol in the LMS where such particles have a radiative impact. In the following section we provide estimates for the radiative impact of this small scale aerosol streamer to assess the importance 375 of WCB uplift processes for the radiative balance of the LMS.

3.4 Impact of potential BB pollution in the tropopause region

As pointed out by Ramanathan and Carmichael (2008) and Räisänen et al. (2022), BC has a positive radiative forcing at the TOA of up to 0.9 Wm^2. Ditas et al. (2018) show from regular observations on flights between Europe and North America that BB plumes show on average 0.14 $\mu\mathrm{g} \cdot \mathrm{m}^{-3}$ of BC and a typical UTLS background of 0.006 $\mu\mathrm{g} \cdot \mathrm{m}^{-3}$. From these observations 380 Ditas et al. (2018) derive an increase in the average heating rate of around 0.07 $\mathrm{K} \cdot \mathrm{d}^{-1}$ by the attribution of BC with a up to 0.44 $\mathrm{K} \cdot \mathrm{d}^{-1}$.

In order to estimate the radiative effect of BB aerosol on the static stability in the present study, we use the available measurements of chemical composition and the dual platform measurements of temperature. The binned vertical profile of the relative mass concentration of the chemical composition including the potential for BC shows the highest estimated amounts around the 385 chemical tropopause below 7500 m (see Fig. 12). Our upper limit estimation yields a maximum possible rA mass concentration of around 0.15 $\mu\mathrm{g}$ (Fig. 8). As expected, with decreasing tropospheric influence the relative mass fraction of rA decreases with altitude as well and is close to zero above 9000 m. Including the large uncertainties of this upper limit estimation, our values are still in the range of BB-affected air, reported by Ditas et al. (2018) with 0.02 $\mu\mathrm{g}$ and we can raise some hypothesis on the radiative impact on the tropopause region and its stratification.

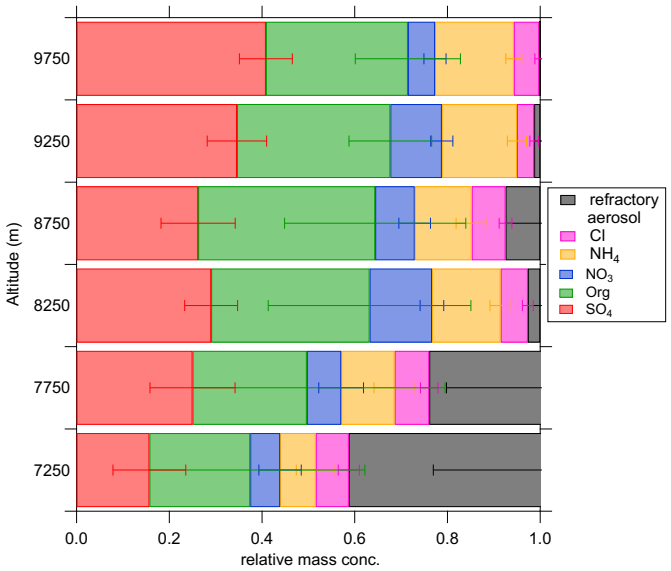

Figure 12. Relative mass concentration for the non-refractory aerosol species (chloride in pink, ammonium in orange, nitrate in blue, organics in green and sulfate in red) and estimated highest possible refractory aerosol (rA) (black) in 500 m vertical bins between 7 and 10 km. The error bars represent the standard deviation in the altitude bins.

Therefore, we make use of the dual platform measurements of temperature and pressure to calculate vertical gradients in potential temperature (θ). We use these gradients to analyze the stratification of the tropopause region and derive a potential radiative forcing. Figure 11c shows the analyzed first pattern in the restricted air space colored with the derived vertical θ gradient. In general, we observe the typical stable stratospheric stratification with positive vertical gradients of θ. Besides the expected stable stratification, we observe a different stratification most prominent at the location of the polluted filament. Here, the gradient changes towards weaker stability close to 0 $\mathrm{K \cdot km^{-1}}$. The location of this anomaly is the same as for the polluted air masses with BB influence (Fig. 11c). This leads to the assumption that this change is related to the streamer of polluted air masses. The observed change in the vertical θ-gradient reaches up to 2 $\mathrm{K \cdot km^{-1}}$. From the trajectories we find that after the WCB uplift there is no influence of cloud liquid and ice water in the UTLS for the last 18 h before the measurements. Additionally, the trajectories indicate a quasi-isentropic transport in the UTLS from the uplift area to the measurement locations with a slight increase in the static stability and PV. However, it is important to say that the trajectories do not include any aerosol data, e.g. aerosol radiative heating. Therefore, considering these observations in the trajectory data started at the Learjet position, we hypothesize that the changes in the static stability may also be forced by radiative effects of the transported rA in the absence of (cirrus) clouds. Referring to the observations by Ditas et al. (2018) typical heating rates as consequence of BC are in the magnitude of 0.07 $\mathrm{K \cdot d^{-1}}$ up to 0.44 $\mathrm{K \cdot d^{-1}}$ in extreme cases, which shows a significant contribution to the radiative feedback on lower stratospheric dynamics. Combining the uncertainties of the rA approximation with potentially included BC and the gradient calculation of potential temperature (31 %, see Bozem et al. (2025)) we end up in the same regime of expected heating rates of roughly 0.1 $\mathrm{K \cdot d^{-1}}$ of the tropopause region after the WCB uplift.

As the transport of BC and BB plumes was mostly studied in the presence of pyroconvection and fast uplift of pollutants to the tropopause region, current studies like this and that of Khaykin et al. (2025) show an additional transport pathway of BB aerosol into the UTLS and especially the LS. This uplift can occur close to the fire locations like in Khaykin et al. (2025) or after low-level long-range transport far away from the pollution source as shown in this study.

4 Conclusions

The influence of WCBs on the UTLS aerosol composition is only rarely discussed in previous studies (e.g., Voigt et al., 2017; Trickl et al., 2024). In our study, we present a case-study of aerosol characteristics in a WCB outflow region over Germany. Here, we observed a small-scale streamer of polluted air masses, more precisely elevated aerosol number concentration between 100 nm and 1 $\mu\mathrm{m}$ with CO mixing ratios larger than 100 ppbv in the chemically stratospheric air (N_2O < 336 ppbv). Further, analysis of the particle size distribution in the pollution event shows a maximum of particles with a diameter between 200 and 400 nm, which is a characteristic of biomass burning size distribution. Further evidence for the influence of biomass burning is found by the offline analysis of impactor samples using a SEM. Here, we find particles which refer to biomass burning, such as soot and carbon dominated particles with larger fractions of potassium. LAGRANTO back trajectories on the basis of ICON global analysis wind fields for the last 10 days before measurement also show biomass burning over Canada as potential source for the observed pollution. However, these trajectories are not able to resolve convective transport either in pyro-convection, boundary-layer convective clouds, or embedded convection in the WCB. According to the trajectory data, the air masses observed by TPEx F07 originate in the lower troposphere over Canada and the Canadian Arctic and crossed spots of active forest fires. These polluted air masses were then transported across the Atlantic within the lower troposphere before subsequent uplift embedded on the edge of a WCB over Europe. This uplift was strong enough to transport the BB aerosol into the UTLS, and after end of ascent likely trigger stratosphere-troposphere exchange. Additionally, we analyzed the chemical composition of the aerosol in the pollution event and during background conditions in the troposphere, the undisturbed LMS and the stratosphere. Here, we estimated the mass concentration of rA by the difference between the total mass measured by the AMS and the UHSAS, under the assumption of a density of 1.5 $\mathrm{g\,cm^{-3}}$. This method yields the highest amounts of rA around the tropopause and rather no rA in the stratosphere. Besides the in-situ measurements of the chemical composition of aerosol particles and trace gases, we used offline filter analyses of collected aerosol particles during the flight. The analysis of these filters needs to be considered with some caution, as consequence of a high background signal for these two flights. But even with this caution, we are able to see some indications for the influence of BB on this day, which supports the found results for BB as source of the pollution.

In addition to the chemical composition and aerosol measurements, we take advantage of the dual platform measurements of temperature and pressure to derive the vertical gradient in potential temperature to describe the radiative impact of this BB intrusion on the UTLS. From this, we observe a change in the gradient of θ by around 2 $\mathrm{K \cdot km^{-1}}$, with a contribution which is caused most likely by the observed rA and BC in this region.

Finally, we were able to show an additional pathway of BB pollution into the extratropical tropopause region by WCB uplift.

In contrast to other studies (Khaykin et al., 2025), we observe this uplift mechanism after low-level long-range transport. The radiative feedback of such transported rBC into the tropopause region now needs to be calculated to show the impact of this additional pathway.

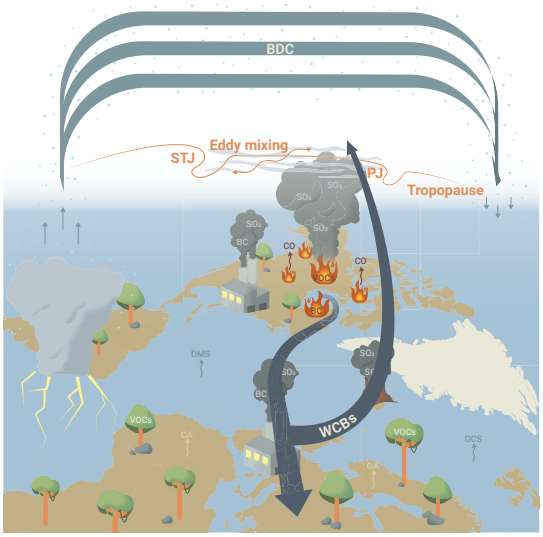

Figure 13. Schematic overview of the observed processes in our study. The polluted air masses from Canadian forest fires travels in the lower and free troposphere across the Atlantic ocean, before strong ascent associated with a WCB over Europe occurs. As consequence of this strong uplift to the tropopause region the polluted air masses are in a region of stratosphere-troposphere exchange and are mixed with chemically stratospheric air masses.

Data availability. The measurement data, model data and trajectory data along the flight path is published on Zenodo (Lachnitt, 2025; Miltenberger, 2025).

Author contributions. PJ set up the study, analyzed the data and wrote the manuscript. PJ, JS, JW are responsible for the AMS and UHSAS data. NE, IK, HB and PH provided CO, N_2O and O_3 data. DK and HCL provided ECMWF data along the flight path. YL provided temperature and humidity data. CR and NS provided the H_2O data. AM and CS provided ICON-EU WCB diagnostics and the LAGRANTO trajectory data. AB and AV sampled and analyzed the SOAP samples. SR provided the mCPC data. ME, SI, KK and LS are responsible for the impactor samples and the analysis in the SEM. All authors contributed and commented on the manuscript.

Competing interests. Some authors are members of the editorial board of journal Atmospheric Chemistry and Physics.

Acknowledgements. The authors acknowledge the team of enviscope GmbH and GFD GmbH for the opportunity to carry out the campaign and the technical support during the campaign. Additionally, the authors thank the graphical office of the MPI-C for the schematic drawing. Furthermore, the authors appreciate the support by Tobias Könemann and Jesse Steiner (both DMT) for their technical support with the UHSAS systems. This publication is generated using Copernicus Atmosphere Monitoring Service Information [2024].

PJ, JS, SB, AB, AV, CS, AM, HCL, DK ,LS, SI, KK, ME, NE, PH, SR and JC acknowledge funding by the Deutsche Forschungsgemeinschaft (DFG, German Research Foundation) – TRR 301 – Project-ID 428312742: "The tropopause region in a changing atmosphere"

Appendix A: Identification of the chemical stratosphere

For this study, we use ozone (O_3) and nitrous oxide (N_2O) to determine the chemical tropopause as reference for tropospheric and stratospheric air masses. This chemical tropopause, based on the mixing ratios and the vertical gradient of both trace gases, is around 308 K potential temperature.

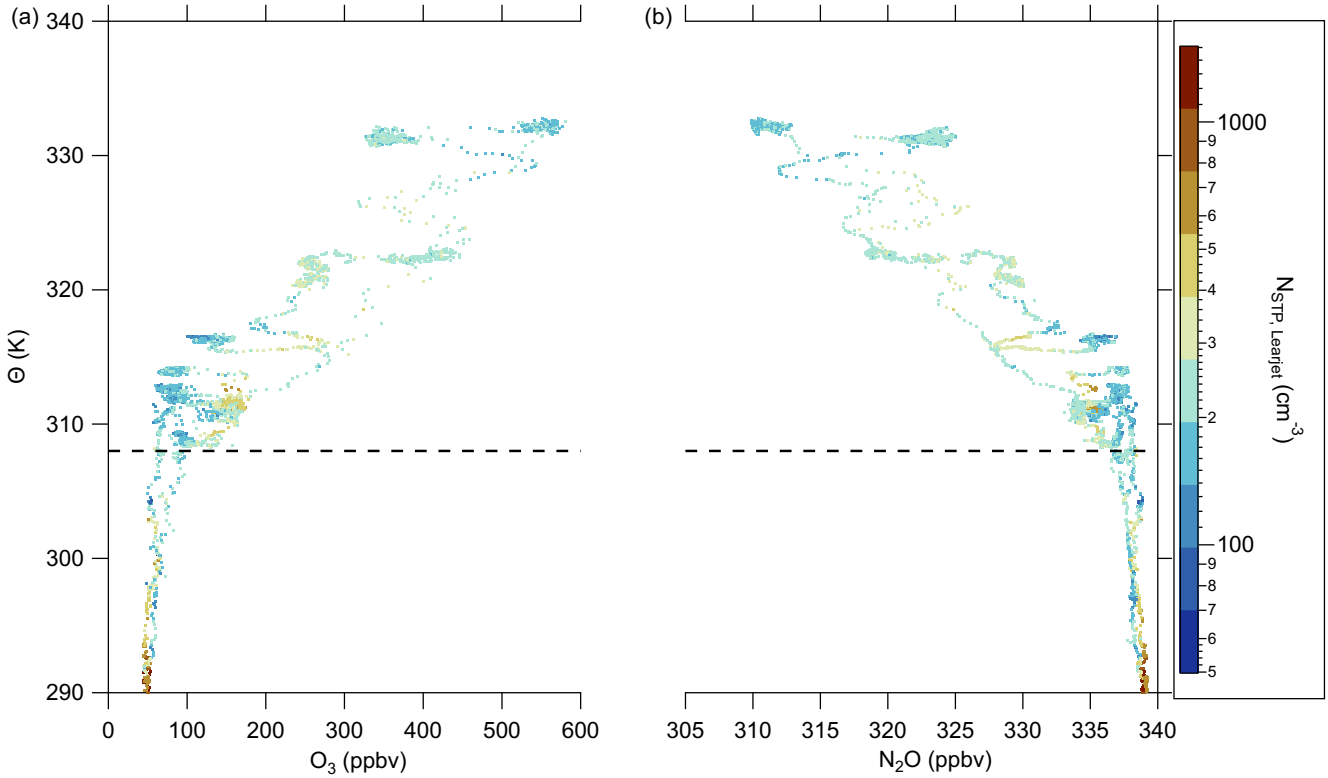

Figure A1. Vertical profiles of O_3 (a) and N_2O (b) for the complete F07, colorcoded with the total aerosol number concentration measured by the UHSAS. The dashed lines visualize the chemical tropopause based on the vertical gradient and the mixing ratios of the individual species.

Appendix B: Identification of mixed air masses

In Appendix B, we introduce tracer-tracer correlation to identify mixing processes between the troposphere and the stratosphere. Therefore, we use the CO versus N_2O (Fig. B1a) correlation. This correlation has also the advantage, that we are able to determine the tropospheric end member of each individual mixing line, which occurs in the correlation. As colorcode we use the information about the flight pattern within the restricted air space, to better identify small-scale mixing occurrence. We observe the most dominant perturbation of the overall mixing line during the first pattern, where the correlation describes a "z-shape" structure. The tropospheric CO end member for this part shows CO mixing ratios over 150 ppbv which is a distinct

marker for mixed pollution into the LMS.

In the correlation between total particle number concentration N_{UHSAS} versus N_2O (Fig. B1b), we identify a mirrored "C-shape" over the complete flight, which is also expected from previous studies in literature (e.g., Borrmann et al., 1993). Here, we observe a similar perturbation during the first pattern with particle number concentration exceeding the background values of the correlation and reaching up to tropospheric values.

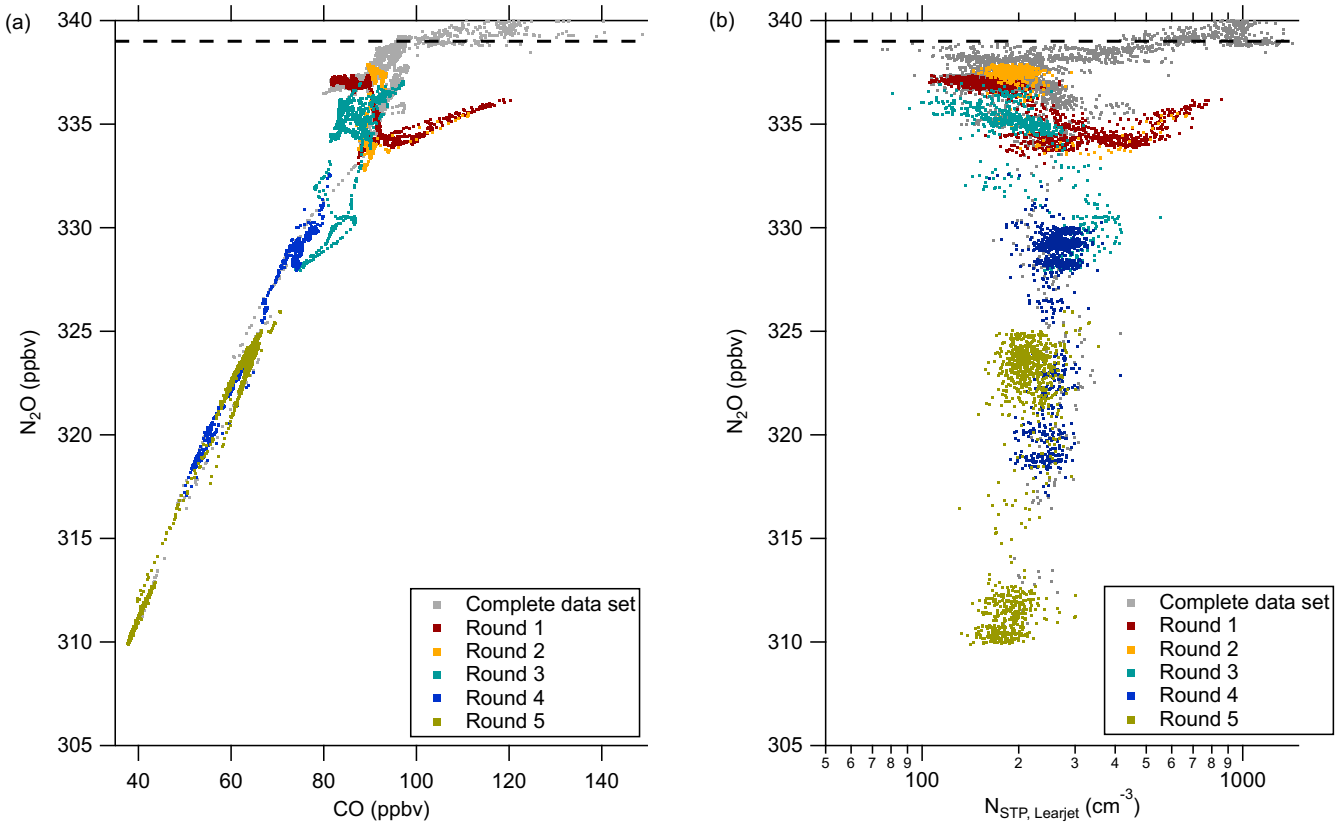

Figure B1. Tracer-Tracer correlation of CO vs. N_2O (a) and N vs. N_2O (b). The colorcode indicates the individual flight pattern in the restricted air space, each pattern is a separate round. The dashed line marks the chemical tropopause.

Appendix C: Definition of the analysis regions and averaging intervals

This section gives detailed information about the time intervals used for averaging the size distributions in Fig. 5 as well as the regions from Fig. 8. We chose 10 s, in order to represent only the main total number concentration peak of the polluted air masses for the size distributions. For comparison between the different measurement regions and events we used the 10 s for all intervals, even if enlarged periods for the background periods had been possible.

The following time periods are used for the averaged size distributions:

Event/Region	Times (UTC)
Pollution	07:25:27-07:25:37
UTLS background	07:26:05-07:26:15
Pollution	07:27:49-07:27:59
tropospheric background	07:32:48-07:32:58
Pollution	07:43:31-07:43:41
UTLS background	07:44:12-07:44:22
Pollution	07:46:32-07:46:42

Table C1. Time periods for the averaged size distributions shown in Fig. 5.

As a consequence of the 30 s time resolution of the AMS, there is no equal distribution of data points between the different measurement regions. The scale of the pollution streamers was too small for obtaining more than three AMS data points for each pollution event. The following time periods are used in the specific region definitions:

Region	Times (UTC)
Troposphere $N_2O > 336$ ppbv	07:20 - 07:23:30 07:30:30 - 07:40:30 07:49:00 - 08:00:00 09:18:30 - 09:30:00
UTLS $330 < N_2O < 336$ ppbv	07:24:00 - 07:25:00 07:26:30 - 07:27:30 07:29:00 - 07:30:00 07:41:00 - 07:42:30 07:44:30 - 07:46:00 07:47:30 - 07:48:30 08:00:00 - 08:05:00 08:16:30 - 08:21:00 09:08:30 - 09:18:00
Biomass Burning filament	07:25:30 - 07:26:00 07:28:00 - 07:28:30 07:43:00 - 07:44:00 07:46:30 - 07:47:00 08:05:30 - 08:16:00
LMS $325 < N_2O < 330$ ppbv	08:23:00 - 08:36:00
Stratosphere $325 > N_2O$	08:37:30 - 09:05:00

Table C2. Time periods for the averaged chemical composition measurements shown in Fig. 8.

Appendix D: Offline filter measurements

To obtain additional information on the organic particle composition, we use filter samples from the SOAP instrument. Note that the filter samples can not be allocated to certain positions of the aircraft, because of the long sampling periods of more than one hour for each filter. These extended periods were necessary to collect sufficient material on the filters, ensuring an adequate signal-to-noise ratio for the subsequent analysis. For this reason, small-scale pollution events are difficult to cover and challenging to detect. Not only the small-scale events but also the dilution within the atmosphere can lead to very low concentrations of certain compounds. Nevertheless, the sampled filters provide some indications of whether the air masses might be influenced by BB or not. For this purpose an analysis using high-resolution mass spectrometry for a selection of BB tracers was performed on the filter extracts. In our analysis these BB tracers are levoglucosan, 4-nitrophenol, phthalic acid and vanillic acid, which are already known as common tracers from previous studies (e.g., Simoneit and Elias, 2001; Bluvshtein et al., 2017; Wang et al., 2022). The sampling times of the filters are summarized in Tab.D1. For the analysis of the filter samples we also need to take Flight 08 into account, because the reference blank filter was also flown during F08. This flight took place directly after Flight 07 and probed partly the same air masses of the earlier flight over the North Sea and Western Germany. Still, the flight blank should provide information about any contamination that might have happened. Some more information on Flight 08 are given in appendix E.

Filter	Times (UTC)
F07, Filter 1	07:14 - 08:05; 09:10 - 09:31
F07, Filter 2	08:08 - 09:03
F08, Filter 1	11:25 - 12:58
F08, Filter 2	12:58 - 14:38

Table D1. Sampling times of SOAP filters during the double flight F07 and F08 on 17 June 2024. F07, Filter 1 corresponds to the time series in Fig. 3.

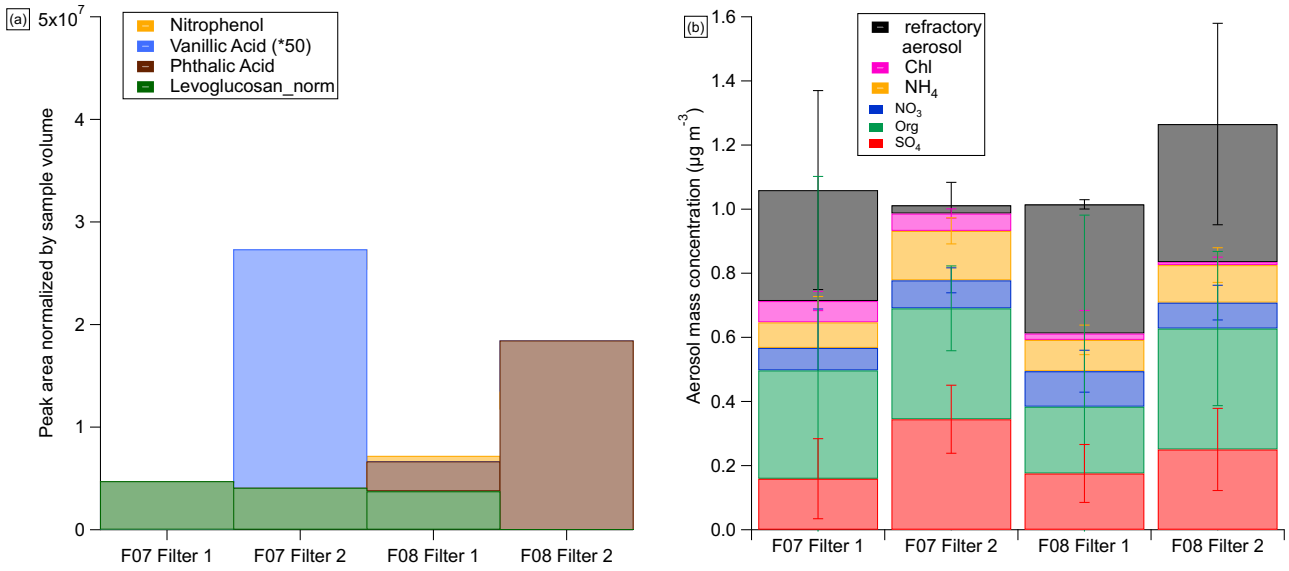

Figure D1. Results of filter analysis for BB species on the probed samples during the double flight on 17 June 2024. The signal of the flight blank was subtracted and the measurements were normalized according to the sampling volume (a). (b) the mean mass concentration, including the standard deviation, of the CARIBIC-AMS data and the estimated amount of rA for the sampling periods of the filter substrates.

A qualitative analysis of the four biomass burning tracers indicated that only two of the tracers were detected on the filter samples (Fig D1). The strongest signal occurs for phthalic acid during Flight 08 followed by a clear signal of vanillic acid during Flight 07. However, the detection of phthalic acid and vanillic acid does not coincide with the observed transient BB periods. Likely these events are too short to become visible by offline analysis. All data are blank corrected with the respective flight blank. A small signal of levoglucosan appears on three out of four samples. However, the levoglucosan results are uncertain due to high background concentrations on the blank filter. The long atmospheric transport of the BB plumes and short lifetimes of the organic species, especially for levoglucosan (0.5 up to 4 days (Hoffmann et al., 2009)), might also explain the low abundance of levoglucosan during the described events. Contamination of the filter substrates due to the double flight without the possibility to exchange the filters in between also resulted in significant blank signals that were subtracted from the samples. The flight blank shows significantly higher intensities than the solvent blank, which indicates that contamination might have occurred and improving sampling strategies is essential. Nevertheless, we can say with caution for the given reasons that the air masses which were probed on the 17 June 2024 show influence of BB to some extent, but there are differences in the processing of the air masses during the transport towards Europe.

Appendix E: Further information on F08

In this section of the appendix, we show some additional data from F08 as motivation to compare it with the presented flight F07. The flight pattern was from the North Sea towards Southwest Germany, close to Koblenz, along the tropopause and in the stratosphere to probe enhanced mixing. In the region over the North Sea the air masses are similar to the probed air masses in the morning flight.

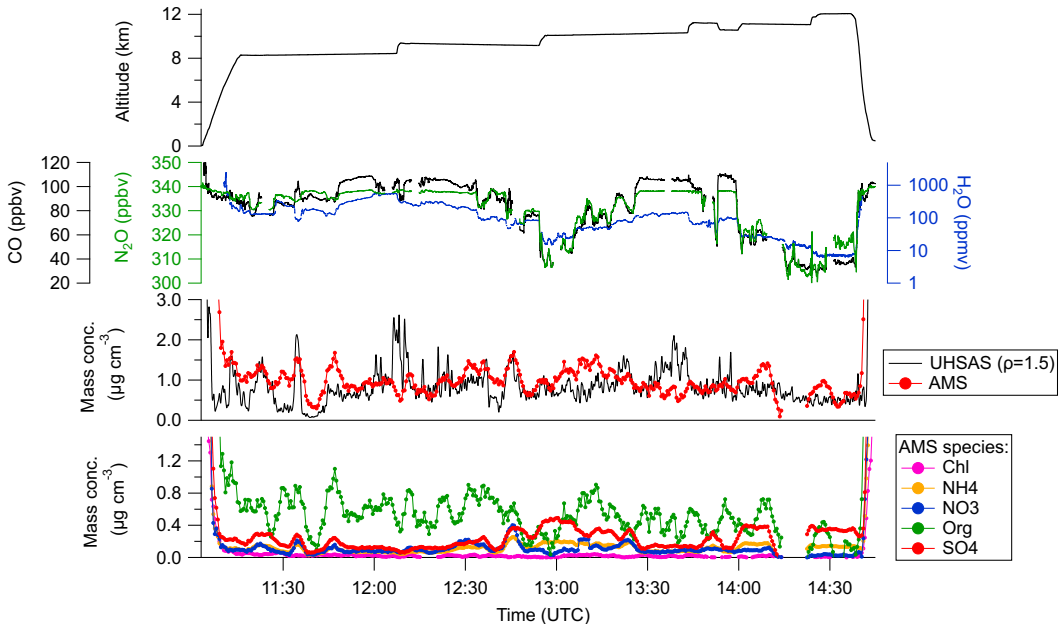

Figure E1. Time series of the in-situ measurements during F08 on 17 June 2024. The top panel shows the GPS altitude, the second panel shows in-situ trace gas measurements of CO (black), N_2O (green) and water vapor (blue). The third row shows the measured mass concentration by the AMS (red) and the UHSAS with a density estimation of 1.5 (black). The lowest panel displays the individual mass concentration from the AMS.

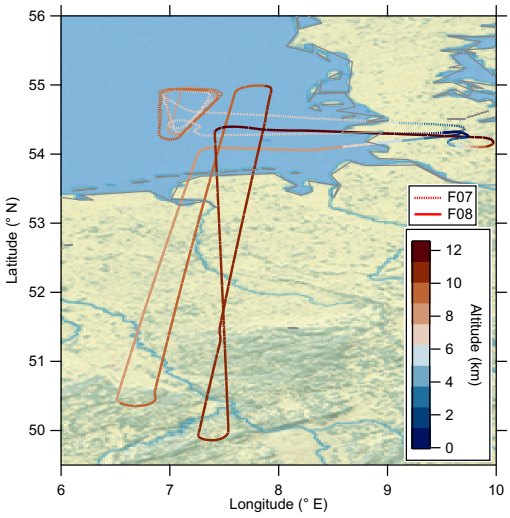

Figure E2. Flightpath of F07 (dashed) and F08 (solid) colorcoded with the GPS altitude.

Appendix F: Additional trajectory information

Here, we show the air mass history of the LAGRANTO trajectories for the single days before the measurement in the large frame with CAMS forecast data with a 0 h lead time for 00:00 UTC each day.

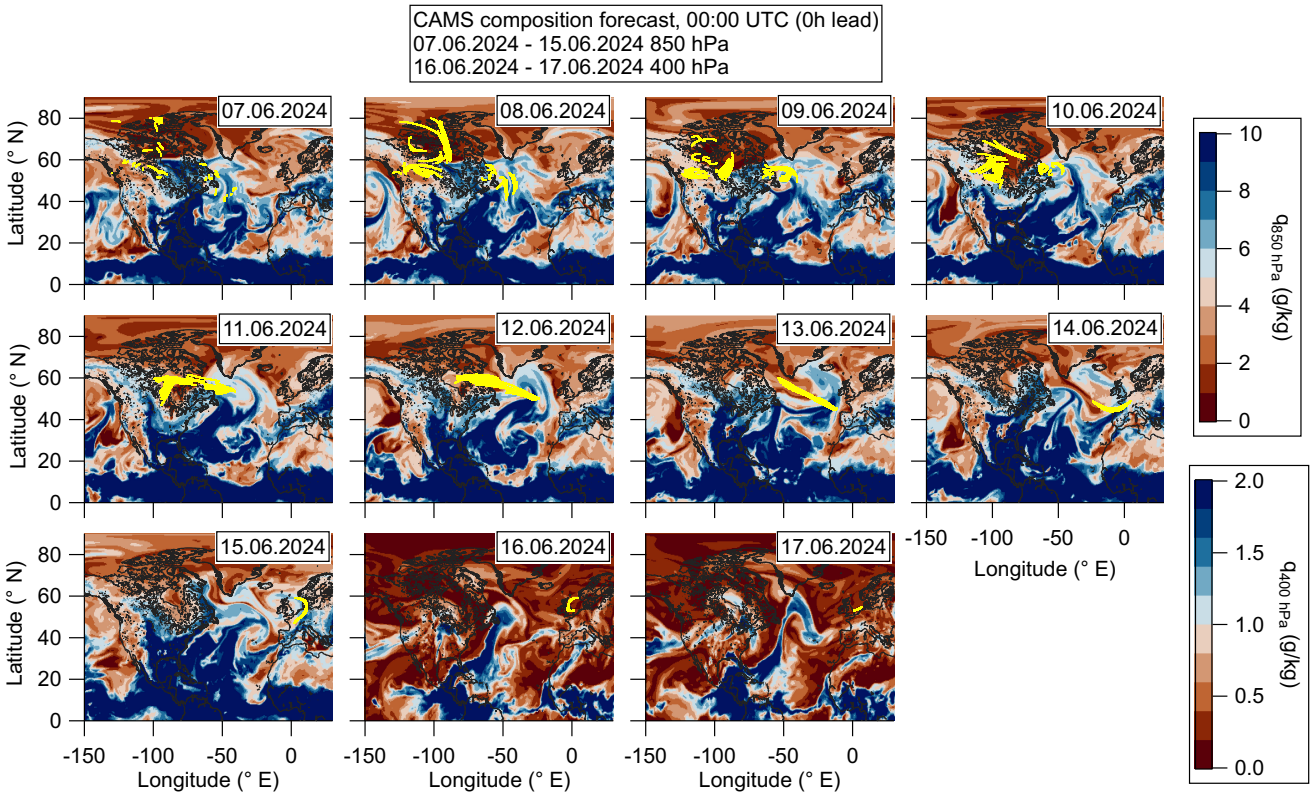

Figure F1. Combination of CAMS forecast data (colored background) and daily split trajectory data (yellow lines). All panels show the CAMS forecast with 0 h lead time for specific humidity (q) on 850 hPa (a-i) and 400 hPa (j-k). The trajectories are split for each 24 h interval to identify the large-scale context of the trajectories.

References

Alonso-Blanco, E., Calvo, A. I., Pont, V., Mallet, M., Fraile, R., and Castro, A.: Impact of Biomass Burning on Aerosol Size Distribution, Aerosol Optical Properties and Associated Radiative Forcing, Aerosol and Air Quality Research, 14, 708–724, https://doi.org/10.4209/aaqr.2013.05.0163, 2014.

Andersson, S. M., Martinsson, B. G., Vernier, J.-P., Friberg, J., Brenninkmeijer, C. A. M., Hermann, M., van Velthoven, P. F. J., and Zahn, A.: Significant radiative impact of volcanic aerosol in the lowermost stratosphere, Nature Communications, 6, https://doi.org/10.1038/ncomms8692, 2015.

Bahreini, R., Ervens, B., Middlebrook, A. M., Warneke, C., de Gouw, J. A., DeCarlo, P. F., Jimenez, J. L., Brock, C. A., Neuman, J. A., Ryerson, T. B., Stark, H., Atlas, E., Brioude, J., Fried, A., Holloway, J. S., Peischl, J., Richter, D., Walega, J., Weibring, P., Wollny, A. G., and Fehsenfeld, F. C.: Organic aerosol formation in urban and industrial plumes near Houston and Dallas, Texas, Journal of Geophysical Research: Atmospheres, 114, https://doi.org/10.1029/2008jd011493, 2009.

Benedetti, A., Morcrette, J., Boucher, O., Dethof, A., Engelen, R. J., Fisher, M., Flentje, H., Huneeus, N., Jones, L., Kaiser, J. W., Kinne, S., Mangold, A., Razinger, M., Simmons, A. J., and Suttie, M.: Aerosol analysis and forecast in the European Centre for Medium-Range Weather Forecasts Integrated Forecast System: 2. Data assimilation, Journal of Geophysical Research: Atmospheres, 114, https://doi.org/10.1029/2008jd011115, 2009.

Bethan, S., Vaughan, G., and Reid, S. J.: A comparison of ozone and thermal tropopause heights and the impact of tropopause definition on quantifying the ozone content of the troposphere, Quarterly Journal of the Royal Meteorological Society, 122, 929–944, https://doi.org/10.1002/qj.49712253207, 1996.

Bluvshtein, N., Lin, P., Flores, J. M., Segev, L., Mazar, Y., Tas, E., Snider, G., Weagle, C., Brown, S. S., Laskin, A., and Rudich, Y.: Broadband optical properties of biomass-burning aerosol and identification of brown carbon chromophores, Journal of Geophysical Research: Atmospheres, 122, 5441–5456, https://doi.org/10.1002/2016jd026230, 2017.

Borrmann, S., Dye, J. E., Baumgardner, D., Wilson, J. C., Jonsson, H. H., Brock, C. A., Loewenstein, M., Podolske, J. R., Ferry, G. V., and Barr, K. S.: In-situ measurements of changes in stratospheric aerosol and the Nsub2/subO-aerosol relationship inside and outside of the polar vortex, Geophysical Research Letters, 20, 2559–2562, https://doi.org/10.1029/93gl01694, 1993.

Bozem, H., Joppe, P., Li, Y., Emig, N., Afchine, A., Breuninger, A., Curtius, J., Hofmann, S., Ismayil, S., Kandler, K., Kunkel, D., Kutschka, A., Lachnitt, H.-C., Petzold, A., Richter, S., Röschenthaler, T., Rolf, C., Schneider, L., Schneider, J., Vogel, A., and Hoor, P.: The TropoPause Composition TOwed Sensor Shuttle (TPC-TOSS): A new airborne dual platform approach for atmospheric composition measurements at the tropopause, https://doi.org/10.5194/egusphere-2025-3175, 2025.

Breuninger, A., Joppe, P., Wilsch, J., Schwenk, C., Bozem, H., Emig, N., Merkel, L., Rossberg, R., Keber, T., Kutschka, A., Waleska, P., Hofmann, S., Richter, S., Ungeheuer, F., Dörholt, K., Hoffmann, T., Miltenberger, A., Schneider, J., Hoor, P., and Vogel, A. L.: Organic aerosols mixing across the tropopause and its implication for anthropogenic pollution of the UTLS, EGUsphere, 2025, 1–30, https://doi.org/10.5194/egusphere-2025-3129, 2025.

Brioude, J., Cooper, O. R., Trainer, M., Ryerson, T. B., Holloway, J. S., Baynard, T., Peischl, J., Warneke, C., Neuman, J. A., De Gouw, J., Stohl, A., Eckhardt, S., Frost, G. J., McKeen, S. A., Hsie, E.-Y., Fehsenfeld, F. C., and Nédélec, P.: Mixing between a stratospheric intrusion and a biomass burning plume, Atmospheric Chemistry and Physics, 7, 4229–4235, https://doi.org/10.5194/acp-7-4229-2007, 2007.

Brock, C. A., Froyd, K. D., Dollner, M., Williamson, C. J., Schill, G., Murphy, D. M., Wagner, N. J., Kupc, A., Jimenez, J. L., Campuzano-Jost, P., Nault, B. A., Schroder, J. C., Day, D. A., Price, D. J., Weinzierl, B., Schwarz, J. P., Katich, J. M., Wang, S., Zeng, L., Weber, R., Dibb, J., Scheuer, E., Diskin, G. S., DiGangi, J. P., Bui, T., Dean-Day, J. M., Thompson, C. R., Peischl, J., Ryerson, T. B., Bourgeois, I., Daube, B. C., Commane, R., and Wofsy, S. C.: Ambient aerosol properties in the remote atmosphere from global-scale in situ measurements, Atmospheric Chemistry and Physics, 21, 15 023–15 063, https://doi.org/10.5194/acp-21-15023-2021, 2021.

Cai, Y., Montague, D. C., Mooiweer-Bryan, W., and Deshler, T.: Performance characteristics of the ultra high sensitivity aerosol spectrometer for particles between 55 and 800nm: Laboratory and field studies, Journal of Aerosol Science, 39, 759–769, https://doi.org/10.1016/j.jaerosci.2008.04.007, 2008.

Canagaratna, M., Jayne, J., Jimenez, J., Allan, J., Alfarra, M., Zhang, Q., Onasch, T., Drewnick, F., Coe, H., Middlebrook, A., Delia, A., Williams, L., Trimborn, A., Northway, M., DeCarlo, P., Kolb, C., Davidovits, P., and Worsnop, D.: Chemical and microphysical characterization of ambient aerosols with the aerodyne aerosol mass spectrometer, Mass Spectrometry Reviews, 26, 185–222, https://doi.org/10.1002/mas.20115, 2007.

Cooper, O. R., Forster, C., Parrish, D., Trainer, M., Dunlea, E., Ryerson, T., Hübler, G., Fehsenfeld, F., Nicks, D., Holloway, J., de Gouw, J., Warneke, C., Roberts, J. M., Flocke, F., and Moody, J.: A case study of transpacific warm conveyor belt transport: Influence of merging airstreams on trace gas import to North America, Journal of Geophysical Research: Atmospheres, 109, https://doi.org/10.1029/2003jd003624, 2004.

Curtius, J., Heinritzi, M., Beck, L. J., Pöhlker, M. L., Tripathi, N., Krumm, B. E., Holzbeck, P., Nussbaumer, C. M., Hernández Pardo, L., Klimach, T., Barmpounis, K., Andersen, S. T., Bardakov, R., Bohn, B., Cecchini, M. A., Chaboureau, J.-P., Dauhut, T., Dienhart, D., Dörich, R., Edtbauer, A., Giez, A., Hartmann, A., Holanda, B. A., Joppe, P., Kaiser, K., Keber, T., Klebach, H., Krüger, O. O., Kürten, A., Mallaun, C., Marno, D., Martinez, M., Monteiro, C., Nelson, C., Ort, L., Raj, S. S., Richter, S., Ringsdorf, A., Rocha, F., Simon, M., Sreekumar, S., Tsokankunku, A., Unfer, G. R., Valenti, I. D., Wang, N., Zahn, A., Zauner-Wieczorek, M., Albrecht, R. I., Andreae, M. O., Artaxo, P., Crowley, J. N., Fischer, H., Harder, H., Herdies, D. L., Machado, L. A. T., Pöhlker, C., Pöschl, U., Possner, A., Pozzer, A., Schneider, J., Williams, J., and Lelieveld, J.: Isoprene nitrates drive new particle formation in Amazon's upper troposphere, Nature, 636, 124–130, https://doi.org/10.1038/s41586-024-08192-4, 2024.

Dang, C., Segal-Rozenhaimer, M., Che, H., Zhang, L., Formenti, P., Taylor, J., Dobracki, A., Purdue, S., Wong, P.-S., Nenes, A., Sedlacek III, A., Coe, H., Redemann, J., Zuidema, P., Howell, S., and Haywood, J.: Biomass burning and marine aerosol processing over the southeast Atlantic Ocean: a TEM single-particle analysis, Atmospheric Chemistry and Physics, 22, 9389–9412, https://doi.org/10.5194/acp-22-9389-2022, 2022.

Ditas, J., Ma, N., Zhang, Y., Assmann, D., Neumaier, M., Riede, H., Karu, E., Williams, J., Scharffe, D., Wang, Q., Saturno, J., Schwarz, J. P., Katich, J. M., McMeeking, G. R., Zahn, A., Hermann, M., Brenninkmeijer, C. A. M., Andreae, M. O., Pöschl, U., Su, H., and Cheng, Y.: Strong impact of wildfires on the abundance and aging of black carbon in the lowermost stratosphere, Proceedings of the National Academy of Sciences, 115, https://doi.org/10.1073/pnas.1806868115, 2018.

Ebert, M., Weigel, R., Kandler, K., Günther, G., Molleker, S., Grooß, J.-U., Vogel, B., Weinbruch, S., and Borrmann, S.: Chemical analysis of refractory stratospheric aerosol particles collected within the arctic vortex and inside polar stratospheric clouds, Atmospheric Chemistry and Physics, 16, 8405–8421, https://doi.org/10.5194/acp-16-8405-2016, 2016.

Finger, F., Werner, F., Klingebiel, M., Ehrlich, A., Jäkel, E., Voigt, M., Borrmann, S., Spichtinger, P., and Wendisch, M.: Spectral optical layer properties of cirrus from collocated airborne measurements and simulations, Atmospheric Chemistry and Physics, 16, 7681–7693, https://doi.org/10.5194/acp-16-7681-2016, 2016.

Frey, W., Eichler, H., de Reus, M., Maser, R., Wendisch, M., and Borrmann, S.: A new airborne tandem platform for collocated measurements of microphysical cloud and radiation properties, Atmospheric Measurement Techniques, 2, 147–158, https://doi.org/10.5194/amt-2-147-2009, 2009.

Fromm, M., Lindsey, D. T., Servranckx, R., Yue, G., Trickl, T., Sica, R., Doucet, P., and Godin-Beekmann, S.: The Untold Story of Pyrocumulonimbus, Bulletin of the American Meteorological Society, 91, 1193–1210, https://doi.org/10.1175/2010bams3004.1, 2010.

Fromm, M., Kablick, G., and Caffrey, P.: Dust-infused baroclinic cyclone storm clouds: The evidence, meteorology, and some implications, Geophysical Research Letters, 43, https://doi.org/10.1002/2016gl071801, 2016.

Froyd, K. D., Murphy, D. M., Sanford, T. J., Thomson, D. S., Wilson, J. C., Pfister, L., and Lait, L.: Aerosol composition of the tropical upper troposphere, Atmospheric Chemistry and Physics, 9, 4363–4385, https://doi.org/10.5194/acp-9-4363-2009, 2009.

Fueglistaler, S., Dessler, A. E., Dunkerton, T. J., Folkins, I., Fu, Q., and Mote, P. W.: Tropical tropopause layer, Reviews of Geophysics, 47, https://doi.org/10.1029/2008rg000267, 2009.

Harrold, T. W.: Mechanisms influencing the distribution of precipitation within baroclinic disturbances, Quarterly Journal of the Royal Meteorological Society, 99, 232–251, https://doi.org/10.1002/qj.49709942003, 1973.

Heitmann, K., Sprenger, M., Binder, H., Wernli, H., and Joos, H.: Warm conveyor belt characteristics and impacts along the life cycle of extratropical cyclones: case studies and climatological analysis based on ERA5, Weather and Climate Dynamics, 5, 537–557, https://doi.org/10.5194/wcd-5-537-2024, 2024.

Helten, M., Smit, H., Sträter, W., Kley, D., Nedelec, P., Zöger, M., and Busen, R.: Calibration and performance of automatic compact instrumentation for the measurement of relative humidity from passenger aircraft, Journal of Geophysical Research: Atmospheres, 103, 25 643–25 652, https://doi.org/10.1029/98jd00536, 1998.

Hoffmann, D., Tilgner, A., Iinuma, Y., and Herrmann, H.: Atmospheric Stability of Levoglucosan: A Detailed Laboratory and Modeling Study, Environmental Science amp; Technology, 44, 694–699, https://doi.org/10.1021/es902476f, 2009.

Holanda, B. A., Franco, M. A., Walter, D., Artaxo, P., Carbone, S., Cheng, Y., Chowdhury, S., Ditas, F., Gysel-Beer, M., Klimach, T., Kremper, L. A., Krüger, O. O., Lavric, J. V., Lelieveld, J., Ma, C., Machado, L. A. T., Modini, R. L., Morais, F. G., Pozzer, A., Saturno, J., Su, H., Wendisch, M., Wolff, S., Pöhlker, M. L., Andreae, M. O., Pöschl, U., and Pöhlker, C.: African biomass burning affects aerosol cycling over the Amazon, Communications Earth amp; Environment, 4, https://doi.org/10.1038/s43247-023-00795-5, 2023.

Johnson, T., Capel, J., and Ollison, W.: Measurement of microenvironmental ozone concentrations in Durham, North Carolina, using a 2B Technologies 205 Federal Equivalent Method monitor and an interference-free 2B Technologies 211 monitor, J. Air Waste Manage. Assoc., 64, 360–371, https://doi.org/10.1080/10962247.2013.839968, 2014.

Joppe, P., Schneider, J., Kaiser, K., Fischer, H., Hoor, P., Kunkel, D., Lachnitt, H.-C., Marsing, A., Röder, L., Schlager, H., Tomsche, L., Voigt, C., Zahn, A., and Borrmann, S.: The influence of extratropical cross-tropopause mixing on the correlation between ozone and sulfate aerosol in the lowermost stratosphere, Atmospheric Chemistry and Physics, 24, 7499–7522, https://doi.org/10.5194/acp-24-7499-2024, 2024.

Junge, C. E., Chagnon, C. W., and Manson, J. E.: STRATOSPHERIC AEROSOLS, Journal of Meteorology, 18, 81–108, https://doi.org/10.1175/1520-0469(1961)018<0081:sa>2.0.co;2, 1961.

Kaiser, J. W., Heil, A., Andreae, M. O., Benedetti, A., Chubarova, N., Jones, L., Morcrette, J.-J., Razinger, M., Schultz, M. G., Suttie, M., and van der Werf, G. R.: Biomass burning emissions estimated with a global fire assimilation system based on observed fire radiative power, Biogeosciences, 9, 527–554, https://doi.org/10.5194/bg-9-527-2012, 2012.

Kalisoras, A., Georgoulias, A. K., Akritidis, D., Allen, R. J., Naik, V., Kuo, C., Szopa, S., Nabat, P., Olivié, D., van Noije, T., Le Sager, P., Neubauer, D., Oshima, N., Mulcahy, J., Horowitz, L. W., and Zanis, P.: Decomposing the effective radiative forcing of anthropogenic aerosols based on CMIP6 Earth system models, Atmospheric Chemistry and Physics, 24, 7837–7872, https://doi.org/10.5194/acp-24-7837-2024, 2024.

Kaluza, T., Kunkel, D., and Hoor, P.: On the occurrence of strong vertical wind shear in the tropopause region: a 10-year ERA5 northern hemispheric study, Weather and Climate Dynamics, 2, 631–651, https://doi.org/10.5194/wcd-2-631-2021, 2021.

Kaluza, T., Kunkel, D., and Hoor, P.: Analysis of turbulence reports and ERA5 turbulence diagnostics in a tropopause-based vertical framework, Geophysical Research Letters, https://doi.org/10.1029/2022gl100036, 2022.

Khaykin, S., Bekki, S., Godin-Beekmann, S., Fromm, M. D., Goloub, P., Hu, Q., Josse, B., Laeng, A., Meziane, M., Peterson, D. A., Pelletier, S., and Thouret, V.: Stratospheric impact of the anomalous 2023 Canadian wildfires: the two vertical pathways of smoke, https://doi.org/10.5194/egusphere-2025-3152, 2025.

Klingebiel, M., Ehrlich, A., Finger, F., Röschenthaler, T., Jakirlić, S., Voigt, M., Müller, S., Maser, R., Wendisch, M., Hoor, P., Spichtinger, P., and Borrmann, S.: A tandem approach for collocated measurements of microphysical and radiative cirrus properties, Atmospheric Measurement Techniques, 10, 3485–3498, https://doi.org/10.5194/amt-10-3485-2017, 2017.

Krause, J., Hoor, P., Engel, A., Plöger, F., Grooß, J.-U., Bönisch, H., Keber, T., Sinnhuber, B.-M., Woiwode, W., and Oelhaf, H.: Mixing and ageing in the polar lower stratosphere in winter 2015–2016, Atmospheric Chemistry and Physics, 18, 6057–6073, https://doi.org/10.5194/acp-18-6057-2018, 2018.

Kremser, S., Thomason, L. W., von Hobe, M., Hermann, M., Deshler, T., Timmreck, C., Toohey, M., Stenke, A., Schwarz, J. P., Weigel, R., Fueglistaler, S., Prata, F. J., Vernier, J.-P., Schlager, H., Barnes, J. E., Antuña-Marrero, J.-C., Fairlie, D., Palm, M., Mahieu, E., Notholt, J., Rex, M., Bingen, C., Vanhellemont, F., Bourassa, A., Plane, J. M. C., Klocke, D., Carn, S. A., Clarisse, L., Trickl, T., Neely, R., James, A. D., Rieger, L., Wilson, J. C., and Meland, B.: Stratospheric aerosol-Observations, processes, and impact on climate: Stratospheric Aerosol, Reviews of Geophysics, 54, 278–335, https://doi.org/10.1002/2015rg000511, 2016.

Kunkel, D., Hoor, P., Kaluza, T., Ungermann, J., Kluschat, B., Giez, A., Lachnitt, H.-C., Kaufmann, M., and Riese, M.: Evidence of small-scale quasi-isentropic mixing in ridges of extratropical baroclinic waves, Atmospheric Chemistry and Physics, 19, 12 607–12 630, https://doi.org/10.5194/acp-19-12607-2019, 2019.

Kunz, A., Konopka, P., Müller, R., and Pan, L. L.: Dynamical tropopause based on isentropic potential vorticity gradients, Journal of Geophysical Research, 116, https://doi.org/10.1029/2010jd014343, 2011.

Kupc, A., Williamson, C., Wagner, N. L., Richardson, M., and Brock, C. A.: Modification, calibration, and performance of the Ultra-High Sensitivity Aerosol Spectrometer for particle size distribution and volatility measurements during the Atmospheric Tomography Mission (ATom) airborne campaign, Atmospheric Measurement Techniques, 11, 369–383, https://doi.org/10.5194/amt-11-369-2018, 2018.

Lachnitt, H.-C.: TPEx 2024 observational data and model data along flight path - Merged, https://doi.org/10.5281/ZENODO.15371527, 2025.

Lachnitt, H.-C., Hoor, P., Kunkel, D., Bramberger, M., Dörnbrack, A., Müller, S., Reutter, P., Giez, A., Kaluza, T., and Rapp, M.: Gravity-wave-induced cross-isentropic mixing: a DEEPWAVE case study, Atmospheric Chemistry and Physics, 23, 355–373, https://doi.org/10.5194/acp-23-355-2023, 2023.

Lary, D. J., Chipperfield, M. P., Pyle, J. A., Norton, W. A., and Riishøjgaard, L. P.: Three-dimensional tracer initialization and general diagnostics using equivalent PV latitude–potential-temperature coordinates, Quarterly Journal of the Royal Meteorological Society, 121, 187–210, https://doi.org/10.1002/qj.49712152109, 1995.

Li, J., Pósfai, M., Hobbs, P. V., and Buseck, P. R.: Individual aerosol particles from biomass burning in southern Africa: 2, Compositions and aging of inorganic particles, Journal of Geophysical Research: Atmospheres, 108, https://doi.org/10.1029/2002jd002310, 2003.

Ma, C., Su, H., Lelieveld, J., Randel, W., Yu, P., Andreae, M. O., and Cheng, Y.: Smoke-charged vortex doubles hemispheric aerosol in the middle stratosphere and buffers ozone depletion, Science Advances, 10, https://doi.org/10.1126/sciadv.adn3657, 2024.

Ma, J., Ungeheuer, F., Zheng, F., Du, W., Wang, Y., Cai, J., Zhou, Y., Yan, C., Liu, Y., Kulmala, M., Daellenbach, K. R., and Vogel, A. L.: Nontarget Screening Exhibits a Seasonal Cycle of PM $_{2.5}$ Organic Aerosol Composition in Beijing, Environmental Science & Technology, 56, 7017–7028, https://doi.org/10.1021/acs.est.1c06905, 2022.

Madonna, E., Wernli, H., Joos, H., and Martius, O.: Warm Conveyor Belts in the ERA-Interim Dataset (1979–2010). Part I: Climatology and Potential Vorticity Evolution, Journal of Climate, 27, 3–26, https://doi.org/10.1175/jcli-d-12-00720.1, 2014.

Mahnke, C., Weigel, R., Cairo, F., Vernier, J.-P., Afchine, A., Krämer, M., Mitev, V., Matthey, R., Viciani, S., D'Amato, F., Ploeger, F., Deshler, T., and Borrmann, S.: The Asian tropopause aerosol layer within the 2017 monsoon anticyclone: microphysical properties derived from aircraft-borne in situ measurements, Atmospheric Chemistry and Physics, 21, 15 259–15 282, https://doi.org/10.5194/acp-21-15259-2021, 2021.

Marelle, L., Raut, J.-C., Thomas, J. L., Law, K. S., Quennehen, B., Ancellet, G., Pelon, J., Schwarzenboeck, A., and Fast, J. D.: Transport of anthropogenic and biomass burning aerosols from Europe to the Arctic during spring 2008, Atmospheric Chemistry and Physics, 15, 3831–3850, https://doi.org/10.5194/acp-15-3831-2015, 2015.

Masson-Delmotte, V., Zhai, P., Pirani, A., Connors, S., Péan, C., Berger, S., Caud, N., Chen, Y., Goldfarb, L., Gomis, M., Huang, M., Leitzell, K., Lonnoy, E., Matthews, J., Maycock, T., Waterfield, T., Yelekçi, O., Yu, R., and Zhou, B. e.: IPCC, 2021: Climate Change 2021: The Physical Science Basis: Working Group I Contribution to the Sixth Assessment Report of the Intergovernmental Panel on Climate Change, Cambridge University Press, United Kingdom and New York, NY, USA, https://doi.org/10.1017/9781009157896, 2023.

Meyer, J., Rolf, C., Schiller, C., Rohs, S., Spelten, N., Afchine, A., Zöger, M., Sitnikov, N., Thornberry, T. D., Rollins, A. W., Bozóki, Z., Tátrai, D., Ebert, V., Kühnreich, B., Mackrodt, P., Möhler, O., Saathoff, H., Rosenlof, K. H., and Krämer, M.: Two decades of water vapor measurements with the FISH fluorescence hygrometer: a review, Atmospheric Chemistry and Physics, 15, 8521–8538, https://doi.org/10.5194/acp-15-8521-2015, 2015.

Miltenberger, A.: TPEx-F07-LAGRANTO-10days-trajectories, https://doi.org/10.5281/ZENODO.16262949, 2025.

Moore, R. H., Wiggins, E. B., Ahern, A. T., Zimmerman, S., Montgomery, L., Campuzano Jost, P., Robinson, C. E., Ziemba, L. D., Winstead, E. L., Anderson, B. E., Brock, C. A., Brown, M. D., Chen, G., Crosbie, E. C., Guo, H., Jimenez, J. L., Jordan, C. E., Lyu, M., Nault, B. A., Rothfuss, N. E., Sanchez, K. J., Schueneman, M., Shingler, T. J., Shook, M. A., Thornhill, K. L., Wagner, N. L., and Wang, J.: Sizing response of the Ultra-High Sensitivity Aerosol Spectrometer (UHSAS) and Laser Aerosol Spectrometer (LAS) to changes in submicron aerosol composition and refractive index, Atmospheric Measurement Techniques, 14, 4517–4542, https://doi.org/10.5194/amt-14-4517-2021, 2021.

Morcrette, J., Boucher, O., Jones, L., Salmond, D., Bechtold, P., Beljaars, A., Benedetti, A., Bonet, A., Kaiser, J. W., Razinger, M., Schulz, M., Serrar, S., Simmons, A. J., Sofiev, M., Suttie, M., Tompkins, A. M., and Untch, A.: Aerosol analysis and forecast in the European Centre for Medium-Range Weather Forecasts Integrated Forecast System: Forward modeling, Journal of Geophysical Research: Atmospheres, 114, https://doi.org/10.1029/2008jd011235, 2009.

Müller, S., Hoor, P., Berkes, F., Bozem, H., Klingebiel, M., Reutter, P., Smit, H. G. J., Wendisch, M., Spichtinger, P., and Borrmann, S.: In situ detection of stratosphere-troposphere exchange of cirrus particles in the midlatitudes, Geophysical Research Letters, 42, 949–955, https://doi.org/10.1002/2014gl062556, 2015.

Murphy, D. M., Cziczo, D. J., Hudson, P. K., and Thomson, D. S.: Carbonaceous material in aerosol particles in the lower stratosphere and tropopause region, Journal of Geophysical Research: Atmospheres, 112, https://doi.org/10.1029/2006jd007297, 2007.

Peterson, D. A., Fromm, M. D., McRae, R. H. D., Campbell, J. R., Hyer, E. J., Taha, G., Camacho, C. P., Kablick, G. P., Schmidt, C. C., and DeLand, M. T.: Australia's Black Summer pyrocumulonimbus super outbreak reveals potential for increasingly extreme stratospheric smoke events, npj Climate and Atmospheric Science, 4, https://doi.org/10.1038/s41612-021-00192-9, 2021.

Petzold, A., Thouret, V., Gerbig, C., Zahn, A., Brenninkmeijer, C. A. M., Gallagher, M., Hermann, M., Pontaud, M., Ziereis, H., Boulanger, D., Marshall, J., Nédélec, P., Smit, H. G. J., Friess, U., Flaud, J.-M., Wahner, A., Cammas, J.-P., Volz-Thomas, A., and Team, I.: Global-scale atmosphere monitoring by in-service aircraft – current achievements and future prospects of the European Research Infrastructure IAGOS, Tellus B: Chemical and Physical Meteorology, 67, 28 452, https://doi.org/10.3402/tellusb.v67.28452, 2015.

Ploeger, F., Diallo, M., Charlesworth, E., Konopka, P., Legras, B., Laube, J. C., Grooß, J.-U., Günther, G., Engel, A., and Riese, M.: The stratospheric Brewer–Dobson circulation inferred from age of air in the ERA5 reanalysis, Atmospheric Chemistry and Physics, 21, 8393–8412, https://doi.org/10.5194/acp-21-8393-2021, 2021.

Räisänen, P., Merikanto, J., Makkonen, R., Savolahti, M., Kirkevåg, A., Sand, M., Seland, , and Partanen, A.-I.: Mapping the dependence of black carbon radiative forcing on emission region and season, Atmospheric Chemistry and Physics, 22, 11 579–11 602, https://doi.org/10.5194/acp-22-11579-2022, 2022.

Ramanathan, V. and Carmichael, G.: Global and regional climate changes due to black carbon, Nature Geoscience, 1, 221–227, https://doi.org/10.1038/ngeo156, 2008.

Resch, J., Wolfer, K., Barth, A., and Kalberer, M.: Effects of storage conditions on molecular-level composition of organic aerosol particles, EGUsphere, 2023, 1–20, publisher: Copernicus Publications Göttingen, Germany, 2023.

Riese, M., Ploeger, F., Rap, A., Vogel, B., Konopka, P., Dameris, M., and Forster, P.: Impact of uncertainties in atmospheric mixing on simulated UTLS composition and related radiative effects, Journal of Geophysical Research: Atmospheres, 117, https://doi.org/10.1029/2012jd017751, 2012.

Rémy, S., Veira, A., Paugam, R., Sofiev, M., Kaiser, J. W., Marenco, F., Burton, S. P., Benedetti, A., Engelen, R. J., Ferrare, R., and Hair, J. W.: Two global data sets of daily fire emission injection heights since 2003, Atmospheric Chemistry and Physics, 17, 2921–2942, https://doi.org/10.5194/acp-17-2921-2017, 2017.

Rémy, S., Kipling, Z., Flemming, J., Boucher, O., Nabat, P., Michou, M., Bozzo, A., Ades, M., Huijnen, V., Benedetti, A., Engelen, R., Peuch, V.-H., and Morcrette, J.-J.: Description and evaluation of the tropospheric aerosol scheme in the European Centre for Medium-Range Weather Forecasts (ECMWF) Integrated Forecasting System (IFS-AER, cycle 45R1), Geoscientific Model Development, 12, 4627–4659, https://doi.org/10.5194/gmd-12-4627-2019, 2019.

Schill, G. P., Froyd, K. D., Murphy, D. M., Kupc, A., Williamson, C., Brock, C. A., Ray, E. A., Chin, M., and Colarco, P. R.: Size Distributions of Biomass Burning Aerosol as a Function of Age and Comparisons to Models, in: AGU Fall Meeting, pp. A26D–02, American Geophysical Union, Chicago, IL, https://agu.confex.com/agu/fm22/meetingapp.cgi/Paper/1196947, 2022.

Schneider, J., Schulz, C., Rubach, F., Ludwig, A., Wilsch, J., Joppe, P., Gurk, C., Molleker, S., Poulain, L., Obersteiner, F., Gehrlein, T., Bönisch, H., Zahn, A., Hoor, P., Emig, N., Bozem, H., Borrmann, S., and Hermann, M.: CARIBIC-AMS: A fully automated aerosol mass spectrometer for operation on routine passenger flights (IAGOS-CARIBIC): Instrument description and first flight application in the UTLS, https://doi.org/10.5194/egusphere-2024-3969, 2025.

Schwarz, J. P., Spackman, J. R., Fahey, D. W., Gao, R. S., Lohmann, U., Stier, P., Watts, L. A., Thomson, D. S., Lack, D. A., Pfister, L., Mahoney, M. J., Baumgardner, D., Wilson, J. C., and Reeves, J. M.: Coatings and their enhancement of black carbon light absorption in the tropical atmosphere, Journal of Geophysical Research: Atmospheres, 113, https://doi.org/10.1029/2007jd009042, 2008.

Schwenk, C. and Miltenberger, A.: The role of ascent timescales for warm conveyor belt (WCB) moisture transport into the upper troposphere and lower stratosphere (UTLS), Atmospheric Chemistry and Physics, 24, 14 073–14 099, https://doi.org/10.5194/acp-24-14073-2024, 2024.

Simoneit, B. R. and Elias, V.: Detecting Organic Tracers from Biomass Burning in the Atmosphere, Marine Pollution Bulletin, 42, 805–810, https://doi.org/10.1016/s0025-326x(01)00094-7, 2001.

Smit, H. G. J., Rohs, S., Neis, P., Boulanger, D., Krämer, M., Wahner, A., and Petzold, A.: Technical Note: Reanalysis of upper troposphere humidity data from the MOZAIC programme for the period 1994 to 2009, Atmospheric Chemistry and Physics, 14, 13 241–13 255, https://doi.org/10.5194/acp-14-13241-2014, 2014.

Sprenger, M. and Wernli, H.: The LAGRANTO Lagrangian analysis tool – version 2.0, Geoscientific Model Development, 8, 2569–2586, https://doi.org/10.5194/gmd-8-2569-2015, 2015.

Theodoritsi, G. N. and Pandis, S. N.: Simulation of the chemical evolution of biomass burning organic aerosol, Atmospheric Chemistry and Physics, 19, 5403–5415, https://doi.org/10.5194/acp-19-5403-2019, 2019.

Thoma, M., Bachmeier, F., Gottwald, F. L., Simon, M., and Vogel, A. L.: Mass spectrometry-based *Aerosolomics* : a new approach to resolve sources, composition, and partitioning of secondary organic aerosol, Atmospheric Measurement Techniques, 15, 7137–7154, https://doi.org/10.5194/amt-15-7137-2022, 2022.

Tinney, E. N., Homeyer, C. R., Elizalde, L., Hurst, D. F., Thompson, A. M., Stauffer, R. M., Vömel, H., and Selkirk, H. B.: A Modern Approach to a Stability-Based Definition of the Tropopause, Monthly Weather Review, 150, 3151–3174, https://doi.org/10.1175/mwr-d-22-0174.1, 2022.

Trickl, T., Vogelmann, H., Fromm, M. D., Jäger, H., Perfahl, M., and Steinbrecht, W.: Measurement report: Violent biomass burning and volcanic eruptions – a new period of elevated stratospheric aerosol over central Europe (2017 to 2023) in a long series of observations, Atmospheric Chemistry and Physics, 24, 1997–2021, https://doi.org/10.5194/acp-24-1997-2024, 2024.

Turhal, K., Plöger, F., Clemens, J., Birner, T., Weyland, F., Konopka, P., and Hoor, P.: Variability and trends in the potential vorticity (PV)-gradient dynamical tropopause, Atmospheric Chemistry and Physics, 24, 13 653–13 679, https://doi.org/10.5194/acp-24-13653-2024, 2024.

Ungeheuer, F., Van Pinxteren, D., and Vogel, A. L.: Identification and source attribution of organic compounds in ultrafine particles near Frankfurt International Airport, Atmospheric Chemistry and Physics, 21, 3763–3775, https://doi.org/10.5194/acp-21-3763-2021, 2021.

Voigt, C., Schumann, U., Minikin, A., Abdelmonem, A., Afchine, A., Borrmann, S., Boettcher, M., Buchholz, B., Bugliaro, L., Costa, A., Curtius, J., Dollner, M., Dörnbrack, A., Dreiling, V., Ebert, V., Ehrlich, A., Fix, A., Forster, L., Frank, F., Fütterer, D., Giez, A., Graf, K., Grooß, J.-U., Groß, S., Heimerl, K., Heinold, B., Hüneke, T., Järvinen, E., Jurkat, T., Kaufmann, S., Kenntner, M., Klingebiel, M., Klimach, T., Kohl, R., Krämer, M., Krisna, T. C., Luebke, A., Mayer, B., Mertes, S., Molleker, S., Petzold, A., Pfeilsticker, K., Port, M., Rapp, M., Reutter, P., Rolf, C., Rose, D., Sauer, D., Schäfler, A., Schlage, R., Schnaiter, M., Schneider, J., Spelten, N., Spichtinger, P., Stock, P., Walser, A., Weigel, R., Weinzierl, B., Wendisch, M., Werner, F., Wernli, H., Wirth, M., Zahn, A., Ziereis, H., and Zöger, M.: ML-CIRRUS: The Airborne Experiment on Natural Cirrus and Contrail Cirrus with the High-Altitude Long-Range Research Aircraft HALO, Bulletin of the American Meteorological Society, 98, 271–288, https://doi.org/10.1175/bams-d-15-00213.1, 2017.

von der Weiden, S.-L., Drewnick, F., and Borrmann, S.: Particle Loss Calculator – a new software tool for the assessment of the performance of aerosol inlet systems, Atmospheric Measurement Techniques, 2, 479–494, https://doi.org/10.5194/amt-2-479-2009, 2009.

von Hobe, M., Ploeger, F., Konopka, P., Kloss, C., Ulanowski, A., Yushkov, V., Ravegnani, F., Volk, C. M., Pan, L. L., Honomichl, S. B., Tilmes, S., Kinnison, D. E., Garcia, R. R., and Wright, J. S.: Upward transport into and within the Asian monsoon anticyclone as inferred from StratoClim trace gas observations, Atmospheric Chemistry and Physics, 21, 1267–1285, https://doi.org/10.5194/acp-21-1267-2021, 2021.

Wang, Q., Wang, S., Cheng, Y. Y., Chen, H., Zhang, Z., Li, J., Gu, D., Wang, Z., and Yu, J. Z.: Chemical evolution of secondary organic aerosol tracers during high-PM2.5 episodes at a suburban site in Hong Kong over 4 months of continuous measurement, Atmospheric Chemistry and Physics, 22, 11 239–11 253, https://doi.org/10.5194/acp-22-11239-2022, 2022.

Yu, P., Toon, O. B., Bardeen, C. G., Zhu, Y., Rosenlof, K. H., Portmann, R. W., Thornberry, T. D., Gao, R.-S., Davis, S. M., Wolf, E. T., de Gouw, J., Peterson, D. A., Fromm, M. D., and Robock, A.: Black carbon lofts wildfire smoke high into the stratosphere to form a persistent plume, Science, 365, 587–590, https://doi.org/10.1126/science.aax1748, 2019.

Yue, G. K.: The formation and growth of sulfate aerosols in the stratosphere, Atmospheric Environment (1967), 15, 549–556, https://doi.org/10.1016/0004-6981(81)90185-2, 1981.

Zahn, A., Brenninkmeijer, C. A. M., Maiss, M., Scharffe, D. H., Crutzen, P. J., Hermann, M., Heintzenberg, J., Wiedensohler, A., Güsten, H., Heinrich, G., Fischer, H., Cuijpers, J. W. M., and van Velthoven, P. F. J.: Identification of extratropical two-way troposphere-stratosphere mixing based on CARIBIC measurements of O3, CO, and ultrafine particles, Journal of Geophysical Research: Atmospheres, 105, 1527–1535, https://doi.org/10.1029/1999jd900759, 2000.

Zöger, M., Afchine, A., Eicke, N., Gerhards, M. T., Klein, E., McKenna, D. S., Morschel, U., Schmidt, U., Tan, V., Tuitjer, F., Woyke, T., and Schiller, C.: Fast in situ stratospheric hygrometers: A new family of balloon-borne and airborne Lyman alpha photofragment fluorescence hygrometers, Journal of Geophysical Research-atmospheres, 104, 1807–1816, https://doi.org/10.1029/1998JD100025, 1999.

3.3 THE TROPOPAUSE COMPOSITION TOWED SENSOR SHUTTLE (TPC-TOSS): A NEW AIRBORNE DUAL PLATFORM APPROACH FOR ATMOSPHERIC COMPOSITION MEASUREMENTS AT THE TROPOPAUSE (BOZEM ET AL., 2025)

Bozem et al. (2025) describe the setup of the new measurement platform TPC-TOSS and briefly the overall TPEx mission. It is an technical publication aiming for the presentation of instrument development, instrument characterization and calibration, and first results of the in-field performance of this platform.
I contributed extensively to the manuscript by providing the calibration and characterization measurements of the UHSAS systems. For this, I created the corresponding figures and wrote all text passages, related to the UHSAS instruments and data analysis. Furthermore, I wrote the campaign overview text, "The TPEx I project". The publication process is still ongoing and at the date of submitting this thesis the first review round has ended and a revised version is in preparation for submission.
For this reason small changes are still possible during the publication process and after acceptance the final publication will get a type-setting by Coperincus.

https://doi.org/10.5194/egusphere-2025-3175
Preprint. Discussion started: 8 July 2025

The TropoPause Composition TOwed Sensor Shuttle (TPC-TOSS): A new airborne dual platform approach for atmospheric composition measurements at the tropopause

Heiko Bozem[1], Philipp Joppe[1,2], Yun Li[3], Nicolas Emig[1], Armin Afchine[4], Anna Breuninger[5], Joachim Curtius[5], Stefan Hofmann[8], Sadath Ismayil[7], Konrad Kandler[7], Daniel Kunkel[1], Arthur Kutschka[8], Hans-Christoph Lachnitt[1], Andreas Petzold[3,6], Sarah Richter[5], Timo Röschenthaler[8], Christian Rolf[4], Lisa Schneider[7], Johannes Schneider[2], Alexander Vogel[5], and Peter Hoor[1]

[1]Johannes Gutenberg University of Mainz, Institute for Atmospheric Physics, Mainz, Germany
[2]Aerosol Chemistry Department, Max Planck Institute for Chemistry, Mainz, Germany
[3]Institute of Climate and Energy Systems 3 – Troposphere, Forschungszentrum Jülich GmbH, Jülich, Germany
[4]Institute of Climate and Energy Systems 4 – Stratosphere, Forschungszentrum Jülich GmbH, Jülich, Germany
[5]Institute for Atmospheric and Environmental Sciences, Goethe University Frankfurt, Frankfurt am Main, Germany
[6]Institute for Atmospheric and Environmental Research, University of Wuppertal, Wuppertal, Germany
[7]Institute for Applied Geoscience, Technical University Darmstadt, Darmstadt, Germany
[8]enviscope GmbH, Frankfurt, Germany

Correspondence: Heiko Bozem (bozemh@uni-mainz.de)

Abstract. In this paper we introduce the new TropoPause Composition TOwed Sensor Shuttle (TPC-TOSS), which constitutes an advanced development of the AIRcraft TOwed Sensor Shuttle (AIRTOSS), introduced by Frey et al. (2009). As part of a tandem measurement platform with a Learjet 35A, both platforms were equipped with redundant instruments for collocated measurements of aerosol size distribution (Ultra-High Sensitivity Aerosol Spectrometer, UHSAS), ozone (2BTech model 205), cloud particles (Back-Scatter Cloud Probe, BCP), as well as relative humidity, temperature and pressure. To measure the exact position of the two platforms as well as the relative distance of the TPC-TOSS to the Learjet a Global Positioning System (GPS) is installed on both platforms. Two identical Inertial Navigation Systems (INS) further allow to monitor attitude angles (roll, pitch, and heading) and accelerations.

Laboratory tests before and ground tests as well as inflight tests during the intensive operation period show a good agreement of the ozone and temperature measurements of better than 4.2 ppbv + 1.1 $\%$ (ozone) and 0.5 $^{\circ}\mathrm{C}$ (temperature) at a noise level of $\pm$ (2 ppbv + 0.5 $\%$) for 2 s data (ozone) and 0.1 K for 1 Hz data (temperature). Stability of the ozone monitor mounted in the TPC-TOSS has been tested and is estimated to be 2.2 ppbv (offset, 1 σ) and 0.7 $\%$ (gain, 1 σ), respectively, based on the drift of offset and gain during regular calibrations between measurement flights in the two weeks operation period.

The new TPC-TOSS was successfully flown during the TPEx I (TropoPause composition gradients and mixing Experiment) mission in June 2024 and performed four flights covering the altitude range between 6 and 12 km. The tropopause was crossed several times as evident from different temperature and ozone gradients as well as gradients of the aerosol number density. With the setup we are able to resolve transient stability and composition gradients ranging from almost zero or even negative to strong positive gradients of up to 25 $\mathrm{K\,km^{-1}}$ for potential temperature and from inverted to strong positive vertical gradients

https://doi.org/10.5194/egusphere-2025-3175
Preprint. Discussion started: 8 July 2025

of ozone of up to 800 $\mathrm{ppbv\,km^{-1}}$, respectively. These gradients are caused by transport and mixing due to convection or shear induced turbulence at the tropopause.

1 Introduction

The tropopause is naturally defined by the change of the vertical temperature gradient from the troposphere and a mostly moist adiabatic temperature lapse rate to neutral or positive temperature gradients due to increased shortwave absorption from ozone production in the stratosphere. According to World Meteorological Organization (WMO, 1957), the tropopause can be defined as the lowest level the temperature lapse rate does not exceed $2\ \mathrm{K\,km^{-1}}$ and stays on average below this value for any layer between this altitude and any level above within the next $2\ \mathrm{km}$. As a consequence the emerging increase of static stability makes the thermal tropopause a transport barrier, which in turn leads to strong gradients of tracers (e.g. Bethan et al., 1996; Hoor et al., 2002; Pan et al., 2004; Bauchinger et al., 2025). In the extratropics, the tropopause location is highly variable in time and space being linked to the synoptic conditions. Further non-conservative (diabatic) processes modify composition gradients and in turn the tropopause location itself. The representation of tropopause gradients is, however, crucial for understanding and quantifying the climate impact of radiatively active substances like water vapor, ozone, ice and aerosol particles (e.g. Randel et al., 2007; Fusina and Spichtinger, 2010). These composition gradients are highly variable as a result of the aforementioned variability of the tropopause as well as mixing processes associated with small scale (and large scale) diabatics (Kunkel et al., 2019; Lachnitt et al., 2023).

Measurements of these composition gradients at small scales are difficult to achieve: remote sensing methods suffer from limited resolution due to vertical or horizontal averaging kernels, vertical soundings only provide single profiles while aircraft measurements deliver data just along the flight trajectory. Highly transient phenomena like turbulent mixing processes or occurrence of cirrus clouds, overshooting anvil tops, etc., cannot be covered by horizontal flight tracks on different legs, since the relevant features may disappear when performing stacked level flights. One approach in former studies was to perform colocated measurements with two aircrafts, for example during CRYSTAL-FACE (Cirrus Regional Study of Tropical Anvils and Cirrus Layers – Florida Area Cirrus Experiment) (Jensen et al., 2004) or HALO-(AC)^3 (Wendisch et al., 2024). While the flights with *Polar 5* and *Polar 6* aircraft (HALO-(AC)^3) could only be performed below $5\ \mathrm{km}$ altitude due to aircraft performance capabilities, coordinated measurements involving two aircraft often suffer from difficulties of exact vertical colocation due to different aircraft speeds, as pointed out by Klingebiel et al. (2017, and references therein)

Simultaneous measurements of such small scale structures may deliver novel information on the effect of transient dynamical processes and their impact on species gradients at the tropopause. In earlier studies, towed sensors were introduced for colocated measurements. There are only very few setups of these devices available. Recently, the Alfred Wegener Institute (AWI) and the Leibniz Institute for Tropospheric Research (TROPOS) developed the T-Bird (Jurányi et al., 2025), a sensor shuttle for turbulence, aerosol and trace species measurements in the lowermost Arctic boundary layer towed by AWIs *Polar* aircrafts. Besides this, only helicopter based dual platform designs are available. Both, ACTOS (Airborne Cloud Turbulence Observation System) (Siebert et al., 2006) and SMART-HELIOS (HELIcopter-borne Observations of Spectral Radiation) (Werner et al.,

https://doi.org/10.5194/egusphere-2025-3175
Preprint. Discussion started: 8 July 2025

2013, 2014) as well as HELiPOD (Pätzold et al., 2023) are instrument platforms developed to be towed by a helicopter for measurements of boundary layer characteristics with respect to clouds and chemical composition or solar spectral reflectivity. To the best of our knowledge, such an approach has not yet been applied to tropopause altitudes or tropopause-relevant composition measurements.

Here, we present a novel development, which builds on previous experiences for a radiation / cirrus payload (Klingebiel et al., 2017; Frey et al., 2009, 2014; Finger et al., 2016). The new setup of the TPC-TOSS (TropoPause Composition TOwed Sensor Shuttle) includes measurements of ozone, GPS information, aerosol size distribution from 100-1000 nm as well as sensors for humidity and temperature. We will present the new setup and will provide uncertainties and individual tests, as well as some examples demonstrating the agreement between the two platforms. Additionally, we will showcase typical results achieved during the first field setup.

2 The TPEx I project

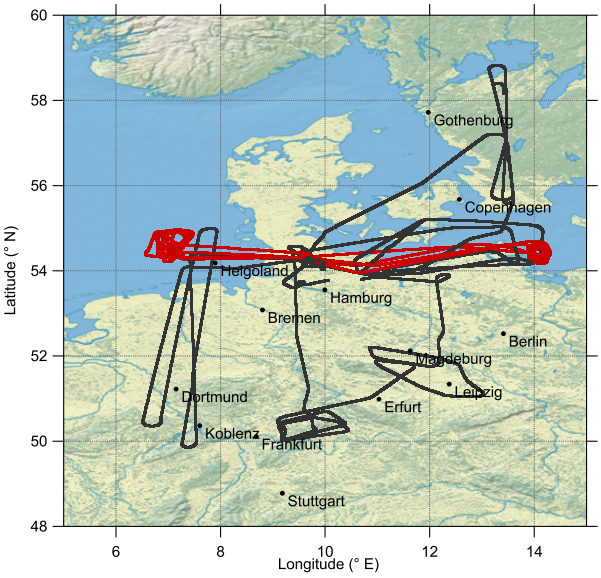

Figure 1. Overview over all conducted measurement flights during the TPEx mission in June 2024. The red colored flight paths are flights with the TPC-TOSS deployed whereas the black lines show the other flights without TPC-TOSS. The map was created from public-domain GIS data found on the Natural Earth website (http://www.naturalearthdata.com, last access: 30 June 2025).

The aircraft campaign TPEx I (TropoPause composition gradients and mixing Experiment) is the central aircraft mission in the collaborative research center TPChange (The TropoPause region in a Changing atmosphere) and took place between 10 and 21 June 2024 based at Hohn airfield in Northern Germany ($54°18'49''$N, $9°32'17''$E). The TPEx I mission addressed questions regarding the water vapor distribution in the upper troposphere and lower stratosphere (UTLS), the identification of mixing at and across the extratropical tropopause induced by diabatic processes and the source apportionment of aerosols and ice-

https://doi.org/10.5194/egusphere-2025-3175
Preprint. Discussion started: 8 July 2025

Table 1. Overview of the research flights with TPC-TOSS during TPEx I.

Flight Nr.	Date	Time	Region
F03	11 June 2024	10:30 - 13:07 UTC	Baltic Sea
F06	14 June 2024	07:07 - 09:18 UTC	Baltic Sea
F07	17 June 2024	07:01 - 09:35 UTC	North Sea
F10	20 June 2024	07:06 - 09:47 UTC	North Sea

nucleating particles (INPs) for understanding the main pathways of transport into the UTLS. Additionally, the mission aimed for studying vertical transport of aerosol particles and trace gases from the planetary boundary layer (PBL) into the UTLS and the effect on the chemical composition of the UTLS and new particle formation (NPF) events as well as cloud particle and cirrus formation.

Therefore, we equipped the research aircraft, a Learjet 35A, with a set of in-situ measurements of trace gases (e.g., CO and ozone) and aerosol quantities (particle size distribution and chemical composition) as well as offline samplers of aerosol and cloud particles and INPs. Furthermore, we used the unique approach of a fully automated towed sensor shuttle (TPC-TOSS) attached to the aircraft with partly redundant instrumentation and deployed during four out of eight scientific flights during TPEx I (Table 1 and Fig. 1). This approach provides observational data of vertical gradients of quantities, such as potential temperature, ozone mixing ratios and particle size distribution for aerosol particles between 95 nm and 1 $\mu\mathrm{m}$. The vertical distance between both platforms is around 200 m in tropopause regions and therefore aimed at resolving transient small scale variability of the tropopause structure and composition induced by small-scale processes (e.g., strong shear or small scale processes within extended cirrus decks).

As a consequence of safety constraints flights with the TPC-TOSS were only allowed in restricted air spaces. For TPEx I we used restricted air spaces over the Baltic Sea close to Usedom and over the North Sea west of Helgoland for the measurement flights. During TPEx I the Learjet reached maximum altitudes of 38000 feet (11500 m) without the towed sensor shuttle and 32000 feet (9700 m) with TPC-TOSS deployed. The maximum flight time was around 2.5 h with and up to 4 h without TPC-TOSS. During the mission in total eight research flights and one test flight were conducted of which four flights used the dual platform approach, two in each restricted air space (Fig. 1).

The scientific flight planning during the mission was performed with the help of high resolution model forecast from the ICON-D2 (ICOsahedral Nonhydrostatic) and the ECMWF (European Centre for Medium-Range Weather Forecasts) model with additional output of the CLaMS-Ice (Chemical Lagrangian Model of the Stratosphere) model for cirrus cloud predictions. In addition, the Mission Support System (MSS) was used for detailed flight planning and routing (Bauer et al., 2022).

The meteorological conditions in June 2024 were quite favorable for the scientific objectives of the mission. In this period several low pressure systems crossed the measurement region. The outflow of associated warm conveyor belts (WCBs) was

https://doi.org/10.5194/egusphere-2025-3175
Preprint. Discussion started: 8 July 2025

Table 2. Overview of the instrumentation of the Learjet as well as the measured quantities.

Instrument	Measured Quantities, Range	Sampling Frequency	Reference
Learjet			
UMAQS	CO, N_2O	1 Hz	Müller et al. (2015)
			Kunkel et al. (2019)
FISH	Gas phase water vapor, 1–1000 ppmv	1 Hz	Rolf et al. (2024)
			Meyer et al. (2015)
			Zöger et al. (1999)
WASUL	Total water vapor, 0.5–60000 ppmv	0.5 Hz	Tátrai et al. (2015)
			Rolf et al. (2024)
FRIDGE/SEM	INP concentration and physico–chemical properties	aerosol sampling	Schrod et al. (2016)
	(elemental composition > 80 nm	15–60 min	Schneider et al. (2024)
	size and morphology > 20 nm)		
CARIBIC-AMS	Chemical composition of non-refractory	30 s	Schneider et al. (2025)
	aerosol particles, 50–800 nm		
SkyOPC	Particle size distribution, 20 nm–3 µm	6 s	Bundke et al. (2015)
UHSAS-C	Particle size distribution, 0.095–1 µm	1 Hz	Cai et al. (2008)
MC-CPC	Aerosol number concentration from 12 nm	1 Hz	
	and 16 nm up to µm range	1 Hz	
ICH-sensor	Temperature and relative humidity	1 Hz	Helten et al. (1998)
GNSS/INS	Position, attitude and velocity	1 Hz	
	Acceleration	100 Hz	

within the range of the Learjet 35A and could be studied (Joppe et al., 2025). Furthermore, highly variable tropopause heights and convection over Germany and parts of Sweden (Konjari et al., 2025) were probed.

Instrumentation

For the TPEx mission the measurement platforms (Learjet including underwing pod "Knuffi" and TPC-TOSS) were equipped with instrumentation for in situ trace gas measurements, INP characterisation, aerosol number concentration, size distribution and composition measurements based on online (in situ) and offline filter analysis methods. These measurements were supplemented by measurements for meteorological parameters (temperature, humidity and pressure) as well as flight attitude, positioning and acceleration information using a GNSS/INS (Global Navigation Satellite System / Inertial Navigation System) navigational sensor. In particular the relative position between Learjet and TPC-TOSS is of major importance for the mea-

https://doi.org/10.5194/egusphere-2025-3175
Preprint. Discussion started: 8 July 2025

Table 3. Overview of the instrumentation of the underwing probe "Knuffi" as well as the measured quantities.

Instrument	Measured Quantities, Range	Sampling Frequency	Reference
Underwing pod "Knuffi"			
2BTech Ozone	O_3, 0–20 ppmv	0.5 Hz	Johnson et al. (2014)
NIXE-CAPS	Number concentration and size distribution of cloud particles, 0.61–937 µm (diameter)	1 Hz	Meyer (2013) Krämer et al. (2020)
SOAP	Organic aerosol molecular composition, 10–2000 nm, five samples including one filter blank per flight	15–140 min each	Breuninger et al. (2025, submitted to ACP)
BCP	concentration of particles with an optical equivalent diameter between 5–75 µm, 0.002–20 cm^{-3}	1 Hz	Beswick et al. (2014)
Offline particle composition, particle size and particle shape, aerosol sampling			
MultiMINI8	30 nm–10 µm	sampling 1–30 min	Ebert et al. (2016)
SPAFIS	100 nm–10 µm	sampling 1–30 min	
NanoPS	$\leq$ 500 nm	sampling 1–30 min	

surements with the dual platform approach. Furthermore, NIXE-CAPS (New Ice eXpEriment - Cloud and Aerosol Particle Spectrometer), installed in an underwing pod attached to the left wing of the Learjet, allows for the characterisation of cloud particles (number concentration, size). Some of the measurements were performed simultaneously on Learjet and TPC-TOSS (Table 2 to Table 4). The focus of this paper is on the TPC-TOSS as part of the dual platform approach. In Sect. 4 we will describe the TPC-TOSS instrumentation in detail while the Learjet instrumentation including the underwing pod instrumentation is characterized briefly in Table 2 and Table 3.

3 Technical design TPC-TOSS

The technical design of TPC-TOSS builds on an earlier version of the towed sensor shuttle (AIRTOSS) described in Klingebiel et al. (2017, and references therein). For TPEx I in June 2024, modifications were necessary to adapt the TPC-TOSS for trace gas and aerosol measurements. The body of the TPC-TOSS has a length of 2.57 m, a diameter of 0.24 m and a net weight of 27 kg. It is capable of carrying a maximum payload of 43 kg. The TPC-TOSS payload during TPEx I is summarized in Table 4 and described in more detail in Sect. 4. Individual instruments and additional equipment can be mounted on an internal aluminum frame that is split in three sections (Fig. 3b). The front section mainly contains the Ultra-High Sensitivity Aerosol Spectrometer (UHSAS-A; "A" denotes the airborne version within TPC-TOSS, "C" in Table 2 denotes the Learjet cabin version) (Sect. 5.3). In the middle part of the TPC-TOSS the battery pack is mounted, which contains 8 lithium iron

https://doi.org/10.5194/egusphere-2025-3175
Preprint. Discussion started: 8 July 2025

Table 4. Overview of the instrumentation TPC-TOSS as well as the measured quantities.

Instrument	Measured Quantities, Range	Sampling Frequency	Reference
TPC-TOSS			
2BTech Ozone	O_3, 0–20 ppmv	0.5 Hz	Johnson et al. (2014)
UHSAS-A	Particle size distribution, 0.095–1 µm	1 Hz	Mahnke et al. (2021)
BCP	concentration of particles with an optical	1 Hz	Beswick et al. (2014)
	equivalent diameter between 5–75 µm, 0.002–20 cm^{-3}		
ICH-sensor	Temperature and relative humidity	1 Hz	Helten et al. (1998)
GNSS/INS	Position, attitude and velocity	1 Hz	
	Acceleration	100 Hz	

Figure 2. Ozone instrument with insulation as mounted inside the TPC-TOSS in the rear part.

phosphate accumulators controlled by a battery management system. Individual cells are configured as such that an output voltage of 25.6 VDC is provided to supply all instrumentation within the TPC-TOSS. The capacity for the battery pack is 50 Ah which allows for the operation of the TPC-TOSS instrumentation for 6–7 h, which exceeds the maximum length of a research flight determined by fuel and Learjet performance. The rear section of the TPC-TOSS internal structure contains the Back-Scatter Cloud Probe (BCP, directly attached to the drag body cover), the 2BTech ozone monitor model 205, GNSS/INS instrumentation and data acquisition. The IAGOS (In-service Aircraft for a Global Observing System) (Petzold et al., 2015) capacitive hygrometer (ICH) for temperature and humidity measurements (rear part), the ozone bypass inlet and outlet (rear part) as well as the two GPS antenna (rear and front part) are mounted directly on the drag body cover which is made of glass-fibre reinforced plastic. As mentioned before, there were some modification of the body cover necessary to mount the GPS

https://doi.org/10.5194/egusphere-2025-3175
Preprint. Discussion started: 8 July 2025

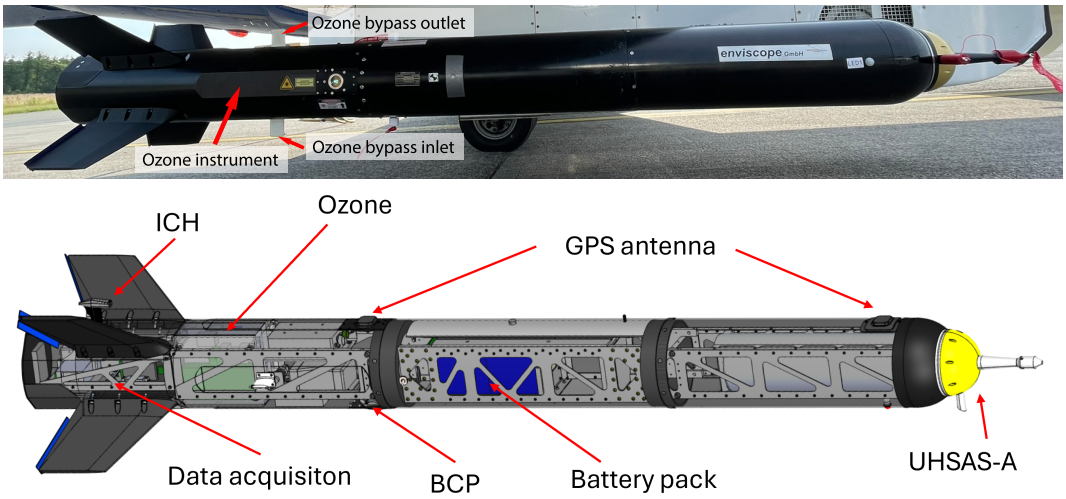

Figure 3. Top: TPC-TOSS with ozone bypass inlet and outlet. The ozone instrument is located in the back of the TPC-TOSS. Note that, while attached to the aircraft, the TPC-TOSS is rotated upward by 90 °. Bottom: Computer-Aided Design (CAD drawing of the TPC-TOSS including the instrumentation and battery pack.

antenna, BCP and the trace gas inlets. The mounting plates for these components were manufactured based on 3D printing to reduce weight.

The ozone instrument was connected to a bypass type tubing system consisting of 1/4" teflon tubing. While the bypass inlet was mounted forward facing, the bypass outlet was mounted backward facing allowing for a high bypass flow of 20–30 slpm to reduce the residence time inside the tubing (Fig. 3). The ozone instrument sampled from the main bypass inlet line using a T-type insertion. The forward facing stainless steel inlet for the UHSAS-A aerosol sampling was part of the main instrument. An internal pump actively maintained sample and sheath flow of 50 and 700 $\mathrm{cm^3\ min^{-1}}$, respectively.

The total weight and power consumption of all instrumentation within TPC-TOSS amounts to 41 kg and 185 W. The individual components within the TPC-TOSS frame and attachments to the towed sensor shuttle cover are positioned to locate the center of gravity of the TPC-TOSS close to the hook (distance of only 120 mm), where the steel wire connecting the TPC-TOSS to the Learjet is attached. The position of the center of gravity is crucial for a stable horizontal position during flight. Air brakes on the wings of the TPC-TOSS further support maintaining a stable flight attitude.

4 Instrument characterization

The following section describes and characterizes the redundant instrumentation installed on both platforms (Learjet including underwing pod and TPC-TOSS) which are a crucial part of the novel dual platform approach to measure ozone and aerosol gradients in the UTLS region.

https://doi.org/10.5194/egusphere-2025-3175
Preprint. Discussion started: 8 July 2025

4.1 GNSS/INS

To analyze colocated measurements on two platforms with respect to gradients of aerosol, trace species and meteorological parameters one requires a precise definition of the position of the individual platform and/or the relative position between both, Learjet and TPC-TOSS. We used a high performance tactical grade GNSS-Aided Inertial Navigation System (GNSS/INS) which uses MEMS (Micro-Electro-Mechanical Systems) inertial sensors in combination with dual multi-frequency GNSS receivers. The used 3DM-GQ7 (MicroStrain company) consists of a 3-axis accelerometer, 3-axis gyroscope, 3-axis magnetometer, a pressure altimeter and a dual GNSS receiver. The system performance given as uncertainty (1 σ) of the most important parameters within the operating temperature range of –40–85 $^{\circ}\mathrm{C}$ is based on manufacturer information as follows: The uncertainty of horizontal and vertical position amounts to 1.25 m and 2 m, respectively. With respect to flight attitude, roll and pitch angles could be derived with an uncertainty of 0.05° while the error for the heading amounts to 0.25°. The error of the measured velocity is 0.05 ms^{-1}.

This sensor was installed on both the Learjet and the TPC-TOSS to get consistent information on position and attitude of the respective platform. Two GPS antennas were installed on each platform located at a horizontal distance of 198 cm on Learjet and 148 cm on TPC-TOSS. The use of two antennas (L1 band at 1600 MHz and L2 band at 1200 MHz) increases the redundancy of the GPS positioning in case one antenna experiences reception issues. Simultaneously, it enables improved heading determination based on the relative position of the two antennas, with the associated uncertainty stated above. Position and attitude information were recorded at a resolution of 1 Hz. In addition, acceleration data were available at 100 Hz, providing insight into turbulent flight conditions experienced by the Learjet and TPC-TOSS.

4.2 IAGOS Capacitive hygrometer ICH

Relative humidity with respect to liquid phase water ($\mathrm{RH_{liq}}$) was measured using an instrument that is also employed in the IAGOS program. The IAGOS capacitive hygrometer (ICH) was mounted in the TPC-TOSS. The ICH, which also measures temperature, consists of a thin-film HUMICAP® capacitive sensor (Vaisala, Finland) whose capacitance depends on the relative humidity of the dielectric layer of the condenser, and a platinum resistance sensor (Pt100) that measures the temperature at the humidity sensing surface. The sensor itself and the applied calibration techniques are described in detail by Helten et al. (1998). The measurement principle is based on the diffusion-limited adsorption of the $\mathrm{H_2O}$ molecules by the dielectric membrane of the sensor. Since diffusion is strongly temperature-dependent, the sensor's response slows down from seconds to a few minutes with decreasing temperatures. The relative humidity and temperature signals are fed into a microprocessor-controlled transmitter unit (HMP230, Vaisala) which passes the signals to the data acquisition system. The data conversion from capacitance signals to relative humidity values is performed offline in a separate data quality assurance and analysis step (Neis et al., 2015a, b). The ICH sensor is mounted at the top of an axisymmetric sensor carrier, which is designed for installation in an appropriate housing (ICH-RS: Model 102 BX, Rosemount Inc., Aerospace Division, USA). The ICH sensor is designed for routine autonomous measurements aboard passenger aircraft. Its passive measurement technique requires no sampling line and pump, thus low demand of maintenance. Before the installation on the aircraft and after 500 h flight hours ($\sim$ four to six

https://doi.org/10.5194/egusphere-2025-3175
Preprint. Discussion started: 8 July 2025

weeks) within the IAGOS framework, an individual calibration of each ICH sensor is necessary, which is accomplished in the environmental simulation chamber at Jülich (Smit et al., 2000). During the TPEx I campaign, the ICH sensor was calibrated before and after the campaign. These calibrations are made over a sensor temperature range between –40–20 °C against a frost point hygrometer (MBW373) at 2–50 % RH_{liq} with a temperature accuracy of ±0.1 K. During flight, in fact, the ambient air is adiabatically compressed in the housing, leading to a significant temperature increase of the air sampled by the sensor (up to 30 °C). Therefore, –40 °C sensor temperature, namely the lowest temperature of the calibration, corresponds to –70 °C in the real atmosphere, which is rarely reached at aircraft cruising altitude. The adiabatic heating is corrected using the Mach number after true aircraft speed (Neis et al., 2015a).

Based on chamber calibration with the MBW373 frost-point mirror and intercomparison with airborne instruments in research aircraft measurement missions (Neis et al., 2015a, b; Rolf et al., 2024), the temperature and RH_{liq} uncertainties produced by the ICH sensor are ±0.32 K and ± (5–6) %, respectively. Therefor, relative humidity with respect to ice (RH_{ice}) and water vapour mixing ratio can also be provided calculated from RH_{liq} and temperature.

4.3 Back-Scatter Cloud Probe (BCP)

The BCP is part of the IAGOS system, and is a compact, lightweight, near-field and single particle backscattering optical spectrometer to measure the concentration and optical equivalent diameter of particles from 5 to 75 µm (Beswick et al., 2014). The BCP features a laser diode emitting focused and linearly polarized light at 658 nm, which passes through a heated glass window in the aircraft skin and focuses on a small region approximately 4 cm away. Light scattered back at a solid angle of 144–156° by particles in the sample volume is collected by lenses and focused onto an avalanche photodiode for detection. The cloud particle number concentration is calculated from the sampling area times the true air speed of the aircraft. It was primarily designed as a real-time qualitative cloud indicator for data quality control of trace gas instruments of the IAGOS system. Subsequent evaluations and investigations (Petzold et al., 2017; Lloyd et al., 2021) reveal that the BCP cloud dataset is also of use for the study of contrail and natural cirrus. Limited by the detectable particle size range, BCP is insufficient for rather small (< 5 µm) and large cirrus particles up to the size of approx. 1 mm in cirrus clouds. The total measurement concentration ranges from 0.002 cm^{-3} to approx. 20 cm^{-3} in cirrus clouds, as observed during IAGOS cruising condition. High cloud particle number concentrations up to 200 cm^{-3} in liquid water clouds were demonstrated to be within the detectability of the BCP by Beswick et al. (2014). Assuming the sample area as reported by Beswick et al. (2014) and a typical mean aircraft cruising speed of 250 ms^{-1}, the estimated lower threshold for cloud particle detection with a temporal resolution of 4 s (IAGOS operation conditions) would be 0.015 cm^{-3}, but with a sampling uncertainty of 50 % according to Poisson statistics (Petzold et al., 2017). During TPEx I, the BCP was integrated into TPC-TOSS and the underwing pod "Knuffi" as it is installed at the fuselage during IAGOS routine measurements.

https://doi.org/10.5194/egusphere-2025-3175
Preprint. Discussion started: 8 July 2025

4.4 Ozone measurements

During TPEx I, ozone was measured using two modified 2BTech model 205 instruments (Johnson et al., 2014). The measurements are based on the absorption of UV at the wavelength 254 nm at ambient pressure. Small pumps are used to continuously purge the instruments at a flow rate of 1.7 $\mathrm{l\,min^{-1}}$ for the underwing pod instrument and 2.6 $\mathrm{l\,min^{-1}}$ for the TPC-TOSS instrument at ground pressure. The flow difference arises from the change from a two-pump to an only one-pump flow scheme for newer versions of the instrument. The instrument was modified for operating at high altitudes within the underwing pod and the TPC-TOSS under low pressure and low temperature conditions. These modifications consisted of an upgrade of the pressure sensor suitable and calibrated for an altitude range up to 25 km, the pump, an additional lamp heater to improve the stability of the UV source, and the addition of an insulation to prevent the instrument from temperatures below freezing point. The instrument is equipped with two absorption cells of which one (cell A) is purged with ambient air at a 2 s time interval to determine the light intensity $I(t_0)$. The air stream for the second cell (cell B) in this time interval is led through an Hopcalite ozone scrubber to remove any ozone to determine the light intensity $I_0(t_0)$ without any absorber present in the cell. During the subsequent 2 s time interval $[t_0, t_1]$ cell A is purged with ozone scrubbed air while cell B is purged with ambient air. At time t_1 an ozone value is calculated for cell A applying Beer's law with the measured ratio of absorption signals $I(t_0)$ and $I_0(t_1)$. For cell B an ozone value is calculated using $I_0(t_0)$ and $I(t_1)$. The ozone value for each cell is further converted into a mixing ratio by applying the measured temperature in the respective cell and the cell pressure and finally stored as the average of both cells at t_1. At time t_2 the ozone value for cell A is calculated using again $I_0(t_1)$ and the new absorption signal $I(t_2)$ while for cell B ozone is determined from $I(t_1)$ and $I_0(t_2)$. Again, the average ozone mixing ratio based on both cells is stored at t_2. As a consequence every individual value in each measurement cell is used twice for the calculation of subsequent mixing ratios leading to an fully independent determination of an ozone value only every 4 s. To account for drifts and asymmetries in the measurement cells, the streams of ambient air and scrubbed air through the cells are switched every 2 s. The minimum time resolution therefore is 2 s, corresponding to approximately 300 m spatial resolution during flight operation.

During TPEx I one instrument was mounted outside the pressurized cabin into the underwing pod ("Knuffi") at ambient pressure. The other instrument was placed into the TPC-TOSS. Temperature and pressure dependencies were characterized in the laboratory before the deployment during TPEx I (Sect. 4.4.3, 4.4.4). To avoid operational temperatures dropping to values below the instrument specifications, both devices were thermaly isolated. Due to safety reasons, the TPC-TOSS had to be powered off while being attached to the aircraft, therefore no active heating could be applied until TPC-TOSS was released.

4.4.1 Noise and drift

Both ozone instruments were extensively checked and tested prior and during the campaign. Noise and drift (as a measure of stability) under different laboratory conditions and during the field campaign on ground have been checked.

To test noise and drift of both instruments we used the Allan variance (Allan, 1966; Werle, 2011). Having pure statistical noise (white noise) the Allan variance should decrease with increasing integration time following the black solid line in Fig. 4 (lower panel). Our instruments show both a constant or even increasing Allan variance up to integration times of 4–6 s

https://doi.org/10.5194/egusphere-2025-3175
Preprint. Discussion started: 8 July 2025

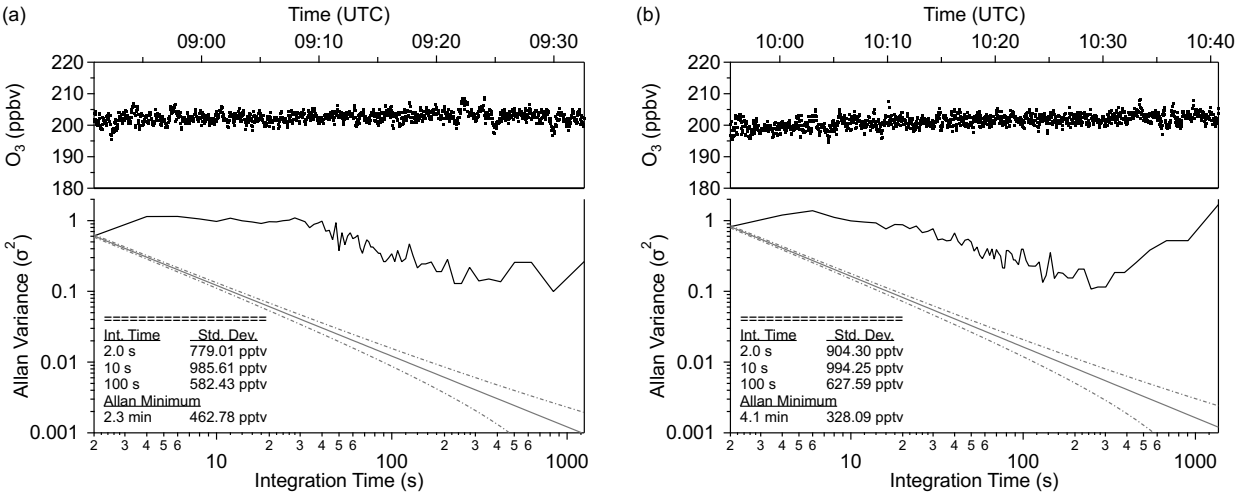

Figure 4. Allan-Werle-plots for the ozone instruments installed on the Learjet (a) and TPC-TOSS (b). Upper panels show the ozone time series from ground tests during the field campaign (8 June 2024 for TPC-TOSS ozone and 9 June 2024 for "Knuffi" ozone) used to calculate the Allan variance.

followed by a decrease of the Allan variance until an optimal integration time of 300–500 s where the Allan variance is at minimum. At larger integration times the slow drift starts to dominate leading to increasing Allan variance. Furthermore a significant deviation from the white noise floor (black line) is observed. According to Werle (2011), additional non-white noise components, e.g., flicker noise, could lead to this deviation. A maximum of the Allan variance at an integration time larger than the lowest time resolution (in our case 2 s) corresponds to a low pass filter characteristic. The low pass filter is usually applied in the frequency domain but its effect could also be observed in the time domain. Signal smoothing or damping effects of fast concentration changes would in turn lead to the observed behavior of the Allan variance. As discussed in section 4.4, the instrument output frequency of the ozone instrument is 2 s but the measurement process itself leads to independent data points only every 4 s. Taking into account that the gas exchange time in the tubing system is on the order of 1 s, data points before the Allan variance maximum are to some degree correlated. This is similar to applying a smoothing or running mean of 4–6 s to the ozone data which increases the Allan variance with integration time. After the maximum, the Allan variance further decreases with integration time but deviates from the black solid line. For the "Knuffi" instrument a significant decrease is observed only after 30 s. For both instruments we observed slow irregular changes of the cell pressure caused by irregular changes of pump capacity of the small internal membrane pumps. These variations most probably add non statistical noise components (flicker noise) to the Allan Variance expressed as the observed deviation from the black line (Werle, 2011). As these cell pressure variations are stronger for the "Knuffi" instrument, the Allan variance for this instrument is stronger affected during the first 20 to 30 s compared to the TPC-TOSS instrument. Similar results for the Allan variance with an Allan maximum around 4 s are reported by Moormann et al. (2025), who operated the same type of instrument on a drone, thereby confirming our laboratory and field tests.

https://doi.org/10.5194/egusphere-2025-3175
Preprint. Discussion started: 8 July 2025

Based on these Allan variance analysis the noise of both instruments under laboratory conditions amounts to 1 ppbv (1 σ) for 2 s data at a mixing ratio of 200 ppbv. The quantification of the drift of both instruments as a measure of stability is done in the following section.

4.4.2 Linearity

To test the linearity of the ozone monitor model 205 we checked the instruments against a calibration source (2B Tech ozone calibration source model 306). The calibration source is calibrated against a NIST traceable standard and is capable of producing ozone with an accuracy and precision better than 1 ppbv in the range 30–100 ppbv ozone or 1 % in the range 95–1000 ppbv (Birks et al., 2018).

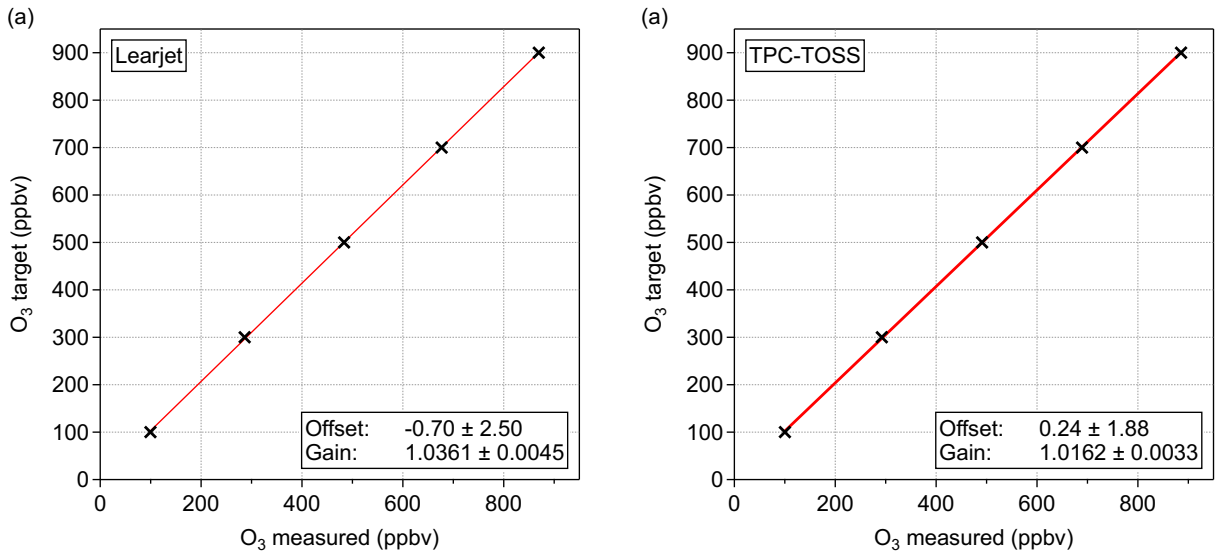

Figure 5. Linearity check of the ozone instruments using the 2B Tech ozone calibration source model 306 in between the research flights on 19 June 2024. Each mixing ratio step consists of three minutes of data after ozone has stabilized at the respective target mixing ratio. (a) results for the Learjet instrument inside "Knuffi" and (b) for the TPC-TOSS instrument.

We tested both instruments in their final mechanical configuration in the field to account for the effect of different inlet lengths. The instruments were both connected to the calibration source and purged with calibrated ozone for ten minutes for each mixing ratio. The mixing ratio was stepwise increased from 100 to 900 ppbv. Figure 5 shows that both instruments exhibit a linear response over the expected data range, deviating from unity by 3.6 % and 1.6 %, rspectively (relative to the factory settings for the implemented gain and offset parameters). The offset was zero within the statistical uncertainty. It is important to note that the newly derived offset and gain parameters were implemented as calibration parameters during post-processing of the ozone data. In this step, the measured ozone values were corrected by applying the offset and gain to the raw data.
We repeated the calibration procedure between research flights and after the campaign, which allows for assessing stability by analyzing the drift in offset and gain during the regular calibrations. For the TPC-TOSS ozone instrument, the offset and gain

https://doi.org/10.5194/egusphere-2025-3175
Preprint. Discussion started: 8 July 2025

drifted by 2.2 ppbv and 0.7 % (1 σ), respectively. For the "Knuffi" instrument, the stability parameter were 2.2 ppbv for the offset and 0.1 % (1 σ) for the gain.

Based on these regular calibrations, we further analyzed the instrument noise over a broader range of mixing ratios, covering the measured mixing ratios during research flights, and compared the results to the Allan variance presented in the previous section. This analysis indicates that a mixing ratio dependent noise component needs to be added. For both the TPC-TOSS and the "Knuffi" instrument the noise for the final mechanical setup is 2 ppbv + 0.5 %. Applying Gaussian error propagation the total uncertainty, which includes both noise and stability, is 3 ppbv + 0.9 % for the TPC-TOSS and 3 ppbv + 0.7 % for the Learjet instrument within the underwing pod.

4.4.3 Temperature dependence

The two ozone monitors model 205 were mounted outside the cabin and thus affected by cold ambient air temperatures during flight. Both instruments were equipped with a cold weather upgrade including lamp heating and a pump capable of operating at temperatures below freezing point. In addition, both instruments were thermally isolated using Basotect® foam to prevent them from cooling below specified temperature ranges during operation. As mentioned before, the ozone instrument on the TPC-TOSS could only be switched on after the TPC-TOSS was released from the Learjet, which was typically under cold conditions.

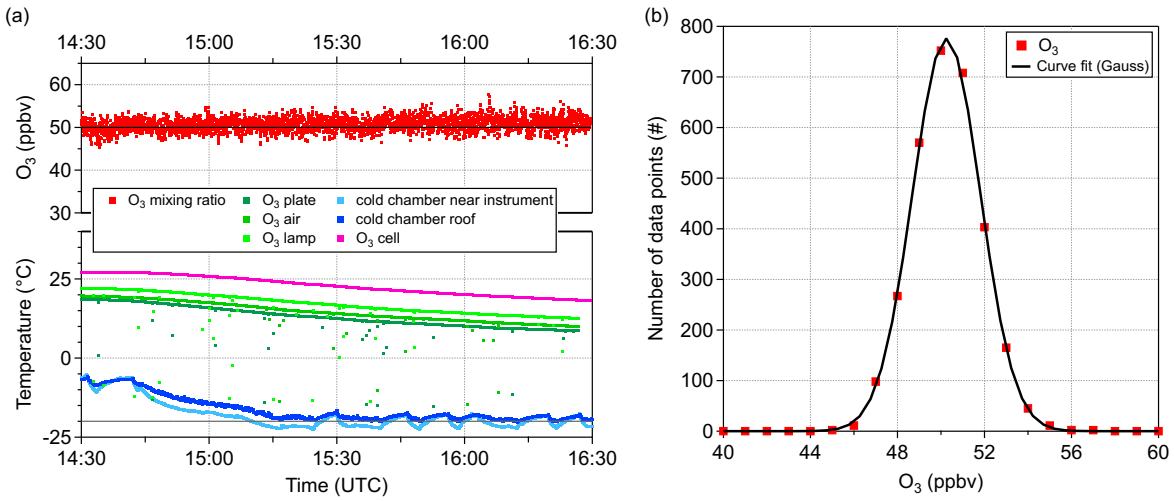

Figure 6. Temperature dependence test of the ozone monitor within a cold chamber. (a) ozone mixing ratio is shown in red. The cell temperature within the ozone monitor is shown in pink and further internal temperature measurements are shown in green colours. Two sensors measuring the air temperatures at different positions inside the cold chamber are shown in blue colors. The dark blue measurement is nearby the ozone monitor and the light blue sensor was located below the roof of the cold chamber. The black line in the upper panel shows the target ozone mixing ratio of 50 ppbv, the grey line in the lower panel shows the target temperature of –20 °C of the cold chamber. (b) histogram of ozone data during the temperature test. Red dots show the distribution of ozone measurements. The black line shows a gaussian curve fit to the measured ozone distribution.

https://doi.org/10.5194/egusphere-2025-3175
Preprint. Discussion started: 8 July 2025

To identify temperature dependencies of the measured ozone data, both instruments were tested in a cold chamber being capable of operating at –20 °C. In the following we only show results from the TPC-TOSS instrument as both instrument show the same behavior inside the cold chamber. The ozone instrument was placed inside the cold chamber and purged with calibration gas at 50 ppbv from the ozone calibration source model 306. The cold chamber was initially operated at approximately –5 °C and was cooled down to –20 °C once the ozone monitor was running inside.

Figure 6 shows the evolution of ozone mixing ratios and internal temperatures of the ozone instrument. Temperature "air" is measured in the air inside the box of the ozone monitor, temperature "lamp" is measured on the lamp housing and temperature "plate" is measured on the plate where all electronics and optics are mounted on. At constant cold chamber temperature (light and dark blue curve in Fig. 6), the ozone cell temperature (pink) and additional temperatures inside the ozone instrument (green colors) were initially stable. They started decreasing as soon as the cold chamber was cooled down to approximately –20 °C. After 75 min of operation at –20 °C, the ozone related temperatures began to stabilize at a level approximately 10 °C lower, but still well above freezing point.

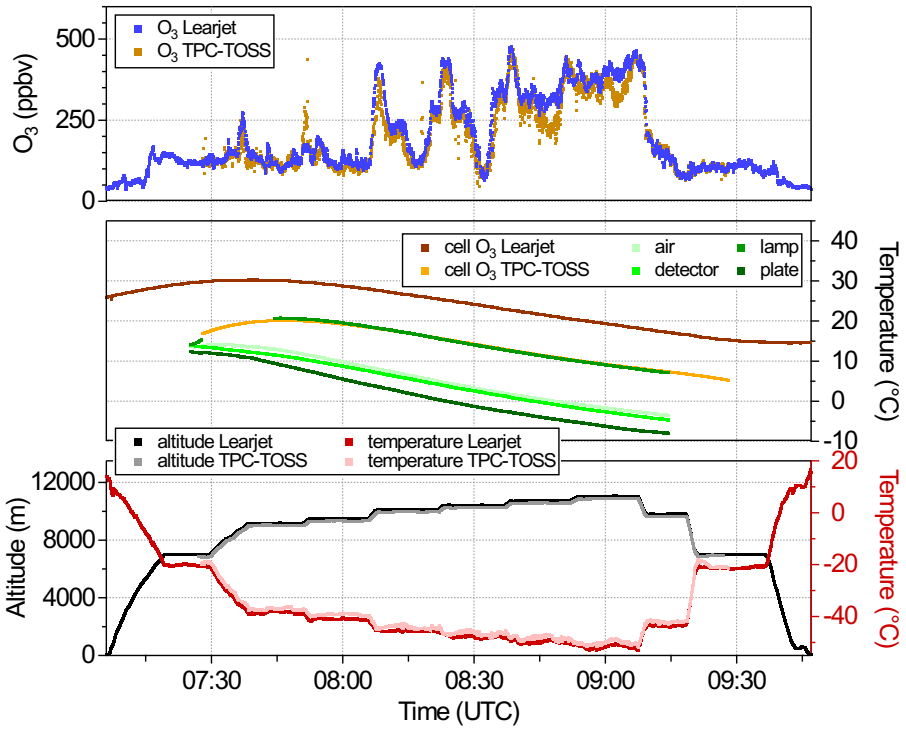

Figure 7. Upper panel: Ozone mixing ratios measured with the ozone monitors in the "Knuffi" (blue) on the Learjet and in the TPC-TOSS (light brown). Middle panel: Temperature evolution of measured cell temperatures for the TPC-TOSS (orange) and "Knuffi" instrument (brown). Green temperature curves represent temperatures measured inside the housing of the ozone monitor. Lower panel: Black and grey dots represent GPS altitude of the Learjet and TPC-TOSS and dark and light red dots represent outside air temperatures measured on Learjet and TPC-TOSS by the ICH, respectively.

https://doi.org/10.5194/egusphere-2025-3175
Preprint. Discussion started: 8 July 2025

Ozone mixing ratios were quite constant during this experiment showing only a very week drift of 1.28 ppbv during two hours of measurements. This drift is within the uncertainty range of ozone generation (1 ppbv in the range 30–100 ppbv ozone) and measurement (3 ppbv + 0.9 %) . The histogram (Fig. 6 right panel) confirms a statistical distribution of the values and thus no indication for non-linearities. Based on these cold chamber tests no temperature dependencies of the ozone monitors was expected.

As outside air temperatures during the research flights were lower than those in the cold chamber tests, we further analyzed the temperature behavior of the ozone instruments during research flight F10 on 20 June 2024 in more detail. Figure 7 shows that cell temperatures within the ozone instruments stayed well above freezing point during research flight F10 despite outside air temperatures dropped below –50 °C at highest flight levels. The temperature measured on the lamp housing closely follows the cell temperature, the three other temperature measures reach values below zero during the second half of the flight. These temperatures are measured in the air inside the box of the ozone monitor (temperature "air"), on the detector housing (temperature "detector") and on the plate where all electronics and optics are mounted on (temperature "plate"). This configuration is similar to the cold chamber test before the campaign. Temperatures below zero do not affect ozone measurements. The observed temperature behavior closely reflects test conditions in the cold chamber test before the measurement campaign except air temperatures during the flight were lower compared to the test environment.

4.4.4 Pressure dependence

The ozone monitor model 205 was successfully operated on airborne platforms in earlier studies by Mynard et al. (2023); Sorooshian et al. (2023), and Yates et al. (2013). In particular the study by Yates et al. (2013) operated the instrument with similar modifications up to altitudes of 9 km using the Alpha Jet research aircraft as part of the Alpha Jet Atmospheric eXperiment (AJAX) with the 2BTech ozone monitor mounted within an underwing pod. Before their measurement campaign they tested the ozone monitor in a pressure chamber at pressures between 200 and 800 hPa, a similar range as during our TPEx I campaign. Based on these pressure tests no significant pressure dependence could be derived and they reported an overall uncertainty of 3 ppbv for 10 s data. These findings compare quite well with our derived uncertainty for the TPC-TOSS instrument of ± (3 ppbv + 0.9 %) for 2 s data. Furthermore, we also did not observe any significant pressure dependency.

4.4.5 Collocated performance test

One key objective for the deployed TPC-TOSS were simultaneous ozone measurements on the two platforms Learjet and TPC-TOSS. We therefore tested the instruments side by side in the lab before and on ground during the campaign to identify any systematic error between the two ozone instruments. Based on ambient air measurements in the lab before the campaign (Fig. 8a, orange shaded area in the histogram), a difference of (0.6 ± 1.9) ppbv between the two instruments was observed. Since the instruments were not in their final setup during the laboratory comparison described before we repeated the side by side comparison during the measurement campaign on ground with both instrument mounted inside the "Knuffi" and inside the TPC-TOSS. This also included the final setup for the inlet tubing providing a calibration of the final flight configuration.

https://doi.org/10.5194/egusphere-2025-3175
Preprint. Discussion started: 8 July 2025

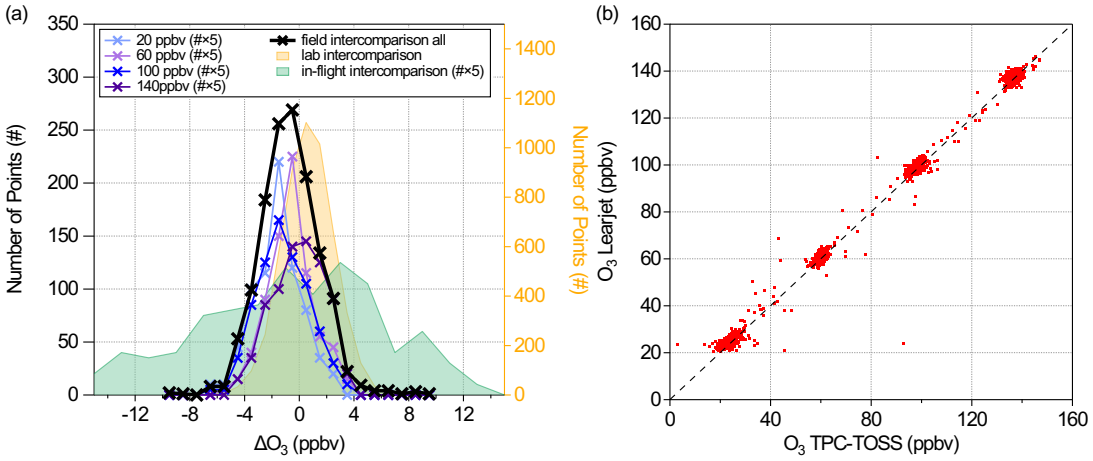

Figure 8. Collocated performance test in the lab before the campaign, during the campaign using the final setup as mounted on the respective platforms across different mixing ratios, and in-flight during research flight F10. (a) histogram of ΔO_3 for the different colocated test environments: lab, field and in-flight. The orange shaded area shows the results from lab measurements. Coloured lines show the results of the field intercomparison for different mixing ratio steps, the black line shows the overall difference of the field intercomparison. The green shaded area shows the 4 min in-flight intercomparison. For better visibility the values of the individual mixing ratio steps and the in-flight data were multiplied by 5. (b) correlation of the ozone intercomparison at the measurement site.

As shown in Fig. 8a, we performed measurements at four different mixing ratios (20 ppbv, 60 ppbv, 100 ppbv and 140 ppbv) by using the external ozone calibration source. The histograms of ΔO_3 between both instruments for the individual mixing ratio levels as well as the whole data set of this experiment agree within 2.5 ppbv (1 σ) based on the average difference between both data sets. The maxima of the individual curves deviate by 1 ppbv from ΔO_3=0 within the uncertainty range of the instruments derived in Sect. 4.4.2. The correlation between both instruments shows that data points are located along the 1:1 line with a deviation of less than 1 % confirming the laboratory tests. The offset between both instruments of 1.6 ppbv lies within the uncertainty range.

During measurement flight F10 on 20 June 2024 we could perform a quasi colocated test between both instruments (Fig. 9). During this flight the retraction of the TPC-TOSS was stopped at around 200 ft cable length before the TPC-TOSS was finally attached to the aircraft and switched off. Therefore the TPC-TOSS was measuring for around four minutes in a distance of just 43 m below the aircraft. This offered the possibility for an in-flight intercomparison of the redundant measurements. In Fig. 9 (a) the dark yellow shaded box marks the time interval of the in-flight intercomparison. The aerosol size distribution measurement results for this intercomparison are discussed in Sec. 5.3. For ozone the ΔO_3 histogram (left panel in (b)) for this part of the flight shows a rather broad distribution of around 25 ppbv centered around zero since ozone mixing ratios still show some atmospheric variations during the flight (Fig. 9 (a)). The observed offset in the maximum of the distribution of around 5 ppbv is most probably due to the fact that there is still a vertical distance of 43 m between both platforms. For typical vertical ozone gradients of around 600–800 ppbv km^{-1} near the tropopause a vertical distance of 50 m would correspond to

https://doi.org/10.5194/egusphere-2025-3175
Preprint. Discussion started: 8 July 2025

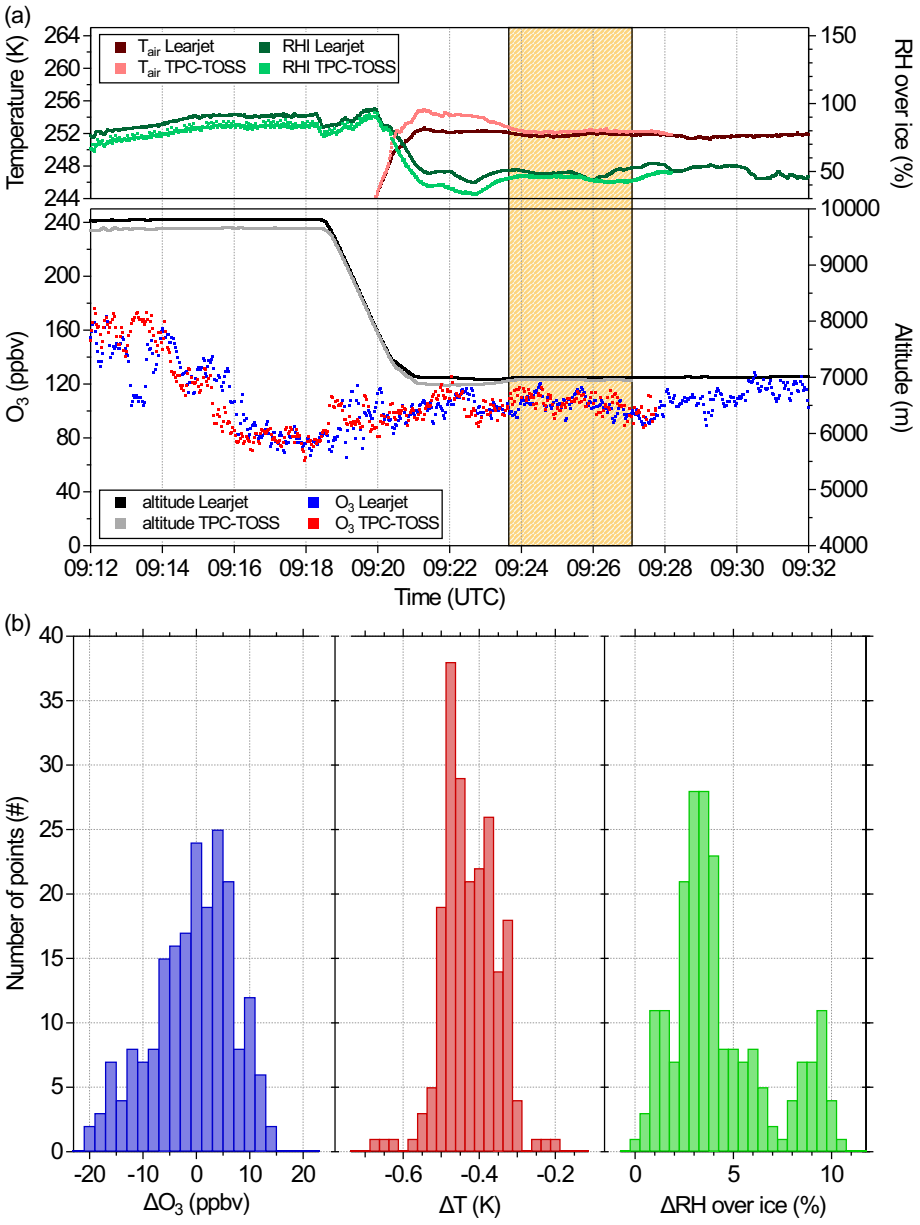

Figure 9. Colocated performance test in-flight during research flight F10 on 20 June 2024. (a) Time series of ozone measurements and GPS altitude (lower panel) from Learjet (ozone: red, altitude: black) and TPC-TOSS (ozone: blue, altitude: grey) as well as measured outside air temperatures (red colors) and relative humidity over ice (RHI) (green colors) in the upper panel. The dark yellow shaded area shows a time interval when the TPC-TOSS was released at minimum safe rope distance (200 ft $\approx$ 61 m) for around four minutes. At that time the vertical distance between Learjet and TPC-TOSS was around 43 m. (b) histograms of the difference between Learjet and TPC-TOSS data within the yellow shaded time interval.

https://doi.org/10.5194/egusphere-2025-3175
Preprint. Discussion started: 8 July 2025

even 30 ppbv or any smaller value when approaching the tropopause. Middle and right panels in Fig. 9 (b) show histograms of the difference of measured air temperature (ΔT) and relative humidity over ice between Learjet and TPC-TOSS. The observed narrow distribution of (ΔT) peeks around –0.5 K which could probably be explained by a dry adiabatic temperature gradient prevailing in the flight region. A typical gradient of 10 $\mathrm{K\,km^{-1}}$ would result in around 0.5 K temperature difference between Learjet and TPC-TOSS at a vertical distance of around 50 m. Assuming a uniform distribution of water vapor mixing ratios in the measurement region, indicated by the uniform distribution of ozone, a higher measured temperature at the TPC-TOSS would result in lower relative humidity values at the TPC-TOSS, which are observed based on the ΔRHI distribution right panel in (b) that is shifted to slightly positive values.

4.5 Aerosol size distribution measurements

For the aerosol measurements, we deployed UHSAS on the TPC-TOSS and the Learjet. These spectrometers are manufactured by Droplet Measurement Technologies (DMT) and measure the size distribution of aerosol particles in the size range between 95 nm and 1000 nm. The measuring principle is based on laser based light scattering in the infrared spectral range. Therefore, UHSAS uses a Nd^{3+}:$YLiF_4$ solid state laser with an operating wavelength of 1054 nm (Cai et al., 2008; Kupc et al., 2018). The laser mode has an intracavity power of approximately 1.1 $\mathrm{kW\,cm^{-2}}$ and is perpendicular to the particle stream. Aerosol particles are actively pumped into the detection unit through a jet assembly with a sample flow of 50 $\mathrm{cm^3\,min^{-1}}$ and are focused to a narrow particle beam with a sheath flow. This sheath flow is in the range of 700 $\mathrm{cm^3\,min^{-1}}$ at sea level for the cabin instrument (UHSAS-C) and controlled by a mass flow controller to 600 $\mathrm{cm^3\,min^{-1}}$ for the UHSAS installed on TPC-TOSS (UHSAS-A). The scattered light is collected by two pairs of Mangin mirrors in the range between 22° and 158° and focused onto the corresponding photodiodes. These photodiodes convert the photocurrent into a voltage which can be assigned to a particle signal by calibration curves.
Figure 10 shows the calculated response of the UHSAS according to Mie theory for a range of refractive indices covering the atmospheric range, similar to (Cai et al., 2008; Mahnke et al., 2021).

4.5.1 Size characterization

The assignment of the particle signal into the corresponding size bin is done by calibrating the four gain stages of the photodiodes in the instrument. This calibration is done in two steps, the relative gain calibration and the absolute gain calibration. For the relative gain calibration the instrument needs a broad distribution of particle sizes to determine the coefficients. In contrast to this method, the absolute gain calibration is performed by using polystyrene latex (PSL) particles of known size. In this step, each particle size is assigned to a measured gain value. Typical particle sizes for the absolute gain calibration by the manufacturer are 100, 150, 270 and 500 nm. In order to verify whether the last calibration is valid and both instrument versions operated during the measurement campaign are comparable, we performed a size characterization measurement before and after the campaign. For this, we generated aerosol particles with different refractive indices using an Atomizer, dried the aerosol flow with a diffusion dryer and generated a monodisperse aerosol stream by an electrostatic classifier (TSI, Model 3080 including X-ray neutralization of multiple charged particles). For the characterization we use ammonium sulfate,

https://doi.org/10.5194/egusphere-2025-3175
Preprint. Discussion started: 8 July 2025

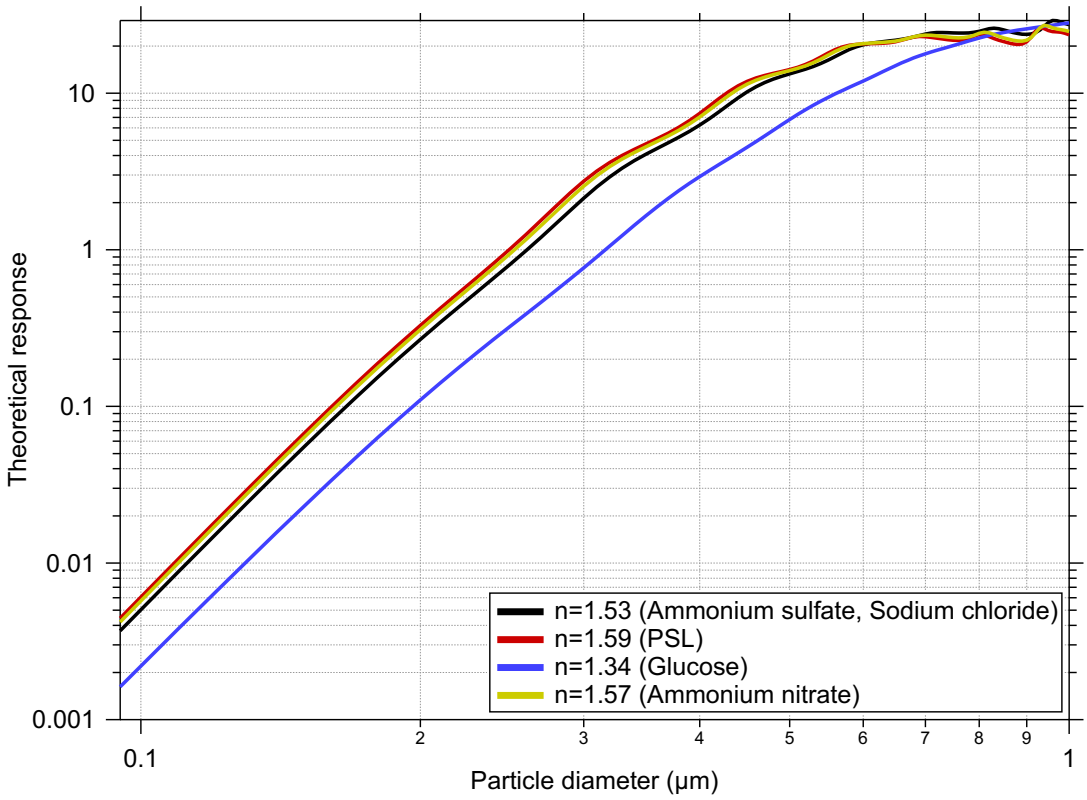

Figure 10. Theoretical response of the UHSAS according to Mie-theory and different refractive indices.

ammonium nitrate, sodium chloride, glucose and PSL. Except for the PSL measurements, we covered the complete size range between 100 and 650 nm in 50 nm steps. For the PSL characterization, we used the sizes 100, 150, 200, 350, 500, 600 and 800 nm. To increase statistics, we performed more than one measurement for most of the sizes up to 450 nm. The results of the characterization measurements are shown in Fig. 11. We observed an offset to smaller diameters in the measurements of both instruments compared to the mobility diameter selected at the classifier and the 1:1 line (Fig. 11a). Depending on the species, the offset varies in the range we expect from the Mie calculations. However, the assignment of the particles into the size bins follows a linear trend with a slope smaller than one and the comparison of both UHSAS systems shows a very good agreement between each other with the results of the size calibrations on the 1:1 line within the noise (Fig. 11b).

Based on these characterization measurement, we are able to introduce a new bin scheme to assign the particle signals to less and broader bins to account for the different refractive indices of the particle types. More precisely, we convert the measured 99 bins into 9 bins of quasi-logarithmic spaced channels (Fig. 17).

https://doi.org/10.5194/egusphere-2025-3175
Preprint. Discussion started: 8 July 2025

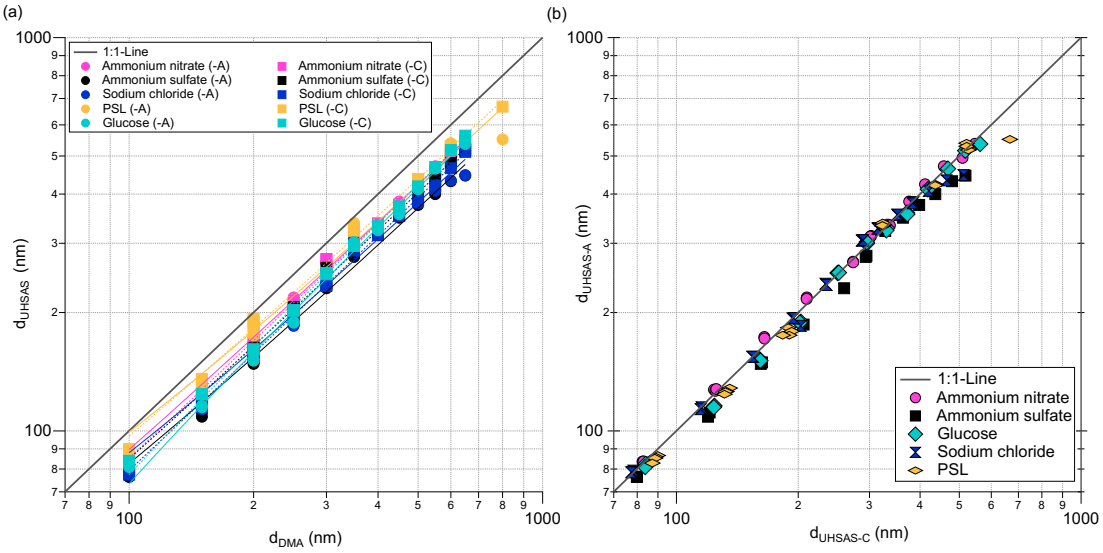

Figure 11. Characterization measurement of the UHSAS systems (-A and -C) for different aerosol particle types; ammonium nitrate (pink), ammonium sulfate (black), sodium chloride (blue), PSL (orange) and glucose (bright blue). The 1:1-line is represented by the grey dashed line. The comparison of the measured UHSAS diameter against the mobility diameter selected by the classifier is shown in (a). The comparison of both UHSAS systems is shown in (b).

4.5.2 Counting efficiency

Furthermore, we investigated the counting efficiency of both instruments. For this, we used the same measurements as for the size calibration and compared the total count number, by adding the counts from all size bins. Figure 12 shows the median values for one minute averages of both instruments, for all particle types measured during the laboratory characterization. The data from both instruments show good agreement and are distributed around the 1:1 line. Figure 13 shows the ratio of the median values as a function of size. Here we can see that in a size range between about 300 and 500 nm, the UHSAS-A showed less particle counts than the UHSAS-C, but showed slightly higher particle counts around 100–200 nm.

https://doi.org/10.5194/egusphere-2025-3175
Preprint. Discussion started: 8 July 2025

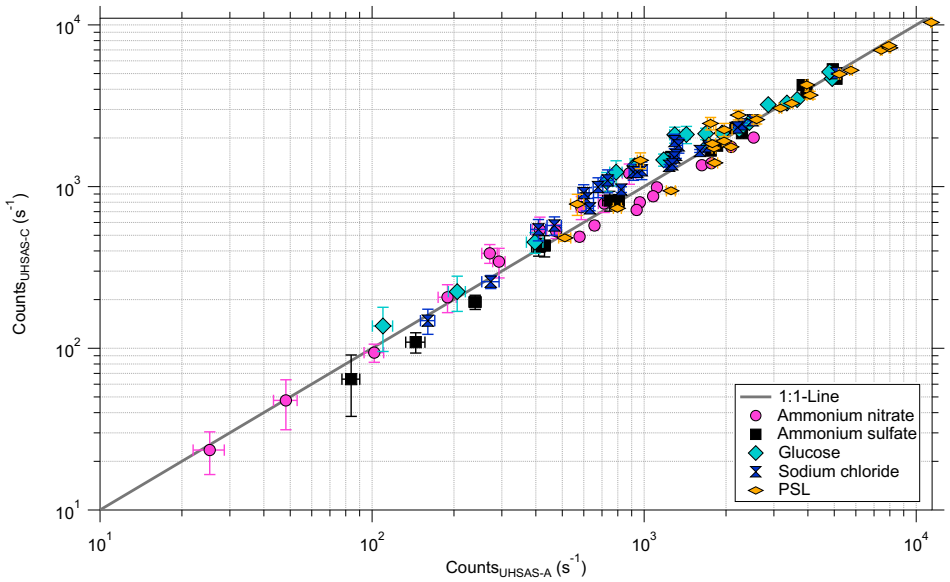

Figure 12. Median of the counts for a one minute measurement interval for different species, sizes and concentrations. The error bars represent half of the interquartile range between the 75 and 25 % percentile.

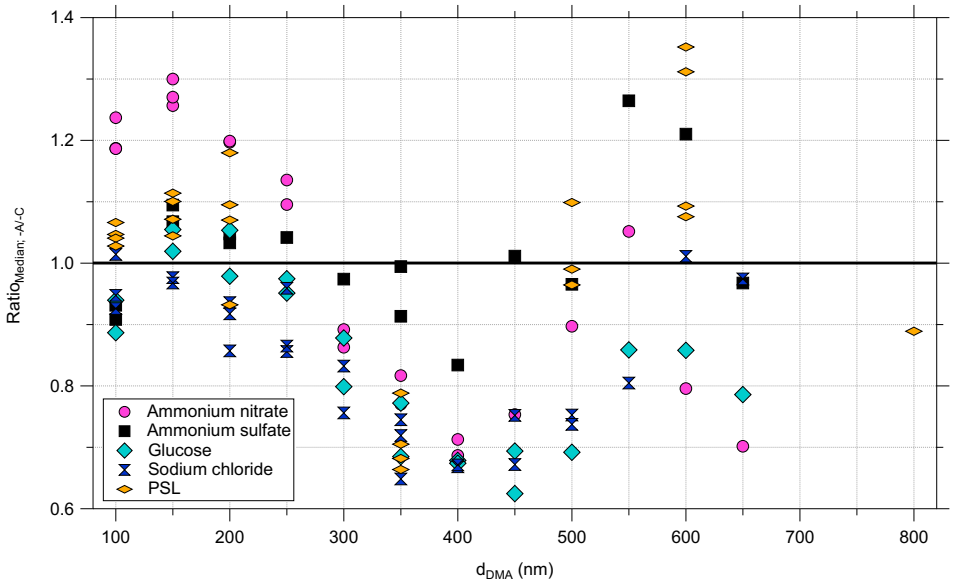

Figure 13. Ratio between the median counts of UHSAS-A divided by the median counts of the UHSAS-C. The colors and symbols indicate the different aerosol species; ammonium nitrate (pink, circle), ammonium sulfate (black, square), glucose (bright blue, tilted square) sodium chloride (blue, hourglass) and PSL (orange, diamond).

https://doi.org/10.5194/egusphere-2025-3175
Preprint. Discussion started: 8 July 2025

5 In-flight performance of TPC-TOSS and atmospheric measurements

5.1 TPC-TOSS attitude and position of platforms

During TPEx I in June 2024 the towed sensor shuttle was expected to have a similar or even improved flight characteristic as on previous campaigns (Frey et al., 2009; Klingebiel et al., 2017; Finger et al., 2016). Changes in instrumentation compared to the AIRTOSS-ICE mission in 2013 led to a more symmetric shape of the front of the drag body as the asymmetric CCP-CDP (Cloud Combination Probe - Cloud Droplet Probe) instrument was exchanged with the UHSAS-A instrument with a inlet tube in the center of the circular area of the TPC-TOSS geometry (Fig. 3 lower panel). The bypass inlet and outlet were symmetrically mounted left and right in back part of the TPC-TOSS (Fig. 3 upper panel). In addition, air brakes were installed on the four wings of the drag body to further improve flight behavior.

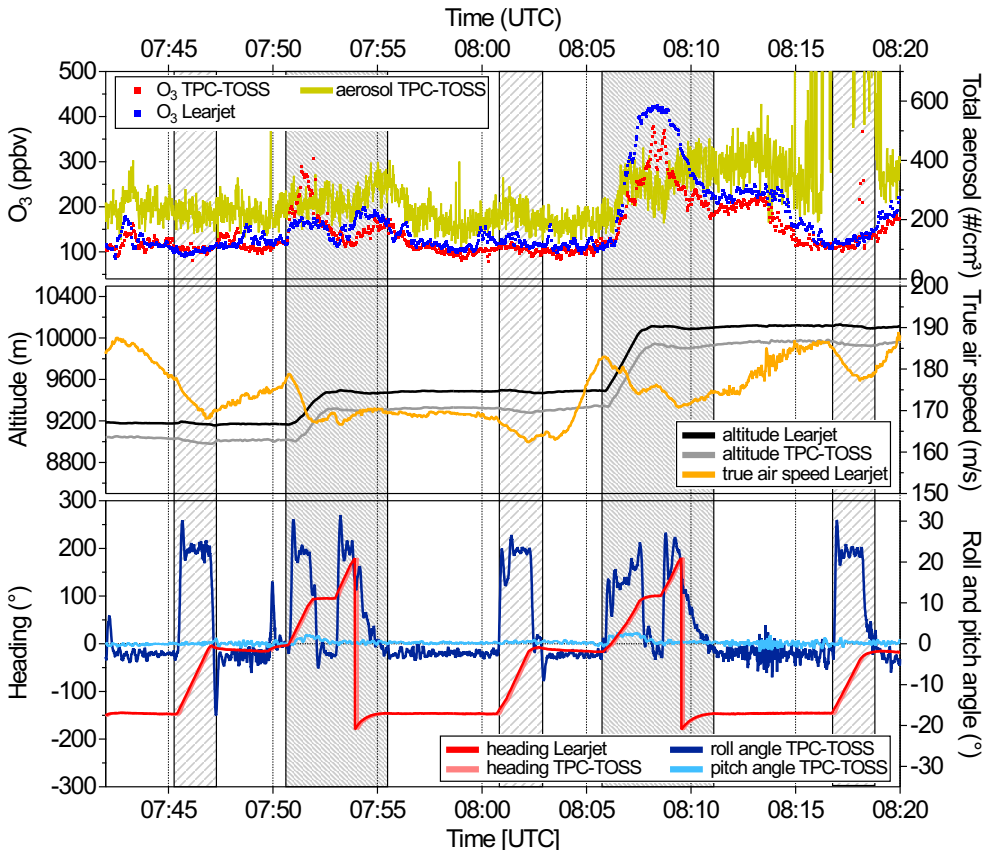

Figure 14. Excerpt from research flight F10 on 20 June 2024 during TPEx 2024. The upper panel shows measured mixing ratio of ozone on Learjet (blue) and TPC-TOSS (red) as well as total aerosol number concentration measured with UHSAS-A (yellow). The middle panel contains Learjet (black) and TPC-TOSS (grey) altitude and true air speed of the Learjet (orange). The lower panels show Learjet and TPC-TOSS heading in red and light red and roll and pitch angle of TPC-TOSS in blue and light blue colors. The first, third and fifth dashed rectangle show turns of Learjet and TPC-TOSS and the second and fourth dashed rectangle mark the combination of turn and climb.

https://doi.org/10.5194/egusphere-2025-3175
Preprint. Discussion started: 8 July 2025

Figure 14 shows flight attitude of the TPC-TOSS in different flight phases (turns, climbs and combination of both) during a part of research flight F10. As shown in Fig. 1 (red flight tracks) the deployment of the TPC-TOSS is only allowed in small restricted air spaces in the North Sea and Baltic Sea with dimensions on the order of 50 x 50 km provoking numerous turns to stay within the air space. At ideal stable flight conditions (no turns and no climb or descent, e.g. F10 7:57:42–8:00:34) the flight behavior is characterized using the following flight parameters. The roll angle of the drag body was stable at –2.43 ± 0.53°, pitch angle average during above mentioned time interval was 0.18 ± 0.16° and yaw angle averaged to –147.45 ± 0.41°. The negative roll angle could be explained by the TPC-TOSS flying slightly sideways from the aircraft which in turn causes an additional force component on the TPC-TOSS to the left from the towing cable (Frey et al., 2009). Pitch and yaw angle stay very stable during undisturbed flight conditions. Deviations from this flight conditions could be introduced by turns (changes in the heading accompanied by changes in the roll angle) and climbs (additional change in the pitch angle) as the TPC-TOSS is slightly accelerated during climb resulting in the nose moving down which in turn gives small positive deviation of the pitch angle. Furthermore, stronger variations in the roll angle at constant conditions flight phases with respect to turns and climbs or descents could be forced by turbulence in the atmosphere. As flights were designed to study the effect of turbulence introduced by for example internal dynamics of cirrus clouds on the chemical composition of the atmosphere it was expected to experience these types of flight conditions. Fortunately, none of the deviations from stable flight conditions affected trace gas and aerosol measurements significantly as shown in the upper panel of Fig. 14. In particular during turns and altitude changes measurements seem unaffected from significant change in the roll angle during flight manouvers. In contrast to previous campaigns that needed a stable roll angle of the TPC-TOSS within ±3° for proper radiation measurements, trace species and aerosol measurements during TPEx I were still possible in turns and climbs and the decay time (time needed for the TPC-TOSS to recover to stable attitude conditions after turns and/or climbs and descents) could still be used as measurement time. In addition temperature and humidity measurements from the ICH sensor on the TPC-TOSS (not shown) seem unaffected during the decay times.

5.2 Meteorological parameters and ozone measurements

The measurements during TPEx I provide simultaneous and colocated in situ measurements of aerosol and ozone at a short vertical distance between the TPC-TOSS and the Learjet. This enables, for the first time, the determination of gradients of these substances in the UTLS based on in situ data. The simultaneous measurements are in particular important for studying the effect of transient small scale dynamics in the UTLS on the composition of and mixing in the respective region. Features associated with small scale turbulent dynamics are often very short in time and limited in space. This makes them often difficult to probe sufficiently with only measurements from an aircraft. Determination of turbulent fluxes require the observations of gradients (e.g. Shapiro, 1980). With the TPC-TOSS this is now possible without correcting for larger time lags due to multiple necessary legs of the aircraft through a turbulent region. However, also with the TPC-TOSS there is lag which needs to be considered, since the TPC-TOSS is up to 900 m behind and up to 200 m sideways of the aircraft. Still, this lag is much smaller than the lag associated with aircraft only measurements and amounts to 5–6 s. The temperature measurements combined with the pressure data provide potential temperature gradients in the UTLS region. This in turn provides a measure of stability in the respective altitude range covered by TPC-TOSS and Learjet. Together with the vertical gradients of ozone and aerosol we

https://doi.org/10.5194/egusphere-2025-3175
Preprint. Discussion started: 8 July 2025

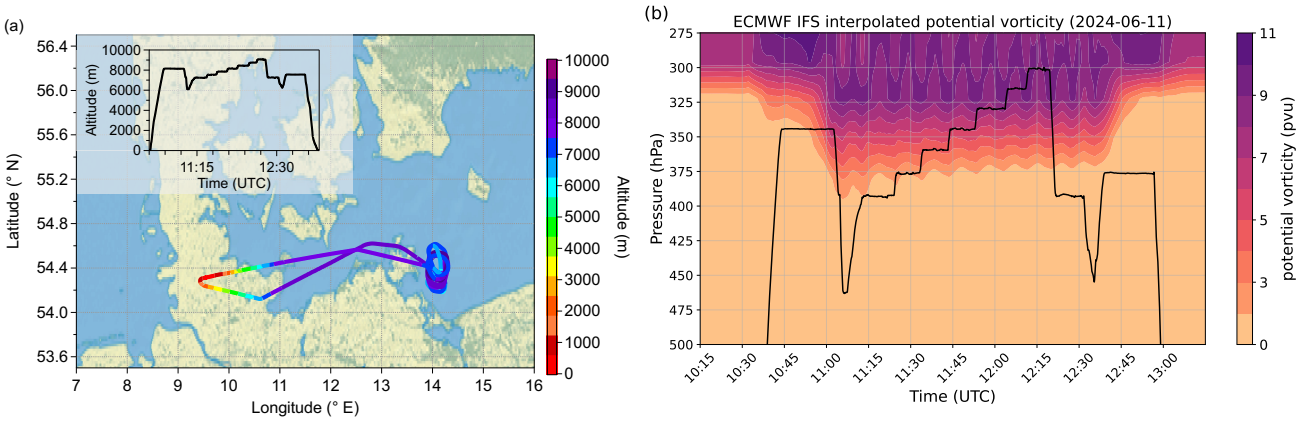

Figure 15. (a) Flight track of research flight F03 during TPEx on 11 June 2024. The flight track is colour coded with altitude as also given by the inset figure. (b) Interpolated potential vorticity from the ECMWF IFS model along the flight track between 500 hPa and 275 hPa. The map was created from public-domain GIS data found on the Natural Earth website (http://www.naturalearthdata.com, last access: 30 June 2025).

can study the effect of changes in stability (triggered for example by clouds) on the composition of the UTLS and also mixing processes.

The advantage of the dual platform approach during TPEx I is summarized in Fig. 16. Figure 15a shows the corresponding flight track of research flight F03 on 11 June 2024 as well as the altitude profile of the flight. The target region was the restricted air space in the Baltic Sea. The aim of that flight was to probe mixing in the upper troposphere and tropopause region within an area of low tropopause altitudes. The flight was planned with stacked flight levels of 1000 ft ($\approx$ 305 m) distance within the restricted air space after the TPC-TOSS was deployed. Figure 15b shows the potential vorticity from the ECMWF IFS (European Centre for Medium Range Weather Forecast - Integrated Forecast System) along the flight track between 275 hPa and 500 hPa. While the early and late parts of the flight are in the troposphere, the Learjet ascended stepwise deeper into the stratosphere during the stacked flight levels.

Figure 16 shows time series of different quantities of that part of the flight when TPC-TOSS was released. The top panel shows the heading of the TPC-TOSS in grey indicating the frequent turns that were flown in the restricted air space. The altitude difference between Learjet and TPC-TOSS is shown in black. On average the TPC-TOSS was located 170 m (range 130 to 200 m depending on flight condition) below the aircraft. Short periods of time increasing 200 m vertical altitude distance between Learjet and TPC-TOSS were only observed during the short climbs to the next flight level. The middle panel shows the difference of ozone (blue) and potential temperature (red) between Learjet and TPC-TOSS derived from collocated measurements of ozone and temperature on TPC-TOSS and Learjet. The lower panel shows the determined gradients of ozone (green) and potential temperature (orange) with altitude. The shaded areas in this figure denotes the errors of the measured and calculated quantities. The altitude is measured with an uncertainty of $\pm$ 2 m, the uncertainty for the temperature measurements is $\pm$ 0.32 K. For the calculation of potential temperature the uncertainty of the determined pressure value of $\pm$ 1 hPa needs to

https://doi.org/10.5194/egusphere-2025-3175
Preprint. Discussion started: 8 July 2025

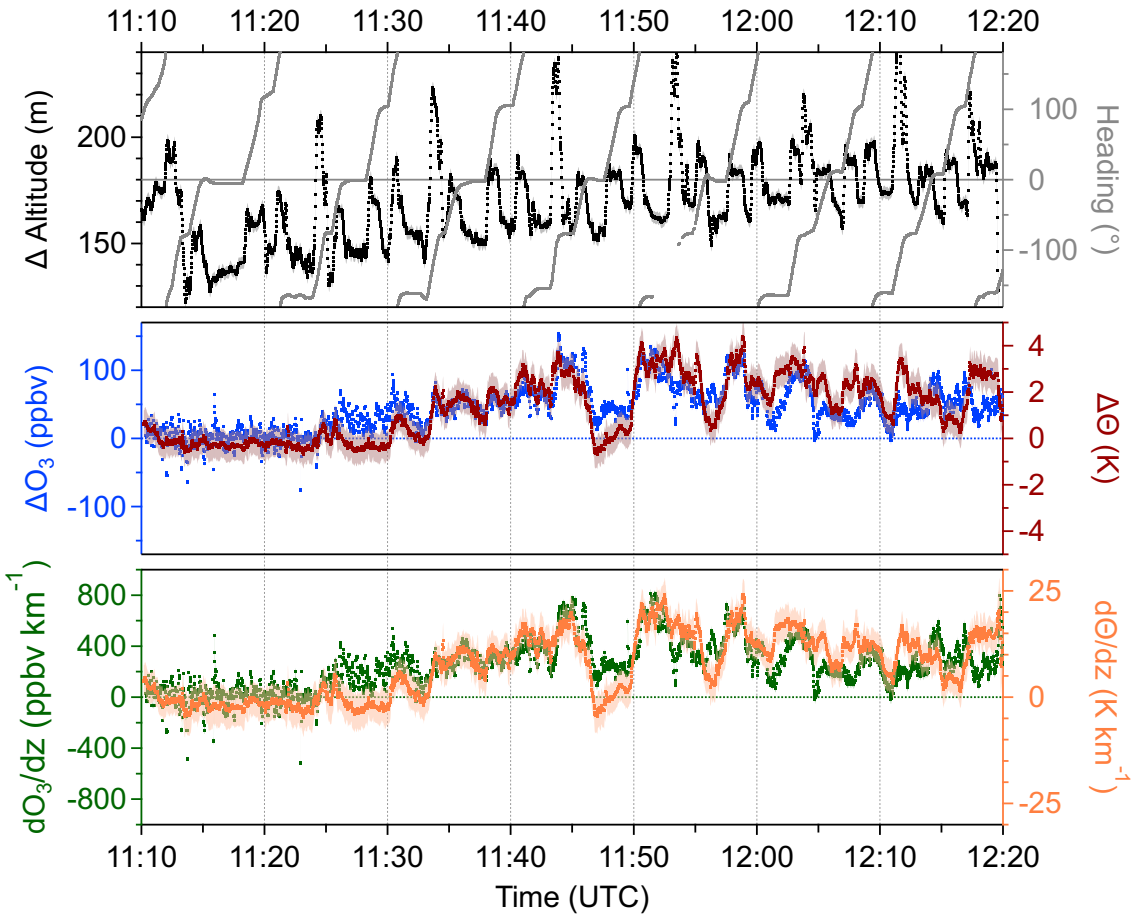

Figure 16. Time series of the altitude difference between Learjet and TPC-TOSS including Learjet heading (upper panel), difference of ozone and potential temperature between both platforms (middle panel) and ozone and theta gradients along the flight (lower panel)

be further considered. Also taking into account the uncertainty for ozone (± (3 ppbv + 0.9 %) for TPC-TOSS and ± (3 ppbv + 0.7 %) for "Knuffi") these individual errors propagate into the determination of the gradients resulting in an uncertainty of the ozone gradient of up to 10 % and for the potential temperature gradient (Θ) the uncertainty amounts to 31 %.

The Θ gradient could now be used to get an indication of stability in the atmosphere. During the first part of the flight with TPC-TOSS released until around 11:25 UTC almost no vertical gradient in ozone and Θ is observed indicating a flight mostly in tropospheric conditions (Fig. 15b). The stratosphere in general is characterized by strong static stability and thus a positive potential temperature gradient. Ozone is strongly increasing with altitude in the stratosphere also resulting in a positive vertical gradient. The increasing vertical gradient in Θ and ozone from 11:25 UTC on until 11:45 UTC thus indicates increasing stratospheric influence. Afterwards there are strong variations observed in the gradients. Reduced vertical gradients in potential temperature could indicate a less stable stratification of the atmosphere with a potential for mixing which in turn could further

https://doi.org/10.5194/egusphere-2025-3175
Preprint. Discussion started: 8 July 2025

reduce the vertical ozone gradient as for example observed between around 11:45 and 11:50 UTC. While a further analysis of Θ and ozone gradients is beyond the scope of this paper, the example of research flight F03 shows the potential of the dual platform approach to identify and study mixing processes in the UTLS regions.

5.3 Aerosol size distribution measurements

For the in-flight performance analysis and comparison of both UHSAS systems at the TPC-TOSS and Learjet we use an interval during flight F10 (20 June 2024). Here, both platforms were operated on the shortest possible vertical distance of about 43 m for several minutes. We averaged the size distribution from both UHSAS systems over 60 seconds (Fig. 17), Also shown in Fig. 17 is the size distribution measured by the Sky-OPC operated in the Learjet cabin.. For this time period, we observe a very good agreement of both UHSAS systems, especially for particles smaller than 500 nm. For particles larger than 500 nm, there are some differences between UHSAS-A and -C, but these differences are smaller than one magnitude and explainable by different gain stitching of the instruments. Additionally, the comparison for particles larger than 250 nm with the SkyOPC shows a good agreement.

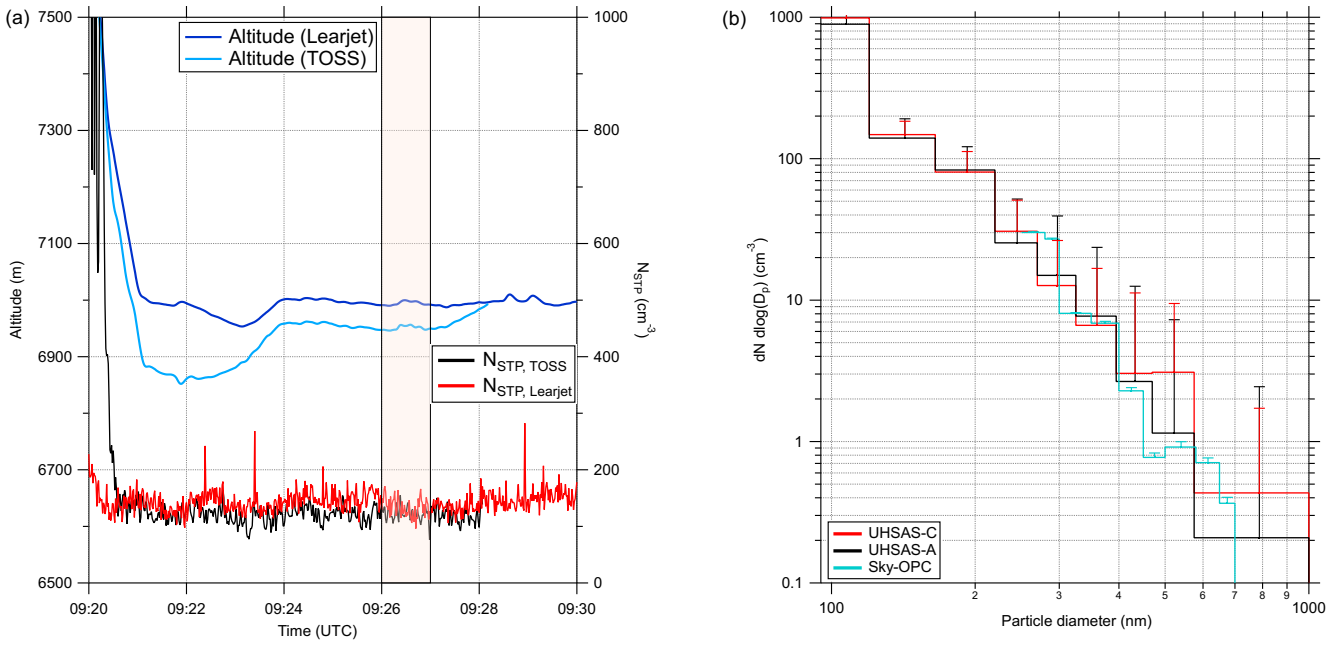

Figure 17. Timeseries of the Learjet and TOSS altitude in combination with the STP corrected number concentrations of both UHSAS (-A and -C) during the last minutes in the restricted airspace of F10 on 20 June 2024 between 09:26:00 and 09:27:00 UTC. (a). The orange box marks the period with the TOSS at the closest safe operation distance to the Learjet (ca. 43 m) for instrument in-flight intercomparison. The averaged size distributions during this period of both UHSAS (-A and -C) and the Sky-OPC at the Learjet is shown in (b). We only show the positive standard deviation of the averaged size distribution as consequence of the logarithmic visualization.

https://doi.org/10.5194/egusphere-2025-3175
Preprint. Discussion started: 8 July 2025

6 Summary and conclusion

During TPEx I, we demonstrated the first closely colocated, simultaneous trace gas and aerosol measurements in the UTLS region using a tandem platform approach, consisting of a Learjet 35A and a redesigned towed sensor shuttle, TPC-TOSS. TPC-TOSS was positioned up to 900 m behind and up to 200 m lateral to the aircraft during flights.

Based on laboratory and field intercomparisons, redundant instrumentation for temperature and ozone measurements on TPC-TOSS and Learjet agree better than 0.45 °C for the temperature data (based on the individual total uncertainties of the respective ICH sensors of 0.32 °C). For ozone the agreement is better than 4.2 ppbv + 1.1 % for the range of ambient ozone measurements (based on total uncertainties of the individual ozone instruments). In addition also aerosol size distribution measurements by the UHSAS instruments on both platforms indicate similar structures for specific flight sections, which is however partly masked by the high natural variability of aerosol number concentration.

Our results showed that the dual platform approach with the instrument performances reported above in particular allows for using measured temperature gradients as an indication for static stability and to further derive ozone gradients based on the simultaneous measurements in two altitudes in the UTLS. Comparing both, ozone and Θ simultaneously at two levels allows to identify the effect of diabatic (Θ changing) processes on the ozone distribution and thus mixing. As an example during research flight F03 (Fig. 16) variations in static stability based on Θ gradients could either be linked to more tropospheric influence or diabatic processes.

Besides trace species measurements two UHSAS instruments on TPC-TOSS and Learjet for the first time allow for the study of the impact of these small scale dynamical features on aerosol concentration and size distribution in the UTLS. A very recent study by Joppe et al. (2025) also used the potential temperature gradient based on the dual platform measurements to further analyze the radiative impact of biomass burning aerosol transported into the UTLS by warm conveyor type transport.

While a more detailed analysis of trace species and aerosol behavior is beyond the scope of this paper, this study highlights the advantages of the successful deployment of the novel re-designed TPC-TOSS providing a unique data set well suited for the analysis of transient small scale dynamics on the UTLS composition during TPEx I in 2024 and future campaigns.

Data availability. In situ data are available from the Zenodo platform (https://doi.org/10.5281/zenodo.15371527). Data from ECMWF for the IFS forecast has been retrieved from the MARS system (https://confluence.ecmwf.int/display/UDOC/MARS+user+documentation). Data description is available from https://www.ecmwf.int/en/forecasts/datasets/set-i.

Author contributions. Author contributions. HB wrote the paper, with significant conceptual input from PH, PJ and YL and critical feedback from all co-authors. HB, JS, PJ, NE, AB, SI, SR, CR, AA and LS operated instruments in the field and analyzed resulting data. DK provided IFS data along the flight path. HCL provided the merged data file for analysis. NE and PH are responsible for ozone, GNSS/INS and UMAQS data. AA and CR are responsible for NIXE-CAPS, FISH and WASUL data. PJ and JS are responsible for UHSAS, SkyOPC and CARIBIC-AMS data. YL and AP are responsible for ICH and BCP data. SR und JC are responsible for MC-CPC data. AB and AV are responsible for

https://doi.org/10.5194/egusphere-2025-3175
Preprint. Discussion started: 8 July 2025

the SOAP data. SI, KK and LS are responsible for the impactor samples and the analysis in the SEM. AK, TR and SH were responsible for planning, manufacturing and certifying the TPC-TOSS.

Competing interests. Some authors are members of the editorial board of the journal Atmospheric Measurement Techniques.

Acknowledgements. The authors acknowledge the team of enviscope GmbH and GFD GmbH for the opportunity to carry out the campaign and the technical support during the campaign.

All Authors acknowledge funding by the Deutsche Forschungsgemeinschaft (DFG, German Research Foundation) – TRR 301 – Project-ID 428312742: “The tropopause region in a changing atmosphere”

https://doi.org/10.5194/egusphere-2025-3175
Preprint. Discussion started: 8 July 2025

References

Allan, D.: Statistics of atomic frequency standards, Proceedings of the IEEE, 54, 221–230, https://doi.org/10.1109/PROC.1966.4634, 1966.

Bauchinger, S., Engel, A., Jesswein, M., Keber, T., Bönisch, H., Obersteiner, F., Zahn, A., Emig, N., Hoor, P., Lachnitt, H.-C., Weyland, F., Ort, L., and Schuck, T. J.: The extratropical tropopause – Trace gas perspective on tropopause definition choice, EGUsphere, pp. 1–29, https://doi.org/10.5194/egusphere-2025-1589, publisher: Copernicus GmbH, 2025.

Bauer, R., Grooß, J.-U., Ungermann, J., Bär, M., Geldenhuys, M., and Hoffmann, L.: The Mission Support System (MSS v7.0.4) and its use in planning for the SouthTRAC aircraft campaign, Geoscientific Model Development, 15, 8983–8997, https://doi.org/10.5194/gmd-15-8983-2022, publisher: Copernicus GmbH, 2022.

Beswick, K., Baumgardner, D., Gallagher, M., Volz-Thomas, A., Nedelec, P., Wang, K.-Y., and Lance, S.: The backscatter cloud probe – a compact low-profile autonomous optical spectrometer, Atmospheric Measurement Techniques, 7, 1443–1457, https://doi.org/10.5194/amt-7-1443-2014, publisher: Copernicus GmbH, 2014.

Bethan, S., Vaughan, G., and Reid, S. J.: A comparison of ozone and thermal tropopause heights and the impact of tropopause definition on quantifying the ozone content of the troposphere, Quarterly Journal of the Royal Meteorological Society, 122, 929–944, https://doi.org/10.1002/qj.49712253207, 1996.

Birks, J. W., Williford, C. J., Andersen, P. C., Turnipseed, A. A., Strunk, S., and Ennis, C. A.: Portable ozone calibration source independent of changes in temperature, pressure and humidity for research and regulatory applications, Atmos. Meas. Tech., 11, 4797–4807, https://doi.org/10.5194/amt-11-4797-2018, 2018.

Bundke, U., Berg, M., Houben, N., Ibrahim, A., Fiebig, M., Tettich, F., Klaus, C., Franke, H., and Petzold, A.: The IAGOS-CORE aerosol package: instrument design, operation and performance for continuous measurement aboard in-service aircraft, Tellus B: Chemical and Physical Meteorology, 67, 28 339, https://doi.org/10.3402/tellusb.v67.28339, 2015.

Cai, Y., Montague, D. C., Mooiweer-Bryan, W., and Deshler, T.: Performance characteristics of the ultra high sensitivity aerosol spectrometer for particles between 55 and 800nm: Laboratory and field studies, Journal of Aerosol Science, 39, 759–769, https://doi.org/10.1016/j.jaerosci.2008.04.007, 2008.

Ebert, M., Weigel, R., Kandler, K., Gunther, G., Molleker, S., Grooß, J. U., Vogel, B., Weinbruch, S., and Borrmann, S.: Chemical analysis of refractory stratospheric aerosol particles collected within the arctic vortex and inside polar stratospheric clouds, Atmospheric Chemistry and Physics, 16, 8405–8421, https://doi.org/10.5194/acp-16-8405-2016, 2016.

Finger, F., Werner, F., Klingebiel, M., Ehrlich, A., Jäkel, E., Voigt, M., Borrmann, S., Spichtinger, P., and Wendisch, M.: Spectral optical layer properties of cirrus from collocated airborne measurements and simulations, Atmospheric Chemistry and Physics, 16, 7681–7693, https://doi.org/10.5194/acp-16-7681-2016, 2016.

Frey, W., Eichler, H., de Reus, M., Maser, R., Wendisch, M., and Borrmann, S.: A new airborne tandem platform for collocated measurements of microphysical cloud and radiation properties, Atmospheric Measurement Techniques, 2, 147–158, https://doi.org/10.5194/amt-2-147-2009, 2009.

Frey, W., Borrmann, S., Fierli, F., Weigel, R., Mitev, V., Matthey, R., Ravegnani, F., Sitnikov, N. M., Ulanovsky, A., and Cairo, F.: Tropical deep convective life cycle: Cb-anvil cloud microphysics from high-altitude aircraft observations, Atmospheric Chemistry and Physics, 14, 13 223–13 240, https://doi.org/10.5194/acp-14-13223-2014, 2014.

Fusina, F. and Spichtinger, P.: Cirrus clouds triggered by radiation, a multiscale phenomenon, Atmospheric Chemistry and Physics, 10, 5179–5190, https://doi.org/10.5194/acp-10-5179-2010, 2010.

https://doi.org/10.5194/egusphere-2025-3175
Preprint. Discussion started: 8 July 2025

Helten, M., Smit, H. G. J., Sträter, W., Kley, D., Nedelec, P., Zöger, M., and Busen, R.: Calibration and performance of automatic compact instrumentation for the measurement of relative humidity from passenger aircraft, Journal of Geophysical Research: Atmospheres, 103, 25 643–25 652, https://onlinelibrary.wiley.com/doi/abs/10.1029/98JD00536, publisher: John Wiley & Sons, Ltd, 1998.

Hoor, P., Fischer, H., Lange, L., Lelieveld, J., and Brunner, D.: Seasonal variations of a mixing layer in the lowermost stratosphere as identified by the CO-O3 correlation from in situ measurements, Journal of Geophysical Research: Atmospheres, 107, ACL 1–1–ACL 1–11, https://doi.org/10.1029/2000JD000289, 2002.

Jensen, E., Starr, D., and Toon, O. B.: Mission investigates tropical cirrus clouds, Eos, Transactions American Geophysical Union, 85, 45–50, https://doi.org/10.1029/2004EO050002, _eprint: https://onlinelibrary.wiley.com/doi/pdf/10.1029/2004EO050002, 2004.

Johnson, T., Capel, J., and Ollison, W.: Measurement of microenvironmental ozone concentrations in Durham, North Carolina, using a 2B Technologies 205 Federal Equivalent Method monitor and an interference-free 2B Technologies 211 monitor, J. Air Waste Manage. Assoc., 64, 360–371, https://doi.org/10.1080/10962247.2013.839968, 2014.

Joppe, P., Schneider, J., Wilsch, J., Bozem, H., Breuninger, A., Curtius, J., Ebert, M., Emig, N., Hoor, P., Ismayil, S., Kandler, K., Kunkel, D., Kurth, I., Lachnitt, H.-C., Li, Y., Miltenberger, A., Richter, S., Rolf, C., Schneider, L., Schwenk, C., Spelten, N., Vogel, A. L., Cheng, Y., and Borrmann, S.: Transport of Biomass Burning Aerosol into the Extratropical Tropopause Region over Europe via Warm Conveyor Belt Uplift, https://doi.org/10.5194/egusphere-2025-1346, 2025.

Jurányi, Z., Lüpkes, C., Stratmann, F., Hartmann, J., Schaefer, J., Jörss, A.-M., Schulz, A., Wetzel, B., Simon, D., Gebhard, E., Stöhr, M., Hofmann, P., Kalmbach, D., Grawe, S., and Herber, A.: The T-Bird – A new aircraft-towed instrument platform to measure turbulence and aerosol properties close to the surface: Introduction to the aerosol measurement system, EGUsphere, pp. 1–27, https://doi.org/10.5194/egusphere-2025-619, publisher: Copernicus GmbH, 2025.

Klingebiel, M., Ehrlich, A., Finger, F., Röschenthaler, T., Jakirlić, S., Voigt, M., Müller, S., Maser, R., Wendisch, M., Hoor, P., Spichtinger, P., and Borrmann, S.: A tandem approach for collocated measurements of microphysical and radiative cirrus properties, Atmospheric Measurement Techniques, 10, 3485–3498, https://doi.org/10.5194/amt-10-3485-2017, 2017.

Konjari, P., Rolf, C., Krämer, M., Afchine, A., Spelten, N., Bartolome Garcia, I., Miltenberger, A., Emig, N., Joppe, P., Schneider, J., Li, Y., Petzold, A., Bozem, H., and Hoor, P.: Stratospheric Hydration and Ice Microphysics of a Convective Overshoot Observed during the TPEx Campaign over Sweden, EGUsphere, pp. 1–27, https://doi.org/10.5194/egusphere-2025-2847, publisher: Copernicus GmbH, 2025.

Krämer, M., Rolf, C., Spelten, N., Afchine, A., Fahey, D., Jensen, E., Khaykin, S., Kuhn, T., Lawson, P., Lykov, A., Pan, L. L., Riese, M., Rollins, A., Stroh, F., Thornberry, T., Wolf, V., Woods, S., Spichtinger, P., Quaas, J., and Sourdeval, O.: A microphysics guide to cirrus – Part 2: Climatologies of clouds and humidity from observations, Atmospheric Chemistry and Physics, 20, 12 569–12 608, https://doi.org/10.5194/acp-20-12569-2020, 2020.

Kunkel, D., Hoor, P., Kaluza, T., Ungermann, J., Kluschat, B., Giez, A., Lachnitt, H. C., Kaufmann, M., and Riese, M.: Evidence of small-scale quasi-isentropic mixing in ridges of extratropical baroclinic waves, Atmos. Chem. Phys., 19, 12 607–12 630, https://doi.org/10.5194/acp-19-12607-2019, 2019.

Kupc, A., Williamson, C., Wagner, N. L., Richardson, M., and Brock, C. A.: Modification, calibration, and performance of the Ultra-High Sensitivity Aerosol Spectrometer for particle size distribution and volatility measurements during the Atmospheric Tomography Mission (ATom) airborne campaign, Atmospheric Measurement Techniques, 11, 369–383, https://doi.org/10.5194/amt-11-369-2018, 2018.

Lachnitt, H.-C., Hoor, P., Kunkel, D., Bramberger, M., Dörnbrack, A., Müller, S., Reutter, P., Giez, A., Kaluza, T., and Rapp, M.: Gravity-wave-induced cross-isentropic mixing: a DEEPWAVE case study, Atmospheric Chemistry and Physics, 23, 355–373, https://doi.org/10.5194/acp-23-355-2023, publisher: Copernicus GmbH, 2023.

https://doi.org/10.5194/egusphere-2025-3175
Preprint. Discussion started: 8 July 2025

Lloyd, G., Gallagher, M., Choularton, T., Krämer, M., Andreas, P., and Baumgardner, D.: In Situ Measurements of Cirrus Clouds on a Global Scale, Atmosphere, 12, 41, https://doi.org/10.3390/atmos12010041, number: 1 Publisher: Multidisciplinary Digital Publishing Institute, 2021.

Mahnke, C., Weigel, R., Cairo, F., Vernier, J.-P., Afchine, A., Krämer, M., Mitev, V., Matthey, R., Viciani, S., D'Amato, F., Ploeger, F., Deshler, T., and Borrmann, S.: The Asian tropopause aerosol layer within the 2017 monsoon anticyclone: microphysical properties derived from aircraft-borne in situ measurements, Atmospheric Chemistry and Physics, 21, 15 259–15 282, https://doi.org/10.5194/acp-21-15259-2021, 2021.

Meyer, J.: Ice Crystal Measurements with the New Particle Spectrometer NIXE-CAPS, Forschungszentrum Jülich, ISBN 978-3-89336-840-2, google-Books-ID: dSL6V0ZeDs0C, 2013.

Meyer, J., Rolf, C., Schiller, C., Rohs, S., Spelten, N., Afchine, A., Zöger, M., Sitnikov, N., Thornberry, T. D., Rollins, A. W., Bozóki, Z., Tátrai, D., Ebert, V., Kühnreich, B., Mackrodt, P., Möhler, O., Saathoff, H., Rosenlof, K. H., and Krämer, M.: Two decades of water vapor measurements with the FISH fluorescence hygrometer: a review, Atmospheric Chemistry and Physics, 15, 8521–8538, https://doi.org/10.5194/acp-15-8521-2015, 2015.

Moormann, L., Böttger, T., Schuhmann, P., Valero, L., Fachinger, F., and Drewnick, F.: The Flying Laboratory FLab: development and application of a UAS to measure aerosol particles and trace gases in the lower troposphere, Atmospheric Measurement Techniques, 18, 1441–1459, https://doi.org/10.5194/amt-18-1441-2025, 2025.

Müller, S., Hoor, P., Berkes, F., Bozem, H., Klingebiel, M., Reutter, P., Smit, H. G. J., Wendisch, M., Spichtinger, P., and Borrmann, S.: In situ detection of stratosphere-troposphere exchange of cirrus particles in the midlatitudes, Geophysical Research Letters, 42, 949–955, https://doi.org/10.1002/2014GL062556, 2015.

Mynard, A., Kent, J., Smith, E. R., Wilson, A., Wivell, K., Nelson, N., Hort, M., Bowles, J., Tiddeman, D., Langridge, J. M., Drummond, B., and Abel, S. J.: Long-term airborne measurements of pollutants over the United Kingdom to support air quality model development and evaluation, Atmospheric Measurement Techniques, 16, 4229–4261, https://doi.org/10.5194/amt-16-4229-2023, 2023.

Neis, P., Smit, H. G., Krämer, M., Spelten, N., and Petzold, A.: Evaluation of the MOZAIC Capacitive Hygrometer during the airborne field study CIRRUS-III, Atmospheric Measurement Techniques, 8, 1233–1243, https://doi.org/10.5194/amt-8-1233-2015, 2015a.

Neis, P., Smit, H. G., Rohs, S., Bundke, U., Krämer, M., Spelten, N., Ebert, V., Buchholz, B., Thomas, K., and Petzold, A.: Quality assessment of MOZAIC and IAGOS capacitive hygrometers: Insights from airborne field studies, Tellus, Series B: Chemical and Physical Meteorology, 6, https://doi.org/10.3402/tellusb.v67.28320, 2015b.

Pan, L. L., Randel, W. J., Gary, B. L., Mahoney, M. J., and Hintsa, E. J.: Definitions and sharpness of the extratropical tropopause: A trace gas perspective, Journal of Geophysical Research D: Atmospheres, 109, 1–11, https://doi.org/10.1029/2004JD004982, 2004.

Petzold, A., Thouret, V., Gerbig, C., Zahn, A., Brenninkmeijer, C. A. M., Gallagher, M., Hermann, M., Pontaud, M., Ziereis, H., Boulanger, D., Marshall, J., Nédélec, P., Smit, H. G. J., Friess, U., Flaud, J.-M., Wahner, A., Cammas, J.-P., Volz-Thomas, A., and TEAM, I.: Global-scale atmosphere monitoring by in-service aircraft – current achievements and future prospects of the European Research Infrastructure IAGOS, Tellus B, 67, 28 452, https://doi.org/10.3402/tellusb.v67.28452, 2015.

Petzold, A., Krämer, M., Neis, P., Rolf, C., Rohs, S., Berkes, F., Smit, H. G. J., Gallagher, M., Beswick, K., Lloyd, G., Baumgardner, D., Spichtinger, P., Nédélec, P., Ebert, V., Buchholz, B., Riese, M., and Wahner, A.: Upper tropospheric water vapour and its interaction with cirrus clouds as seen from IAGOS long-term routine in situ observations, Faraday Discussions, 200, 229–249, https://doi.org/10.1039/C7FD00006E, 2017.

https://doi.org/10.5194/egusphere-2025-3175
Preprint. Discussion started: 8 July 2025

Pätzold, F., Bretschneider, L., Nowak, S., Brandt, B., Schlerf, A., Asmussen, M. O., Bollmann, S., Bärfuss, K., Harm-Altstädter, B., Hecker, P., Wehner, B., van der Wall, B. G., Sachs, T., Huntrieser, H., Roiger, A., and Lampert, A.: HELiPOD—Revolution and evolution of a helicopter-borne measurement system for multidisciplinary research in demanding environments, Elementa: Science of the Anthropocene, 11, 00 031, https://doi.org/10.1525/elementa.2023.00031, 2023.

Randel, W. J., Wu, F., and Forster, P.: The Extratropical Tropopause Inversion Layer: Global Observations with GPS Data, and a Radiative Forcing Mechanism, Journal of the Atmospheric Sciences, 64, 4489–4496, https://doi.org/10.1175/2007JAS2412.1, 2007.

Rolf, C., Rohs, S., Smit, H. G. J., Krämer, M., Bozóki, Z., Hofmann, S., Franke, H., Maser, R., Hoor, P., and Petzold, A.: Evaluation of compact hygrometers for continuous airborne measurements, Meteorologische Zeitschrift, pp. 15–34, https://doi.org/10.1127/metz/2023/1187, publisher: Schweizerbart'sche Verlagsbuchhandlung, 2024.

Schneider, J., Schulz, C., Rubach, F., Ludwig, A., Wilsch, J., Joppe, P., Gurk, C., Molleker, S., Poulain, L., Obersteiner, F., Gehrlein, T., Bönisch, H., Zahn, A., Hoor, P., Emig, N., Bozem, H., Borrmann, S., and Hermann, M.: CARIBIC-AMS: A fully automated aerosol mass spectrometer for operation on routine passenger flights (IAGOS-CARIBIC): Instrument description and first flight application in the UTLS, https://doi.org/10.5194/egusphere-2024-3969, 2025.

Schneider, L., Schrod, J., Weber, D., Bingemer, H., Kandler, K., Curtius, J., and Ebert, M.: Analyzing the chemical composition, morphology and size of ice-nucleating particles by coupling a scanning electron microscope to an offline diffusion chamber, EGUsphere, pp. 1–33, https://doi.org/10.5194/egusphere-2024-2797, publisher: Copernicus GmbH, 2024.

Schrod, J., Danielczok, A., Weber, D., Ebert, M., Thomson, E. S., and Bingemer, H. G.: Re-evaluating the Frankfurt isothermal static diffusion chamber for ice nucleation, Atmospheric Measurement Techniques, 9, 1313–1324, https://doi.org/10.5194/amt-9-1313-2016, publisher: Copernicus GmbH, 2016.

Shapiro, M. A.: Turbulent Mixing within Tropopause Folds as a Mechanism for the Exchange of Chemical Constituents between the Stratosphere and Troposphere, Journal of the Atmospheric Sciences, 37, 994–1004, https://doi.org/10.1175/1520-0469(1980)037<0994:TMWTFA>2.0.CO;2, 1980.

Siebert, H., Franke, H., Lehmann, K., Maser, R., Saw, E. W., Schell, D., Shaw, R. A., and Wendisch, M.: Probing Finescale Dynamics and Microphysics of Clouds with Helicopter-Borne Measurements, Bulletin of the American Meteorological Society, 87, 1727–1738, https://doi.org/10.1175/BAMS-87-12-1727, publisher: American Meteorological Society Section: Bulletin of the American Meteorological Society, 2006.

Smit, H. G. J., Kley, D., Sträter, W., and Helten, M.: Environmental simulation facility to calibrate airborne ozone and humidity sensors, Tech. Rep. PreJuSER-60217, Forschungszentrum Jülich GmbH Zentralbibliothek, Verlag, https://juser.fz-juelich.de/record/60217, 2000.

Sorooshian, A., Alexandrov, M. D., Bell, A. D., Bennett, R., Betito, G., Burton, S. P., Buzanowicz, M. E., Cairns, B., Chemyakin, E. V., Chen, G., Choi, Y., Collister, B. L., Cook, A. L., Corral, A. F., Crosbie, E. C., van Diedenhoven, B., DiGangi, J. P., Diskin, G. S., Dmitrovic, S., Edwards, E.-L., Fenn, M. A., Ferrare, R. A., van Gilst, D., Hair, J. W., Harper, D. B., Hilario, M. R. A., Hostetler, C. A., Jester, N., Jones, M., Kirschler, S., Kleb, M. M., Kusterer, J. M., Leavor, S., Lee, J. W., Liu, H., McCauley, K., Moore, R. H., Nied, J., Notari, A., Nowak, J. B., Painemal, D., Phillips, K. E., Robinson, C. E., Scarino, A. J., Schlosser, J. S., Seaman, S. T., Seethala, C., Shingler, T. J., Shook, M. A., Sinclair, K. A., Smith Jr., W. L., Spangenberg, D. A., Stamnes, S. A., Thornhill, K. L., Voigt, C., Vömel, H., Wasilewski, A. P., Wang, H., Winstead, E. L., Zeider, K., Zeng, X., Zhang, B., Ziemba, L. D., and Zuidema, P.: Spatially coordinated airborne data and complementary products for aerosol, gas, cloud, and meteorological studies: the NASA ACTIVATE dataset, Earth System Science Data, 15, 3419–3472, https://doi.org/10.5194/essd-15-3419-2023, publisher: Copernicus GmbH, 2023.

https://doi.org/10.5194/egusphere-2025-3175
Preprint. Discussion started: 8 July 2025

Tátrai, D., Bozóki, Z., Smit, H., Rolf, C., Spelten, N., Krämer, M., Filges, A., Gerbig, C., Gulyás, G., and Szabó, G.: Dual-channel photoacoustic hygrometer for airborne measurements: background, calibration, laboratory and in-flight intercomparison tests, Atmospheric Measurement Techniques, 8, 33–42, https://doi.org/10.5194/amt-8-33-2015, publisher: Copernicus GmbH, 2015.

Wendisch, M., Crewell, S., Ehrlich, A., Herber, A., Kirbus, B., Lüpkes, C., Mech, M., Abel, S. J., Akansu, E. F., Ament, F., Aubry, C., Becker, S., Borrmann, S., Bozem, H., Brückner, M., Clemen, H.-C., Dahlke, S., Dekoutsidis, G., Delanoë, J., De La Torre Castro, E., Dorff, H., Dupuy, R., Eppers, O., Ewald, F., George, G., Gorodetskaya, I. V., Grawe, S., Groß, S., Hartmann, J., Henning, S., Hirsch, L., Jäkel, E., Joppe, P., Jourdan, O., Jurányi, Z., Karalis, M., Kellermann, M., Klingebiel, M., Lonardi, M., Lucke, J., Luebke, A. E., Maahn, M., Maherndl, N., Maturilli, M., Mayer, B., Mayer, J., Mertes, S., Michaelis, J., Michalkov, M., Mioche, G., Moser, M., Müller, H., Neggers, R., Ori, D., Paul, D., Paulus, F. M., Pilz, C., Pithan, F., Pöhlker, M., Pörtge, V., Ringel, M., Risse, N., Roberts, G. C., Rosenburg, S., Röttenbacher, J., Rückert, J., Schäfer, M., Schaefer, J., Schemann, V., Schirmacher, I., Schmidt, J., Schmidt, S., Schneider, J., Schnitt, S., Schwarz, A., Siebert, H., Sodemann, H., Sperzel, T., Spreen, G., Stevens, B., Stratmann, F., Svensson, G., Tatzelt, C., Tuch, T., Vihma, T., Voigt, C., Volkmer, L., Walbröl, A., Weber, A., Wehner, B., Wetzel, B., Wirth, M., and Zinner, T.: Overview: quasi-Lagrangian observations of Arctic air mass transformations – introduction and initial results of the HALO–(AC)^3 aircraft campaign, Atmos. Chem. Phys., 24, 8865–8892, https://doi.org/10.5194/acp-24-8865-2024, 2024.

Werle, P.: Accuracy and precision of laser spectrometers for trace gas sensing in the presence of optical fringes and atmospheric turbulence, Appl. Phys. B, 102, 313–329, https://doi.org/10.1007/s00340-010-4165-9, 2011.

Werner, F., Siebert, H., Pilewskie, P., Schmeissner, T., Shaw, R. A., and Wendisch, M.: New airborne retrieval approach for trade wind cumulus properties under overlying cirrus, Journal of Geophysical Research: Atmospheres, 118, 3634–3649, https://doi.org/10.1002/jgrd.50334, _eprint: https://agupubs.onlinelibrary.wiley.com/doi/pdf/10.1002/jgrd.50334, 2013.

Werner, F., Ditas, F., Siebert, H., Simmel, M., Wehner, B., Pilewskie, P., Schmeissner, T., Shaw, R. A., Hartmann, S., Wex, H., Roberts, G. C., and Wendisch, M.: Twomey effect observed from collocated microphysical and remote sensing measurements over shallow cumulus, Journal of Geophysical Research: Atmospheres, 119, 1534–1545, https://doi.org/10.1002/2013JD020131, _eprint: https://agupubs.onlinelibrary.wiley.com/doi/pdf/10.1002/2013JD020131, 2014.

Yates, E. L., Iraci, L. T., Roby, M. C., Pierce, R. B., Johnson, M. S., Reddy, P. J., Tadić, J. M., Loewenstein, M., and Gore, W.: Airborne observations and modeling of springtime stratosphere-to-troposphere transport over California, Atmospheric Chemistry and Physics, 13, 12 481–12 494, https://doi.org/10.5194/acp-13-12481-2013, 2013.

Zöger, M., Afchine, A., Eicke, N., Gerhards, M.-T., Klein, E., McKenna, D. S., Mörschel, U., Schmidt, U., Tan, V., Tuitjer, F., Woyke, T., and Schiller, C.: Fast in situ stratospheric hygrometers: A new family of balloon-borne and airborne Lyman α photofragment fluorescence hygrometers, Journal of Geophysical Research: Atmospheres, 104, 1807–1816, https://doi.org/10.1029/1998JD100025, _eprint: https://onlinelibrary.wiley.com/doi/pdf/10.1029/1998JD100025, 1999.

4

CONCLUSION

Small-scale atmospheric processes, for example cross-tropopause mixing, are difficult to investigate as it is challenging to cover these processes by atmospheric modeling due to the limited availability of high-resolution in-situ measurements at the tropopause region.
However, it is important to study these processes as they influence the chemical composition of the tropopause region and as consequence influence the radiation balance of the atmosphere.
In this thesis, two case-studies based on in-situ airborne measurements are presented. These studies improve the understanding of aerosol particles in the UTLS region. With the gained knowledge, the questions from the beginning can now be partly answered, even if some deeper analysis on the global scale of these processes is still necessary.

How is the ExTL defined by aerosol particles, compared to trace gas observations?

This question is not answered directly in the presented studies, but can be answered to some extend by the performed data analysis. Here, it is found that aerosol particles do not show a strictly defined transition across the extratropical tropopause, such as CO does. Though, in the absence of additional sources, of for example sulfur compounds, SO_4 can be used as additional marker for stratospheric air masses as it correlates almost linearly with O_3 in the LMS. Other chemical compounds measured by the AMS were also analyzed, but did not show any clear transition regime between tropospheric and stratospheric character. In contrast, these compounds show a sharp gradient across the tropopause instead of a smooth transition over several Kelvin potential temperature in the vertical.

What is the influence of small-scale dynamical processes, such as turbulent mixing, on the aerosol particles in the ExTL?

Small-scale cross tropopause mixing influences the chemical composition of aerosol particles in the UTLS.
The presented study by Joppe et al. (2024) shows that volcanic eruptions with subsequent cross-tropopause mixing are from importance, although they are not reaching the stratosphere directly but the upper troposphere and the tropopause region. Here, not only the direct mixing of solid aerosol particles

has an impact. Additionally, the mixing of precursor gases, such as SO_2, influences the sulfate aerosol in the LMS through the process of gas-to-particle conversion. If this occurs always or only under specific atmospheric conditions, for instance the location of the eruption relative to the jet stream, needs some more analysis with long-term observations to cover more volcanic eruptions under different atmospheric conditions.
Besides the effect of volcanic eruptions, this thesis shows another mechanism which contributes to small-scale gradients in the chemical composition of the aerosol within the UTLS, namely WCB uplift after low-level long-range transport.
Joppe et al. (2025) show that small to medium size wildfires in Canada also influence the aerosol composition over Europe. More precisely, the fire emissions get transported in low-level across the Atlantic and then get lifted by a WCB into the UTLS with subsequent cross-tropopause mixing. From this presented study, it seems like wet deposition of polluted aerosol is not efficient enough to remove these pollutants during the saturated uplift process. However, the question how the aerosol survives the transport can not be answered by now but is an open question for upcoming studies. Thus, the found results are from high interest as they indicate an additional pathway for BB aerosol into the UTLS besides the already known processes like pyro-convection. The importance of this subject is also discussed in a quite similar study with local WCB uplift close to the fire locations that was just published by Khaykin et al. (2025).

Which role does small-scale cross-tropopause mixing play on the radiation budget in the extratropical UTLS?

This question might be the most important question to answer, since it is important to know and understand the impact of aerosol particles on the radiation budget. This thesis is not able to provide a complete answer since it is based on measurement results and these measurements are limited in space and time and do not provide a full climatological view on aerosol particles in the UTLS.
Nevertheless, especially the study of Joppe et al. (2025), provides at least some indications on the possible radiative impact of cross-tropopause mixing of aerosol particles. Here, the TPC-TOSS was equipped with temperature measurements which give the opportunity to calculate vertical gradients in potential temperature. Here, these measurements offer some indications that the observed BB aerosol pollution leads to some small changes of the vertical gradient of potential temperature. The robustness of these indications, also for some larger pollution events, needs to be investigated in upcoming studies.

4.1 OUTLOOK

As pointed out before, this thesis is based on several case-studies which provide some new and important findings of aerosol particles in the UTLS. However, some questions remain open and partly some new questions arose during the discussion of the results.

First of all, the representation of non-stratospheric volcanic eruptions within global climate models is from interest to gain better estimations of the stratospheric sulfate aerosol. Here, some first studies are done by Matthias Kohl from the MPIC in close collaboration to this thesis and it is planned to publish these results in an upcoming manuscript using also the results by Kohl et al. (2025).

Further, it would be highly interesting to examine a global and long-term data set with respect to potential non-stratospheric volcanic eruptions. Here, the In-service Aircraft for a Global Observing System - Civil Aircraft for the Regular Investigation of the Atmosphere Based on an Instrument Container (IAGOS-CARIBIC) data are from great value. Moreover, an additional open question from this thesis, but also the study from Joppe et al. (2025), is the importance of these small-scale processes on the total aerosol in the UTLS and how much additional aerosol mass they bring into the UTLS. Therefore, it would be interesting to study mass-balances of aerosol compounds in the UTLS and their significance to large-scale processes.

One further open question which is based on the results of Joppe et al. (2025) is the aerosol processing within a WCB uplift event with respect to efficiency of wet deposition.

Finally, it can be concluded that this thesis offers valuable results, indicating that cross-tropopause mixing of aerosol particles and its precursor gases influence the chemical composition of the UTLS. However, it still leaves and provides open questions for upcoming research to further understand the importance of these processes and observations.

Part II

APPENDIX

A

SUPPLEMENTARY INFORMATION TO CHAPTER 1

A.1 CROSS-TROPOPAUSE MIXING

Cross-tropopause mixing can be identified by using so-called tracer-tracer correlation plots. Here, it is necessary to correlate one tropospheric and one stratospheric tracer against each other.
A tropospheric tracer has sources only in the troposphere and a rather constant stratospheric background mixing ratio. Here, CO or H_2O are suitable tracers for the use as tropospheric tracer. In contrast to this, a stratospheric tracer shows an increase or decrease in the stratosphere and a constant mixing ratio in the troposphere. Therefore, O_3 or N_2O can be used.
In the absence of cross-tropopause mixing, these tracer-tracer correlations show an L-shape, as each tracer has some variability within its regime, but they only connect in the edge of the L, which would mark the tropopause. In the atmosphere, cross-tropopause mixing occurs and therefore the typical L-shape is not purely found. More precisely, diagonal lines which connect the tropospheric with the stratospheric regime are observed. These lines are called mixing-lines as they represent mixing as connection and transition from tropospheric to stratospheric air masses or vice versa (see Fig. 19). The slope of these mixing-lines is not constant and can vary under different meteorological conditions (Fischer et al., 2000; Hoor et al., 2002).

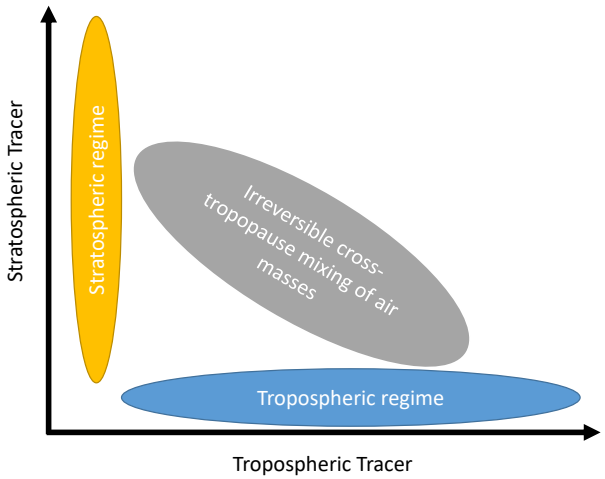

Figure 19: Illustration of tracer-tracer correlations with mixing-lines and how they can be used to identify cross-tropopause mixing.

B

SUPPLEMENTARY INFORMATION TO CHAPTER 2

B.1 BIN-SCHEMES OF THE UHSAS

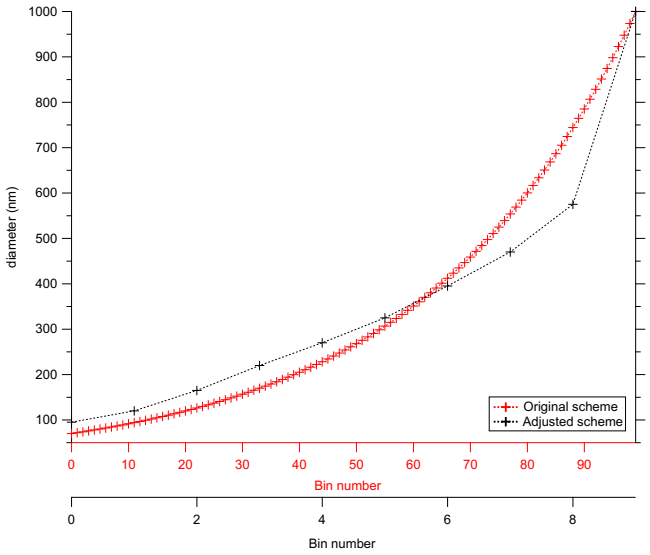

Figure 20: Overview of the bin boundaries of the old (red) and the new (black) bin-scheme used for the UHSAS analysis.

B.2 UHSAS-C INLET TUBING

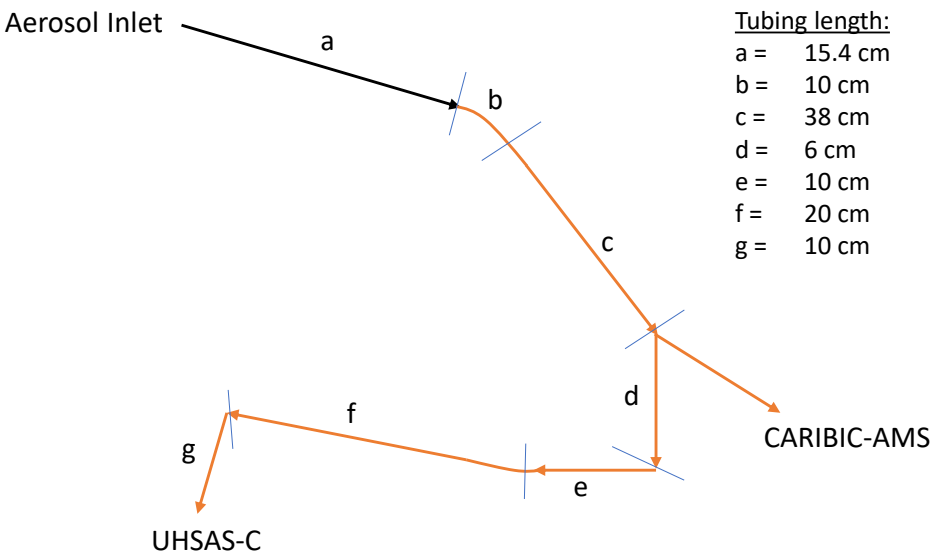

Figure 21: Sketch of the inlet design inside the Learjet cabin. The black tubing has an inner diameter of 1/4 inch stainless steel and all orange tubings are 1/8 inch stainless steel. The blue bars indicate the different sections of the inlet.

Table 1: Inlet tubing lengths configuration as input for the Particle Loss Calculator by von der Weiden et al. (2009).

Connected instruments	Flow ($L\,min^{-1}$)	Tube length (m)	1. & 2. inner diameter (mm)	Inclination angle (°)	Bend angle (°)
UHSAS-C, AMS	0.15	0.154	6.35	30	0
UHSAS-C, AMS	0.15	0.1	3.175	30	30
UHSAS-C, AMS	0.15	0.38	3.175	30	0
UHSAS-C	0.05	0.06	3.175	30	35
UHSAS-C	0.05	0.1	3.175	0	90
UHSAS-C	0.05	0.2	3.175	0	10
UHSAS-C	0.05	0.1	3.175	90	90

B.3 FLIGHT OVERVIEW TPEX

Table 2: Overview of the flights carried out during the TPEx misson in June 2024. The aircraft was based at Hohn airfield, Germany. Further, the information is given whether the TPC-TOSS was deployed during the flight or not. Times are given in UTC.

Date	Flight number	TOSS	Take-Off	Landing	Flight Duration
07.06.2024	F01	yes	07:36	09:53	02:17
11.06.2024	F03	yes	10:30	13:07	02:37
12.06.2024	F04	no	10:39	14:11	03:32
13.06.2024	F05	no	10:18	14:09	03:51
14.06.2024	F06	yes	07:07	09:18	02:11
17.06.2024	F07	yes	07:01	09:35	02:34
17.06.2024	F08	no	11:03	14:46	03:43
18.06.2024	F09	no	12:53	16:38	03:45
20.06.2024	F10	yes	07:06	09:46	02:40

B.4 DATA AVAILABILITY OF THE UHSAS DURING TPEX

The data availability of the UHSAS-C is influenced by some software issues, where the software freezes and it was only possible to solve by a complete restart of the instrument. As the operator was responsible for more instruments, this problem was not always directly recognized.
The UHSAS-A was running autonomously on the TPC-TOSS and started up after the release of the TPC-TOSS. During F06 no data was recorded due to a broken cable at one detector.

Table 3: Overview on the data availability of both UHSAS instruments during the TPEx mission.

Flight number	Learjet flight time (min)	TPC-TOSS flight time (min)	UHSAS-C availability (min)	UHSAS-A availability (min)	UHSAS-C Coverage	UHSAS-A Coverage
F03	157	79	157	79	100%	100%
F04	212	0	197	n.a.	93%	n.a.
F05	231	0	222	n.a.	96%	n.a.
F06	131	63	131	0	100%	0%
F07	154	111	138	111	90%	100%
F08	223	0	222	n.a.	99%	n.a.
F09	225	0	211	n.a.	93%	n.a.
F10	160	120	144	120	90%	100%
Total	1493	373	1422	310	95%	83%

B.5 COMPLEMENTARY DATA

The following table provides a more detailed overview of the additional observational data used in this thesis and the studies presented in Chap. 3.

Table 4: Complementary measurement data used in Chap. 3.

Species	Instrument Measurement platform	Reference	Used in Chapter:
CO	TRISTAR (HALO)	Tadic et al., 2017	3.1
O3	FAIRO (HALO)	Zahn et al., 2012	3.1
CO	PICARRO G2401 (DLR-Falcon)	N/A	3.1
O3	UV photometer (TE49C) (DLR-Falcon)	N/A	3.1
SO2	AIMS (DLR-Falcon)	Voigt et al., 2014	3.1
HNO3	AIMS (DLR-Falcon)	Voigt et al., 2014	3.1
CO	UMAQS (Learjet)	Müller et al., 2015	3.2
N2O	UMAQS (Learjet)	Müller et al., 2015	3.2
O3	2BTech Model 205 (Learjet, wingpod)	Bozem et al., 2025	3.2
T, RH	MOZAIC capacacitive hygrometer (Learjet + TPC-TOSS)	Petzold et al., 2015	3.2
H2O	FISH (Learjet)	Zöger et al., 1999	3.2
Organic aerosol samples	SOAP (Learjet, wingpod)	Breuninger et al., 2025	3.2
Aerosol impactor samples	MultiMINI8 cascade impactor (Learjet, wingpod)	Ebert et al., 2016	3.2

BIBLIOGRAPHY

Andreae, M. O. (Jan. 2007). „Aerosols Before Pollution“. *Science*, 315, 50–51. ISSN: 1095-9203. DOI: 10.1126/science.1136529. URL: http://dx.doi.org/10.1126/science.1136529.

Andreae, M. O., D. A. Hegg, and U. Baltensperger (2009). „Sources and nature of atmospheric aerosols“. *Aerosol pollution impact on precipitation: a scientific review*. Springer, pp. 45–89.

Arias, P. A., N. Bellouin, E. Coppola, R. G. Jones, G. Krinner, J. Marotzke, V. Naik, M. D. Palmer, G.-K. Plattner, J. Rogelj, et al. (2021). „Technical summary“. *Climate Change 2021: The Physical Science Basis. Contribution of Working Group I to the Sixth Assessment Report of the Intergovernmental Panel on Climate Change*, pp. 33–144. DOI: 10.1017/9781009157896.002. URL: https://www.ipcc.ch/report/sixth-assessment-report-working-group-i/.

Bauer, R., J.-U. Grooß, J. Ungermann, M. Bär, M. Geldenhuys, and L. Hoffmann (Dec. 2022). „The Mission Support System (MSS v7.0.4) and its use in planning for the SouthTRAC aircraft campaign“. *Geoscientific Model Development*, 15, 8983–8997. ISSN: 1991-9603. DOI: 10.5194/gmd-15-8983-2022. URL: http://dx.doi.org/10.5194/gmd-15-8983-2022.

Beaudor, M., D. Hauglustaine, J. Lathière, M. Van Damme, L. Clarisse, and N. Vuichard (Feb. 2025). „Evaluating present-day and future impacts of agricultural ammonia emissions on atmospheric chemistry and climate“. *Atmospheric Chemistry and Physics*, 25, 2017–2046. ISSN: 1680-7324. DOI: 10.5194/acp-25-2017-2025. URL: http://dx.doi.org/10.5194/acp-25-2017-2025.

Behera, S. N., M. Sharma, V. P. Aneja, and R. Balasubramanian (Aug. 2013). „Ammonia in the atmosphere: a review on emission sources, atmospheric chemistry and deposition on terrestrial bodies“. *Environmental Science and Pollution Research*, 20, 8092–8131. ISSN: 1614-7499. DOI: 10.1007/s11356-013-2051-9. URL: http://dx.doi.org/10.1007/s11356-013-2051-9.

Bethan, S., G. Vaughan, and S. J. Reid (Apr. 1996). „A comparison of ozone and thermal tropopause heights and the impact of tropopause definition on quantifying the ozone content of the troposphere“. *Quarterly Journal*

of the Royal Meteorological Society, 122, 929–944. ISSN: 1477-870X. DOI: 10.1002/qj.49712253207. URL: http://dx.doi.org/10.1002/qj.49712253207.

Birmili, W., T. Göbel, A. Sonntag, L. Ries, R. Sohmer, S. Gilge, I. Levin, and A. Stohl (Dec. 2010). „A case of transatlantic aerosol transport detected at the Schneefernerhaus Observatory (2650 m) on the northern edge of the Alps“. *Meteorologische Zeitschrift*, 19, 591–600. ISSN: 0941-2948. DOI: 10.1127/0941-2948/2010/0465. URL: http://dx.doi.org/10.1127/0941-2948/2010/0465.

Birner, T., D. Sankey, and T. G. Shepherd (July 2006). „The tropopause inversion layer in models and analyses“. *Geophysical Research Letters*, 33. ISSN: 1944-8007. DOI: 10.1029/2006gl026549. URL: http://dx.doi.org/10.1029/2006GL026549.

Birner, T., A. Dörnbrack, and U. Schumann (July 2002). „How sharp is the tropopause at midlatitudes?“ *Geophysical Research Letters*, 29. ISSN: 1944-8007. DOI: 10.1029/2002gl015142. URL: http://dx.doi.org/10.1029/2002GL015142.

Bohren, C. F. and D. R. Huffman (Apr. 1998). *Absorption and Scattering of Light by Small Particles*. Wiley. ISBN: 9783527618156. DOI: 10.1002/9783527618156. URL: http://dx.doi.org/10.1002/9783527618156.

Bönisch, H., A. Engel, T. Birner, P. Hoor, D. W. Tarasick, and E. A. Ray (Apr. 2011). „On the structural changes in the Brewer-Dobson circulation after 2000“. *Atmospheric Chemistry and Physics*, 11, 3937–3948. ISSN: 1680-7324. DOI: 10.5194/acp-11-3937-2011. URL: http://dx.doi.org/10.5194/acp-11-3937-2011.

Boucher, O. (2015). *Atmospheric Aerosols: Properties and Climate Impacts*. Springer Netherlands. ISBN: 9789401796491. DOI: 10.1007/978-94-017-9649-1. URL: http://dx.doi.org/10.1007/978-94-017-9649-1.

Bozem, H., P. Joppe, Y. Li, N. Emig, A. Afchine, A. Breuninger, J. Curtius, S. Hofmann, S. Ismayil, K. Kandler, D. Kunkel, A. Kutschka, H.-C. Lachnitt, A. Petzold, S. Richter, T. Röschenthaler, C. Rolf, L. Schneider, J. Schneider, A. Vogel, and P. Hoor (July 2025). „The TropoPause Composition TOwed Sensor Shuttle (TPC-TOSS): A new airborne dual platform approach for atmospheric composition measurements at the tropopause“. DOI: 10.5194/egusphere-2025-3175. URL: http://dx.doi.org/10.5194/egusphere-2025-3175.

Brasseur, G. P. and D. J. Jacob (2017). „Formulations of Radiative, Chemical, and Aerosol Rates“. *Modeling of Atmospheric Chemistry*. Cambridge University Press, 205–252.

Breuninger, A., P. Joppe, J. Wilsch, C. Schwenk, H. Bozem, N. Emig, L. Merkel, R. Rossberg, T. Keber, A. Kutschka, P. Waleska, S. Hofmann, S. Richter, F. Ungeheuer, K. Dörholt, T. Hoffmann, A. Miltenberger, J. Schneider, P. Hoor, and A. L. Vogel (July 2025). „Organic aerosols mixing across the tropopause and its implication for anthropogenic pollution of the UTLS“. DOI: 10.5194/egusphere-2025-3129. URL: http://dx.doi.org/10.5194/egusphere-2025-3129.

Brewer, A. W. (Oct. 1949). „Evidence for a world circulation provided by the measurements of helium and water vapour distribution in the stratosphere“. *Quarterly Journal of the Royal Meteorological Society*, 75, 351–363. ISSN: 1477-870X. DOI: 10.1002/qj.49707532603. URL: http://dx.doi.org/10.1002/qj.49707532603.

Butchart, N. (June 2014). „The Brewer-Dobson circulation“. *Reviews of Geophysics*, 52, 157–184. ISSN: 1944-9208. DOI: 10.1002/2013rg000448. URL: http://dx.doi.org/10.1002/2013RG000448.

Cai, Y., D. C. Montague, W. Mooiweer-Bryan, and T. Deshler (Sept. 2008). „Performance characteristics of the ultra high sensitivity aerosol spectrometer for particles between 55 and 800nm: Laboratory and field studies“. *Journal of Aerosol Science*, 39, 759–769. ISSN: 0021-8502. DOI: 10.1016/j.jaerosci.2008.04.007. URL: http://dx.doi.org/10.1016/j.jaerosci.2008.04.007.

Campuzano-Jost, P., C. D. Clark, H. Maring, D. S. Covert, S. Howell, V. Kapustin, K. A. Clarke, E. S. Saltzman, and A. J. Hynes (Oct. 2003). „Near-Real-Time Measurement of Sea-Salt Aerosol during the SEAS Campaign: Comparison of Emission-Based Sodium Detection with an Aerosol Volatility Technique“. *Journal of Atmospheric and Oceanic Technology*, 20, 1421–1430. ISSN: 1520-0426. DOI: 10.1175/1520-0426(2003)020<1421:nmosad>2.0.co;2. URL: http://dx.doi.org/10.1175/1520-0426(2003)020<1421:NMOSAD>2.0.CO;2.

Canagaratna, M., J. Jayne, J. Jimenez, J. Allan, M. Alfarra, Q. Zhang, T. Onasch, F. Drewnick, H. Coe, A. Middlebrook, A. Delia, L. Williams, A. Trimborn, M. Northway, P. DeCarlo, C. Kolb, P. Davidovits, and D. Worsnop (Jan. 2007). „Chemical and microphysical characterization of ambient aerosols with the aerodyne aerosol mass spectrometer“. *Mass*

Spectrometry Reviews, 26, 185–222. ISSN: 1098-2787. DOI: 10.1002/mas.20115. URL: http://dx.doi.org/10.1002/mas.20115.

Carlton, A. G., C. Wiedinmyer, and J. H. Kroll (July 2009). „A review of Secondary Organic Aerosol (SOA) formation from isoprene“. *Atmospheric Chemistry and Physics*, 9, 4987–5005. ISSN: 1680-7324. DOI: 10.5194/acp-9-4987-2009. URL: http://dx.doi.org/10.5194/acp-9-4987-2009.

Ceppi, P., F. Brient, M. D. Zelinka, and D. L. Hartmann (May 2017). „Cloud feedback mechanisms and their representation in global climate models“. *WIREs Climate Change*, 8. ISSN: 1757-7799. DOI: 10.1002/wcc.465. URL: http://dx.doi.org/10.1002/wcc.465.

Cohen, N. Y., E. P. Gerber, and O. Bühler (Sept. 2014). „What Drives the Brewer–Dobson Circulation?“ *Journal of the Atmospheric Sciences*, 71, 3837–3855. ISSN: 1520-0469. DOI: 10.1175/jas-d-14-0021.1. URL: http://dx.doi.org/10.1175/JAS-D-14-0021.1.

Copernicus Atmosphere Monitoring Service (2022). “CAMS global biomass burning emissions based on fire radiative power (GFAS)”. DOI: 10.24381/A05253C7. URL: https://ads.atmosphere.copernicus.eu/doi/10.24381/a05253c7.

Curtius, J. (Nov. 2006). „Nucleation of atmospheric aerosol particles“. *Comptes Rendus. Physique*, 7, 1027–1045. ISSN: 1878-1535. DOI: 10.1016/j.crhy.2006.10.018. URL: http://dx.doi.org/10.1016/j.crhy.2006.10.018.

Curtius, J., M. Heinritzi, L. J. Beck, M. L. Pöhlker, N. Tripathi, B. E. Krumm, P. Holzbeck, C. M. Nussbaumer, L. Hernández Pardo, T. Klimach, K. Barmpounis, S. T. Andersen, R. Bardakov, B. Bohn, M. A. Cecchini, J.-P. Chaboureau, T. Dauhut, D. Dienhart, R. Dörich, A. Edtbauer, A. Giez, A. Hartmann, B. A. Holanda, P. Joppe, K. Kaiser, T. Keber, H. Klebach, O. O. Krüger, A. Kürten, C. Mallaun, D. Marno, M. Martinez, C. Monteiro, C. Nelson, L. Ort, S. S. Raj, S. Richter, A. Ringsdorf, F. Rocha, M. Simon, S. Sreekumar, A. Tsokankunku, G. R. Unfer, I. D. Valenti, N. Wang, A. Zahn, M. Zauner-Wieczorek, R. I. Albrecht, M. O. Andreae, P. Artaxo, J. N. Crowley, H. Fischer, H. Harder, D. L. Herdies, L. A. T. Machado, C. Pöhlker, U. Pöschl, A. Possner, A. Pozzer, J. Schneider, J. Williams, and J. Lelieveld (Dec. 2024). „Isoprene nitrates drive new particle formation in Amazon’s upper troposphere“. *Nature*, 636, 124–130. ISSN: 1476-4687. DOI: 10.1038/s41586-024-08192-4. URL: http://dx.doi.org/10.1038/s41586-024-08192-4.

DeMott, P. J., T. C. J. Hill, C. S. McCluskey, K. A. Prather, D. B. Collins, R. C. Sullivan, M. J. Ruppel, R. H. Mason, V. E. Irish, T. Lee, C. Y. Hwang, T. S. Rhee, J. R. Snider, G. R. McMeeking, S. Dhaniyala, E. R. Lewis, J. J. B. Wentzell, J. Abbatt, C. Lee, C. M. Sultana, A. P. Ault, J. L. Axson, M. Diaz Martinez, I. Venero, G. Santos-Figueroa, M. D. Stokes, G. B. Deane, O. L. Mayol-Bracero, V. H. Grassian, T. H. Bertram, A. K. Bertram, B. F. Moffett, and G. D. Franc (Dec. 2015). „Sea spray aerosol as a unique source of ice nucleating particles“. *Proceedings of the National Academy of Sciences*, 113, 5797–5803. ISSN: 1091-6490. DOI: 10.1073/pnas.1514034112. URL: http://dx.doi.org/10.1073/pnas.1514034112.

Dines, W. (1919). „The characteristics of the free atmosphere“. *Geophysical Memoirs, Meteorological Office, London, United Kingdom*, 13, pp. 47–76. URL: https://digital.nmla.metoffice.gov.uk/IO_69c4ee61-f9df-47e0-b37f-71a1a2d43a1a/.

DMT (2013). “Ultra-High Sensitivity Aerosol Spectrometer Airborne (UHSAS-A) Operator Manual”.

Dobson, G. M. B. (1956). „Origin and distribution of the polyatomic molecules in the atmosphere“. *Proceedings of the Royal Society of London. Series A. Mathematical and Physical Sciences*, 236, pp. 187–193.

Drewnick, F., S. S. Hings, P. DeCarlo, J. T. Jayne, M. Gonin, K. Fuhrer, S. Weimer, J. L. Jimenez, K. L. Demerjian, S. Borrmann, and D. R. Worsnop (July 2005). „A New Time-of-Flight Aerosol Mass Spectrometer (TOF-AMS)—Instrument Description and First Field Deployment“. *Aerosol Science and Technology*, 39, 637–658. ISSN: 1521-7388. DOI: 10.1080/02786820500182040. URL: http://dx.doi.org/10.1080/02786820500182040.

Ebert, M., R. Weigel, K. Kandler, G. Günther, S. Molleker, J.-U. Grooß, B. Vogel, S. Weinbruch, and S. Borrmann (July 2016). „Chemical analysis of refractory stratospheric aerosol particles collected within the arctic vortex and inside polar stratospheric clouds“. *Atmospheric Chemistry and Physics*, 16, 8405–8421. ISSN: 1680-7324. DOI: 10.5194/acp-16-8405-2016. URL: http://dx.doi.org/10.5194/acp-16-8405-2016.

Eckhardt, S., A. Stohl, H. Wernli, P. James, C. Forster, and N. Spichtinger (Jan. 2004). „A 15-Year Climatology of Warm Conveyor Belts“. *Journal of Climate*, 17, 218–237. ISSN: 1520-0442. DOI: 10.1175/1520-0442(2004)017<0218:aycowc>2.0.co;2. URL: http://dx.doi.org/10.1175/1520-0442(2004)017<0218:AYCOWC>2.0.CO;2.

Ertel, H. (Sept. 1942). „Ein neuer hydrodynamischer Erhaltungssatz“. *Die Naturwissenschaften*, 30, 543–544. ISSN: 1432-1904. DOI: 10.1007/bf01475602. URL: http://dx.doi.org/10.1007/bf01475602.

Fischer, H., F. G. Wienhold, P. Hoor, O. Bujok, C. Schiller, P. Siegmund, M. Ambaum, H. A. Scheeren, and J. Lelieveld (Jan. 2000). „Tracer correlations in the northern high latitude lowermost stratosphere: Influence of cross-tropopause mass exchange“. *Geophysical Research Letters*, 27, 97–100. ISSN: 1944-8007. DOI: 10.1029/1999gl010879. URL: http://dx.doi.org/10.1029/1999GL010879.

Forster, P., T. Storelvmo, W. Armour, W. Collins, J.-L. Dufrense, D. Frame, D. Lunt, T. Mauritsen, M. Palmer, M. Watanabe, M. Wild, and H. Zhang (2021). „The Earth's Energy Budget, Climate Feedbacks, and Climate Sensitivity“. *Climate Change 2021: The Physical Science Basis. Contribution of Working Group I to the Sixth Assessment Report of the Intergovernmental Panel on Climate Change*, pp. 923–1054. DOI: https://doi.org/10.1017/9781009157896.009. URL: https://www.cambridge.org/core/books/climate-change-2021-the-physical-science-basis/earths-energy-budget-climate-feedbacks-and-climate-sensitivity/AE57C97E588FF3060C7C7E47DD4F3C6E.

Froyd, K. D., D. M. Murphy, T. J. Sanford, D. S. Thomson, J. C. Wilson, L. Pfister, and L. Lait (July 2009). „Aerosol composition of the tropical upper troposphere“. *Atmospheric Chemistry and Physics*, 9, 4363–4385. ISSN: 1680-7324. DOI: 10.5194/acp-9-4363-2009. URL: http://dx.doi.org/10.5194/acp-9-4363-2009.

Gettelman, A., P. Hoor, L. L. Pan, W. J. Randel, M. I. Hegglin, and T. Birner (Aug. 2011). „THE EXTRATROPICAL UPPER TROPOSPHERE AND LOWER STRATOSPHERE“. *Reviews of Geophysics*, 49. ISSN: 1944-9208. DOI: 10.1029/2011rg000355. URL: http://dx.doi.org/10.1029/2011RG000355.

Gilardoni, S. and S. Fuzzi (2017). „Chemical Composition of Aerosols of Different Origin“. *Atmospheric Aerosols*. John Wiley and Sons, Ltd. Chap. 4, pp. 183–221. ISBN: 9783527336449. DOI: https://doi.org/10.1002/9783527336449.ch4. eprint: https://onlinelibrary.wiley.com/doi/pdf/10.1002/9783527336449.ch4. URL: https://onlinelibrary.wiley.com/doi/abs/10.1002/9783527336449.ch4.

Guermoui, M., R. Abdelaziz, K. Gairaa, L. Djemoui, and S. Benkaciali (Jan. 2020). „New temperature-based predicting model for global solar radiation

using support vector regression“. *International Journal of Ambient Energy*, 43, 1397–1407. ISSN: 2162-8246. DOI: 10.1080/01430750.2019.1708792. URL: http://dx.doi.org/10.1080/01430750.2019.1708792.

Hansen, J., A. Lacis, R. Ruedy, and M. Sato (Jan. 1992). „Potential climate impact of Mount Pinatubo eruption“. *Geophysical Research Letters*, 19, 215–218. ISSN: 1944-8007. DOI: 10.1029/91gl02788. URL: http://dx.doi.org/10.1029/91GL02788.

Harrold, T. W. (Apr. 1973). „Mechanisms influencing the distribution of precipitation within baroclinic disturbances“. *Quarterly Journal of the Royal Meteorological Society*, 99, 232–251. ISSN: 1477-870X. DOI: 10.1002/qj.49709942003. URL: http://dx.doi.org/10.1002/qj.49709942003.

Hegglin, M. I., C. D. Boone, G. L. Manney, and K. A. Walker (Feb. 2009). „A global view of the extratropical tropopause transition layer from Atmospheric Chemistry Experiment Fourier Transform Spectrometer O3, H2O, and CO“. *Journal of Geophysical Research: Atmospheres*, 114. ISSN: 0148-0227. DOI: 10.1029/2008jd009984. URL: http://dx.doi.org/10.1029/2008JD009984.

Heintzenberg, J., F. Raes, S. E. Schwartz, I. Ackermann, P. Artaxo, T. S. Bates, C. Benkovitz, K. Bigg, T. Bond, J.-L. Brenguier, F. L. Eisele, J. Feichter, A. I. Flossman, S. Fuzzi, H.-F. Graf, J. M. Hales, H. Herrmann, T. Hoffmann, B. Huebert, R. B. Husar, R. Jaenicke, B. Kärcher, Y. Kaufman, G. S. Kent, M. Kulmala, C. Leck, C. Liousse, U. Lohmann, B. Marticorena, P. McMurry, K. Noone, C. O'Dowd, J. E. Penner, A. Pszenny, J.-P. Putaud, P. K. Quinn, U. Schurath, J. H. Seinfeld, H. Sievering, J. Snider, I. Sokolik, F. Stratmann, R. van Dingenen, D. Westphal, A. S. Wexler, A. Wiedensohler, D. M. Winker, and J. Wilson (2003). „Tropospheric Aerosols“. *Atmospheric Chemistry in a Changing World: An Integration and Synthesis of a Decade of Tropospheric Chemistry Research*. Ed. by G. P. Brasseur, R. G. Prinn, and A. A. P. Pszenny. Springer Berlin Heidelberg. Berlin, Heidelberg, pp. 125–156. ISBN: 978-3-642-18984-5. DOI: 10.1007/978-3-642-18984-5_4. URL: https://doi.org/10.1007/978-3-642-18984-5_4.

Heitmann, K., M. Sprenger, H. Binder, H. Wernli, and H. Joos (Apr. 2024). „Warm conveyor belt characteristics and impacts along the life cycle of extratropical cyclones: case studies and climatological analysis based on ERA5“. *Weather and Climate Dynamics*, 5, 537–557. ISSN: 2698-4016. DOI: 10.5194/wcd-5-537-2024. URL: http://dx.doi.org/10.5194/wcd-5-537-2024.

Hersbach, H., B. Bell, P. Berrisford, S. Hirahara, A. Horányi, J. Muñoz-Sabater, J. Nicolas, C. Peubey, R. Radu, D. Schepers, A. Simmons, C. Soci, S. Abdalla, X. Abellan, G. Balsamo, P. Bechtold, G. Biavati, J. Bidlot, M. Bonavita, G. De Chiara, P. Dahlgren, D. Dee, M. Diamantakis, R. Dragani, J. Flemming, R. Forbes, M. Fuentes, A. Geer, L. Haimberger, S. Healy, R. J. Hogan, E. Hólm, M. Janisková, S. Keeley, P. Laloyaux, P. Lopez, C. Lupu, G. Radnoti, P. de Rosnay, I. Rozum, F. Vamborg, S. Villaume, and J. Thépaut (June 2020). „The ERA5 global reanalysis“. *Quarterly Journal of the Royal Meteorological Society*, 146, 1999–2049. ISSN: 1477-870X. DOI: 10.1002/qj.3803. URL: http://dx.doi.org/10.1002/qj.3803.

Hoffmann, T., J. R. Odum, F. Bowman, D. Collins, D. Klockow, R. C. Flagan, and J. H. Seinfeld (Feb. 1997). „Formation of Organic Aerosols from the Oxidation of Biogenic Hydrocarbons“. *Journal of Atmospheric Chemistry*, 26, 189–222. ISSN: 1573-0662. DOI: 10.1023/a:1005734301837. URL: http://dx.doi.org/10.1023/A:1005734301837.

Hoinka, K. P. (Dec. 1997). „Die Tropopause: Entdeckung, Definition, Bestimmung“. *Meteorologische Zeitschrift*, 6, 281–303. ISSN: 0941-2948. DOI: 10.1127/metz/6/1997/281. URL: http://dx.doi.org/10.1127/metz/6/1997/281.

Holton, J. R., P. H. Haynes, M. E. McIntyre, A. R. Douglass, R. B. Rood, and L. Pfister (Nov. 1995). „Stratosphere-troposphere exchange“. *Reviews of Geophysics*, 33, 403–439. ISSN: 1944-9208. DOI: 10.1029/95rg02097. URL: http://dx.doi.org/10.1029/95RG02097.

Hoor, P., C. Gurk, D. Brunner, M. I. Hegglin, H. Wernli, and H. Fischer (Aug. 2004). „Seasonality and extent of extratropical TST derived from in-situ CO measurements during SPURT“. *Atmospheric Chemistry and Physics*, 4, 1427–1442. ISSN: 1680-7324. DOI: 10.5194/acp-4-1427-2004. URL: http://dx.doi.org/10.5194/acp-4-1427-2004.

Hoor, P., H. Fischer, L. Lange, J. Lelieveld, and D. Brunner (Mar. 2002). „Seasonal variations of a mixing layer in the lowermost stratosphere as identified by the CO-O3 correlation from in situ measurements“. *Journal of Geophysical Research: Atmospheres*, 107. ISSN: 0148-0227. DOI: 10.1029/2000jd000289. URL: http://dx.doi.org/10.1029/2000JD000289.

Hoskins, B. I. (Jan. 1991). „Towards a PV-θ view of the general circulation“. *Tellus A: Dynamic Meteorology and Oceanography*, 43, p. 27. ISSN: 1600-0870. DOI: 10.3402/tellusa.v43i4.11936. URL: http://dx.doi.org/10.3402/tellusa.v43i4.11936.

Inness, A., A.-M. Blechschmidt, I. Bouarar, S. Chabrillat, M. Crepulja, R. J. Engelen, H. Eskes, J. Flemming, A. Gaudel, F. Hendrick, V. Huijnen, L. Jones, J. Kapsomenakis, E. Katragkou, A. Keppens, B. Langerock, M. de Mazière, D. Melas, M. Parrington, V. H. Peuch, M. Razinger, A. Richter, M. G. Schultz, M. Suttie, V. Thouret, M. Vrekoussis, A. Wagner, and C. Zerefos (May 2015). „Data assimilation of satellite-retrieved ozone, carbon monoxide and nitrogen dioxide with ECMWF's Composition-IFS". *Atmospheric Chemistry and Physics*, 15, 5275–5303. ISSN: 1680-7324. DOI: 10.5194/acp-15-5275-2015. URL: http://dx.doi.org/10.5194/acp-15-5275-2015.

Jacobson, M. Z. (Feb. 2001). „Strong radiative heating due to the mixing state of black carbon in atmospheric aerosols". *Nature*, 409, 695–697. ISSN: 1476-4687. DOI: 10.1038/35055518. URL: http://dx.doi.org/10.1038/35055518.

Jaenicke, R. (Jan. 1980a). „Atmospheric aerosols and global climate". *Journal of Aerosol Science*, 11, 577–588. ISSN: 0021-8502. DOI: 10.1016/0021-8502(80)90131-7. URL: http://dx.doi.org/10.1016/0021-8502(80)90131-7.

Jaenicke, R. (1980b). „Natural aerosols". *Annals of the New York Academy of Sciences*, 338, pp. 317–329.

Joppe, P., J. Schneider, K. Kaiser, H. Fischer, P. Hoor, D. Kunkel, H.-C. Lachnitt, A. Marsing, L. Röder, H. Schlager, L. Tomsche, C. Voigt, A. Zahn, and S. Borrmann (July 2024). „The influence of extratropical cross-tropopause mixing on the correlation between ozone and sulfate aerosol in the lowermost stratosphere". *Atmospheric Chemistry and Physics*, 24, 7499–7522. ISSN: 1680-7324. DOI: 10.5194/acp-24-7499-2024. URL: http://dx.doi.org/10.5194/acp-24-7499-2024.

Joppe, P., J. Schneider, J. Wilsch, H. Bozem, A. Breuninger, J. Curtius, M. Ebert, N. Emig, P. Hoor, S. Ismayil, K. Kandler, D. Kunkel, I. Kurth, H.-C. Lachnitt, Y. Li, A. Miltenberger, S. Richter, C. Rolf, L. Schneider, C. Schwenk, N. Spelten, A. L. Vogel, Y. Cheng, and S. Borrmann (Apr. 2025). „Transport of Biomass Burning Aerosol into the Extratropical Tropopause Region over Europe via Warm Conveyor Belt Uplift". DOI: 10.5194/egusphere-2025-1346. URL: http://dx.doi.org/10.5194/egusphere-2025-1346.

Kaiser, J. W., A. Heil, M. O. Andreae, A. Benedetti, N. Chubarova, L. Jones, J.-J. Morcrette, M. Razinger, M. G. Schultz, M. Suttie, and G. R. van der Werf (Jan. 2012). „Biomass burning emissions estimated with a global fire assimilation system based on observed fire radiative power".

Biogeosciences, 9, 527–554. ISSN: 1726-4189. DOI: 10.5194/bg-9-527-2012. URL: http://dx.doi.org/10.5194/bg-9-527-2012.

Kaiser, K. (2024). „Chemical composition and transformation of submicron aerosol particles in the outflow of major population centres“. PhD thesis. DOI: 10.25358/OPENSCIENCE-10408. URL: https://openscience.ub.uni-mainz.de/handle/20.500.12030/10426.

Kalnay, E., M. Kanamitsu, R. Kistler, W. Collins, D. Deaven, L. Gandin, M. Iredell, S. Saha, G. White, J. Woollen, Y. Zhu, A. Leetmaa, R. Reynolds, M. Chelliah, W. Ebisuzaki, W. Higgins, J. Janowiak, K. C. Mo, C. Ropelewski, J. Wang, R. Jenne, and D. Joseph (Mar. 1996). „The NCEP/NCAR 40-Year Reanalysis Project“. *Bulletin of the American Meteorological Society*, 77, 437–471. ISSN: 1520-0477. DOI: 10.1175/1520-0477(1996)077<0437:tnyrp>2.0.co;2. URL: http://dx.doi.org/10.1175/1520-0477(1996)077<0437:TNYRP>2.0.CO;2.

Kaluza, T., D. Kunkel, and P. Hoor (May 2019). „Composite analysis of the tropopause inversion layer in extratropical baroclinic waves“. *Atmospheric Chemistry and Physics*, 19, 6621–6636. ISSN: 1680-7324. DOI: 10.5194/acp-19-6621-2019. URL: http://dx.doi.org/10.5194/acp-19-6621-2019.

Khaykin, S., S. Bekki, S. Godin-Beekmann, M. D. Fromm, P. Goloub, Q. Hu, B. Josse, A. Laeng, M. Meziane, D. A. Peterson, S. Pelletier, and V. Thouret (July 2025). „Stratospheric impact of the anomalous 2023 Canadian wildfires: the two vertical pathways of smoke“. DOI: 10.5194/egusphere-2025-3152. URL: http://dx.doi.org/10.5194/egusphere-2025-3152.

Kohl, M., C. Brühl, J. Schallock, H. Tost, P. Jöckel, A. Jost, S. Beirle, M. Höpfner, and A. Pozzer (July 2025). „New submodel for emissions from Explosive Volcanic ERuptions (EVER v1.1) within the Modular Earth Submodel System (MESSy, version 2.55.1)“. *Geoscientific Model Development*, 18, 3985–4007. ISSN: 1991-9603. DOI: 10.5194/gmd-18-3985-2025. URL: http://dx.doi.org/10.5194/gmd-18-3985-2025.

Kok, J. F., T. Storelvmo, V. A. Karydis, A. A. Adebiyi, N. M. Mahowald, A. T. Evan, C. He, and D. M. Leung (Jan. 2023). „Mineral dust aerosol impacts on global climate and climate change“. *Nature Reviews Earth and Environment*, 4, 71–86. ISSN: 2662-138X. DOI: 10.1038/s43017-022-00379-5. URL: http://dx.doi.org/10.1038/s43017-022-00379-5.

Konopka, P. and L. L. Pan (Sept. 2012). „On the mixing-driven formation of the Extratropical Transition Layer (ExTL)“. *Journal of Geophysical*

Research: Atmospheres, 117. ISSN: 0148-0227. DOI: 10.1029/2012jd017876. URL: http://dx.doi.org/10.1029/2012JD017876.

Kremser, S., L. W. Thomason, M. von Hobe, M. Hermann, T. Deshler, C. Timmreck, M. Toohey, A. Stenke, J. P. Schwarz, R. Weigel, S. Fueglistaler, F. J. Prata, J.-P. Vernier, H. Schlager, J. E. Barnes, J.-C. Antuña-Marrero, D. Fairlie, M. Palm, E. Mahieu, J. Notholt, M. Rex, C. Bingen, F. Vanhellemont, A. Bourassa, J. M. C. Plane, D. Klocke, S. A. Carn, L. Clarisse, T. Trickl, R. Neely, A. D. James, L. Rieger, J. C. Wilson, and B. Meland (May 2016). „Stratospheric aerosol-Observations, processes, and impact on climate: Stratospheric Aerosol“. *Reviews of Geophysics*, 54, 278–335. ISSN: 8755-1209. DOI: 10.1002/2015rg000511. URL: http://dx.doi.org/10.1002/2015RG000511.

Kroll, J. H. and J. H. Seinfeld (May 2008). „Chemistry of secondary organic aerosol: Formation and evolution of low-volatility organics in the atmosphere“. *Atmospheric Environment*, 42, 3593–3624. ISSN: 1352-2310. DOI: 10.1016/j.atmosenv.2008.01.003. URL: http://dx.doi.org/10.1016/j.atmosenv.2008.01.003.

Kunkel, D., P. Hoor, T. Kaluza, J. Ungermann, B. Kluschat, A. Giez, H.-C. Lachnitt, M. Kaufmann, and M. Riese (Oct. 2019). „Evidence of small-scale quasi-isentropic mixing in ridges of extratropical baroclinic waves“. *Atmospheric Chemistry and Physics*, 19, 12607–12630. ISSN: 1680-7324. DOI: 10.5194/acp-19-12607-2019. URL: http://dx.doi.org/10.5194/acp-19-12607-2019.

Kunz, A., P. Konopka, R. Müller, and L. L. Pan (Jan. 2011a). „Dynamical tropopause based on isentropic potential vorticity gradients“. *Journal of Geophysical Research*, 116. ISSN: 0148-0227. DOI: 10.1029/2010jd014343. URL: http://dx.doi.org/10.1029/2010JD014343.

Kunz, A., L. L. Pan, P. Konopka, D. E. Kinnison, and S. Tilmes (Dec. 2011b). „Chemical and dynamical discontinuity at the extratropical tropopause based on START08 and WACCM analyses: CHEMICAL AND DYNAMICAL DISCONTINUITY“. *Journal of Geophysical Research: Atmospheres*, 116. ISSN: 0148-0227. DOI: 10.1029/2011jd016686. URL: http://dx.doi.org/10.1029/2011JD016686.

Kupc, A., C. Williamson, N. L. Wagner, M. Richardson, and C. A. Brock (Jan. 2018). „Modification, calibration, and performance of the Ultra-High Sensitivity Aerosol Spectrometer for particle size distribution and volatility measurements during the Atmospheric Tomography Mission

(ATom) airborne campaign". *Atmospheric Measurement Techniques*, 11, 369–383. ISSN: 1867-8548. DOI: 10.5194/amt-11-369-2018. URL: http://dx.doi.org/10.5194/amt-11-369-2018.

Lachnitt, H.-C., P. Hoor, D. Kunkel, M. Bramberger, A. Dörnbrack, S. Müller, P. Reutter, A. Giez, T. Kaluza, and M. Rapp (Jan. 2023). „Gravity-wave-induced cross-isentropic mixing: a DEEPWAVE case study". *Atmospheric Chemistry and Physics*, 23, 355–373. ISSN: 1680-7324. DOI: 10.5194/acp-23-355-2023. URL: http://dx.doi.org/10.5194/acp-23-355-2023.

Lacis, A., J. Hansen, and M. Sato (Aug. 1992). „Climate forcing by stratospheric aerosols". *Geophysical Research Letters*, 19, 1607–1610. ISSN: 1944-8007. DOI: 10.1029/92gl01620. URL: http://dx.doi.org/10.1029/92GL01620.

Li, J., B. E. Carlson, Y. L. Yung, D. Lv, J. Hansen, J. E. Penner, H. Liao, V. Ramaswamy, R. A. Kahn, P. Zhang, O. Dubovik, A. Ding, A. A. Lacis, L. Zhang, and Y. Dong (May 2022). „Scattering and absorbing aerosols in the climate system". *Nature Reviews Earth and Environment*, 3, 363–379. ISSN: 2662-138X. DOI: 10.1038/s43017-022-00296-7. URL: http://dx.doi.org/10.1038/s43017-022-00296-7.

Liou, K.-N. (2002). *An introduction to atmospheric radiation*. Vol. 84. Elsevier.

Löber, M., L. Bondorf, T. Grein, S. Reiland, S. Wieser, F. Epple, F. Philipps, and T. Schripp (Aug. 2024). „Investigations of airborne tire and brake wear particles using a novel vehicle design". *Environmental Science and Pollution Research*, 31, 53521–53531. ISSN: 1614-7499. DOI: 10.1007/s11356-024-34543-9. URL: http://dx.doi.org/10.1007/s11356-024-34543-9.

Madonna, E., H. Wernli, H. Joos, and O. Martius (Jan. 2014). „Warm Conveyor Belts in the ERA-Interim Dataset (1979–2010). Part I: Climatology and Potential Vorticity Evolution". *Journal of Climate*, 27, 3–26. ISSN: 1520-0442. DOI: 10.1175/jcli-d-12-00720.1. URL: http://dx.doi.org/10.1175/JCLI-D-12-00720.1.

Mahnke, C., R. Weigel, F. Cairo, J.-P. Vernier, A. Afchine, M. Krämer, V. Mitev, R. Matthey, S. Viciani, F. D'Amato, F. Ploeger, T. Deshler, and S. Borrmann (Oct. 2021). „The Asian tropopause aerosol layer within the 2017 monsoon anticyclone: microphysical properties derived from aircraft-borne in situ measurements". *Atmospheric Chemistry and Physics*, 21, 15259–15282. ISSN: 1680-7324. DOI: 10.5194/acp-21-15259-2021. URL: http://dx.doi.org/10.5194/acp-21-15259-2021.

McGraw, Z., K. DallaSanta, L. M. Polvani, K. Tsigaridis, C. Orbe, and S. E. Bauer (Feb. 2024). „Severe Global Cooling After Volcanic Super-Eruptions? The Answer Hinges on Unknown Aerosol Size“. *Journal of Climate*, 37, 1449–1464. ISSN: 1520-0442. DOI: 10.1175/jcli-d-23-0116.1. URL: http://dx.doi.org/10.1175/JCLI-D-23-0116.1.

McKenna, D. S., P. Konopka, J. Grooß, G. Günther, R. Müller, R. Spang, D. Offermann, and Y. Orsolini (Aug. 2002). „A new Chemical Lagrangian Model of the Stratosphere (CLaMS) 1. Formulation of advection and mixing“. *Journal of Geophysical Research: Atmospheres*, 107. ISSN: 0148-0227. DOI: 10.1029/2000jd000114. URL: http://dx.doi.org/10.1029/2000JD000114.

Middlebrook, A. M., R. Bahreini, J. L. Jimenez, and M. R. Canagaratna (Mar. 2012). „Evaluation of Composition-Dependent Collection Efficiencies for the Aerodyne Aerosol Mass Spectrometer using Field Data“. *Aerosol Science and Technology*, 46, 258–271. ISSN: 1521-7388. DOI: 10.1080/02786826.2011.620041. URL: http://dx.doi.org/10.1080/02786826.2011.620041.

Mie, G. (Jan. 1908). „Beiträge zur Optik trüber Medien, speziell kolloidaler Metallösungen“. *Annalen der Physik*, 330, 377–445. ISSN: 1521-3889. DOI: 10.1002/andp.19083300302. URL: http://dx.doi.org/10.1002/andp.19083300302.

Miller, R. L. and I. Tegen (Dec. 1998). „Climate Response to Soil Dust Aerosols“. *Journal of Climate*, 11, 3247–3267. ISSN: 1520-0442. DOI: 10.1175/1520-0442(1998)011<3247:crtsda>2.0.co;2. URL: http://dx.doi.org/10.1175/1520-0442(1998)011<3247:CRTSDA>2.0.CO;2.

Molineaux, B. and P. Ineichen (July 1996). „Impact of Pinatubo aerosols on the seasonal trends of global, direct and diffuse irradiance in two northern mid-latitude sites“. *Solar Energy*, 58, 91–101. ISSN: 0038-092X. DOI: 10.1016/0038-092x(96)00051-5. URL: http://dx.doi.org/10.1016/0038-092X(96)00051-5.

Müller, S., P. Hoor, F. Berkes, H. Bozem, M. Klingebiel, P. Reutter, H. G. J. Smit, M. Wendisch, P. Spichtinger, and S. Borrmann (Feb. 2015). „In situ detection of stratosphere-troposphere exchange of cirrus particles in the midlatitudes“. *Geophysical Research Letters*, 42, 949–955. ISSN: 1944-8007. DOI: 10.1002/2014gl062556. URL: http://dx.doi.org/10.1002/2014GL062556.

Murphy, D. M., K. D. Froyd, I. Bourgeois, C. A. Brock, A. Kupc, J. Peischl, G. P. Schill, C. R. Thompson, C. J. Williamson, and P. Yu (June 2021). „Radiative and chemical implications of the size and composition of aerosol particles in the existing or modified global stratosphere“. *Atmospheric Chemistry and Physics*, 21, 8915–8932. ISSN: 1680-7324. DOI: 10.5194/acp-21-8915-2021. URL: http://dx.doi.org/10.5194/acp-21-8915-2021.

Pan, L. L., W. J. Randel, B. L. Gary, M. J. Mahoney, and E. J. Hintsa (Dec. 2004). „Definitions and sharpness of the extratropical tropopause: A trace gas perspective“. *Journal of Geophysical Research: Atmospheres*, 109. ISSN: 0148-0227. DOI: 10.1029/2004jd004982. URL: http://dx.doi.org/10.1029/2004JD004982.

Pandis, S. N., A. S. Wexler, and J. H. Seinfeld (June 1995). „Dynamics of Tropospheric Aerosols“. *The Journal of Physical Chemistry*, 99, 9646–9659. ISSN: 1541-5740. DOI: 10.1021/j100024a003. URL: http://dx.doi.org/10.1021/j100024a003.

Petzold, A., A. Döpelheuer, C. Brock, and F. Schröder (Sept. 1999). *Journal of Geophysical Research: Atmospheres*, 104, 22171–22181. ISSN: 0148-0227. DOI: 10.1029/1999jd900460. URL: http://dx.doi.org/10.1029/1999JD900460.

Petzold, A. and B. Kärcher (2012). „Aerosols in the Atmosphere“. *Atmospheric Physics*. Springer Berlin Heidelberg, 37–53. ISBN: 9783642301834. DOI: 10.1007/978-3-642-30183-4_3. URL: http://dx.doi.org/10.1007/978-3-642-30183-4_3.

Petzold, A., V. Thouret, C. Gerbig, A. Zahn, C. A. M. Brenninkmeijer, M. Gallagher, M. Hermann, M. Pontaud, H. Ziereis, D. Boulanger, J. Marshall, P. Nédélec, H. G. J. Smit, U. Friess, J.-M. Flaud, A. Wahner, J.-P. Cammas, A. Volz-Thomas, and I. Team (Jan. 2015). „Global-scale atmosphere monitoring by in-service aircraft – current achievements and future prospects of the European Research Infrastructure IAGOS“. *Tellus B: Chemical and Physical Meteorology*, 67, p. 28452. ISSN: 0280-6509. DOI: 10.3402/tellusb.v67.28452. URL: http://dx.doi.org/10.3402/tellusb.v67.28452.

Pikmann, J., F. Drewnick, F. Fachinger, and S. Borrmann (Nov. 2024). „Particulate emissions from cooking: emission factors, emission dynamics, and mass spectrometric analysis for different cooking methods“. *Atmospheric Chemistry and Physics*, 24, 12295–12321. ISSN: 1680-7324. DOI:

10.5194/acp-24-12295-2024. URL: http://dx.doi.org/10.5194/acp-24-12295-2024.

Ploeger, F., M. Diallo, E. Charlesworth, P. Konopka, B. Legras, J. C. Laube, J.-U. Grooß, G. Günther, A. Engel, and M. Riese (June 2021). „The stratospheric Brewer–Dobson circulation inferred from age of air in the ERA5 reanalysis“. *Atmospheric Chemistry and Physics*, 21, 8393–8412. ISSN: 1680-7324. DOI: 10.5194/acp-21-8393-2021. URL: http://dx.doi.org/10.5194/acp-21-8393-2021.

Ramanathan, V. and G. Carmichael (Mar. 2008). „Global and regional climate changes due to black carbon“. *Nature Geoscience*, 1, 221–227. ISSN: 1752-0908. DOI: 10.1038/ngeo156. URL: http://dx.doi.org/10.1038/ngeo156.

Rautenhaus, M., G. Bauer, and A. Dörnbrack (Jan. 2012). „A web service based tool to plan atmospheric research flights“. *Geoscientific Model Development*, 5, 55–71. ISSN: 1991-9603. DOI: 10.5194/gmd-5-55-2012. URL: http://dx.doi.org/10.5194/gmd-5-55-2012.

Riese, M., F. Ploeger, A. Rap, B. Vogel, P. Konopka, M. Dameris, and P. Forster (Aug. 2012). „Impact of uncertainties in atmospheric mixing on simulated UTLS composition and related radiative effects“. *Journal of Geophysical Research: Atmospheres*, 117. ISSN: 0148-0227. DOI: 10.1029/2012jd017751. URL: http://dx.doi.org/10.1029/2012JD017751.

Rossby, C. (Jan. 1940). „PLANETARY FLOW PATTERNS IN THE ATMOSPHERE“. *Quarterly Journal of the Royal Meteorological Society*, 66, 68–87. ISSN: 1477-870X. DOI: 10.1002/j.1477-870x.1940.tb00130.x. URL: http://dx.doi.org/10.1002/j.1477-870X.1940.tb00130.x.

Rémy, S., Z. Kipling, J. Flemming, O. Boucher, P. Nabat, M. Michou, A. Bozzo, M. Ades, V. Huijnen, A. Benedetti, R. Engelen, V.-H. Peuch, and J.-J. Morcrette (Nov. 2019). „Description and evaluation of the tropospheric aerosol scheme in the European Centre for Medium-Range Weather Forecasts (ECMWF) Integrated Forecasting System (IFS-AER, cycle 45R1)“. *Geoscientific Model Development*, 12, 4627–4659. ISSN: 1991-9603. DOI: 10.5194/gmd-12-4627-2019. URL: http://dx.doi.org/10.5194/gmd-12-4627-2019.

Rémy, S., A. Veira, R. Paugam, M. Sofiev, J. W. Kaiser, F. Marenco, S. P. Burton, A. Benedetti, R. J. Engelen, R. Ferrare, and J. W. Hair (Feb. 2017). „Two global data sets of daily fire emission injection heights since 2003“. *Atmospheric Chemistry and Physics*, 17, 2921–2942. ISSN: 1680-7324. DOI:

10.5194/acp-17-2921-2017. URL: http://dx.doi.org/10.5194/acp-17-2921-2017.

Santer, B. D., C. Bonfils, J. F. Painter, M. D. Zelinka, C. Mears, S. Solomon, G. A. Schmidt, J. C. Fyfe, J. N. S. Cole, L. Nazarenko, K. E. Taylor, and F. J. Wentz (Feb. 2014). „Volcanic contribution to decadal changes in tropospheric temperature“. *Nature Geoscience*, 7, 185–189. ISSN: 1752-0908. DOI: 10.1038/ngeo2098. URL: http://dx.doi.org/10.1038/ngeo2098.

Schneider, J., C. Schulz, F. Rubach, A. Ludwig, J. Wilsch, P. Joppe, C. Gurk, S. Molleker, L. Poulain, F. Obersteiner, T. Gehrlein, H. Bönisch, A. Zahn, P. Hoor, N. Emig, H. Bozem, S. Borrmann, and M. Hermann (Jan. 2025). „CARIBIC-AMS: A fully automated aerosol mass spectrometer for operation on routine passenger flights (IAGOS-CARIBIC): Instrument description and first flight application in the UTLS“. DOI: 10.5194/egusphere-2024-3969. URL: http://dx.doi.org/10.5194/egusphere-2024-3969.

Schneider, J., R. Weigel, T. Klimach, A. Dragoneas, O. Appel, A. Hünig, S. Molleker, F. Köllner, H.-C. Clemen, O. Eppers, P. Hoppe, P. Hoor, C. Mahnke, M. Krämer, C. Rolf, J.-U. Grooß, A. Zahn, F. Obersteiner, F. Ravegnani, A. Ulanovsky, H. Schlager, M. Scheibe, G. S. Diskin, J. P. DiGangi, J. B. Nowak, M. Zöger, and S. Borrmann (Jan. 2021). „Aircraft-based observation of meteoric material in lower-stratospheric aerosol particles between 15 and 68° N“. *Atmospheric Chemistry and Physics*, 21, 989–1013. ISSN: 1680-7324. DOI: 10.5194/acp-21-989-2021. URL: http://dx.doi.org/10.5194/acp-21-989-2021.

Schrod, J., E. S. Thomson, D. Weber, J. Kossmann, C. Pöhlker, J. Saturno, F. Ditas, P. Artaxo, V. Clouard, J.-M. Saurel, M. Ebert, J. Curtius, and H. G. Bingemer (Dec. 2020). „Long-term deposition and condensation ice-nucleating particle measurements from four stations across the globe“. *Atmospheric Chemistry and Physics*, 20, 15983–16006. ISSN: 1680-7324. DOI: 10.5194/acp-20-15983-2020. URL: http://dx.doi.org/10.5194/acp-20-15983-2020.

Schulz, C., J. Schneider, B. Amorim Holanda, O. Appel, A. Costa, S. S. de Sá, V. Dreiling, D. Fütterer, T. Jurkat-Witschas, T. Klimach, C. Knote, M. Krämer, S. T. Martin, S. Mertes, M. L. Pöhlker, D. Sauer, C. Voigt, A. Walser, B. Weinzierl, H. Ziereis, M. Zöger, M. O. Andreae, P. Artaxo, L. A. T. Machado, U. Pöschl, M. Wendisch, and S. Borrmann (Oct. 2018). „Aircraft-based observations of isoprene-epoxydiol-derived secondary organic aerosol (IEPOX-SOA) in the tropical upper tropo-

sphere over the Amazon region“. *Atmospheric Chemistry and Physics*, 18, 14979–15001. ISSN: 1680-7324. DOI: 10.5194/acp-18-14979-2018. URL: http://dx.doi.org/10.5194/acp-18-14979-2018.

Schwenk, C. and A. Miltenberger (Dec. 2024). „The role of ascent timescales for warm conveyor belt (WCB) moisture transport into the upper troposphere and lower stratosphere (UTLS)“. *Atmospheric Chemistry and Physics*, 24, 14073–14099. ISSN: 1680-7324. DOI: 10.5194/acp-24-14073-2024. URL: http://dx.doi.org/10.5194/acp-24-14073-2024.

Seinfeld, J. H. and S. N. Pandis (2016). *Atmospheric chemistry and physics: from air pollution to climate change*. John Wiley & Sons.

Soden, B. J., R. T. Wetherald, G. L. Stenchikov, and A. Robock (Apr. 2002). „Global Cooling After the Eruption of Mount Pinatubo: A Test of Climate Feedback by Water Vapor“. *Science*, 296, 727–730. ISSN: 1095-9203. DOI: 10.1126/science.296.5568.727. URL: http://dx.doi.org/10.1126/science.296.5568.727.

Solomon, S., K. H. Rosenlof, R. W. Portmann, J. S. Daniel, S. M. Davis, T. J. Sanford, and G.-K. Plattner (Mar. 2010). „Contributions of Stratospheric Water Vapor to Decadal Changes in the Rate of Global Warming“. *Science*, 327, 1219–1223. ISSN: 1095-9203. DOI: 10.1126/science.1182488. URL: http://dx.doi.org/10.1126/science.1182488.

Spichtinger, P. and K. M. Gierens (Jan. 2009a). „Modelling of cirrus clouds – Part 1a: Model description and validation“. *Atmospheric Chemistry and Physics*, 9, 685–706. ISSN: 1680-7324. DOI: 10.5194/acp-9-685-2009. URL: http://dx.doi.org/10.5194/acp-9-685-2009.

Spichtinger, P. and K. M. Gierens (Apr. 2009b). „Modelling of cirrus clouds – Part 2: Competition of different nucleation mechanisms“. *Atmospheric Chemistry and Physics*, 9, 2319–2334. ISSN: 1680-7324. DOI: 10.5194/acp-9-2319-2009. URL: http://dx.doi.org/10.5194/acp-9-2319-2009.

Sprenger, M. and H. Wernli (Aug. 2015). „The LAGRANTO Lagrangian analysis tool – version 2.0“. *Geoscientific Model Development*, 8, 2569–2586. ISSN: 1991-9603. DOI: 10.5194/gmd-8-2569-2015. URL: http://dx.doi.org/10.5194/gmd-8-2569-2015.

Stein, A. F., R. R. Draxler, G. D. Rolph, B. J. B. Stunder, M. D. Cohen, and F. Ngan (Dec. 2015). „NOAA's HYSPLIT Atmospheric Transport and Dispersion Modeling System“. *Bulletin of the American Meteorological*

Society, 96, 2059–2077. ISSN: 1520-0477. DOI: 10.1175/bams-d-14-00110.1. URL: http://dx.doi.org/10.1175/BAMS-D-14-00110.1.

Szopa, S., V. Naik, B. Adhikary, P. Artaxo, T. Berntsen, W. Collins, S. Fuzzi, L. Gallardo, A. Kiendler-Scharr, Z. Klimont, H. Liao, N. Unger, and P Zanis (2021). „Short-lived Climate Forcers“. *Climate Change 2021: The Physical Science Basis. CWorking Group I Contribution to the Sixth Assessment Report of the Intergovernmental Panel on Climate Change*, pp. 817–922. DOI: https://doi.org/10.1017/9781009157896.008.

Tadic, I., U. Parchatka, R. Königstedt, and H. Fischer (Apr. 2017). „In-flight stability of quantum cascade laser-based infrared absorption spectroscopy measurements of atmospheric carbon monoxide“. *Applied Physics B*, 123. ISSN: 1432-0649. DOI: 10.1007/s00340-017-6721-z. URL: http://dx.doi.org/10.1007/s00340-017-6721-z.

Thompson, D. W. J., S. Solomon, P. J. Kushner, M. H. England, K. M. Grise, and D. J. Karoly (Oct. 2011). „Signatures of the Antarctic ozone hole in Southern Hemisphere surface climate change“. *Nature Geoscience*, 4, 741–749. ISSN: 1752-0908. DOI: 10.1038/ngeo1296. URL: http://dx.doi.org/10.1038/ngeo1296.

Tinney, E. N., C. R. Homeyer, L. Elizalde, D. F. Hurst, A. M. Thompson, R. M. Stauffer, H. Vömel, and H. B. Selkirk (Dec. 2022). „A Modern Approach to a Stability-Based Definition of the Tropopause“. *Monthly Weather Review*, 150, 3151–3174. ISSN: 1520-0493. DOI: 10.1175/mwr-d-22-0174.1. URL: http://dx.doi.org/10.1175/MWR-D-22-0174.1.

Tuck, A. F., D. Baumgardner, K. R. Chan, J. E. Dye, J. W. Elkins, S. J. Hovde, K. K. Kelly, M. Loewenstein, J. J. Margitan, R. D. May, J. R. Podolske, M. H. Proffitt, K. H. Rosenlof, W. L. Smith, C. R. Webster, and J. C. Wilson (Jan. 1997). „The Brewer-Dobson Circulation In the Light of High Altitude In Situ Aircraft Observations“. *Quarterly Journal of the Royal Meteorological Society*, 123, 1–69. ISSN: 1477-870X. DOI: 10.1002/qj.49712353702. URL: http://dx.doi.org/10.1002/qj.49712353702.

Turhal, K., F. Plöger, J. Clemens, T. Birner, F. Weyland, P. Konopka, and P. Hoor (Dec. 2024). „Variability and trends in the potential vorticity (PV)-gradient dynamical tropopause“. *Atmospheric Chemistry and Physics*, 24, 13653–13679. ISSN: 1680-7324. DOI: 10.5194/acp-24-13653-2024. URL: http://dx.doi.org/10.5194/acp-24-13653-2024.

Vetter, T. (2004). „Berechnung der Mie-Streufunktionen zur Kalibrierung optischer Partikelzähler“. German. diplomathesis. Johannes Gutenberg-Universität Mainz.

Voigt, C., P. Jessberger, T. Jurkat, S. Kaufmann, R. Baumann, H. Schlager, N. Bobrowski, G. Giuffrida, and G. Salerno (Mar. 2014). „Evolution of CO2, SO2, HCl, and HNO3in the volcanic plumes from Etna“. *Geophysical Research Letters*, 41, 2196–2203. ISSN: 0094-8276. DOI: 10.1002/2013gl058974. URL: http://dx.doi.org/10.1002/2013GL058974.

Voigt, C., J. Lelieveld, H. Schlager, J. Schneider, J. Curtius, R. Meerkötter, D. Sauer, L. Bugliaro, B. Bohn, J. N. Crowley, T. Erbertseder, S. Groß, V. Hahn, Q. Li, M. Mertens, M. L. Pöhlker, A. Pozzer, U. Schumann, L. Tomsche, J. Williams, A. Zahn, M. Andreae, S. Borrmann, T. Bräuer, R. Dörich, A. Dörnbrack, A. Edtbauer, L. Ernle, H. Fischer, A. Giez, M. Granzin, V. Grewe, H. Harder, M. Heinritzi, B. A. Holanda, P. Jöckel, K. Kaiser, O. O. Krüger, J. Lucke, A. Marsing, A. Martin, S. Matthes, C. Pöhlker, U. Pöschl, S. Reifenberg, A. Ringsdorf, M. Scheibe, I. Tadic, M. Zauner-Wieczorek, R. Henke, and M. Rapp (Aug. 2022). „Cleaner Skies during the COVID-19 Lockdown“. *Bulletin of the American Meteorological Society*, 103, E1796–E1827. ISSN: 1520-0477. DOI: 10.1175/bams-d-21-0012.1. URL: http://dx.doi.org/10.1175/BAMS-D-21-0012.1.

Von der Weiden, S.-L., F. Drewnick, and S. Borrmann (Sept. 2009). „Particle Loss Calculator – a new software tool for the assessment of the performance of aerosol inlet systems“. *Atmospheric Measurement Techniques*, 2, 479–494. ISSN: 1867-8548. DOI: 10.5194/amt-2-479-2009. URL: http://dx.doi.org/10.5194/amt-2-479-2009.

Wallace, J. M. and P. V. Hobbs (2006). *Atmospheric science: an introductory survey*. Vol. 92. Elsevier.

Wild, M., M. Z. Hakuba, D. Folini, P. Dörig-Ott, C. Schär, S. Kato, and C. N. Long (Aug. 2018). „The cloud-free global energy balance and inferred cloud radiative effects: an assessment based on direct observations and climate models“. *Climate Dynamics*, 52, 4787–4812. ISSN: 1432-0894. DOI: 10.1007/s00382-018-4413-y. URL: http://dx.doi.org/10.1007/s00382-018-4413-y.

World Meteorological Organization, WMO (1957). *Meteorology - A three dimensional science*. Vol. 6, pp. 134–138. URL: https://library.wmo.int/idurl/4/42003.

Zahn, A., J. Weppner, H. Widmann, K. Schlote-Holubek, B. Burger, T. Kühner, and H. Franke (Feb. 2012). „A fast and precise chemiluminescence ozone detector for eddy flux and airborne application“. *Atmospheric Measurement Techniques*, 5, 363–375. ISSN: 1867-8548. DOI: 10.5194/amt-5-363-2012. URL: http://dx.doi.org/10.5194/amt-5-363-2012.

Zöger, M., A. Engel, D. S. McKenna, C. Schiller, U. Schmidt, and T. Woyke (Jan. 1999). „Balloon-borne in situ measurements of stratospheric H2O, CH4 and H2 at midlatitudes“. *Journal of Geophysical Research: Atmospheres*, 104, 1817–1825. ISSN: 0148-0227. DOI: 10.1029/1998jd100024. URL: http://dx.doi.org/10.1029/1998JD100024.

LIST OF FIGURES

LIST OF TABLES

ACRONYMS

GENERAL ACRONYMS

AC^3	Arctic amplification: Climate relevant atmospheric and surface processes and feedback mechanisms
ACP	Atmospheric Chemistry and Physics
AMS	aerosol mass spectrometer
AMT	Atmospheric Measurement Techniques
BB	biomass burning
BBOA	biomass burning organic aerosol
BC	black carbon
BDC	Brewer-Dobson circulation
CAMS	Copernicus Atmosphere Monitoring Service
CAFE-EU	Chemistry of the Atmosphere: Field Experiment over Europe
CARIBIC	Civil Aircraft for the Regular Investigation of the Atmosphere Based on an Instrument Container
CCN	cloud condensation nuclei
CLaMS	Chemical Lagrangian Model of the Stratosphere
CPC	condensation particle counter
C-ToF-AMS	compact time-of-flight aerosol mass spectrometer
CRC	Collaborative Research Centre
DFG	Deutsche Forschungsgemeinschaft
DLR	German Aerospace Center
DLR-FX	DLR Flight Experiments
DMA	differential mobility analyzer
DMT	Droplet Measurement Technologies
DWD	Deutscher Wetterdienst
ECMWF	European Centre for Medium-Range Weather Forecast
ERA5	ECMWF reanalysis fifth generation
ERF	effective radiative forcing
ExTL	extratropical transition layer

FRP	fire radiative power
FZJ	Forschungszentrum Jülich
GFAS	global fire assimilation system
GFD	Gesellschaft für Flugzieldarstellung GmbH
GPS	Global Positioning System
GUF	Goethe University Frankfurt am Main
HALO	High Altitude and LOng range research aircraft
HYSPLIT	Hybrid Single-Particle Lagrangian Integrated Trajectory model
IAGOS	In-service Aircraft for a Global Observing System
IAGOS-CARIBIC	In-service Aircraft for a Global Observing System - Civil Aircraft for the Regular Investigation of the Atmosphere Based on an Instrument Container
ICAO-ISA	International Civil Aviation Organization-International Standard Atmosphere
ICNAA	International Conference on Nucleation and Atmospheric Aerosols
ICON	Icosahedral Nonhydrostatic
IFS	Integrated Forecasting System
INP	ice nucleating particle
IPA	Institute for Physics of the Atmosphere, Mainz
IPCC	Intergovernmental Panel on Climate Change
JGU	Johannes Gutenberg University Mainz
KIT	Karlsruhe Institute of Technology
LAGRANTO	Lagrangian analysis tool
LMS	lowermost stratosphere
LRT	lapse-rate tropopause
MERRA2	Modern-Era Retrospective Analysis for Research and Applications, Version 2
MFC	mass flow controller
MCP	micro-channel plate
MPIC	Max Planck Institute for Chemistry
MSS	mission support system
NCEP	National Centers for Environmental Prediction
NCAR	National Center for Atmospheric Research

NOAA	National Oceanic and Atmospheric Administration
NPF	new particle formation
OA	organic aerosol
OPC	optical particle counter
PBL	planetary boundary layer
PLC	particle loss calculator
PJ	polar (front) jet stream
POA	primary organic aerosol
PSL	polystyrene latex
PV	potential vorticity
PVU	potential vorticity unit
rBC	refractory black carbon
SEM	scanning electron microscope
SOA	secondary organic aerosol
SOAP	sampler for organic aerosol particles
STP	standard temperature and pressure
STJ	sub-tropical jet stream
TOA	top of the atmosphere
TPChange	The Tropopause Region in a Changing Atmosphere
TPC-TOSS	Tropopause Composition Towed Sensor Shuttle
TPEx	Tropopause composition gradients and mixing experiment
TuDa	Technical University Darmstadt
UHSAS	Ultra-High Sensitivity Aerosol Spectrometer
UHSAS-A	airborne UHSAS
UHSAS-C	cabin UHSAS
UT	upper troposphere
UTLS	upper troposphere and lower stratosphere
VOC	volatile organic compound
WCB	warm conveyor belt
WMO	World Meteorological Organization

PHYSICAL SYMBOLS

m/z	m	mass to charge ratio

CHEMICAL SYMBOLS

CH_4	methane
Chl	chloride
CO	carbon monoxide
DMS	dimethyl sulfide
EC	elemental carbon
H_2O	water
HNO_3	nitric acid
NH_3	ammonia
NH_4	ammonium
NO_x	nitrogen oxides
N_2O	nitrous oxide
NO_3	nitrate
OC	organic carbon
OCS	carbonyl sulfide
O_3	ozone
SO_2	sulfur dioxide
SO_4	sulfate

LIST OF PUBLICATIONS

PEER REVIEWED PUBLICATIONS

Joppe, P., Schneider J., Kaiser K., Hoor P., Lachnitt H.-C., Tomsche, L., Voigt C., Schlager H., Marsing A., Zahn A., Röder L., Fischer H., Borrmann S. "The influence of extratropical cross-tropopause mixing on the correlation between ozone and sulfate aerosol in the lowermost stratosphere". ACP, https://doi.org/10.5194/acp-24-7499-2024, published 03 July 2024 .

Curtius, J., Heinritzi, M., Beck, L. J., Pöhlker, M. L., Tripathi, N., Krumm, B. E., ...**Joppe, P.**, ... and Lelieveld, J. (2024). "Isoprene nitrates drive new particle formation in Amazon's upper troposphere". Nature, 636(8041), 124-130, https://doi.org/10.1038/s41586-024-08192-4

Ehrlich, A., Crewell, S., Herber, A., Klingebiel, M., Lüpkes, C., Mech, M., ...**Joppe, P.**, ... and Wendisch, M. (2025). "A comprehensive in situ and remote sensing data set collected during the HALO–$(\mathcal{AC})^3$ aircraft campaign". Earth System Science Data, 17(3), 1295-1328, https://doi.org/10.5194/essd-17-1295-2025

Nussbaumer, C. M., Pozzer, A., Hewson, M., Ort, L., Krumm, B., Byron, J., Williams, J., **Joppe, P.**, Obersteiner, F., Zahn, A., Fischer, H. (2025). "Low tropospheric ozone over the Indo-Pacific warm pool related to non-electrified convection". *Geophysical Research Letters*, 52(5), e2024GL112788, https://doi.org/10.1029/2024GL112788.

Riese, M., Hoor, P., Rolf, C., Kunkel, D., Vogel, B., Köllner, F., ... , **Joppe, P.**,..., Zahn, A., Ziereis, H., Zlotos, L.O. (2025) "Long-range transport of polluted Asian summer monsoon air to high latitudes during the PHILEAS campaign in the boreal summer 2023". *Bulletin of the American Meteorological Society*, BAMS-D, https://doi.org/10.1175/BAMS-D-24-0232.1.

Wendisch, M., Crewell, S., Ehrlich, A., Herber, A., Kirbus, B., Lüpkes, C., ..., **Joppe, P.**, ... and Zinner, T. (2024). "Overview: quasi-Lagrangian observations of Arctic air mass transformations–introduction and initial results of the HALO–$(\mathcal{AC})^3$ aircraft campaign". Atmospheric Chemistry and Physics, 24(15), 8865-8892, https://doi.org/10.5194/acp-24-8865-2024

PUBLICATIONS UNDER REVIEW

Joppe, P., Schneider, J., Wilsch, J., Bozem, H., Breuninger, A., Curtius, J., ... & Borrmann, S. (2025). "Transport of Biomass Burning Aerosol into the Extratropical Tropopause Region over Europe via Warm Conveyor Belt Uplift". EGUsphere, 2025, 1-39.

Bozem, H., **Joppe, P.**, Li, Y., Emig, N., Afchine, A., Breuninger, A., ... & Hoor, P. (2025). "The TropoPause Composition TOwed Sensor Shuttle (TPC-TOSS): A new airborne dual platform approach for atmospheric composition measurements at the tropopause". EGUsphere, 2025, 1-34.

Schneider, J., Schulz, C., Rubach, F., Ludwig, A., Wilsch, J., **Joppe, P.**, ... & Hermann, M. (2025). "CARIBIC-AMS: A fully automated aerosol mass spectrometer for operation on routine passenger flights (IAGOS-CARIBIC): Instrument description and first flight application in the UTLS". EGUsphere, 2025, 1-36.

Breuninger, A., **Joppe, P.**, Wilsch, J., Schwenk, C., Bozem, H., Emig, N., ... & Vogel, A. L. (2025). "Organic aerosols mixing across the tropopause and its implication for anthropogenic pollution of the UTLS". EGUsphere, 2025, 1-30.

Konjari, P., Rolf, C., Krämer, M., Afchine, A., Spelten, N., Bartolome Garcia, I., ... , **Joppe, P.**, ... & Hoor, P. (2025). "Stratospheric Hydration and Ice Microphysics of a Convective Overshoot Observed during the TPEx Campaign over Sweden". EGUsphere, 2025, 1-27.

Kessler, S. D., Emig, N., Lachnitt H.-C., Kunkel, D., Bozem, H., Bense, V., **Joppe, P.**, Kaluza, T., Grooß, J.-U., Zahn, A., Ziereis, H., Riese, M., Hoor, P. " Biomass burning in Australia: No evidence for carbonyl sulfide (OCS) enhancement in fire plumes from in-situ measurements during SouthTRAC". Submitted to GRL, 2025

FIRST AUTHOR CONFERENCE CONTRIBUTIONS

Joppe, P., Schneider J., Kaiser K., Hoor P., Lachnitt H.-C., Tomsche, L., Voigt C., Schlager H., Marsing A., Zahn A., Röder L., Fischer H., Borrmann S. "The influence of extratropical cross-tropopause mixing on the correlation between ozone and sulfate aerosol in the lowermost stratosphere". Poster presentation. *HALO Status Seminar*, Oberpfaffenhofen, Germany, 07–09 November, 2023.

Joppe, P., Schneider J., Kaiser K., Hoor P., Kunkel, D., Lachnitt H.-C., Tomsche, L., Voigt C., Schlager H., Marsing A., Zahn A., Röder L., Fischer H., Borrmann S. "The influence of extratropical cross-tropopause mixing on the correlation between ozone and sulfate aerosol in the lowermost stratosphere". Oral presentation. *IAGOS User's Meeting*, Brussels, Belgium, 14–16 November, 2023.

Joppe, P., Schneider J., Kaiser K., Hoor P., Lachnitt H.-C., Tomsche, L., Voigt C., Schlager H., Marsing A., Zahn A., Röder L., Fischer H. Borrmann S. "The influence of extratropical cross-tropopause mixing on the correlation between ozone and sulfate aerosol in the lowermost stratosphere". Oral presentation. *TPChallenges International Conference*, Mainz, Germany, 11–15 March, 2024.

Joppe, P., Schneider J., Kaiser K., Hoor P., Lachnitt H.-C., Tomsche, L., Voigt C., Schlager H., Marsing A., Zahn A., Röder L., Fischer H., Borrmann S. "The influence of extratropical cross-tropopause mixing on the correlation between ozone and sulfate aerosol in the lowermost stratosphere". Poster presentation. https://doi.org/10.5194/egusphere-egu24-5076, Abstract EGU24-5076 . *European Geoscience Union General Assembly*, Vienna, Austria, 14-19 April, 2024.

Joppe, P., , Schneider J., Kaiser K., Hoor P., Lachnitt H.-C., Tomsche, L., Voigt C., Schlager H., Marsing A., Zahn A., Röder L., Fischer H., Borrmann S. "The influence of non-stratospheric volcanic eruptions on the stratospheric sulfate aerosol". Oral presentation. *VolImpact/SSiRC Workshop*, Greifswald, Germany, 23-25 April, 2025.

Joppe, P., **Eppers, O.**, Schneider J., Wilsch J., Bozem H., Breuninger A., Curtius J., Emig N., Hoor P., Kunkel D., Lachnitt H.-C., Kurth I., Li Y., Miltenberger A., Richter S., Rolf C., Schwenk C., Spelten N., Tost H., Vogel A., Cheng Y. and Borrmann S. "Observation of biomass burning aerosol from Canada in a warm conveyor belt outflow event over Europe during TPEx". Poster presentation. https://doi.org/10.5194/egusphere-egu25-15106 *European Geoscience Union General Assembly*, Vienna, Austria, 28 April-02 May, 2025.

Joppe, P., Schneider J., Wilsch J., Bozem H., Breuninger A., Curtius J., Emig N., Hoor P., Kunkel D., Lachnitt H.-C., Kurth I., Li Y., Miltenberger A., Richter S., Rolf C., Schwenk C., Spelten N., Tost H., Vogel A., Cheng Y. and Borrmann S. "Warm conveyor belt uplift as source for long-range transported biomass burning aerosol in the extratropical lowermost stratosphere over Europe". Oral presentation. *D-A-CH conference*, Bern, Switzerland, 23-27 June, 2025.

Joppe, P., Schneider J., Kaiser K., Wilsch J., Bozem H., Breuninger A., Curtius J., Emig N., Fischer H., Hoor P., Kunkel D., Kurth I., Lachnitt H.-C., Li Y., Marsing A., Miltenberger A., Richter S., Röder L., Rolf C., Schwenk C., Spelten N., Tomsche, L., N., Tost H., Vogel A., Voigt C., Schlager H., Zahn A., Cheng Y. and Borrmann S. "The influence of small-scale processes on the chemical composition of aerosol particles in the extratropical UTLS". Oral presentation. *International Conference on Nucleation and Atmospheric Aerosols (*ICNAA), Vienna, Austria, 23-28 August, 2025

CONTRIBUTIONS TO THIS THESIS

The presented work was made possible by the valuable and helpful contributions of colleagues that are acknowledged here.

This work was financially funded by the Deutsche Forschungsgemeinschaft (DFG) CRC 301, TPChange, grant no. 428312742 as well as internal resources of the Institute of Atmospheric Physics at the Johannes Gutenberg University Mainz and the former Particle (now: Aerosol) Chemistry Department at the Max Planck Institute for Chemistry.

In Chapter 1, some schematics were done by Dom Jack from the graphical office of the Max Planck Institute for Chemistry in Mainz. These schematics are marked with the according credits to the editor and are designed by the input by myself. All other graphics in this chapter are done by myself or cited using the according license and stated in the figure caption.

In Chapter 2 the schematic of the experimental setup was done by Dom Jack from the graphical office of the Max Planck Institute for Chemistry in Mainz based on my input. The data of the Learjet and TOSS altitude for the in-flight comparison were provided by Nicolas Emig, Heiko Bozem and Peter Hoor from the Institute of Atmospheric Physics at the Johannes Gutenberg University Mainz.
The particle loss calculation was carried out by myself with the measured inlet length by myself and Jonas Wilsch from the Max Planck Institute for Chemistry.
The overview map of the TPEx campaign was created using the public GIS data, provided on the Natural Earth website (http://www.naturalearthdata.com) with last access on 30 June 2025.
The meteorological overview of June 2024 was done with the reanalysis data from NCEP-NCAR, provided by NOAA-PSL, Boulder Colorado (https://psl.noaa.gov/, last access: 06 August 2025).

Chapter 3 presents three different studies which are currently published or in peer-review. These studies contain many different complementary data sets. This whole work would not have been possible without the contribution by the co-authors and therefore the detailed author contributions are also part of each publication itself. However, in the following the individual work by the colleagues is listed.
In the study in Sect. 3.1, data was collected with a huge effort of many people

and the whole campaign team during the COVID-19 lockdown in Germany. The C-ToF-AMS and OPC data was provided by Johannes Schneider and Katharina Kaiser. The SO_2 and nitric acid (HNO_3) measurements onboard the DLR-Falcon were provided by Laura Tomsche, Andreas Marsing and Christiane Voigt. Hans Schlager provided the CO and O_3 data from the DLR-Falcon. Andreas Zahn contributed with the O_3 measurements onboard HALO. Horst Fischer and Lenard Röder were responsible for the CO instrument on HALO.
The aircraft position and altitude data is provided by the Mess- und Sensortechnik of the DLR.
The campaign logistics was organized by DLR Flight Experiments (DLR-FX) with an excellent work of the pilots, making these data sets possible.
The analysis of this data was done by myself with conceptional input by Katharina Kaiser and Johannes Schneider. Additional meteorological data and LAGRANTO trajectory data for the analysis were provided by Hans-Christoph Lachnitt and Daniel Kunkel.
The study in Sect. 3.2 uses data from the TPEx mission which envolves many colleagues from the TPChange project and the companies enviscope GmbH for logistics and technical support as well as GFD GmbH for provision of the aircraft and the pilots.
During the campaign, I was responsible for the UHSAS and the corresponding data with support of Jonas Wilsch and Johannes Schneider, who also supported with the data of the CARIBIC-AMS and the OPC.
Nicolas Emig, Isabel Kurth, Heiko Bozem and Peter Hoor carried out the measurements of CO, N_2O and O_3 and were also responsible for the Global Positioning System (GPS) data from the Learjet and the TPC-TOSS.
Daniel Kunkel and Hans-Christoph Lachnitt supported the data analysis and the forecast by providing ECMWF data, also interpolated along the flight path.
Yun Li carried out the temperature and humidity measurements on the Learjet and the TPC-TOSS.
Christian Rolf and Nicole Spelten provided H_2O measurements from the Learjet.
Annette Miltenberger and Cornelis Schwenk supported the data analysis with LAGRANTO back trajectories.
Anna Breuninger and Alexander Vogel were responsible for the sampler for organic aerosol particles (SOAP) samples and the analysis of this data.
Martin Ebert, Konrad Kandler and Lisa Schneider provided data from the impactor and the analysis, using SEM.
Sarah Richter provided aerosol data from condensation particle counter (CPC) measurements.

The study in Sect. 3.3 was mainly done with the contribution of Heiko

Bozem and colleagues, as it describes the setup of the TPC-TOSS for the TPEx mission.
Here, I contributed during the conceptualization and scientific discussion to the overall manuscript and provided the part on the UHSAS characterization and calibration before and after the campaign. For the latter, I received help from Tobias Könemann and Jesse Steiner, both at DMT, to repair the UHSAS-A and during a first try on the laser alignment. When these attempts were unsuccessful, the instrument was sent to Jesse Steiner to try a best possible solution, even though support of the UHSAS-A had already been discontinued a few years ago.
Furthermore, I contributed to the manuscript by providing the campaign description.

DANKSAGUNG

Diese Arbeit wäre nicht ohne die Unterstützung einiger Kolleginnen und Kollegen, Freunde und Familie möglich gewesen. Hierfür möchte ich mich bei allen Wegbegleitern herzlich bedanken.
Die persönliche Danksagung wurde aus Datenschutzgründen von dieser elektronischen Version der Dissertation entfernt.

CURRICULUM VITAE

The curriculum vitae is not included in the electronic version.

DECLARATION

I hereby declare that I wrote the submitted dissertation without any unauthorized external assistance and used only sources acknowledged in the work. All textual passages which are appropriated verbatim or paraphrased from published and unpublished texts as well as all information obtained from oral sources are duly indicated and listed in accordance with bibliographical rules. In carrying out this research, I complied with the rules of standard scientific practice as formulated in the statutes of Johannes Gutenberg University Mainz to insure standard scientific practice. Therefore, used data for the publications is published onto Zenodo or was already published on the HALO-database with access by request.
For the translation of the English abstract written by myself into German, I used the help of DeepL Translate in order to keep the meaning of the translation as close as possible to the written English text. I checked the translation and corrected it wherever necessary.
Further, I used DeepL Write in order to check the grammar and to reformulate some passages of the dissertation. I checked these reformulations so that the meaning was not changed during the suggestions by DeepL Write. All other external contributions to data and analyses, presented in this study, are specified in detail on p. 189.

Mainz, 15 September 2025

Philipp Joppe